Coulomb explosion imaging of polyatomic molecules with femtosecond optical and XFEL pulses

by

Keyu Chen

B.S., Ocean University of China, China, 2018

AN ABSTRACT OF A DISSERTATION

submitted in partial fulfillment of the
requirements for the degree

DOCTOR OF PHILOSOPHY

Department of Physics
College of Arts and Sciences

KANSAS STATE UNIVERSITY
Manhattan, Kansas

2025

Abstract

Light-induced chemical reactions are essential processes that have a profound impact on various aspects of human life and technology. A prime example is photosynthesis, where photons from sunlight drive the conversion of water and carbon dioxide into oxygen and glucose, supporting vital life processes. Similarly, light-induced molecular dynamics are at the heart of photovoltaic technologies, which convert photon energy into electrical energy, providing a key energy source. Additionally, extensive research and practical applications exist in the field of molecular and biomolecular switches, where, among other applications, photons are employed to regulate enzyme activities. From a broader perspective, animals and humans can also be seen as undergoing a form of photosynthesis, as we produce vitamin D_3 in our skin when exposed to sunlight. The photochemical reaction involving the ring opening in the 1,3-cyclohexadiene molecule serves as a model system for the photosynthetic process of pre-vitamin D generation.

A thorough understanding of photo-induced molecular dynamics is essential for advancing our knowledge of these phenomena and enhancing our technological capabilities. Capturing such dynamics in real time has long been a challenge due to the ultrafast (femtosecond) timescales on which many fundamental chemical processes, including bond breaking, isomerization, and ring conversion, occur. Recent advancements in ultrafast spectroscopies and the development of intense light sources, from table-top optical lasers to X-ray free-electron lasers (XFELs), have enabled researchers to visualize these ultrafast dynamics in real time, acquiring a sequence of timed snapshots of evolving molecular structures. Among the most promising techniques for such 'molecular movie making' is the so-called Coulomb Explosion Imaging (CEI), which reveals molecular structures by rapidly ionizing molecules to highly charged states and detecting the momenta of the resulting ion fragments. When

implemented in a pump–probe configuration, where a pump light pulse initiates a reaction and a delayed probe pulse maps it with Coulomb explosion, CEI can provide unique insights into the evolution of molecular geometries on ultrafast timescales.

A successful application of the CEI technique to studies of polyatomic systems relevant to chemistry requires a detailed understanding of the fragmentation processes involved in the formation of Coulomb explosion patterns and of the observables involved in their formation. The main goals of this thesis are (i) to explore such fragmentation dynamics in a few model systems, (ii) to gain detailed understanding of the mechanisms involved in the laser-driven CEI, (iii) to develop efficient routines for handling and representing multidimensional CEI observables, and (iv) to use the developed procedure and the knowledge gained to image light-driven ring conversion reactions.

This thesis aims to investigate three different model systems. First, it focuses on the CEI of ethylene (C_2H_4) driven by intense femtosecond near-infrared laser pulses. Ethylene, a typical unsaturated hydrocarbon molecule, represents an attractive model system for CEI of polyatomic molecules because of its relative simplicity, accessibility for theory, and its planar geometry in the ground state of the neutral molecule. At the same time, it has enough complexity for studying different multi-particle breakup channels, particularly those involving one or more of the four hydrogen atoms, whose detection is one of the important capabilities of the CEI technique. The experimental results and detailed simulations presented here reveal and characterize competing concerted and sequential mechanisms involved in the formation of Coulomb explosion patterns for a triply-charged molecule, disentangle two different four-body breakup pathways for quadruple ionization ('cis-' and 'trans-fragmentation'), and explore possibilities and challenges for CEI relying on full atomization of the molecule (breakup into six atomic ions).

As a second model system, this thesis addresses CEI of 2(5H)-thiophenone (C_4H_4OS) employing intense femtosecond laser and XFEL pulses. Here, we first present static CEI patterns for this molecule obtained with 2.6 keV X-ray pulses at the European XFEL and

with table-top near-infrared lasers. The results show that a three-dimensional structure of such a complex, non-planar system can be mapped using CEI, including the 3D arrangement of its hydrogen atoms. While the data obtained with XFEL pulses ionizing the sulfur K-edge are more robust and exhibit much higher signal to noise ratio, the same signatures of the 3D molecular structure can still be revealed in the experiments with near-infrared lasers when using appropriate data analysis procedures. As a second step, we apply laser-driven CEI to image ring opening in 2(5H)-thiophenone (thiophenone) triggered by the absorption of an ultraviolet (UV) photon. The CEI patterns map the femtosecond evolution of this ring opening reaction, complementing earlier results obtained with time-resolved photoelectron spectroscopy and ultrafast electron diffraction.

Finally, we perform detailed simulations of the CEI of ring conversion dynamics in the 2,3-dihydrofuran (C_4H_6O) molecule upon deep-UV excitation and present the first experimental results demonstrating the feasibility of mapping this photoreaction with CEI employing table-top near-infrared lasers.

Overall, this thesis demonstrates the capability of CEI to image molecular structures and track ultrafast dynamics across a range of systems, and provides several essential recipes for understanding and representing multidimensional CEI data. These findings contribute to the broader understanding of photo-induced molecular reactions and provide a foundation for future studies of ultrafast photochemical processes.

Coulomb explosion imaging of polyatomic molecules with femtosecond optical and XFEL pulses

by

Keyu Chen

B.S., Ocean University of China, China, 2018

A DISSERTATION

submitted in partial fulfillment of the
requirements for the degree

DOCTOR OF PHILOSOPHY

Department of Physics
College of Arts and Sciences

KANSAS STATE UNIVERSITY
Manhattan, Kansas

2025

Approved by:

Major Professor
Artem Rudenko

Copyright

Keyu Chen

2025

Abstract

Light-induced chemical reactions are essential processes that have a profound impact on various aspects of human life and technology. A prime example is photosynthesis, where photons from sunlight drive the conversion of water and carbon dioxide into oxygen and glucose, supporting vital life processes. Similarly, light-induced molecular dynamics are at the heart of photovoltaic technologies, which convert photon energy into electrical energy, providing a key energy source. Additionally, extensive research and practical applications exist in the field of molecular and biomolecular switches, where, among other applications, photons are employed to regulate enzyme activities. From a broader perspective, animals and humans can also be seen as undergoing a form of photosynthesis, as we produce vitamin D_3 in our skin when exposed to sunlight. The photochemical reaction involving the ring opening in the 1,3-cyclohexadiene molecule serves as a model system for the photosynthetic process of pre-vitamin D generation.

A thorough understanding of photo-induced molecular dynamics is essential for advancing our knowledge of these phenomena and enhancing our technological capabilities. Capturing such dynamics in real time has long been a challenge due to the ultrafast (femtosecond) timescales on which many fundamental chemical processes, including bond breaking, isomerization, and ring conversion, occur. Recent advancements in ultrafast spectroscopies and the development of intense light sources, from table-top optical lasers to X-ray free-electron lasers (XFELs), have enabled researchers to visualize these ultrafast dynamics in real time, acquiring a sequence of timed snapshots of evolving molecular structures. Among the most promising techniques for such 'molecular movie making' is the so-called Coulomb Explosion Imaging (CEI), which reveals molecular structures by rapidly ionizing molecules to highly charged states and detecting the momenta of the resulting ion fragments. When

implemented in a pump–probe configuration, where a pump light pulse initiates a reaction and a delayed probe pulse maps it with Coulomb explosion, CEI can provide unique insights into the evolution of molecular geometries on ultrafast timescales.

A successful application of the CEI technique to studies of polyatomic systems relevant to chemistry requires a detailed understanding of the fragmentation processes involved in the formation of Coulomb explosion patterns and of the observables involved in their formation. The main goals of this thesis are (i) to explore such fragmentation dynamics in a few model systems, (ii) to gain detailed understanding of the mechanisms involved in the laser-driven CEI, (iii) to develop efficient routines for handling and representing multidimensional CEI observables, and (iv) to use the developed procedure and the knowledge gained to image light-driven ring conversion reactions.

This thesis aims to investigate three different model systems. First, it focuses on the CEI of ethylene (C_2H_4) driven by intense femtosecond near-infrared laser pulses. Ethylene, a typical unsaturated hydrocarbon molecule, represents an attractive model system for CEI of polyatomic molecules because of its relative simplicity, accessibility for theory, and its planar geometry in the ground state of the neutral molecule. At the same time, it has enough complexity for studying different multi-particle breakup channels, particularly those involving one or more of the four hydrogen atoms, whose detection is one of the important capabilities of the CEI technique. The experimental results and detailed simulations presented here reveal and characterize competing concerted and sequential mechanisms involved in the formation of Coulomb explosion patterns for a triply-charged molecule, disentangle two different four-body breakup pathways for quadruple ionization ('cis-' and 'trans-fragmentation'), and explore possibilities and challenges for CEI relying on full atomization of the molecule (breakup into six atomic ions).

As a second model system, this thesis addresses CEI of 2(5H)-thiophenone (C_4H_4OS) employing intense femtosecond laser and XFEL pulses. Here, we first present static CEI patterns for this molecule obtained with 2.6 keV X-ray pulses at the European XFEL and

with table-top near-infrared lasers. The results show that a three-dimensional structure of such a complex, non-planar system can be mapped using CEI, including the 3D arrangement of its hydrogen atoms. While the data obtained with XFEL pulses ionizing the sulfur K-edge are more robust and exhibit much higher signal to noise ratio, the same signatures of the 3D molecular structure can still be revealed in the experiments with near-infrared lasers when using appropriate data analysis procedures. As a second step, we apply laser-driven CEI to image ring opening in 2(5H)-thiophenone (thiophenone) triggered by the absorption of an ultraviolet (UV) photon. The CEI patterns map the femtosecond evolution of this ring opening reaction, complementing earlier results obtained with time-resolved photoelectron spectroscopy and ultrafast electron diffraction.

Finally, we perform detailed simulations of the CEI of ring conversion dynamics in the 2,3-dihydrofuran (C_4H_6O) molecule upon deep-UV excitation and present the first experimental results demonstrating the feasibility of mapping this photoreaction with CEI employing table-top near-infrared lasers.

Overall, this thesis demonstrates the capability of CEI to image molecular structures and track ultrafast dynamics across a range of systems, and provides several essential recipes for understanding and representing multidimensional CEI data. These findings contribute to the broader understanding of photo-induced molecular reactions and provide a foundation for future studies of ultrafast photochemical processes.

Table of Contents

Table of Contents x

List of Figures xv

Acknowledgements xxv

Dedication xxvii

Preface xxviii

1 Introduction 1

2 Initiating and probing molecular dynamics with light 7

2.1 Basics of light-molecule interactions 7

2.1.1 Electronic structure of molecules 7

2.1.2 Photoabsorption and Franck-Condon principle 11

2.1.3 Single-photon and multi-photon X-ray ionization 13

2.1.4 Laser-induced strong-field ionization 14

2.2 UV-induced photochemistry of ring molecules 16

2.2.1 UV-induced dynamics in 2(5H)-thiophenone 18

2.3 Coulomb explosion imaging 23

2.3.1 Concerted vs. sequential fragmentation and Native frame analysis . . 25

2.3.2 Coulomb explosion simulation 28

2.3.3 Data representation of Coulomb explosion simulation 29

2.3.4 Combining Coulomb explosion simulation with Native frame analysis 33

3 Experimental methods 36

3.1 X-ray Free Electron Laser (XFEL) . . . 37

3.2 Ultrafast laser system and optical layout . . . 43

3.2.1 Chirped pulse amplification . . . 44

3.2.2 Frequency-Resolved Optical Gating (FROG) . . . 46

3.2.3 Cross-correlation frequency-resolved optical gating . . . 48

3.2.4 Harmonic generation and nonlinear optics . . . 49

3.2.5 Pulse compression . . . 54

3.3 COLd Target Recoil Ion Momentum Spectrometer (COLTRIMS) . . . 61

3.3.1 Supersonic gas jet . . . 63

3.3.2 Spectrometer and detectors . . . 64

3.4 Data acquisition and processing for photoion measurements . . . 68

3.4.1 Coulomb explosion imaging: data representations . . . 73

4 Coulomb explosion imaging of ethylene with intense laser pulses 77

4.1 Three-body fragmentation in $C_2H_4{}^{3+}$ . . . 79

4.1.1 Three-body concerted breakup . . . 84

4.1.2 Three-body sequential fragmentation channel via $CH_2{}^{+}$ + $CH_2{}^{2+}$ intermediate . . . 87

4.1.3 Three-body sequential fragmentation channel via H^{+} + $C_2H_3{}^{2+}$ intermediate . . . 93

4.2 Four-body fragmentation in $C_2H_4{}^{4+}$ . . . 95

4.2.1 Coulomb explosion simulation for four-body fragmentation . . . 96

4.2.2 Disentangling signatures of cis- and trans-fragmentation in experimental data . . . 101

4.2.3 Modified Newton diagrams for more intuitive representation of four-body breakup . . . 105
4.3 Fragmentation of multiply charged ethylene into six atomic ions . . . 109
4.3.1 Coulomb explosion simulation for six-body complete fragmentation of ethylene . . . 110
4.3.2 Characterizing ethylene fragmentation into six atomic ions with incomplete coincident measurements . . . 115
4.3.3 Identifying individual hydrogens in the simulated six-body breakup data . . . 123
4.4 Conclusion . . . 128

5 UV-induced Coulomb explosion imaging of ring conversion dynamics in 2(5H)-thiophenone 130

5.1 X-ray induced Coulomb explosion imaging of 2(5H)-thiophenone . . . 131
5.1.1 Experimental conditions . . . 132
5.1.2 Experimental results compared with Coulomb explosion simulation of ground-state 2(5H)-thiophenone . . . 133
5.1.3 Experimental results under different representations compared with Coulomb explosion simulation . . . 138
5.2 Coulomb explosion imaging of UV-induced ring conversion dynamics of 2(5H)-thiophenone using table-top lasers . . . 144
5.2.1 Static Coulomb explosion imaging of thiophenone with intense NIR pulses . . . 145
5.2.2 UV-induced ring opening of 2(5H)-thiophenone probed with intense NIR pulses . . . 149
5.2.3 Conclusion . . . 157

6 Coulomb explosion imaging of ring conversion dynamics in 2,3-dihydrofuran 159

6.1 Coulomb explosion simulation of 2,3-dihydrofuran fragmentation 162

6.1.1 Coulomb explosion simulation of excited-state 2,3-dihydrofuran using *ab initio* multiple spawning (AIMS) simulations 165

6.2 Coulomb explosion imaging of UV-induced ring conversion dynamics in 2,3-dihydrofuran 178

6.2.1 Coulomb explosion imaging of 2,3-dihydrofuran with intense NIR pulses 179

6.2.2 UV pump–NIR probe experiment on 2,3-dihydrofuran 180

6.3 Conclusion and outlook 184

7 Summary and outlook 187

Bibliography 191

A Coulomb explosion imaging of three-body and four-body complete fragmentation of ethylene 221

A.1 Coulomb explosion imaging of three-body complete fragmentation of ethylene 221

A.1.1 Theoretical calculations provided 221

A.1.2 Concerted breakup and experimental data 223

A.1.3 Sequential breakup and experimental data 224

A.2 Coulomb explosion imaging of four-body complete fragmentation of ethylene 243

A.2.1 Theoretical calculations provided 243

A.2.2 Experimental data and simulation 244

B Appendix B 251

B.1 Appendix for Chapter 3 251

B.1.1 XFROG traces from third harmonic generation 251

B.2 Appendix for Chapter 5 251

B.3 Acronyms 256
B.4 List of Publications 257

List of Figures

1.1 **1896 plaque published in 'Nouvelle Iconographie de la Salpetrière', a medical journal.** 2

2.1 **Schematic potential energy curve showing ground and the first two excited electronic states of thiophenone.** 17

2.2 **Theoretically calculated ground-state equilibrium structure of thiophenone and the excited photoproducts.** 19

2.3 **Simulation of UV-induced molecular dynamics of thiophenone studied using TRPES.** 20

2.4 **Time-resolved relative populations of thiophenone and its major photoproducts following UV excitation.** 22

2.5 **Native frame coordination transformation.** 27

2.6 **Simulated KERs of ethylene three-body fragmentation.** 30

2.7 **Simulated conventional normalized relative Newton diagrams for ethylene molecule fragmentation.** 31

2.8 **Simulated momentum distributions of ion fragments of ethylene.** . 32

2.9 **Example of molecular frame transformation using ethylene.** 33

2.10 **Example of Native frame analysis of ethylene.** 35

3.1 **Schematic layout of the Linac Coherent Light Source (LCLS), the first hard X-ray free-electron laser.** 38

3.2 **Schematic plot of self-amplified spontaneous emission SASE.** 41

3.3 **Single-shot (a) and averaged (b) X-ray spectra measured in SASE mode (red) and self-seeded mode (blue).** . . . 44
3.4 **A schematic view of the evolution of pulse duration and amplitude during chirped-pulse amplification.** . . . 45
3.5 **Typical PULSAR output spectrum after second amplification stage.** 46
3.6 **SHG-FROG trace and setup overview.** . . . 48
3.7 **Nonlinear frequency mixing with a $\chi^{(2)}$ nonlinear crystal.** . . . 51
3.8 **Diagram of the PULSAR COLTRIMS optical arrangement.** . . . 52
3.9 **THG and FHG spectra.** . . . 53
3.10 **Schematic of prism compressors.** . . . 57
3.11 **XFROG traces measured at fixed delay stage position.** . . . 60
3.12 **Scheme of a reaction microscope.** . . . 62
3.13 **Scheme of MCP detector.** . . . 67
3.14 **Measured TOF spectra of ethylene.** . . . 71
3.15 **Photoion-photoion coincidence (PIPICO) maps of different channels of ethylene.** . . . 72
3.16 **Full Photoion-photoion-photoion coincidence (Tri-PICO) maps of ethylene.** . . . 72
3.17 **Kinetic energy release (KER) of (a) three- and (b) four-body fragmentation of ethylene from experiment.** . . . 73
3.18 **Exemplary Newton diagrams of the three-body fragmentation of ethylene from experimental data.** . . . 74
3.19 **Raw 3D momentum distribution of the four-body complete fragmentation data of ethylene with H^+, H^+, CH^+, and CH^+ detected.** 75

4.1 **Illustration of possible fragmentation scenarios for the three-body fragmentation channel of triply-charged ethylene.** 80
4.2 **Experimental Newton diagrams for ethylene three-body breakup into $H^+ + CH^+ + CH_2{}^+$ fragments.** 82
4.3 **Measured and simulated kinetic energy distributions of three-body fragmentation of ethylene.** 82
4.4 **Native frame analysis of three-body fragmentation of ethylene from experimental data.** 83
4.5 **Native frame analysis from the simulated three-body concerted breakup of ethylene.** 84
4.6 **Concerted three-body breakup events selected from the experimental data of ethylene compared with CES predictions.** 86
4.7 **Two-body fragmentation of $C_2H_4^{3+}$.** 88
4.8 **Native frame analysis of Coulomb explosion simulation of ethylene.** 91
4.9 **Three-body sequential fragmentation of ethylene via $CH_2^{2+} + CH_2^+$: simulation and experimental Analysis.** 92
4.10 **Three-body sequential fragmentation of ethylene via $H^+ + C_2H_3{}^{2+}$: simulation and experimental analysis.** 94
4.11 **Schematics of the four-body fragmentation channel of ethylene.** . 96
4.12 **Ground state geometry of ethylene modeled with Wigner distribution at 60 K.** 97
4.13 **Charge distributions and simulated momentum distribution from CES of ethylene four-body fragmentation.** 98
4.14 **Normalized Newton diagrams of trans- and cis-fragmentation of four-body breakup of ethylene obtained from CES.** 100

4.15 **Experimental Newton diagrams for four-body complete fragmentation of ethylene.** . . . 102
4.16 **Experimental separation of the contributions from trans- and cis-fragmentation of four-body breakup of ethylene.** . . . 103
4.17 **Comparison of KER for cis- and trans-fragmentation of four-body breakup of ethylene: CES simulation vs. experimental data.** . . . 104
4.18 **Vectors used for defining the (x, y)-momentum plane in Newton diagrams from CES of four-body breakup of ethylene.** . . . 106
4.19 **Comparison of measured and simulated modified Newton diagrams of complete four-body trans- and cis-fragmentation of ethylene using different molecular frame definitions.** . . . 108
4.20 **Sketch of the experimental setup and intuitive representation of the six-body fragmentation of ethylene.** . . . 110
4.21 **Vectors used for defining the (x, y)-momentum plane in Newton diagrams from CES of six-body complete fragmentation of ethylene.** 111
4.22 **Newton diagrams of six-body complete fragmentation of ethylene from Coulomb explosion simulation.** . . . 112
4.23 **Correlated angular distributions obtained from the CES of six-body complete fragmentation of ethylene in spherical coordinate representation.** . . . 114
4.24 **Experimental data represented using Newton diagrams for three, four- and five-body 'incomplete' channels with one C^+ ion detected of ethylene.** . . . 117
4.25 **Normalized angular distribution (ϕ) of H^+ momentum from different incomplete fragmentation channels of ethylene. (1 C^+ detected)** 118
4.26 **Newton diagrams for three-body $H^+ + C^+ + C^+$ channel of ethylene.** 120

4.27 **Newton diagrams for four- and five-body incomplete channels of ethylene with two C^+ detected.** . . . 121
4.28 **Normalized angular distribution (ϕ) of H^+ momentum from different incomplete fragmentation channels of ethylene. (2 C^+ detected)** 122
4.29 **Three-dimensional momentum distributions of ion fragments from six-body Coulomb explosion of ethylene.** . . . 124
4.30 **Three-dimensional momentum distributions of ion fragments from six-body CES of ethylene after randomization.** . . . 126
4.31 **Three-dimensional momentum distributions of ion fragments from six-body CES of ethylene after order rearrangement.** . . . 127

5.1 **Schematic of the experimental setup and molecular frame used for presenting Coulomb explosion data of thiophenone.** . . . 134
5.2 **Comparing the experimental data with Coulomb explosion simulation for ground-state thiophenone: H^+.** . . . 136
5.3 **Comparing the experimental data with Coulomb explosion simulation for ground-state thiophenone: C^+.** . . . 137
5.4 **Different representations of experimental ion momenta of thiophenone.** . . . 139
5.5 **Three-dimensional H^+ momentum distributions represented in spherical polar coordinates for various molecular geometries of thiophenone and its photoproduct.** . . . 142
5.6 **Newton diagrams of four-body fragmentation channels in (x, y)-plane of thiophenone.** . . . 145
5.7 **Three-dimensional H^+ momentum distributions of thiophenone represented in spherical polar coordinate.** . . . 148

5.8 **Cross-correlation of Argon ion as a function of pump–probe delay.** 149

5.9 **Newton diagrams of CES results for different groups of molecular geometries of thiophenone.** 151

5.10 **Projections of the three-dimensional momentum distributions for different groups of molecular geometries of thiophenone.** 152

5.11 **Newton diagrams showing C^+ momentum distributions at different pump–probe delays for $C^+ + C^+ + O^+ + S^+$ coincidence channel of thiophenone.** 154

5.12 **Newton diagrams of O^+ momentum distributions of thiophenone at different pump–probe delays for $C^+ + C^+ + O^+ + S^+$ coincidence channel of thiophenone.** 154

5.13 **Delay-dependent yields and angular distributions of O^+ ions from $C^+ + C^+ + O^+ + S^+$ coincidence channel of thiophenone.** 156

5.14 **2D map of delay-dependent (O^+, S^+) momentum angle for (a) $H^+ + C^+ + O^+ + S^+$ and (b) $C^+ + C^+ + O^+ + S^+$ coincidence channels of thiophenone.** 157

6.1 **VUV absorption spectra of 2,3-DHF.** 160

6.2 **Simulated KE distributions for 2,3-DHF Coulomb explosions.** . . . 164

6.3 **Newton diagrams from CES of the ground-state 2,3-DHF.** 164

6.4 **Three-dimensional momentum distributions of H^+ (a–d) and C^+ (e–h) ions from CES of ground-state 2,3-DHF represented in spherical polar coordinates.** 166

6.5 **KE obtained from CES of the AIMS trajectories for all excited-state 2,3-DHF geometries as a function of time for each C^+ fragment.** 169

6.6 **Same as Fig. 6.5 but only for the ring-opened geometries from CES of excited-state 2,3-DHF.** . . . 170
6.7 **Same as Fig. 6.5 but for the ring-puckered geometries from CES of excited-state 2,3-DHF.** . . . 170
6.8 **Same as Fig. 6.5 but for the ring-closed, non-puckered geometries from CES of excited-state 2,3-DHF.** . . . 171
6.9 **Same as Fig. 6.5 but for the three-membered ring group from CES of excited-state 2,3-DHF.** . . . 171
6.10 **Newton diagrams obtained from CES based on the AIMS trajectories for different excited-state geometries of 2,3-DHF.** . . . 172
6.11 **Newton diagrams obtained from CES of 2,3-DHF based on the AIMS trajectories for the ring-closed (non-puckered) group .** . . . 173
6.12 **Newton diagrams obtained from CES of 2,3-DHF based on the AIMS trajectories for the ring-puckered group.** . . . 175
6.13 **Same as Fig. 6.12 but for ring-opened group from CES of excited-state 2,3-DHF .** . . . 175
6.14 **3D momentum distribution of carbon ions obtained from Coulomb explosion simulations of the AIMS trajectories for excited-state geometries of 2,3-DHF** . . . 176
6.15 **(a–c) 3D momentum distributions of C^+ ions in spherical polar coordinates from CES of AIMS trajectories for excited-state 2,3-DHF; (d–f) corresponding azimuthal angle distributions.** . . . 177
6.16 **Azimuthal angle ϕ for carbon ion momenta as a function of time obtained from CES of the AIMS trajectories for excited-state 2,3-DHF** . . . 178

6.17 **Non-normalized Newton diagrams of the four- (a) and five-body (b) coincidence channels shown in (x, y)-plane from IR-probed only 2,3-DHF experiment** . . . 179

6.18 **KEDs of the four-body (a) and five-body (b) coincidence channels of 2,3-DHF from experiment.** . . . 180

6.19 **(a) Delay-dependent yield of four-body coincidence channel: $C^+ + C^+ + C^+ + O^+$ of 2,3-DHF. (b) Parent ion ($C_4H_6O^+$) yield as a function of pump–probe delay.** . . . 181

6.20 **Newton diagrams of the four-body coincidence channel of 2,3-DHF at different pump–probe delay bins**. . . . 183

6.21 **Angular distribution of the carbon ions from 2,3-DHF experiment as a function of pump–probe delay.** . . . 184

A.1 Theory Calculation of potential energy surface of triply-charged ethylene obtained from Dr. Paresh Modak and Prof. Loren Greenman. . . . 222

A.2 Native frame analysis of ethylene experimental data of three-body fragmentation. . . . 224

A.3 Newton diagrams for three-body concerted breakup of ethylene experimental data. . . . 225

A.4 Separated three-body concerted breakup of ethylene experimental data and Coulomb explosion simulation comparison. . . . 226

A.5 Three-body concerted breakup of ethylene experimental data separation. . . . 227

A.6 PIPICO maps of two-body fragmentation of ethylene used for analyzing the sequential breakup channels. . . . 228

A.7 Three-body sequential fragmentation of ethylene via $CH_2^+ + CH_2^{2+}$: simulation and experimental data analysis. . . . 229

A.8 Separated three-body sequential fragmentation channel of ethylene experimental data via $CH_2^+ + CH_2^{2+}$ intermediate. 230
A.9 Energy difference from PES of triply-charged ethylene of C–C bond extension, C–H bond stays in Franck-Condon point. 1D projection of Fig. A.1. 231
A.10 Energy difference from PES of triply-charged ethylene of C–H bond extension with C–C bond already extended to 150.92 Å. 1D projection of Fig. A.1. . . 232
A.11 CES of three-body fragmentation of ethylene via $CH_2^+ + CH_2^{2+}$ sequential breakup. 234
A.12 CES of three-body fragmentation of ethylene via $CH_2^+ + CH_2^{2+}$ sequential breakup with different rotation in the second step v1. 235
A.13 CES of three-body fragmentation of ethylene via $CH_2^+ + CH_2^{2+}$ sequential breakup with different rotation in the second step v2. 236
A.14 CES of three-body fragmentation of ethylene via $CH_2^+ + CH_2^{2+}$ sequential breakup with different rotation in the second step v3. 237
A.15 CES of three-body fragmentation of ethylene via $CH_2^+ + CH_2^{2+}$ sequential breakup with different rotation in the second step v2 with more sampling angles. 238
A.16 Three-body sequential fragmentation of ethylene via $H^+ + {C_2H_3}^{2+}$: simulation and experimental data comparison. 239
A.17 Energy difference from PES of triply-charged ethylene of C–H bond extension, C–C bond stays in Franck-Condon point. 1D projection of Fig. A.1. 240
A.18 Energy difference from PES of triply-charged ethylene of C–C bond extension with C–H bond extended already to 75.88 Å. 1D projection of Fig. A.1. . . . 241
A.19 CES of three-body fragmentation of ethylene via $H^+ + C_2H_3^{2+}$ sequential breakup with initial propagation time at 1 ps. 242

A.20 CES of three-body fragmentation of ethylene via $H^+ + C_2H_3^{2+}$ sequential breakup with initial propagation time at 100 fs. 243
A.21 CES of three-body fragmentation of ethylene via $H^+ + C_2H_3^{2+}$ sequential breakup with initial propagation time at 300 fs. 244
A.22 CES of three-body fragmentation of ethylene via $H^+ + C_2H_3^{2+}$ sequential breakup with initial propagation time at 500 fs. 245
A.23 CES of three-body fragmentation of ethylene via $H^+ + C_2H_3^{2+}$ sequential breakup with initial propagation time at 700 fs. 246
A.24 CES of three-body fragmentation of ethylene via $H^+ + C_2H_3^{2+}$ sequential breakup with initial propagation time at 50 ps. 247
A.25 Theory calculation of quadruply-charged ethylene potential energy surface. . 248
A.26 Newton diagrams of four-body cis-fragmentation of ethylene using CES. . . . 248
A.27 Modified Newton diagrams of four-body cis-fragmentation of ethylene from CES with different definitions of the momentum plane. 249
A.28 Modified Newton diagrams of four-body trans-fragmentation of ethylene from CES with different definitions of the molecular momentum plane. 249
A.29 Newton diagrams of four-body complete fragmentation of ethylene (experimental data for 2000 V voltage difference along the spectrometer). 250
A.30 Detected ion fragments acceptance: angular distribution from four-body complete fragmentation of ethylene experimental data. 250

B.1 Prism compression of third harmonic generation 252
B.2 Newton diagrams of O^+ momentum distributions at different pump–probe delays from $H^+ + C^+ + O^+ + S^+$ coincidence channel of thiophenone experimental data. 252

B.3 Quantified yield of O^+ momentum distribution projections from $H^+ + C^+ + O^+ + S^+$ coincidence channel of thiophenone experimental data. 253
B.4 2D map of angular distribution of relative O^+ momentum yield of thiophenone experimental data. 255

Acknowledgments

This work was supported by the Chemical Sciences, Geosciences, and Biosciences Division, Office of Basic Energy Sciences, Office of Science, US Department of Energy, under Award No. DEFG02-86ER13491.

This thesis would not have been possible without the support and help of extraordinary colleagues, to whom I am forever indebted. My deepest gratitude goes to everyone who helped and encouraged me throughout this journey. First and foremost, I would like to express my sincere thanks to my advisor, Prof. Artem Rudenko. You have not only taught me how to think critically and scientifically, but also how to remain patient, optimistic, and clear-minded under pressure. Your deep scientific knowledge, combined with your enthusiasm and energy, has been a constant source of motivation throughout my Ph.D. journey, and your guidance will continue to inspire me in the future. I am also deeply grateful to you for providing me with the opportunity to travel and take part in experiments at various national and international laboratories. These invaluable experiences have significantly broadened my scientific perspective and technical skills.

I am also incredibly grateful to Prof. Daniel Rolles for his critical insights on various projects. His comments, suggestions, and thought-provoking questions were instrumental in maintaining the quality and rigor of my research. I would like to sincerely thank my committee members: Prof. Artem Rudenko, Prof. Daniel Rolles, Prof. Uwe Thumm and Prof. Dinh-Liem Nguyen. Thank you, Prof. Thumm—your Quantum Mechanics courses have truly inspired me! Thank you, Prof. Nguyen, for kindly joining my committee as the outside member and stepping in to replace my previous committee member.

I have worked with the amazing graduate students and postdocs at James R. Macdonald lab (JRML) throughout these years. I would like to thank Surjendu Bhattacharyya for helping me throughout my Ph.D. You have been a good mentor and friend. I learned a

lot from you and I enjoyed our work in PULSAR COLTRIMS. I also appreciate working with Enliang Wang, Kurtis Borne, Anbu Venkatachalam, Shashank Pathak, Travis Severt, Farzaneh Ziaee, Huynh Lam, John Searles, Zane Phelps, Xiang Li, Chandan Bagdia, Lana Chaleunrath-Pham, Sanduni Kudagama, Tu Thanh Nguyen, Avijit Duley and Smita Ganguly throughout these years at JRML in some form or another. None of these experiments and research would have been possible without the support of Kevin Carnes, who built and maintained the DAQ system and Charles Fehrenbach, who always provided us a beautiful laser beam. The JRML technical staff, especially Justin Millette and Chris Aikens, helped maintain smooth operations. I would also like to thank Vince Needham for his assistance with computer support.

The experiment performed at European XFEL in Hamburg wouldn't be possible without Rebecca Bolls, Alice Green, Till Jahnke and the professional SQS team. I'm also very thankful to Yusong Liu from SLAC. I would also like to thank all the staff of the physics department, especially Kim Coy, who always took care of us, and all the friends I made here during this journey.

Finally, I would like to thank my parents for everything they did for me.

Dedication

To my parents, Longqiang and Chuanwu, for their endless love and support.

Chapter 1

Introduction

For a long time in history, humans sought to capture the intricate details of various objects and to trace the motion of fast-moving subjects. This effort can be traced back to the Victorian era of the 1840s and the emergence of chrono-photography, a photographic technique developed to look at objects in motion soon after the introduction of photography in 1839[1,2]. Later on, in 1895, the advent of X-ray technology enabled capturing much more 'detailed' images. Röntgen[3], who discovered X-ray radiation, immediately realized that X-rays could have medical applications, as illustrated in the famous picture shown in Fig. 1.1. John Hall-Edwards used this approach in a surgical operation as early as 1896, when he radiographed a hand with a needle stuck in it[4].

It was soon realized that a superior light source can enhance visibility, offer novel perspectives, and significantly advance the level of details that can be obtained using electromagnetic radiation as an imaging tool. Therefore, the development of more and more elaborated light sources in a very broad range of wavelengths was (and still remains) one of the important scientific and technological drivers during the 20th and 21st centuries. The important milestones relevant for this work include the discovery of synchrotron radiation in 1940s, which led to the construction of dedicated accelerator-based X-ray sources and brought up unique imaging capabilities, the advent of lasers in the 1960s, which revolution-

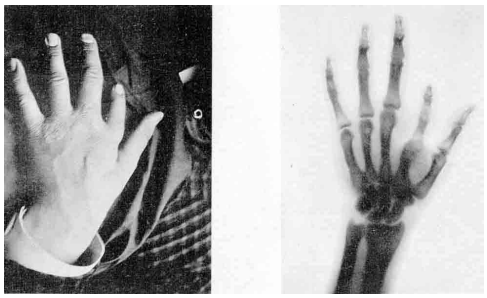

Figure 1.1: ***1896 plaque published in 'Nouvelle Iconographie de la Salpetrière', a medical journal.***
The left pictures shows a hand deformity, on the right the same hand is seen using radiography. The authors named the technique Röntgen photography.[5]

ized both scientific and technological applications of light, and the development of X-ray free-electron lasers over the last two decades.

One of the important aspects enabled by the advances of lasers is the ability to track the evolution of fast-moving systems. With the advent of femtosecond-duration laser pulses, it became possible to study many light-induced molecular processes in the time domain. These studies developed into the whole new field of *femtochemistry*[6], focusing on time-resolved studies of light-driven molecular dynamics. When molecules absorb light, they undergo rapid electronic and structural changes on femtosecond timescales, which are central to processes such as photosynthesis, vision, and solar energy conversion. Understanding these ultrafast dynamics is essential for revealing reaction mechanisms and guiding the design of light-controlled systems in chemistry, biology, and materials science.

Over the past few decades, numerous techniques have been developed to investigate ultrafast light-induced molecular dynamics employing different types of pump–probe spectroscopy. Technologically, these methods can be categorized based on their detection modality: capturing photons, electrons (either as direct probes or resulting from photoionization), or molecular fragments such as ions and neutrals. Scientifically, some of the techniques focus on the evolving electronic configuration of molecules, while others are more suitable for studying the motion of the nuclei, i.e., the evolution of molecular geometry. Nowadays,

one of the widely used approaches for studying ultrafast changes of electronic structures includes femtosecond (or even attosecond) transient absorption spectroscopy, in which a pump pulse initiates the reaction and the absorption spectrum of a probe pulse is measured as a function of pump–probe delay[7]. Another powerful approach is valence-shell time-resolved photoelectron spectroscopy (TRPES), where the probe pulse ionizes the evolving system, and the time-dependent electronic configuration is deduced from the measured kinetic energies of the photoelectrons. These approaches can be connected to evolving molecular geometry using theory, enabling time-resolved mapping of chemical reaction pathways[8,9]. Methods typically used for direct imaging of the changing molecular geometry (i.e., tracing the motion of the atomic nuclei) include several diffraction-based techniques. One of them is X-ray diffraction, where scattered X-ray photons encode structural information of the molecular target. Already very successful for static structural imaging at synchrotron radiation sources, with the development of XFELs, this technique has significantly advanced the imaging of transient molecular structures[10]. Ultrafast electron diffraction (UED) is also widely used for capturing real-time structural changes in molecules. In a typical UED experiment, a pulsed beam of high-energy electrons scatters off the sample, and the resulting diffraction pattern encodes the atomic positions at the moment of probing, allowing the reconstruction of transient molecular structures. Owing to the strong interaction between electrons and matter, UED[11,12] provides higher scattering cross sections than X-ray methods, making it especially useful for studying dilute gas-phase targets. Varieties of this concept employing the molecule's own electrons to image its structure include laser-induced electron diffraction[13], where the ionized electrons are driven back to the parent ion by the oscillating laser field, inner-shell photoelectron diffraction[14], where the photoelectrons emitted from a localized core level of a particular atom form a diffraction pattern by scattering on its neighbors.

Most of these techniques utilize an excitation (pump) pulse that prepares the molecular sample in an electronically excited state, initiating wavepacket dynamics. After a controlled

delay, a subsequent probe pulse interacts with the evolving molecular wavepacket, projecting it onto another state. This projection yields measurable observables and contains encoded information about the ultrafast molecular evolution.

While widely successful for imaging a variety of important light-induced reactions, the techniques listed above still face a number of limitations. To name a few, transient absorption and TRPES techniques are not directly sensitive to the positions of the nuclei and require significant theoretical calculations to connect to the molecular structure. Diffraction-based methods, which can directly reveal the geometry of a molecule, have much higher scattering cross sections for heavier fragments, as the cross section scales with the atomic number Z. As a result, these methods have difficulty directly mapping the positions of hydrogen atoms. Due to the rather low absolute scattering cross sections, X-ray diffraction struggles with low-density gas-phase samples of small molecules. For UED, the achievable temporal resolution is still limited to 100 fs because of the duration of the electron pulses available. Moreover, most of these techniques deal with an ensemble of molecules, which results in averaging the observables over different spatial orientations, struggles with disentangling mixed photoinduced processes, and experiences difficulties in mapping weak, minor reaction channels.

To overcome some of these limitations, the present thesis explores the capabilities of Coulomb explosion imaging (CEI), a technique that enables very intuitive mapping of molecular geometries by detecting several photo-ions generated by multiple ionization of a molecule and subsequent fragmentation of the created highly-charged molecular ion. Initially developed for the collisions of fast molecular ion beams with thin foils[15], this approach can provide few-femtosecond time resolution when used as a probe in pump–probe experiments with ultrashort laser pulses. In this work, CEI driven by femtosecond laser and XFEL pulses was applied to several model systems, with the central goal to establish basic experimental routines, understand and partially overcome the limitations of this technique, and employ it to study some exemplary photochemical reactions unfolding on a femtosec-

ond time scale. All experiments described in this thesis utilize coincidence momentum imaging of several (three to five) ionic fragments, employing COLd Target Recoil Ion Momentum Spectroscopy (COLTRIMS)[16,17] as a technical tool to achieve these goals. Such highly-dimensional measurements required the development and application of advanced data analysis procedures and detailed Coulomb explosion simulations, which constitute a substantial part of this work.

The work on this dissertation provided me with an invaluable opportunity to engage in a broad spectrum of research projects and experimental work conducted at both the James R. Macdonald Laboratory (JRML) and international facilities such as the European XFEL. The studies presented here represent a focused selection of projects to which I made substantial contributions.

The thesis document is organized as follows. Chapter 2 introduces the background needed to understand ultrafast photochemistry problems that are addressed in this work, introduces the basics of the CEI approach in comparison with other time-resolved techniques, and provides a detailed description of Coulomb explosion simulations (CES) used to guide experiments and to facilitate data interpretation. Chapter 3 discusses the basic principles and specific characteristics of the laser sources used, including some fundamentals of free-electron lasers, describes the COLTRIMS setups used at the JRML and at the European XFEL, and explains main data acquisition and analysis procedures employed in Coulomb explosion imaging experiments.

Chapter 4 presents the results of Coulomb explosion imaging experiments on ethylene performed with near-infrared laser pulses at the JRML. This work focuses on complete characterization of three- and four-body breakup channels and on the analysis of the events resulting from the complete atomization of the molecule (i.e., six-body) breakup, which is studied by detecting three, four, or five of the six resulting atomic ions in coincidence. The Chapter highlights a detailed comparison between CES and experimental results employing Newton diagrams, kinetic energy, and angular distributions of the fragments, as well as

recently developed Native frame analyses[18,19]. Chapter 5 focuses on the Coulomb explosion imaging of thiophenone. The first section presents the results from a submitted manuscript on static Coulomb explosion imaging of thiophenone performed using the European XFEL, highlighting the ability of XFEL-driven CEI to capture the 3D molecular structure including in-plane and out-of-plane proton positions. The second part of this chapter investigates UV-induced ring-opening dynamics in thiophenone using time-resolved CEI with a tabletop laser system in JRML. Chapter 6 focuses on the CES of the UV-induced ring conversion dynamics of 2,3-dihydrofuran (2,3-DHF) and presents preliminary experimental results highlighting the feasibility of this study. Finally, Chapter 7 provides a summary of the work presented in this thesis and a brief outlook for the near future developments.

Chapter 2

Initiating and probing molecular dynamics with light

The goal of this chapter is to provide some fundamentals that are needed to present and interpret the main results of this work. Starting with several basic concepts of molecular physics, we will then discuss regimes of light-molecule interactions relevant for this thesis and make a brief introduction to the photochemistry of ring molecules. It will be followed by an introduction in Coulomb explosion imaging as the main experimental approach used in this work, and presentation of Coulomb explosion simulations, which are used throughout this thesis. Physical variables used in this chapter are given in atomic units.

2.1 Basics of light-molecule interactions

2.1.1 Electronic structure of molecules

For a molecule composed of the number of N_{nuc} nuclei having atomic numbers $z_1, ..., z_{N_{nuc}}$, the Hamiltonian operator will be:

$$H_{mol} = T_{el} + T_{nuc} + V_{el-el} + V_{nuc-nuc} + V_{el-nuc} \tag{2.1}$$

With given electron mass m_{el} and the n^{th} nucleus mass M_n, the corresponding terms of kinetic energy of electron $T_{el} = \sum_{j=1}^{N_{el}} \frac{P_j^2}{2m_{el}}$ and nuclei $T_{nuc} = \sum_{n=1}^{N_{nuc}} \frac{P_n^2}{2M_n}$, repulsive Coulomb pair interaction between electrons V_{el-el}, the nuclei $V_{nuc-nuc}$, and the attractive interaction between electrons and nuclei V_{el-nuc} from eq. (2.1) are:

$$H_{mol} = \sum_{j=1}^{N_{el}} \frac{P_j^2}{2m_{el}} + \sum_{n=1}^{N_{nuc}} \frac{P_n^2}{2M_n} + \frac{1}{2} \sum_{i \neq j} \frac{e^2}{|\boldsymbol{r}_i - \boldsymbol{r}_j|} + \frac{1}{2} \sum_{m \neq n} \frac{z_m z_n e^2}{|\boldsymbol{R}_m - \boldsymbol{R}_n|} - \sum_{j,n} \frac{z_n e^2}{|\boldsymbol{r}_j - \boldsymbol{R}_n|} \quad (2.2)$$

where e is the electron charge, $\boldsymbol{r}_i$ is the position of the ith electron, $\boldsymbol{R}_m$ denotes the position of the m^{th} nucleus, P_j is the momentum of the jth electron and P_n is the momentum of the n^{th} nucleus. For a defined molecular system, the stationary properties can be used to solve the time-dependent non-relativistic Schrödinger equation:

$$H_{mol}\Phi(\boldsymbol{r}; \boldsymbol{R}) = E\Phi(\boldsymbol{r}; \boldsymbol{R}) \quad (2.3)$$

The Hamiltonian can be separated into nuclear Hamiltonian H_{nuc} and electronic Hamiltonian H_{ele} by separating the terms which depend only on the electronic and nuclear coordinates except for the attractive interaction between electrons and nuclei.

$$H_{nuc} = \sum_{n=1}^{N_{nuc}} \frac{P_n^2}{2M_n} + \frac{1}{2} \sum_{m \neq n} \frac{z_m z_n e^2}{|\boldsymbol{R}_m - \boldsymbol{R}_n|} \quad (2.4)$$

$$H_{ele} = \sum_{j=1}^{N_{el}} \frac{P_j^2}{2m_{el}} + \frac{1}{2} \sum_{i \neq j} \frac{e^2}{|\boldsymbol{r}_i - \boldsymbol{r}_j|} - \sum_{j,n} \frac{z_n e^2}{|\boldsymbol{r}_j - \boldsymbol{R}_n|} \quad (2.5)$$

In reality, the nuclei are not fixed and the nuclear motion does influence the electron dynamics. However, the ratio of nucleus mass to electron mass is approximately 1836 to 1, so the nuclear motion is much slower than the electronic motion. Assuming that electrons instantaneously respond to nuclear dynamics, the electronic state $\phi(r; \boldsymbol{R})$ can be solved with

fixed nuclear positions:

$$H_{ele}\phi(\boldsymbol{r};\boldsymbol{R}) = E_k^{ele}(R)\phi_k(\boldsymbol{r};\boldsymbol{R}) \tag{2.6}$$

In other words, under the Born-Oppenheimer separation, the interaction between nuclei and electrons, away from conical intersections, depends only on the nuclear dynamics *adiabatically*, which enables the separation of electronic and nuclear wavefunctions. Therefore, the molecular state can be expressed as a linear combination of basis functions:

$$\Phi(\boldsymbol{r};\boldsymbol{R}) = \sum_k \Theta_k(\boldsymbol{R})\phi_k(\boldsymbol{r};\boldsymbol{R}) \tag{2.7}$$

The expansion coefficients $\Theta_k(\boldsymbol{R})$ from eq. (2.7) depend on nuclear motions. So to solve this, we can insert eq. (2.7) back into eq. (2.3):

$$\begin{aligned} H_{mol}\Phi(\boldsymbol{r};\boldsymbol{R}) &= (H_{ele} + T_{nuc} + V_{nuc-nuc})\Phi(\boldsymbol{r};\boldsymbol{R}) \\ &= \sum_k (E_k^{ele}(R) + T_{nuc} + V_{nuc-nuc})\Theta_k(\boldsymbol{R})\phi_k(\boldsymbol{r};\boldsymbol{R}) \\ &= \epsilon \sum_k \Theta_k(\boldsymbol{R})\phi_k(\boldsymbol{r};\boldsymbol{R}) \end{aligned} \tag{2.8}$$

To solve for the expansion coefficient, $\Theta_k(\boldsymbol{R})$, we can multiply eq. (2.8) with $\phi_j^*(\boldsymbol{r};\boldsymbol{R})$ and use the orthonormality condition $\langle\psi_j|\psi_k\rangle = \delta_{jk}$:

$$\begin{aligned} \int dr\phi_j^*(\boldsymbol{r};\boldsymbol{R})H_{mol}\Phi(\boldsymbol{r};\boldsymbol{R}) &= [E_j^{ele}(R) + V_{nuc-nuc}]\Theta_j(\boldsymbol{R}) \\ &+ \sum_j \int dr\phi_j^*(\boldsymbol{r};\boldsymbol{R})T_{nuc}\phi_k(\boldsymbol{r};\boldsymbol{R})\Theta_k(\boldsymbol{R}) \\ &= \epsilon \sum_j \Theta_j(\boldsymbol{R}) \end{aligned} \tag{2.9}$$

From eq. (2.9), the nuclear kinetic energy operator can be substituted from eq. (2.2)

while $P_n = -i\nabla_{R_n}$:

$$T_{nuc}\phi_k(\boldsymbol{r};\boldsymbol{R})\Theta_k(\boldsymbol{R}) = -\sum_n \frac{1}{2M_n}[\nabla^2_{R_n}\phi_k(\boldsymbol{r};\boldsymbol{R})\Theta_k(\boldsymbol{R}) + \phi_k(\boldsymbol{r};\boldsymbol{R})\nabla^2_{R_n}\Theta_k(\boldsymbol{R}) \\ +2\nabla_{R_n}\phi_k(\boldsymbol{r};\boldsymbol{R})\nabla_{R_n}\Theta_k(\boldsymbol{R})] \tag{2.10}$$

The last term is the nuclear kinetic energy only working on $\Theta_k(\boldsymbol{R})$, so we can convert other terms into *nonadiabatic* operators:

$$\hat{\eta}_{jk} = \int dr\phi_j(\boldsymbol{r};\boldsymbol{R})T_{nuc}\phi_k(\boldsymbol{r};\boldsymbol{R}) - \sum_n \frac{1}{M_n}[\int dr\phi_j(\boldsymbol{r};\boldsymbol{R})\nabla_{R_n}\phi_k(\boldsymbol{r};\boldsymbol{R})]\nabla_{R_n} \tag{2.11}$$

This operator is attributed to the nonadiabatic coupling between different electronic states (when $j \neq k$) corresponding to nuclear motions. Combine eq. (2.9), eq. (2.10) and eq. (2.11):

$$(T_{nuc} + E^{ele}_j(R) + V_{nuc-nuc} + \hat{\eta}_{jj})\Theta_j(\boldsymbol{R}) = \epsilon\Theta_j - \sum_{j\neq k}\hat{\eta}_{jk}\Theta_k \tag{2.12}$$

This can also be interpreted as stationary Schrödinger equation with transition between different electronic state due to the electronic nonadiabatic coupling $\hat{\eta}_{jk}$. Under the Born-Oppenheimer approximation, the nonadiabatic coupling can be neglected. So eq. 2.12 can be rewritten as[20,21]:

$$[-\sum_n \frac{\nabla^2_{R_n}}{2M_n} + U_{nuc}(\boldsymbol{R})]\Theta_k(\boldsymbol{R}) = \boldsymbol{E}\Theta_k(\boldsymbol{R}) \tag{2.13}$$

where the nuclear potential energy surface is:

$$U_{nuc}(\boldsymbol{R}) = \frac{1}{2}\sum_{m\neq n}\frac{z_m z_n e^2}{|\boldsymbol{R}_m - \boldsymbol{R}_n|} + E^{ele}_k(R) \tag{2.14}$$

The potential energy surfaces along the adiabatic coordinates define the vibrational states. Molecular wavepackets can transit between these degenerate potential energy surfaces without absorption or radiation, and these regions are called conical intersections. In the vicinity

of those regions, the Born-Oppenheimer approximation breaks down, allowing nonadiabatic coupling to take place. Therefore, the Born-Oppenheimer approximation cannot be applied when there is strong coupling between different electronic states, where the nuclei can rapidly change in response to the wavepacket moving from one region of the potential hypersurfaces to another[22,23].

2.1.2 Photoabsorption and Franck-Condon principle

If a molecule absorbs a photon with sufficient energy, it can be promoted to a higher electronic state, transferring part of the nuclear wavepacket to an excited-state potential energy surface (PES). Because electronic transitions occur much faster than nuclear motion, the excitation is effectively instantaneous (i.e., it is a *vertical* transition from one point of the initial PES to the same nuclear configuration on the excited-state surface). As a result, the transition takes place without any immediate change in nuclear configuration.

Absorption or emission of a photon and the intensities of vibronic transitions can be described by the Franck-Condon principle. The transition probability amplitude from the ground state ψ to the excited state $\psi^{'}$ can be represented as[24]:

$$P = \langle \psi^{'} | \boldsymbol{\mu} | \psi \rangle = \int \psi^{'*} \boldsymbol{\mu} \psi d\tau \tag{2.15}$$

The molecular dipole operator $\boldsymbol{\mu}$ is determined by the charge e and the locations $\boldsymbol{r}_i$ of the electrons along with the nuclei charges eZ_j and the locations $\boldsymbol{R}_j$:

$$\boldsymbol{\mu} = \boldsymbol{\mu}_e + \boldsymbol{\mu}_N = -e \sum_i \boldsymbol{r}_i + e \sum_j Z_j \boldsymbol{R}_j \tag{2.16}$$

Under the Born-Oppenheimer approximation, which is the fundamental assumption of the Franck-Condon principle, the wavefunction ψ can be separated into electronic, vibrational, and spin parts, where the vibrational wavefunction also depends on the spatial co-

ordinates of the nuclei:

$$\psi = \psi_e \psi_v \psi_s \tag{2.17}$$

So eq. (2.15) can be represented as:

$$\begin{aligned} P = \langle \psi_e' \psi_v' \psi_s' | \boldsymbol{\mu} | \psi_e \psi_v \psi_s \rangle &= \int \psi_e'^* \psi_v'^* \psi_s'^* (\boldsymbol{\mu}_e + \boldsymbol{\mu}_N) \psi_e \psi_v \psi_s d\tau \\ &= \int \psi_e'^* \psi_v'^* \psi_s'^* \boldsymbol{\mu}_e \psi_e \psi_v \psi_s d\tau + \int \psi_e'^* \psi_v'^* \psi_s'^* \boldsymbol{\mu}_N \psi_e \psi_v \psi_s d\tau \\ = \int \psi_v'^* \psi_v d\tau_n \int \psi_e'^* \boldsymbol{\mu}_e \psi_e d\tau_e \int \psi_s'^* \psi_s d\tau_s &+ \int \psi_e'^* \psi_e d\tau_e \int \psi_v'^* \boldsymbol{\mu}_N \psi_v d\tau_v \int \psi_s'^* \psi_s d\tau_s \end{aligned} \tag{2.18}$$

The integral over the electron coordinates $\int \psi_e'^* \psi_e d\tau_e$ is zero due to the electronic states being orthogonal to each other, so the whole second term becomes zero. The first integral in the first term $\int \psi_v'^* \psi_v d\tau_n$ is the vibrational overlap integral in their respective electronic state.

$$S(v, v') = \int \psi_v'^* \psi_v d\tau_n \tag{2.19}$$

The relative intensities of the vibrational transition are proportional to the square of these electric dipole moments $|S(v, v')|^2$. This is also called the Franck-Condon factor. The remaining two integrals compose the probability amplitude that determines the electric spatial and spin selection rules.

Photoionization

If a molecule absorbs a photon with energy larger than the binding energy of one of its electrons, the system may transition to an electronic state above the ionization threshold, allowing the electron to escape, leaving behind a positively charged ion. In this case, the molecule is said to undergo photoionization[25,26]. Photoionization is a fundamental light-matter interaction process, which unfolds on an ultrafast (nearly instantaneous) time cale and plays a central role in many experimental schemes for probing electronic structure and

dynamics. In molecules, photoionization can lead to complex fragmentation pathways, where the removal of an electron alters the potential energy landscape and initiates nuclear motion. The details of the photoionization process depend on both the electronic structure of the molecule and the absorbed photon energy, and differ largely for valence-shell and inner-shell ionization. The properties of the ejected electron(s) or created ion fragments, such as its momentum distribution, kinetic energy, angular distribution, and integrated yields, can be measured in the laboratory or molecular frame, providing time-resolved insight into the evolving electronic and nuclear structure of the system.

2.1.3 Single-photon and multi-photon X-ray ionization

Photoionization induced by X-rays represents an important subset of ionization processes that includes interaction with both valence-shell and core-shell electrons. Here, a single high-energy photon can eject either a core or a valence electron from an atom or a molecule, depending on the relation between the photon energy and the specific binding energies of electrons in different shells. However, at X-ray energies, whenever core-shell ionization is energetically available, its ionization cross section is typically much larger than the cross section for valence ionization, so that the core-shell interactions dominate. Correspondingly, the X-ray photon energy can be tuned to maximize the photoionization from a specific core-shell of a particular atom in a molecule. Since the core electrons are localized, this X-ray property enables the targeting of a specific element and thus a specific region in a larger system. Because of this, X-ray ionization plays a fundamental role in ultrafast spectroscopy and imaging techniques, especially at high photon energies accessed through synchrotrons and X-ray free-electron lasers (XFELs). In the single-photon ionization regime, X-ray photoionization is linear with respect to the number of photons (or, in other words, with the X-ray pulse energy), typically resulting in a well-defined interaction that can be treated perturbatively. This process dominates under moderate X-ray flux and is widely used for site-specific probing of electronic structure via techniques such as X-ray photoelectron

spectroscopy (XPS) and time-resolved photoelectron spectroscopy (TRPES). Core-shell X-ray ionization leaves a system in an energetically unstable state because it creates an inner-shell vacancy and thus is typically accompanied by a relaxation process filling the created hole. This can occur via fluorescence or ejection of one or more electrons via Auger-Meitner decay[27], with the latter being a dominant process for lighter elements. Therefore, in the X-ray regime, the absorption of a single photon typically leads to the ejection of two or (for heavy elements and deeper levels) more electrons and thus leaves the molecule in a doubly or multiply charged state.

At XFELs, multiphoton X-ray ionization can occur. Here, two or more photons are absorbed either simultaneously or sequentially within the XFEL pulse duration, because of the extremely high photon flux provided by XFELs. This nonlinear interaction leads to highly charged ions, sequential Auger-Meitner decay sequences, and various charge redistribution processes. These dynamics facilitate the Coulomb explosion of a molecule, making it especially relevant for studies involving intense X-ray pulses and radiation damage[28,29]. Multiphoton processes are often accompanied by complex electron dynamics and are crucial for techniques such as X-ray-induced Coulomb explosion imaging (X-CEI) and ultrafast structural probes that rely on multiple ionization channels. The balance between single-photon and multiphoton processes depends strongly on the photon flux (in other words, on the X-ray pulse energy and focus size), pulse duration, and individual ionization cross-sections, which must be carefully considered in the interpretation of X-ray pump–probe experiments.

2.1.4 Laser-induced strong-field ionization

If the photon energy is below the ionization potential of a molecule and thus single-photon induced ionization is energetically forbidden, ionization can still happen if the energy of two or several photons can be combined. This can occur if the light source involved is intense enough. Such processes are referred to as two-photon or multiphoton[25,30,26] ionization[31,32]. At even higher light intensities, the electric field strength of the light pulse

becomes comparable to the Coulomb binding field of valence electrons. Under such conditions, multiphoton ionization, tunneling ionization, or over-the-barrier ionization can occur depending on the Keldysh parameter γ[33], which distinguishes between perturbative and non-perturbative regimes. For $\gamma > 1$, ionization can be easier understood in terms of a multiphoton process, whereas for $\gamma < 1$, it is more convenient to treat the electric field of the light as an electromagnetic wave and consider ionization as tunneling or an over-the-barrier process. In the optical domain, the Keldysh parameter approaches 1 for intense laser fields exceeding 10^{13} W/cm^2. In this regime, one often speaks about 'strong-field' ionization (SFI).

$$\gamma = \omega\sqrt{2I_p/eE} \tag{2.20}$$

Eq. 2.20 shows the equation for the Keldysh parameter, where ω is the laser frequency, I_p is the ionization potential, and E is the electric field strength of the laser. In the experiments discussed in this thesis, ultrafast near-infrared laser pulses at intensities well above 10^{14} W/cm^2 were used to induce strong-field ionization of gas-phase organic molecules. At such high intensities, molecules can undergo multiple ionization events within a single pulse, often resulting in Coulomb explosion[17,34]. The ionization process initiates the dynamics by creating one or more charges on the molecule, thereby altering the potential energy surface and triggering ultrafast nuclear motion. This charge redistribution can lead to direct bond cleavage (fragmentation) or activate complex dissociation pathways involving intermediate species. Strong-field ionization is thus a key mechanism for initiating time-resolved pump–probe experiments aimed at exploring molecular dynamics on femtosecond timescales.

In contrast to intense near-infrared pulses used to induce Coulomb explosion, the intensities of femtosecond UV pulses used in this work to initiate the dynamics in 2(5H)-thiophenone (thiophenone) or 2,3-dihydrofuran (2,3-DHF) molecules are typically kept rather low to ensure that the pump step in this experiment is restricted to a single-photon excitation. At the conditions needed to achieve efficient pumping, a possibility of two- or three-photon ionization by the UV pump pulse still needs to be considered.

2.2 UV-induced photochemistry of ring molecules

Ultraviolet (UV) light plays a central role in driving photochemical processes in molecules by providing sufficient photon energy to access electronically excited states. These excitations can lead to various outcomes, including bond cleavage, isomerization[35], charge transfer, and the formation of transient intermediates[8]. UV-induced photochemistry enables selective excitation of valence electrons and triggers structural changes on the femtosecond timescale. With recent advances in ultrafast light sources and time-resolved pump–probe techniques, it is now possible to directly probe the ultrafast molecular dynamics of ring molecules.

A particularly intriguing class of photochemical transformations are electrocyclic ring-conversion reactions such as ring-opening or ring-puckering. These processes are typically driven by nuclear motion along steep potential energy surfaces and occur within a few hundred femtoseconds. Owing to their speed, reversibility, and sensitivity to excitation conditions, electrocyclic reactions are widely studied in the context of molecular switching[36,37,38], optical data storage[36], and nanoscale logic and mechanical devices[39,40,41]. One classic example is the UV-induced ring-opening of cyclohexadiene (CHD) to form cyclohexatriene (CHT), a step that is also central to vitamin D_3 synthesis in biological systems[12]. This system has been thoroughly investigated using techniques such as x-ray and electron diffraction[42,43,44], photoelectron spectroscopy, and mass spectrometry[45,46]. These early studies contributed to the formulation of the Woodward–Hoffmann rules[47], which provide a theoretical framework for understanding symmetry-allowed reaction pathways in pericyclic processes[48,49]. While early ultrafast investigations focused primarily on CHD, more recent studies have expanded to include other model systems, particularly heterocyclic compounds, in order to uncover general principles governing electrocyclic reactions across a wider range of molecular frameworks.

Building on these foundational studies, in this work, UV-induced photochemistry is investigated in 2(5H)-thiophenone (C_4H_4OS, hereafter referred to as thiophenone) and 2,3-dihydrofuran (hereafter referred to as 2,3-DHF)—two representative organic molecules

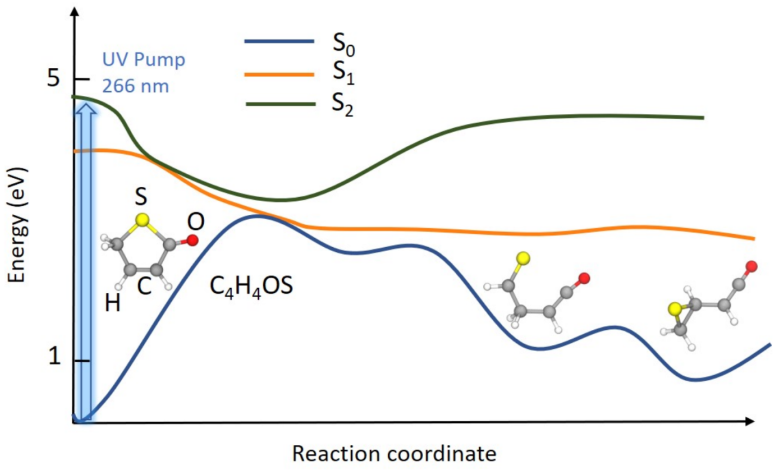

Figure 2.1: ***Schematic potential energy curve showing ground and the first two excited electronic states of thiophenone.***
Qualitative potential energy curves for the ground (S0), first (S1), and second (S2) electronic excited states of thiophenone. Adapted from Pathak and Ibele et al.[8].

with distinct structural and electronic properties. Ethylene, as a prototypical hydrocarbon molecule, is also included as a reference system for benchmarking π-bond breaking and Coulomb explosion dynamics; however, only IR-induced fragmentation data are presented for ethylene. Thiophenone, with its aromatic ring and sulfur–oxygen functionality, exhibits rich excited-state behavior, including ultrafast ring-opening and isomerization into a three-membered episulfide structure, as reported in previous studies[8]. 2,3-DHF, a five-membered oxygen-containing heterocycle, serves as a model system for exploring UV-driven ring-conversion dynamics, including out-of-plane puckering and fragmentation. By initiating dynamics with femtosecond UV pulses and tracking molecular evolution using pump–probe Coulomb explosion imaging, we resolve both the structural and temporal changes following photoexcitation. This section focuses on the role of UV excitation in driving molecular distortions, with particular emphasis on identifying the resulting different photoproducts from previous work.

2.2.1 UV-induced dynamics in 2(5H)-thiophenone

Heterocyclic compounds, particularly those containing sulfur and nitrogen atoms within their ring structures, play a vital role in biological systems. These molecules are integral components of various naturally occurring substances, including vitamins, pigments, and antibiotics. Furthermore, they are widely utilized in the development of pharmaceuticals, dyes, and pesticides. Investigating the photochemical behavior of these heterocyclic compounds—specifically, the rules that govern their photon-induced reactions—can provide valuable insights into the chemistry of more complex biological and synthetic systems.

An earlier study by Murdock *et al.*[50] investigated the ring-opening dynamics of thiophenone in the liquid phase, where the molecule was dissolved in acetonitrile (CH_3CN). This experiment successfully confirmed the occurrence of ring-opening by identifying ketene as a primary photoproduct and provided the first estimate of the timescale associated with this process, which was found to be less than 1 ps. Since the formation time and distribution of photoproducts are often influenced by solvent interactions[51], it is of significant interest to perform comparable studies in the gas phase, where the absence of solvent allows for the isolation of intrinsic molecular dynamics and distinctly different relaxation pathways.

Fig. 2.1 illustrates the qualitative potential energy curves for the ground (S_0), first (S_1), and second (S_2) electronically excited states of thiophenone. As indicated by the blue arrow, absorption of a single ultraviolet photon at approximately 266 nm (4.66 eV) promotes the molecule from the S_0 to the S_2 state. Following this excitation, the population can efficiently relax to the ground electronic state via nonadiabatic transitions at the S_2/S_1 and S_1/S_0 conical intersections along the C–S bond extension coordinate[50]. Upon returning to the ground state, the molecule may either proceed to form ring-opened photoproducts or revert to a vibrationally hot ring-closed thiophenone species.

Fig. 2.2 presents selected ground-state photoproduct geometries of thiophenone and their relative energies, as predicted by Murdock *et al.*[50]. These structures, including the equilibrium geometry of the parent molecule and three possible ring-opened isomers, were optimized

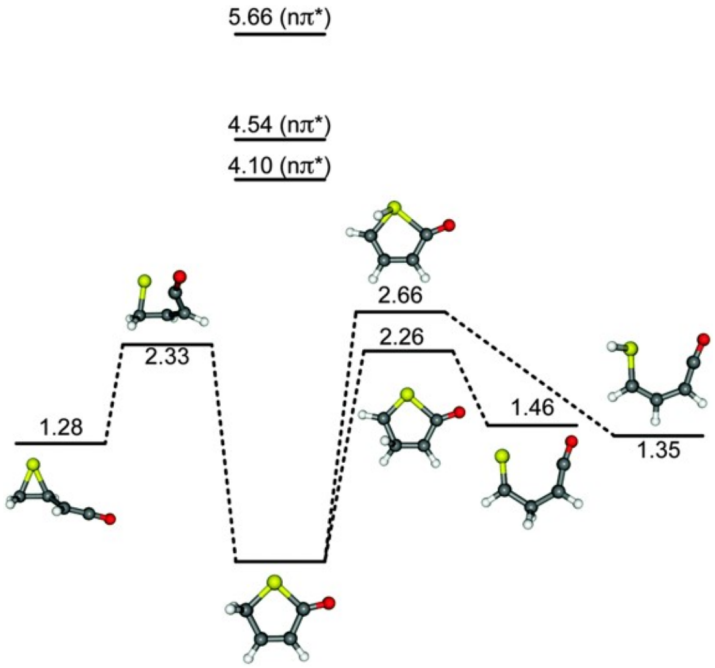

Figure 2.2: ***Theoretically calculated ground-state equilibrium structure of thiophenone and the excited photoproducts.***
All energies shown are relative to the ground state of thiophenone. Adapted from Murdock et al.[50].

using MP2/6-311+G(d,p) calculations. Understanding the formation and energetics of these species is essential for interpreting the outcome of UV-induced photochemistry dynamics.

From the simulation shown in the paper[8], to understand the relaxation dynamics of thiophenone following UV photoexcitation, *ab initio* potential energy surfaces (PESs) were constructed using XMS(4)-CASPT2(10/8) along linear interpolations in internal coordinates (LIICs) between critical geometries. As shown in Fig. 2.3 (a), these calculations revealed that the S_2 state population rapidly relaxes to the S_0 state through the S_2/S_1 and S_1/S_0 conical intersections along the C–S bond extension coordinate. Simultaneously, the evolution of cationic states (D_0, D_1) along these pathways showed smooth energy changes, supporting their relevance to the observed binding energy (BE) shifts in photoelectron spectra. The inset in Fig. 2.3(a) displays the growth of ΔE between the cation and neutral singlet states, consistent with change in the of time-dependent spectra.

Time-dependent trajectory surface hopping (TSH) simulations[8] (as shown in Fig. 2.3(b))

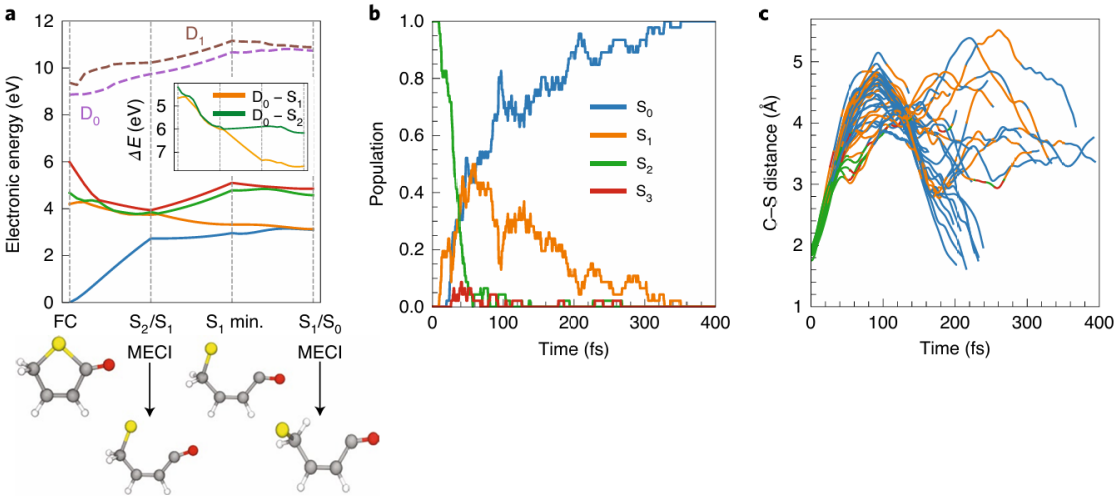

Figure 2.3: ***Simulation of UV-induced molecular dynamics of thiophenone studied using TRPES.***

Figure is adapted from Pathak and Ibele et al.[8]*. (a) Potential energy surfaces (PESs) of the lowest singlet electronic states (solid lines: S_0 in blue, S_1 in orange, S_2 in green, S_3 in red) and cationic doublet states (dashed lines) of thiophenone, calculated along linear interpolations in internal coordinates (LIIC) between critical geometries. Energies were computed using XMS(4)-CASPT2(10/8) for the neutral and XMS(4)-CASPT2(9/8) for the cation. Grey vertical lines mark minima and minimum-energy conical intersections (MECIs), located using SA(4)-CASSCF(10/8), and molecular geometries are shown below. The inset displays the energy gaps (ΔE) between the cationic D_0 state and the neutral S_1/S_2 states along each LIIC path. (b)Time-dependent population dynamics of the S_3, S_2, S_1, and S_0 states derived from trajectory surface hopping (TSH) simulations based on 46 trajectories. (c) C–S bond distance evolution for each trajectory, color-coded by electronic state, showing rapid bond extension followed by internal conversion through $S_2 \rightarrow S_1 \rightarrow S_0$. TSH trajectories were terminated upon encountering electronic structure instabilities on the ground state.*

initiated on the S_2 surface near the ground-state equilibrium geometry confirmed ultrafast internal conversion, with complete population transfer to S_0 within 350 fs, driven by ballistic ring-opening motion. The evolution of the C–S bond distance for each trajectory (Fig. 2.3 (c)) illustrated the structural bifurcation into ring-opened and ring-closed (vibrationally hot) molecules. Experimentally observed shifts in photoelectron binding energies, moving from narrow S_2 features to broader $S_0^{\#}$ signal, were consistent with the calculated ionization energies and support this relaxation model. In conclusion, the combined PES, TSH (as shown in Fig. 2.3(a-c)), and TRPES results firmly establish that UV excitation leads to prompt nonadiabatic decay of thiophenone through sequential state crossings, resulting in a mixture of structurally distinct ground-state products within a few hundred femtoseconds (350 fs).

The MeV-UED measurements, complemented by theoretical modeling[11], offer rich dynamical insights into the ultrafast relaxation behavior of thiophenone that were previously inaccessible. Following UV excitation and subsequent relaxation to the electronic ground state (S_0), the molecule enters a highly reactive ring-opened biradical configuration. This intermediate follows multiple reaction pathways: some trajectories lead to the reformation of the ring-closed parent structure, evident from a delayed rise in population observed around 250 fs, while others progress toward the formation of ring-opened photoproducts or episulfide derivatives. These distinct fates illustrate the complexity of the relaxation landscape and emphasize the importance of competing reaction channels and branching dynamics on the sub-picosecond timescale.

Fig. 2.4 illustrates the time-dependent evolution[11] of photoproduct populations, extracted from both nonadiabatic and Born–Oppenheimer (NA+BO) molecular dynamics simulations as well as experimental UED data. Upon UV excitation, the parent thiophenone molecule (blue trace) rapidly undergoes C–S bond cleavage, yielding a biradical species (orange trace), which subsequently evolves into an episulfide product (yellow trace) within 200 fs. The episulfide becomes the dominant product by 2 ps.

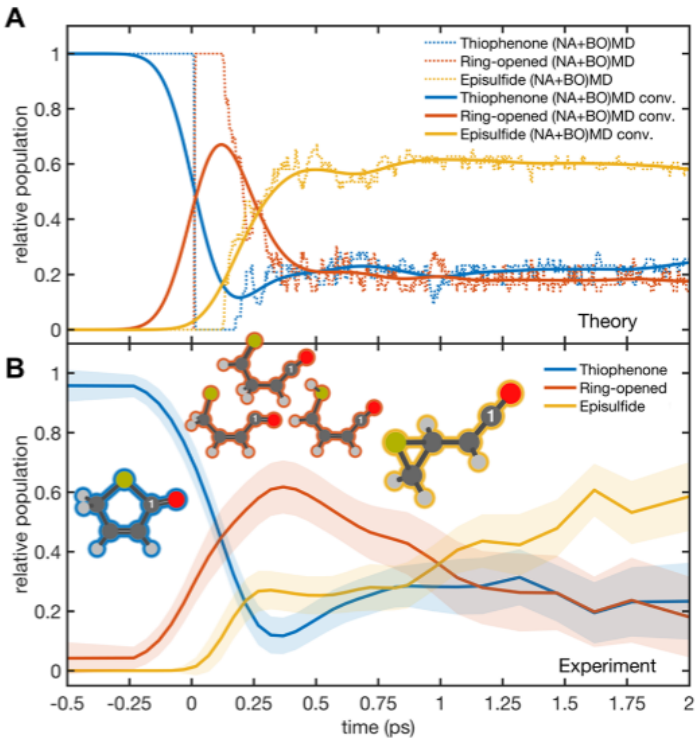

Figure 2.4: ***Time-resolved relative populations of thiophenone and its major photoproducts following UV excitation.***
Adapted from Nunes et al.[11]*. (A) Simulated populations obtained from combined nonadiabatic and Born–Oppenheimer molecular dynamics (NA+BO MD) trajectories: thiophenone (blue), ring-opened isomers (orange), and episulfide (yellow). Dotted lines represent raw simulation data, while solid lines include convolution with the instrument response function (IRF). (B) Corresponding experimental product populations extracted from ultrafast electron diffraction (UED) measurements.*

In conclusion, the combined insights from *ab initio* potential energy surface calculations, time-dependent surface hopping simulations, and ultrafast experimental probes such as TRPES and MeV-UED collectively establish a comprehensive picture of thiophenone's ultrafast relaxation dynamics following UV excitation. Theoretical simulations (Fig. 2.3(a–c)) confirm that excitation to the S_2 state is followed by rapid internal conversion through sequential conical intersections, resulting in ground-state population transfer within 350 fs and accompanied by ballistic ring-opening motion. Complementary MeV-UED measurements and NA+BO molecular dynamics simulations (Fig. 2.4) reveal the structural evolution of the ring-opened biradical and its subsequent branching into either re-closed thiophenone or episulfide photoproducts, the latter (episulfide) emerging as the dominant species within 2 ps. Together, these findings highlight the critical role of nonstatistical nuclear dynamics and multiple relaxation pathways in shaping the early-time photoproduct distribution, demonstrating that a detailed understanding of such processes requires a synergistic approach combining ultrafast structural probes and high-level quantum dynamics modeling. The main goal of the experimental work on thiophenone presented in Chapter 5 of this thesis is to advance the existing understanding of UV-induced dynamics in thiophenone, providing data on the ring-opening step itself with sub-100 fs temporal resolution, and to develop experimental procedures which would enable discriminating between the reaction products that differ only by the position of hydrogen atoms. These goals will be addressed here employing the Coulomb explosion imaging approach.

2.3 Coulomb explosion imaging

Coulomb explosion imaging[15] (CEI) is a powerful method for imaging simple molecular structures and molecular dynamics[52,53,54,55] by rapidly removing many electrons from molecules. In the experimental work presented in this thesis, CEI was employed to investigate laser-molecule interactions that typically lead to the removal of the most weakly bound

valence electrons, resulting in a distribution of ionic fragments and possibly neutral species. The ensuing rapid fragmentation is driven by strong Coulomb repulsion between the multiply charged ions, leading to their spatial separation. These ionic fragments retain geometric information about the original molecular structure and, in time-resolved experiments, can also reveal dynamic evolution when measured as a function of pump–probe delay.

The corresponding total Coulomb potential energy is given by:

$$E_{total} = \sum_{\substack{i,j \\ j \neq i}} E_{ij} = \sum_{\substack{i,j \\ j \neq i}} \frac{1}{4\pi\varepsilon_0} \frac{q_i q_j}{r_{ij}} \tag{2.21}$$

The measured kinetic energy release (KER) is not uniquely determined by the initial geometry of the molecule and thus cannot, on its own, be used to directly infer molecular structure. Instead, structural information is encoded in the momenta imparted to the atomic fragments. In a coincident Coulomb explosion imaging (CEI) experiment, the full 3D asymptotic momentum vectors $\vec{p}_k$ of each ionized fragment are measured.

Assuming instantaneous ionization and a purely Coulombic potential energy surface (PES) in the final state, the relationship between the measured momenta and the Coulomb forces allows the reconstruction of the initial molecular geometry. This connection is established through equations that relate the measured momentum vectors to the real-space position vectors $\{\vec{r}_i\}$ of the constituent atoms:

$$\vec{p}_i = \sum_{j \neq i} m_i \vec{v}_i = \sum_{j \neq i} \int_{t_0}^{\infty} \vec{F}_{ij}(t)\, dt \tag{2.22}$$

where $\vec{F}_k(t)$ is the Coulomb force acting on a particle i due to all other charged fragments, and the integration begins at the instant of ionization t_0. These equations form the basis for retrieving absolute molecular geometries from momentum measurements.

The trajectories of the ion fragments can be modeled using a coupled set of nonlinear ordinary differential equations, arising from their mutual Coulomb repulsion. The motion of

the fragments is governed by Newton's equations, which yield the time-dependent position, velocity, and acceleration vectors for each ion.

To retrieve structural and dynamical information using CEI, both ionization and fragmentation must occur on a timescale shorter than that of nuclear motion, ensuring that the molecule remains near its equilibrium geometry during the explosion. Under this condition, the measured momenta of the ionic fragments can be used to reconstruct the molecular geometry prior to the Coulomb explosion. It is important to note that in a pump–probe configuration, both pulses interact with the molecule, but in fundamentally different ways: a low-intensity pump pulse is used to initiate dynamics without causing ionization, while a subsequent, high-intensity NIR probe pulse induces strong-field multi-photon ionization, triggering the explosion process. The resulting process of rapid fragmentation and mutual separation between the charged fragments occurs due to the strong Coulomb repulsion between the fragment ions produced by the probe pulse.

2.3.1 Concerted vs. sequential fragmentation and Native frame analysis

In order to provide meaningful information on the geometric structure of the molecule via CEI, not only ionization but also fragmentation must occur on a short timescale. That means the molecular breakup has to occur in a concerted manner. In a concerted fragmentation pathway, all relevant bonds break simultaneously upon ionization, and the resulting ions repel each other from their initial positions based on Coulombic forces. This typically results in fragments producing localized angular distributions when viewed in the Native frame[19]. For example, a molecule may first break into an intermediate fragment and a light ion, followed by a delayed second fragmentation of the intermediate. This leads to a uniform angular distribution signature when viewed in the Native frame[19], as the initial explosion dynamics are modified by subsequent motion and charge redistribution. Therefore, a sequential process does not allow for a direct relation between the initial geometry and

observed fragmentation pattern and thus is ill-suited for CEI.

To disentangle concerted and sequential processes, a new data analysis framework based on the so-called Native frame concept has recently been developed[18,56,19]. Native frame analysis is a powerful technique for interpreting multi-body molecular fragmentation dynamics by transforming measured fragment momenta into the molecular coordinate system defined by the initial geometry of the molecule. Unlike the laboratory frame, where overlapping effects can obscure the true breakup dynamics, Native frame preserves the internal symmetry and spatial relationships of the molecular structure at the time of ionization. This transformation enables a more intuitive identification of fragmentation pathways, such as distinguishing between concerted (simultaneous) and sequential (stepwise) breakups, based on angular correlations and momentum vector alignments.

In particular, Rajput et al.[18] introduced this approach to disentangle three-body fragmentation mechanisms in CO_2^{3+}, demonstrating that the dissociation pathway strongly depends on the total energy available. Their results showed that different energy regimes favor different breakup mechanisms, highlighting the value of Native frame analysis for gaining insight into the timing, geometry, and ultrafast dynamics of molecular dissociation processes that are not readily apparent in the lab frame.

Severt et al.[19] presented an extended Native frame analysis to disentangle concerted and sequential fragmentation mechanisms in three-body Coulomb explosion events. By employing Jacobi coordinates and transforming the fragment momenta into a reduced-dimensional representation (see Fig. 2.5), the method enables the clear identification of fragmentation pathways. Applied to the strong-field ionization of carbonyl sulfide (OCS), the technique reveals signatures of rotational motion in the intermediate fragments indicative of sequential breakup. The angular correlations in the Native frame, especially in conjugate Jacobi momenta, allow for distinguishing between one-step and multi-step dissociation dynamics. This refined Native frame approach offers a generalized and robust framework for interpreting complex fragmentation patterns in polyatomic systems.

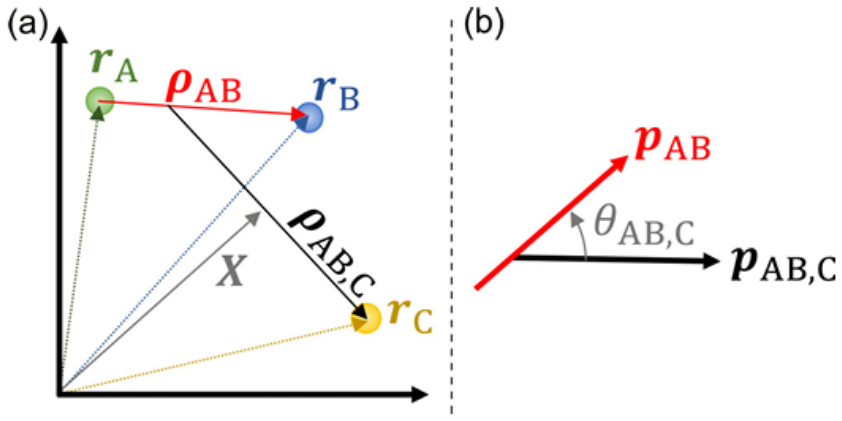

Figure 2.5: ***Native frame coordination transformation.***
Adapted from Severt et al.[19]*. (a) Definition of the Jacobi coordinates* $\boldsymbol{\rho}_{AB}$ *and* $\boldsymbol{\rho}_{AB,C}$ *for a generic triatomic molecule ABC, along with the center-of-mass position vector* $\mathbf{X}$*, all defined in a laboratory-fixed frame. (b) The angle* $\theta_{AB,C}$ *between the conjugate momenta* $\mathbf{p}_{AB}$ *and* $\mathbf{p}_{AB,C}$*, which is used to distinguish between concerted and sequential fragmentation mechanisms.*

To interpret the observed molecular breakup patterns, we compared concerted and sequential fragmentation mechanisms using Coulomb explosion simulations in the molecule's native coordinate frame. This analysis allows us to distinguish between simultaneous and stepwise bond dissociation processes by examining the momentum correlations of fragment ions.

The final momentum vectors and kinetic energy distribution of the fragments were calculated and then transformed into the native molecular frame to analyze the angular correlations and the KER of each fragmentation step. Experimental data exhibiting back-to-back recoil momentum vectors were attributed to concerted fragmentation, while broader or skewed distributions suggested sequential behavior.

This frame-based comparison provides deeper insight into the fragmentation dynamics and helps to determine whether the molecular breakup proceeds via a single-step or multi-step dissociation pathway under strong-field ionization conditions.

2.3.2 Coulomb explosion simulation

To gain insight into the fragmentation dynamics observed in our experiments, we performed Coulomb explosion simulations (CES) based on classical trajectory modeling generated by Newton-X software[57] and quantum chemical calculations. Theoretical tools like time-dependent density functional theory (TD-DFT) and surface-hopping dynamics packages[57] complement our experimental approach by providing insight into the ground vibrational states of molecules.

CES assumes that upon ionization, the molecule undergoes rapid charge separation, and the resulting ionic fragments repel each other purely via Coulombic forces. Initial atomic positions were taken from optimized geometries obtained using *ab initio* quantum chemistry calculations[57]. Upon removal of electrons, partial[58] or full positive charges were assigned to atomic centers according to the experimental charge states. The classical equations of motion were then solved numerically to track the time evolution of the ionic positions and momenta. The simulated fragment momentum distributions were compared directly with the experimental data. Overall, the CES provides a useful tool to link final fragment geometries to the original molecular structure and validate our structural assignment.

Limitations of the modeling include neglect of electron correlation, non-Coulombic interactions at short range, and potential nuclear motion before full ionization. Despite these simplifications, the simulation captures key features of the experimental data and supports our interpretation of the dissociation dynamics.

There are some initial assumptions for Coulomb explosion simulation:

1. We apply fixed geometries and fixed initial velocities of specific molecules for simulation.
2. All final charged states of the fragments are known.
3. There are only vertical transitions from the potential surfaces.
4. All final electronic states' potential energy surfaces are purely Coulombic.

Under these assumptions, if we have one set of geometries, then we can get one set of

corresponding final-state momenta. These assumptions neglect both the field-induced rearrangement of atomic positions and any initial momenta imparted during ionization by the intense laser field. Under these conditions, the classical equations of motion for each ion can be solved immediately after the explosion. Classical trajectory simulations are performed using standard numerical integration methods such as the Runge–Kutta algorithm[59,60], initiated from a set of known geometries. The accuracy of the simulation is evaluated by comparing the calculated asymptotic momenta to experimentally measured values. MATLAB's built-in ODE solver `ode45` was used[61] to perform this type of calculation from the geometry (nuclear position) information to momentum distribution.

The initial molecular geometry can be sampled from the equilibrium geometries of the ground state using a Wigner distribution generated by Newton-X[57] to account for the vibrational states. Alternatively, excited-state geometries calculated using methods such as TD-DFT or surface hopping (TSH) can be employed to model conditions relevant to UV-photon triggered pump–probe experiments. The final momentum distribution is obtained by numerically solving the classical equations of motion with an ODE solver[61], using a propagation time of 500 ps to ensure that the fragments are sufficiently separated so that Coulomb interactions become negligible.

2.3.3 Data representation of Coulomb explosion simulation

With the assumptions outlined earlier, we introduce several forms of data representation commonly used in CES and the corresponding experimental data. These representations help visualize and analyze the fragmentation dynamics and momentum correlations of the ionized fragments.

Kinetic energy release

The kinetic energy distributions (KED) of different ion fragments as well as total kinetic energy release (KER) of a particular channel can be directly compared to experimental data.

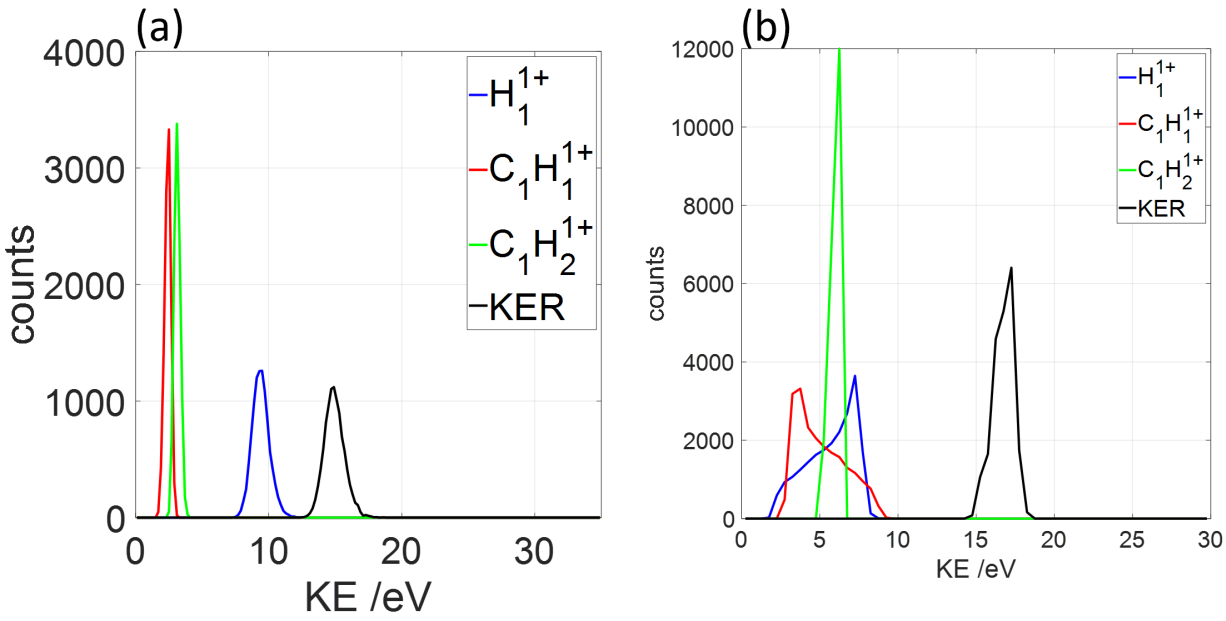

Figure 2.6: ***Simulated KERs of ethylene three-body fragmentation.***
KER of ethylene three-body complete fragmentation via (a) concerted breakup and (b) sequential breakup through a CH_2^+ + CH_2^{2+} intermediate. The superscript on each ion fragment label indicates the charge state, while the subscript denotes the number of atoms in that fragment.

As an example, for distinguishing between the concerted and sequential breakup of three-body fragmentation of ethylene, subtle differences in the kinetic energy distributions (KEDs) of the final fragments can be observed. These differences are reflected in the simulated KER spectra, enabling us to trace and differentiate the fragmentation geometry based on the energy signatures captured in the KER plots as shown in Fig. 2.6.

Newton diagrams and 3-D momentum distribution

To analyze the angular correlations between ion fragments and gain insight into the fragmentation dynamics, Newton diagrams were employed. A Newton diagram maps fragment momentum vectors in the molecular center-of-mass frame[62]. These diagrams provide a visual representation of momentum conservation in multi-particle breakups. In the context of molecular fragmentation, particularly within ion momentum imaging techniques such as COLTRIMS, Newton diagrams have become a standard tool for interpreting three-

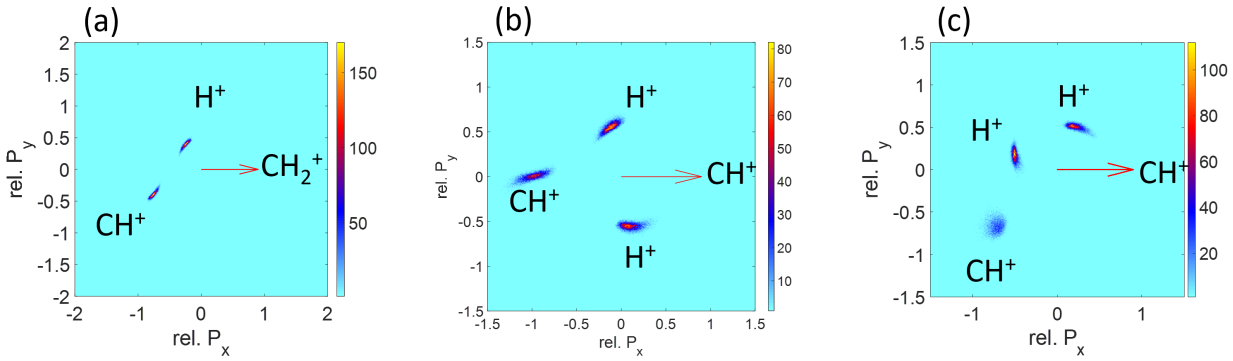

Figure 2.7: ***Simulated conventional normalized relative Newton diagrams for ethylene molecule fragmentation.***
Conventional normalized relative Newton diagrams of (a) three-body (H^+ + CH^+ + $CH_2{}^+$) fragmentation channel, (b) four-body (H^+ + CH^+ + H^+ + CH^+) trans-fragmentation channel (hydrogens from the opposite side of C–C bond are fragmented), and (c) four-body (H^+ + CH^+ + H^+ + CH^+) cis-fragmentation (hydrogens from the same side of C–C bond are fragmented) of the CES of concerted breakup using Wigner distribution at 60K of ground-state ethylene optimized at the B3LYP/aug-cc-pVDZ level of theory using Newton-X software[57].

dimensional momentum data.

In a typical Newton diagram, the momentum of one selected fragment (often the heaviest or the most stable) is fixed along the $x-$axis, and the momenta of the remaining fragments are plotted relative to its momentum distribution. This allows for direct visualization of the angular relationships between fragments. In addition, Newton diagrams can reveal structural signatures, such as differences between cis- , and trans- fragmentation, through their characteristic angular distributions as shown in Fig. 2.7(b) and (c). We simulate the fragmentation pathways of ethylene molecule and this is shown in Fig. 2.7, where the momentum distribution of the heaviest fragment is selected where the momentum distribution of $CH_2{}^+$ or CH^+ is used as the reference unit vector to construct the molecular plane.

To improve the visualization of molecular structure and to generalize Newton diagram representation for cases where more than three particles have been detected, several forms of modified Newton diagrams will be introduced in Chapter 4.

In addition to the Newton diagram, which displays ion momenta projected onto a single plane, the full three-dimensional momentum distributions of the ion fragments can also

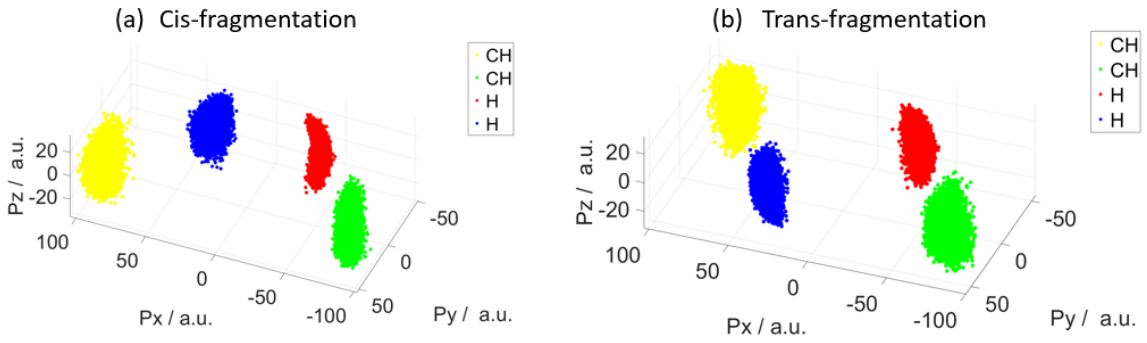

Figure 2.8: ***Simulated momentum distributions of ion fragments of ethylene.*** *'Raw' (without representation using Newton diagrams in the molecular frame) momentum distributions of ion fragment from the four-body of ethylene via (a) cis-fragmentation pathway and (b) trans-fragmentation pathway using CES.*

be visualized and analyzed. These distributions provide a more complete picture of the fragmentation dynamics, especially in complex multi-body breakups. Fig. 2.8 shows the simulated momentum distributions of each ion fragment (H^+, H^+, CH^+, CH^+) resulting from the four-body complete fragmentation of ethylene in both cis and trans configurations. The momentum components along the P_x, P_y, and P_z axes are plotted to illustrate the distinct spatial characteristics of the two fragmentation pathways. Notably, differences between the cis- and trans-fragmentation channels are clearly observable in the 3D momentum distributions, providing further insight beyond what can be inferred from planar projections alone.

Angular distribution and projection

Another important form of data representation is the relative angular distribution of ion momenta. To gain deeper insight, we transform the momentum distribution from the Cartesian coordinates used in the Newton diagram representation to spherical coordinate. For example, in the case of ethylene, with the molecular frame defined as shown in Fig. 2.9(a), the corresponding angular distribution of proton momentum is presented in Fig. 2.9(b). The details are discussed in Chapter 4.

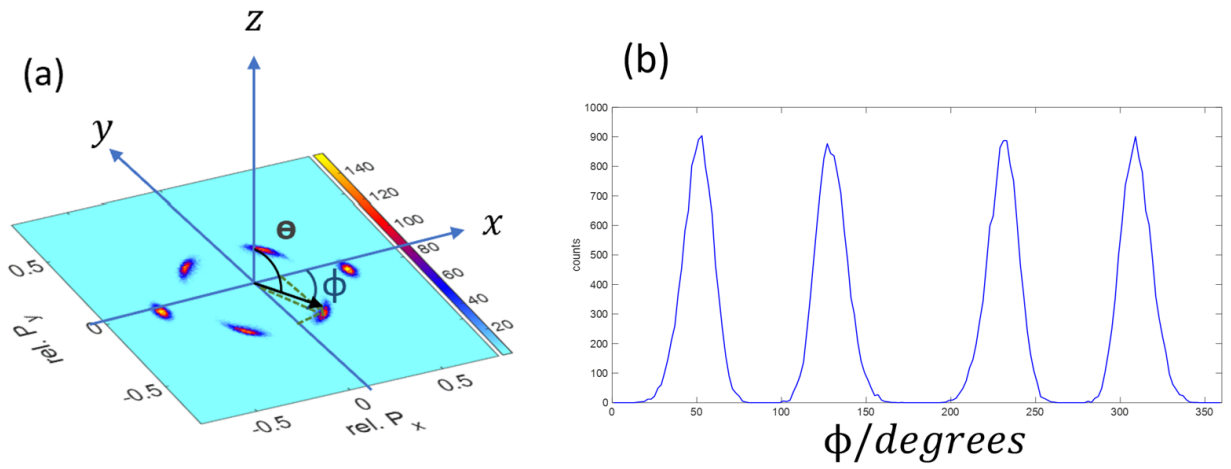

Figure 2.9: ***Example of molecular frame transformation using ethylene.*** *(a) Transformation of molecular frame of ethylene represented from Cartesian coordinates to spherical polar coordinate. (b) Projected ϕ angular distribution of proton momentum.*

2.3.4 Combining Coulomb explosion simulation with Native frame analysis

By combining CES with Native frame analysis, we can simulate the momentum distribution of molecular fragmentation and distinguish between concerted and sequential fragmentation pathways. To evaluate these scenarios, we performed CESs using both instantaneous (concerted) and 'time-delayed' (sequential) charge localization models, allowing comparison of the resulting fragment momentum distributions. For the 'time-delayed' CES, an n-body fragmentation event can be modeled as $(n-1)$ sequential steps of two-body CES, although the exact approach depends on the specific molecule in practice.

For example, in the three-body fragmentation of ethylene yielding final ion fragments H^+, CH^+, and CH_2^+ following triple ionization, a concerted breakup is simulated by assigning charges to the center of mass (COM) of each fragment and propagating their motion under Coulombic repulsion. In contrast, sequential breakup simulations, such as breakups via CH_2^{2+} + CH_2^+ or $C_2H_3^{2+}$ + H^+ pathways, are modeled in two steps. First, a two-body Coulomb explosion is simulated without fully exploding the internal fragments. The rotational motion and relative orientation of the intermediate species are then allowed to evolve

for a defined delay time before the second explosion step is applied. The time delay for each step can be guided by quantum chemical calculations or literature-reported dissociation timescales like those we used for the sequential breakup simulation for ethylene three-body breakup via $C_2H_3^{2+}$ + H^+ pathway introduced in Appendix. A.1.3. Furthermore, we can also try different rotation patterns, as we simulated various rotations for the CH_2^{2+} + CH_2^+ sequential breakup pathway introduced in Appendix. A.1.3. This approach allows us to mimic sequential dynamics and study their distinct signatures in momentum space.

N(KER$_{A-B}$, $\Theta_{AB,\ C}$) distributions

For Native frame analysis, the most used data representation is the 2D plot of KER_{AB} vs $\theta_{AB,C}$ which is defined in the Native frame as shown in Fig. 2.5. The kinetic energy release (KER) in the second step, KER_{AB}[56,19,18] which is:

$$KER_{AB} = \frac{P_{AB}^2}{\mu_{AB}} \tag{2.23}$$

where the P_{AB} is conjugate momentum, defined by $P_{AB} = \mu_{AB}(\frac{P_B}{m_B} - \frac{P_A}{m_A})$, the reduced mass μ_{AB} can be obtained from $\frac{1}{\mu_{AB}} = \frac{1}{m_A} + \frac{1}{m_B}$. $\theta_{AB,C}$ can be defined as:

$$\theta_{AB,C} = \cos^{-1}(\frac{P_{AB,C} \cdot P_{AB}}{|P_{AB,C}||P_{AB}|}) \tag{2.24}$$

Under these definitions, we can obtain the CES represented in the Native frame, as shown in Fig. 2.10. These different representations of CES data combined with Native frame analysis provide valuable guidance for interpreting experimental data. Moreover, experimental data can be directly compared with the simulation results across multiple forms of representation, facilitating a more comprehensive structural and molecular dynamics analysis.

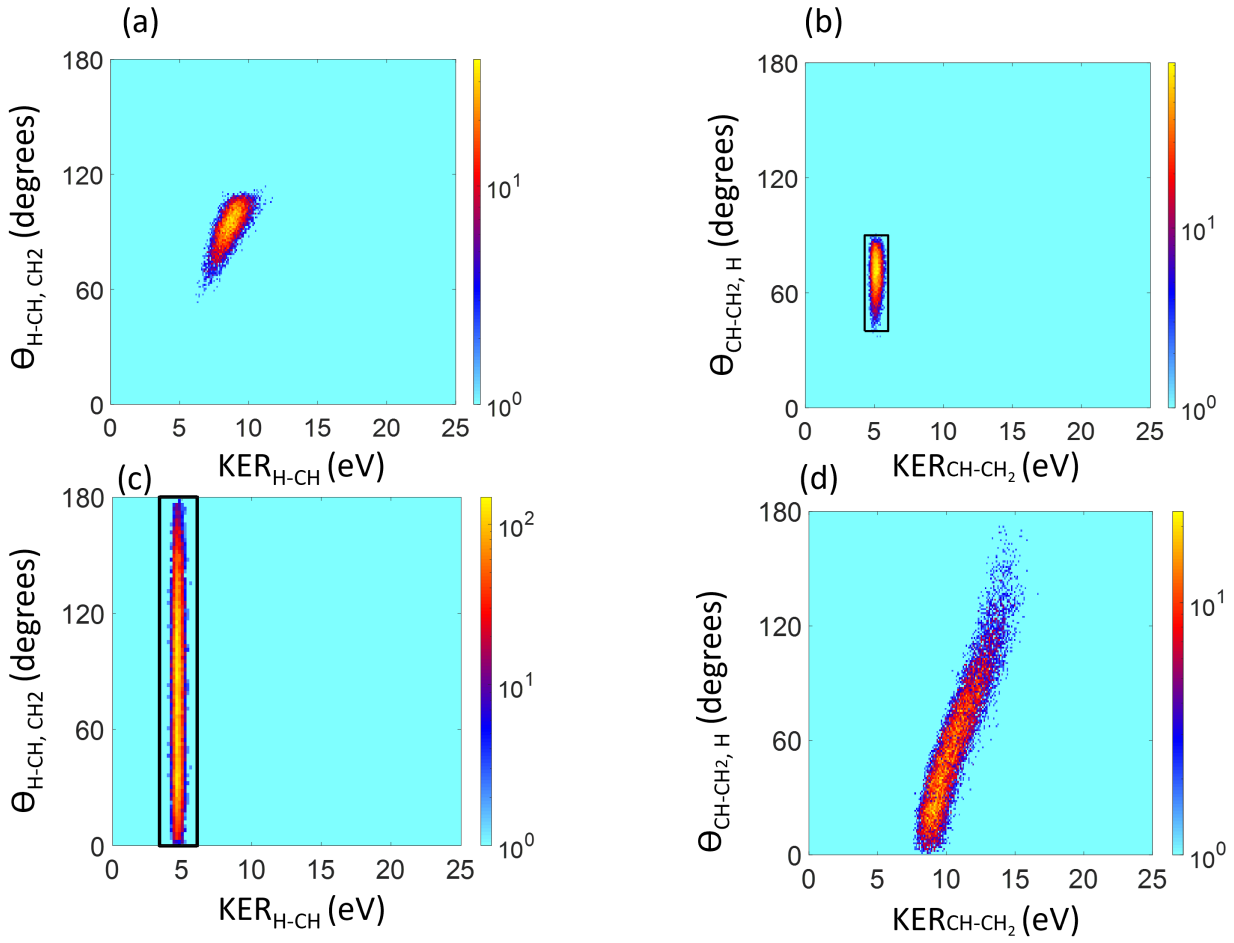

Figure 2.10: ***Example of Native frame analysis of ethylene.***
(a) $N(KER_{H-CH}, \Theta_{H-CH, CH_2})$ distributions and (b) $N_{KER_{CH-CH_2}}, \Theta_{CH-CH_2, H}$ distributions for three-body fragmentation channel: H^+, CH^+, and CH_2^+ of the CES of concerted breakup; (c) $N(KER_{H-CH}, \Theta_{H-CH, CH_2})$ distributions and (d) $N(KER_{CH-CH_2}, \Theta_{CH-CH_2, H})$ distributions for three-body fragmentation channel: H^+, CH^+, and CH_2^+ of the CES of sequential breakup via $CH_2^+ + CH_2^{2+}$ intermediate. The data in all panels are scaled down in energy and momentum as guided by the theory as explained in Section 4.1.

Chapter 3

Experimental methods

The goal of this thesis is to investigate photoinduced ultrafast molecular dynamics. To achieve this goal, we mainly use a laser system known as PULSAR in the James R. Macdonald Laboratory (JRML), a 10 kHz Ti:Sapphire-based laser with a central wavelength of 790 nm. A specific description of this laser system is given in ref.[63]. For the experiment on UV-induced ring conversion dynamics of 2(5H)-thiophenone (thiophenone) in Chapter 5, we used the third harmonic of the PULSAR laser output centered around 262 nm as a pump. For earlier experiments on furan[54] and for preliminary studies on 2,3-dihydrofuran (DHF) described in Chapter 6, we used the fourth harmonic of the PULSAR output centered around 197 nm to induce ring conversion dynamics. The primary development and technical improvement achieved in this work is the generation of short UV pulses achieved by optimized pulse compression. With these developments, we can obtain the high-temporal resolution required for the experiments presented here, in particular for studying the ring opening in 2(5H)-thiophenone.

In most of the experiments, an intense NIR (near-infrared) pulse as a probe to multiply ionize the molecules and inducing Coulomb explosion. In the first part of Chapter 5, we also employed intense X-ray pulses from the European XFEL operated at 2.6 keV photon energy to induce the Coulomb explosion of thiophenone.

In all of the experiments presented here, to obtain the three-dimensional (3D) momentum information of the ionic fragments that we used to map laser-induced molecular dynamics, we employ a standard COLd Target Recoil Ion Momentum Spectrometer (COLTRIMS). This experimental setup, which includes a spectrometer, a supersonic gas jet equipped with a heating tape for liquid sample, and a time- and position-sensitive multi-hit detector, allows us to record the 3D momenta of several created ions, which are needed for Coulomb explosion imaging.

This Chapter describes some basic principles of the light sources used in this work (Ti:Sapphire NIR laser and XFEL pulses), details the 3rd and 4th harmonic generation schemes, and provides a basic description of the COLTRIMS spectrometer used. At the end of the Chapter, a brief introduction of the data acquisition scheme, data sorting, analysis, and representation procedures is also given.

3.1 X-ray Free Electron Laser (XFEL)

X-ray Free-Electron Lasers (XFELs) opened the way to generate ultra-intense ultrashort X-ray pulses. FEL was first proposed by John Madey[64] and demonstrated[65] by his group at Stanford in the 1970s. The European XFEL facility used in this work generates X-ray pulses with many properties (like relative bandwidth, brightness, and coherence) comparable to conventional ultrafast lasers, as they produce polarized and collimated light beams[66]. The pulse duration of XFELs can reach down to the attosecond[67], which makes them a great light source for time-resolved pump–probe experiments.

Unlike conventional lasers, which use a cavity and optics systems for beam propagating back and forth until saturation, XFELs achieve the gain by sending electron beams from linear accelerators to a long undulator where the X-ray power increases exponentially by pumping energy from the electron beam through the Self-Amplified Spontaneous Emission (SASE) process. With this scheme, FELs can generate intense pulses in the extreme

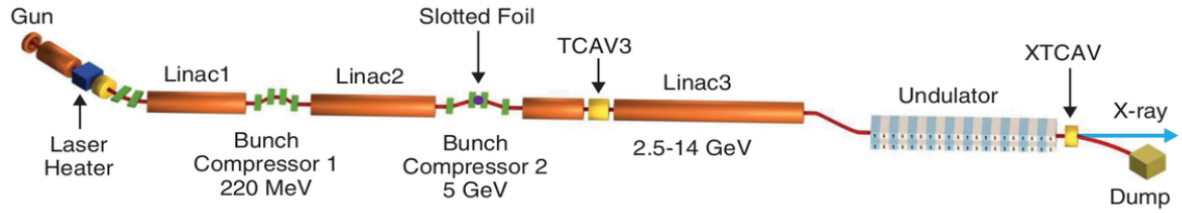

Figure 3.1: ***Schematic layout of the Linac Coherent Light Source (LCLS), the first hard X-ray free-electron laser.***
The facility consists of an injector and radio frequency (RF) linear accelerator, followed by bunch compressors, undulator sections, and multiple experimental hutches. Coherent X-ray pulses are generated through the self-amplified spontaneous emission (SASE) process in the undulator section. Adapted from Bostedt et al.[69].

ultraviolet (XUV) and X-ray regimes.

Specific properties of XFELs, in particular a combination of X-ray photon energies, short pulse durations, and high intensities, enable novel measurement schemes in photochemistry that are not feasible with conventional optical laser sources. For example, their ability to target a specific atom in a polyatomic system by setting the photon energy slightly above the binding energy of a core-electron shell of this atom enables site-specific probing of dynamics. Furthermore, high intensities of XFELs can drive multiphoton ionization processes where target atoms or molecules can be promoted to extremely high charge states[28,68].

Fig. 3.1 illustrates the layout of the first operational XFEL, the Linac Coherent Light Source (LCLS). There are three sections the electron bunch travels through after being generated by the electron gun, with bunch charges in the pC to nC range. Firstly, the electron bunch acquires a high peak current (exceeding 1000 A) with confined energy and angular spread through three stages of linear accelerators (Linac) separated by two compressors with slotted foil for ultrashort pulse generation. Then the electron bunches are guided to the undulator for generating the X-ray radiation. In the end, the electron dump can separate the X-rays pulse from the electron bunches.

The X-rays with high energy are produced in the undulator through the resonant inter-

action between the incoming electron bunch and their radiated X-rays.

Undulator radiation

The beam of electrons is generated by a short laser pulse, and it is ejected from a photocathode located inside a microwave cavity and accelerated to up to several GeV energies. For the study in this thesis, the FEL used is from the European XFEL facility in Hamburg. The European XFEL accelerator can currently energize electrons up to 17.5 giga-electronvolts (GeV)[70]. Then the electrons are sent to the undulator. The undulator is an array consisting of a periodic structure of dipole magnets as shown in Fig. 3.1. The dimensionless undulator strength parameter, K, is defined by[71]:

$$K = \frac{eB\lambda_\mu}{2\pi m_e c} \tag{3.1}$$

where λ_μ is the spatial period of the undulator magnets and B is the magnetic field on axis. The Lorentz force from this magnetic field causes the electron bunches in the beam to wiggle transversely, traveling along a sinusoidal path about the axis of the undulator. In the undulator, the motion of the electrons appears as a transverse harmonic oscillator emitting radiation in a corresponding oscillator angular frequency. The wavelength of the radiation can be tuned by adjusting the energy of the electron beam and the undulator parameter K. The wavelength of the emitted radiation on the axis of electron propagation is given by[72]:

$$\lambda_r = \frac{\lambda_u}{2\gamma^2}(1 + \frac{K}{2}) \tag{3.2}$$

where γ is the relativistic Lorentz factor which is also a dimensionless quantity. Due to Lorentz contraction, the undulator is shortened by a γ factor. This emitted radiation at wavelength λ_r is observed in the laboratory frame which brings the second γ factor. The radiated power can be derived from the Larmor formula which is used to calculate the total power radiated by a non-relativisitic point charge as it accelerates. The average power

radiated into the central cone which is defined as containing $1/N$ relative spectral bandwidth (where N is the number of magnet periods)[73]:

$$\bar{P}_{cen} \simeq \frac{\pi e^2 c\gamma^2}{\varepsilon_0 \lambda_u^2 N} \frac{K^2}{(1 + K^2/2)^2} \tag{3.3}$$

As multi-electron bunches traverse the undulator, the radiated power is much greater. There is one key difference between FELs and synchrotrons which is that the electrons radiate in phase due to being spatially arranged within the bunch, while the electrons are randomly distributed within the bunch, resulting in the random phase relation among emitted wave trains. The geometry of the linear assembly of undulators in FELs enables phase-correlated electric and magnetic fields, which is also called *microbunching*.

Microbunching and SASE

Microbunching happens due to the emitted radiation and the neighboring electrons interacting with each other within the undulator which is different from synchrotron radiation with the electron bunch length typically larger than the X-ray wavelength. The concentration of electrons into very narrow slices within the undulator is called microbunching.

Since both the relativistic electrons and the electromagnetic wave have a sinusoidal spatial profile, the electron bunch gains or loses energy to the electromagnetic field depending on the electron velocity vector direction. In some instances in the undulator, if the electrons have a wiggling direction parallel to the electric field, the electrons lose energy due to a smaller Lorentz factor γ, while other electrons which have anti-parallel wiggling directions gain energy. This process leads to coherent radiation of the formed microbunches. As electrons gain energy traveling faster in the longitudinal direction and those higher energy electrons catch up to lower energy electrons, the formation of microbunches of electrons at multiples of the wavelength λ_r radiates in phase, producing light with higher intensity.

For each undulator period, the wavefront of the emitted light pulses slips ahead of the

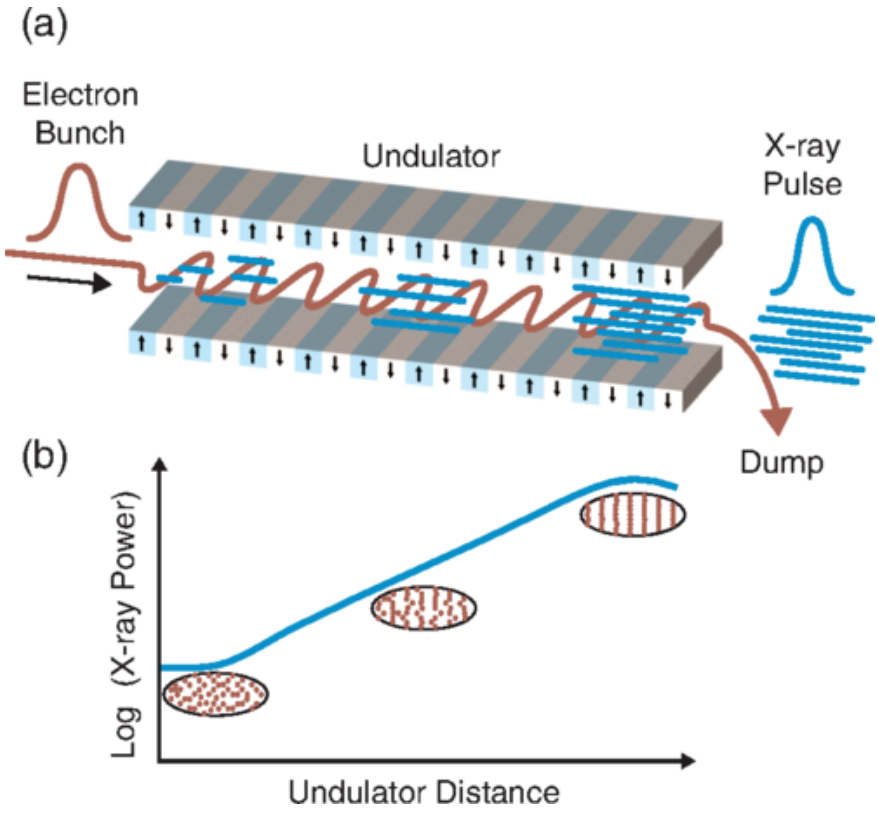

Figure 3.2: ***Schematic plot of self-amplified spontaneous emission SASE.***

(a) Schematic of a high-gain self-amplified spontaneous emission (SASE) free-electron laser. (b) Exponential gain process in a SASE free-electron laser. The relativistic electron beam travels through a long undulator, where initial shot noise in the beam generates spontaneous radiation that interacts back with the beam. Both the radiation power and the electron beam microbunching grow exponentially along the undulator until saturation is reached. Adapted from Bostedt et al. [69] .

electron bunch by one wavelength λ_r per undulator period. The slippage length is the total length of the wavefront that slips ahead of the corresponding electron at the undulator exit. This slippage ensures the interaction between the pulses of electromagnetic waves and the electrons throughout the whole undulator, leading to further microbunching and exponentially increased radiation[74]. However, once the bunch period reaches the radiation wavelength, microbunching starts to saturate, resulting in no further increase in X-ray power as shown in Fig. 3.2[69].

In FELs, the electron bunches serve as the gain medium as in the conventional laser where the gain medium provides the amplification to the stimulated radiation for bound electrons. The electron bunches provide the stimulated radiation to the emitted X-ray radiation associated with unbound electrons. The peak power of the X-ray radiation, which increases with microbunching after this resonant interaction, is given by[69]:

$$P_z \propto e^{\frac{z}{L_g}} \tag{3.4}$$

As z is the electron longitudinal traveling direction, L_g is the power gain-length:

$$L_g \approx \frac{\lambda_u}{4\pi\sqrt{3}\rho} \tag{3.5}$$

where ρ is the FEL Pierce parameter, which has a typical value of about 10^{-3}[75].

The generation of the XFEL pulses can start with the radiation from the first few undulator sections along with exponential X-ray power growth happening in the remaining undulator sections, which is called Self-Amplified Spontaneous Emission (SASE). This is the main process for FELs at European XFEL SQS used in this work.

The SASE process starts with an electron bunch being injected into an undulator. The produced X-rays from SASE FELs have limited temporal coherence due to the interaction startup process introducing shot noise[71]. This startup process causes random phase shift between the pulses where there are different wavelengths to be radiated. SASE energy spectra

show a noise-like distribution of intense spikes on top of a lower-amplitude background[72]. The spikes will change on a shot-to-shot basis randomly. The phase shifts lead to short coherence within the pulse, causing the quasi-coherent emitted beam.

However, the undulators are tuned to generate maximum fluence at the desired wavelength to enable SASE, thereby providing intense pulses of high-energy photons. For photoelectron or X-ray absorption measurements, it is important to obtain single-shot diagnostics, especially for broad bandwidths. The stochastic properties of the SASE pulses can degrade the spectral quality when averaging several shots.

An alternative scheme which can make the XFEL pulse spectrum narrower and smoother is to start the amplification process by introducing seeding radiation at the beginning of the undulator[76,77]. The difference between those two processes is how the electron beam modulates to induce microbunching. Since it is hard to get seeding radiation at the wavelengths of typical XFELs, a promising version of this approach for XFELs is self-seeding. Here, a thin diamond crystal inserted in the beam path produces a train of monochromatic wakefields that trail the main X-ray pulse by a few tens of femtoseconds[78,79]. By using a magnetic chicane to detour the electron bunch so that the electron bunch and the wake overlap in time, the monochromatic seed signal can be amplified in the downstream undulators. The examples of single-shot and averaged spectra of SASE and self-seeded XFEL pulses are shown in Fig. 3.3. In this work, only SASE pulses from the European XFEL have been used.

3.2 Ultrafast laser system and optical layout

This section is partially adapted from sections 3.1-3.3 of the Ph.D. thesis of former group member, Farzaneh Ziaee[81], since we used the same core optical setup. However, as outlined below, significant modifications have been made to the optical layout. In particular, optimized third- and fourth-harmonic generation setups as well as the improved pulse compression

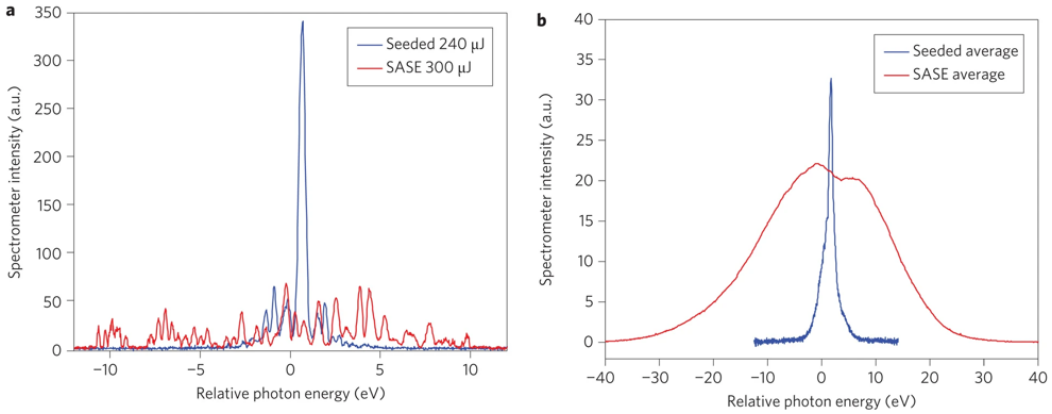

Figure 3.3: ***Single-shot (a) and averaged (b) X-ray spectra measured in SASE mode (red) and self-seeded mode (blue).***
The full width at half maximum (FWHM) of the single-shot self-seeded spectrum. The vertical scales are in the same arbitrary units for both (a) and (b). For the SASE measurements, the chicane was turned off, whereas it was necessarily activated for the self-seeded mode. Adapted from Amann et al.[80].

results represent new developments driven by the author of this thesis.

The laser system used for the experiments at JRML is called PULSAR, short for Prairie Ultrafast Light Source for Attosecond Research. The laser is composed of a Ti:Sapphire oscillator and a Ti:Sapphire two-staged multi-pass amplifier[82,30,83] generating linearly P-polarized 2 mJ pulses at 10 kHz. The pulse duration (full width at half maximum in intensity) measured from the experiment results is around 28 fs with a central wavelength near 790nm[63].

3.2.1 Chirped pulse amplification

The first part of this laser system is a Kerr-lens mode-locked Ti:Sapphire femtosecond oscillator[84,85,86]from KM Labs. A nonlinear titanium-doped Ti:Sapphire crystal acts as a lens for the laser beam with a Gaussian beam intensity profile. Inside the laser cavity, this crystal is optically pumped by a frequency-doubled $Nd : YVO_4$ (Verdi) laser at 532nm. Mode-locking is achieved through the nonlinear Kerr effect, enabling the formation of high-

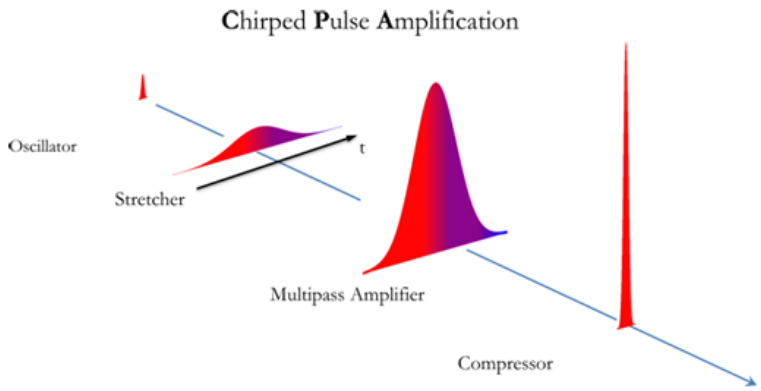

Figure 3.4: ***A schematic view of the evolution of pulse duration and amplitude during chirped-pulse amplification.***

Figure is adapted from Zohrabi et al.[87].

intensity pulses within the cavity. Although the broad gain bandwidth supports many cavity modes, ultrashort pulse generation occurs when these modes are phase-locked via mode-locking, resulting in constructive interference over a very short time window. This produces ultrashort pulses with a repetition rate of 75.2 MHz and an average output power of 300 mW, corresponding to a pulse energy of 4 nJ. Later, a prism pair within the oscillator compensates for group-velocity dispersion (GVD), compressing the pulses to a duration of 14 femtoseconds.

Chirped pulse amplification (CPA) is a technique for amplifying an ultrashort laser pulse up to the petawatt(10^{15} W) level, with the laser pulse being stretched out temporally and spectrally, then amplified, and then compressed again[88,83] (See Fig. 3.4).

The output from the oscillator is stretched to tens of picoseconds(ps) using a grating-based stretcher. After the stretcher, the repetition rate is reduced to 10 kHz[88,89]and the selected subset of the laser pulses is amplified by the multi-pass amplifier stage which is pumped by a double frequency intracavity, Q-switched Nd: YLF laser. There are two stages for amplification: the first stage is made up of 14 passes through the Ti:Sapphire gain medium, which amplifies the pulse energy up to about 1mJ, and the second stage is composed of 5 passes through another Ti:Sapphire gain medium which increases the pulse

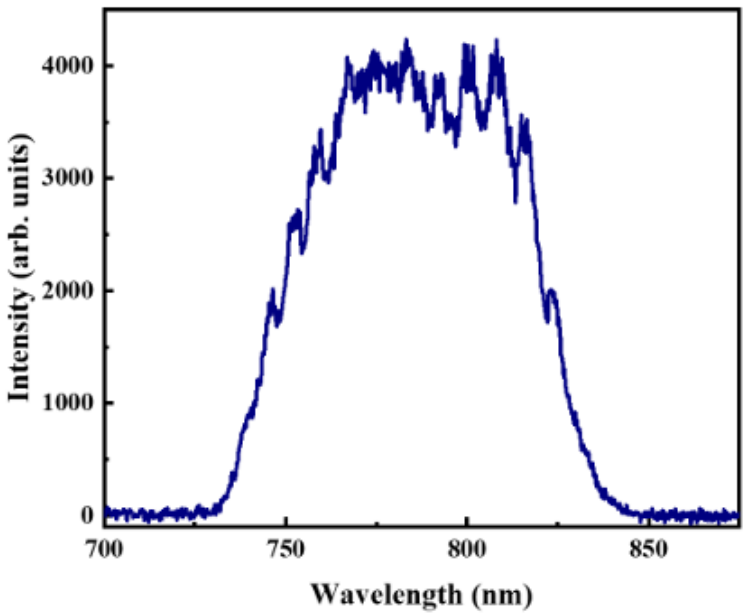

Figure 3.5: ***Typical PULSAR output spectrum after second amplification stage.***

Figure is adapted from Ziaee et al.[81] .

energy up to 2mJ. In the end, the grating-based compressor compressed the beam around 28 fs FWHM (for the experiments of these studies).

3.2.2 Frequency-Resolved Optical Gating (FROG)

For performing ultrafast time-resolved pump–probe experiments, pulse duration of the laser heavily impacts the outcome results[90]. To characterize the laser pulses, we employ the Frequency-Resolved Optical Gating (FROG) method, first demonstrated by Trebino in 1991[90], which can give a frequency resolved autocorrelation[91] signal with pulse duration and phase information included.

This method starts with splitting the measured pulse into two identical halves with delay separation. Both pulses are focused on a rapidly responding nonlinear medium for temporal

overlap. The intensity of the signal detected can be written as:

$$I(\tau) = |\int_{-\infty}^{+\infty} \varepsilon(t)\varepsilon(t-\tau)dt|^2 \tag{3.6}$$

The ε represents the electric field of the measured pulse and τ is the time delay between the identical pulses. $\varepsilon(t-\tau)$ is also known as the 'gate' pulse. The pulse duration of the laser can be retrieved from $I(\tau)$. There are different types of FROG for different purposes of pulse characterization, such as polarization gating (PG-FROG) which can measure a pulse with a much broader spectral range with more intuitive traces yields but requires higher pulse intensity[92], and transient grating (TG-FROG)[93] which is useful for measuring UV pulses and self-diffraction (SD-FROG)[94] which can be used in various spectral regions, including deep UV. These FROG methods are built and modified based on the second harmonic generation (SHG-FROG) which we use in these studies for the characterization of the PULSAR pulses. Comparing to the general layout of the FROG setup as shown in Fig. 3.6, we additionally use a neutral density (ND) filter for attenuating the measured laser pulses. The SHG-FROG trace of the spectrogram of the autocorrelation $I^{SHG}(\omega,\tau)$ can be adapted from eq (3.6):

$$I^{SHG}(\omega,\tau) = |\int_{-\infty}^{+\infty} \varepsilon(t)\varepsilon(t-\tau)e^{-i\omega t}dt|^2 \tag{3.7}$$

The 2D map Fig. 3.6(b) of the trace intensity as a function of wavelength and the time delay between identical pulses is generated from the detector signal combined with an iterative devolution algorithm[95,96] for reconstructing the electric field with a guessed electric field for initiation. The typical measured PULSAR FROG trace with a pulse duration around 28 fs FWHM is shown in Fig. 3.6(a). However, SHG-FROG cannot distinguish between positive and negative chirped pulses as it is insensitive to the time inversion.

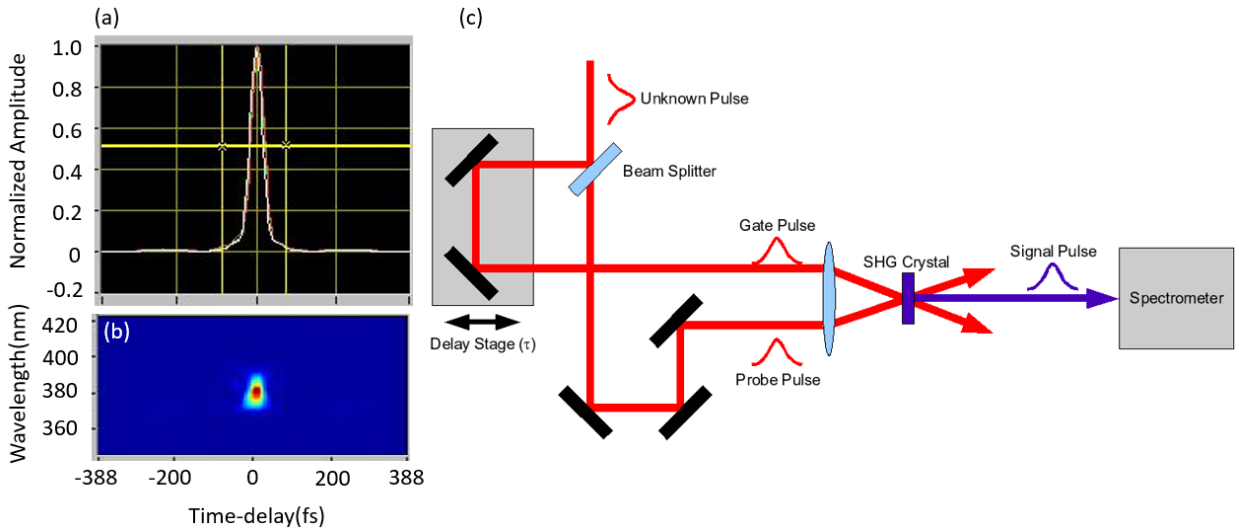

Figure 3.6: ***SHG-FROG trace and setup overview.***

(a) 1D projection of the FROG trace along the time-delay axis extracted from (b); (b) 2D FROG trace map measured from our experiment; (c) Schematic layout of a FROG apparatus. Adapted from Trebino *et al.*[90].

3.2.3 Cross-correlation frequency-resolved optical gating

For the pulses generated later with non-linear frequency conversion in a nonlinear crystal[97], Cross-correlation frequency-resolved optical gating (X-FROG) is employed for characterization of the pulses for which the wavelengths lie in the ultraviolet (UV) region. However, for UV pulses, the achievable phase-matched spectral range of the crystal, the dispersion-induced broadening by the material, and the transparent spectral range of the crystal have severe effects in the characterization for pulses of deeper UV regions due to the non-linear process compared to NIR pulses.

XFROG is combined with a gate pulse using by difference frequency generation (DFG), rather than splitting the test pulse as in standard FROG. Using DFG-XFROG, an ultrafast UV pulse with weak intensity can be characterized. Adapted from eq. (3.7), we can get the output XFROG trace denoted as:

$$I^{XFROG}(\omega,\tau) = |\int_{-\infty}^{+\infty} \varepsilon(t)\varepsilon_g(t-\tau)e^{-i\omega t}dt|^2 \tag{3.8}$$

where the ε_g is the electric field of the gate pulse. In our experiments for UV-induced molecular dynamics investigation, we employ SHG-FROG so that we use an intense NIR pulse which is already characterized by FROG measurement as the gate pulse. The XFROG trace I^{XFROG} combined with the known gate pulse ε_g can be used to characterize the UV pulses $\varepsilon(t)$. In these experiments of these studies, we use the FWHM of the cross-correlation to obtain the UV pulse duration by calculating:

$$\tau_{UV} = \sqrt{\tau^2_{XFROG} - \tau^2_{NIR}} \tag{3.9}$$

as the τ_{UV}, τ_{XFROG} and τ_{NIR} are the FWHM of the UV, NIR, and the XFROG trace of the two pulses.

3.2.4 Harmonic generation and nonlinear optics

For performing the UV-induced molecular dynamics investigation experiments, we need to use UV pulses for triggering the process which is generated by nonlinear frequency conversion. There are different types of frequency generation of nonlinear processes shown in Fig. 3.7 in a susceptibility χ^2 crystal medium.

Nonlinear optics

Nonlinear optics is the study of how light interacts with materials in ways that depend on the intensity of the light, leading to phenomena like frequency doubling and self-focusing. In this study, we used the non-linear crystal such as a type-I Barium Borate (BBO) crystal with a cut angle of 29.2° and a thickness of 150 μm for high harmonics generation. To study the propagation of the electric field in the laser, we consider the optical field in a

second-order nonlinear medium which contains two frequency components in the form of[98]:

$$\varepsilon(t) = \varepsilon_1 e^{-i\omega_1 t} + \varepsilon_2 e^{-i\omega_2 t} + ... \tag{3.10}$$

where the ε_1 and ε_2 are the amplitudes of the electric field with frequencies of ω_1 and ω_2. With an electric field applied, the polarization of a medium depends linearly on the field at low intensities and nonlinearly at high intensities due to the electric charge oscillation and electromagnetic radiation. The polarization of a medium can be denoted as a function of the electric susceptibility of the medium[98]:

$$P_x(t) = \chi^{(1)}\varepsilon^1 + \chi^{(2)}\varepsilon^2 + \chi^{(3)}\varepsilon^3 + ... + \chi^{(i)}\varepsilon^i + ... \tag{3.11}$$

The coefficients $\chi^{(i)}$ $(i \geq 2)$ are the higher order non linear optical susceptibilities. If we insert the second-order contribution 3.10 into the polarization 3.11, then we can get the second order of the polarization categorized with different frequency components:

$$P_x^2(t) \approx \varepsilon_1^2 + \varepsilon_2^2 + \varepsilon_1^2 e^{-2i\omega_1 t} + \varepsilon_2^2 e^{-2i\omega_2 t} + \varepsilon_1\varepsilon_2 e^{-i(\omega_1+\omega_2)t} + \varepsilon_1\varepsilon_2 e^{-i(\omega_1-\omega_2)t} \tag{3.12}$$

From this equation, the first two terms correspond to direct current (DC) polarization. The second and third terms are related to second harmonic generation (SHG). The fifth term is associated with sum frequency generation (SFG), and the last term is difference frequency generation (DFG).

Another way of understanding these nonlinear processes is by approaching with laws of momentum and energy conservation. The SFG process can be noted as:

$$\hbar\omega_1 + \hbar\omega_2 = \hbar(\omega_1 + \omega_2) \tag{3.13}$$

As SFG includes creating a new frequency of the field by summing the mixing frequencies ω_1 and ω_2, the conversion efficiency of this process depends on the phase matching and the

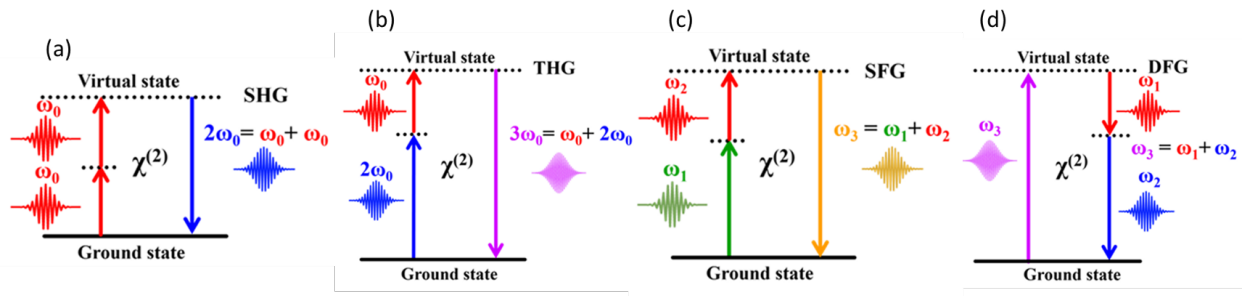

Figure 3.7: ***Nonlinear frequency mixing with a $\chi^{(2)}$ nonlinear crystal.***

(a) Sum-Frequency Generation (SFG); (b) Second-Harmonic Generation (SHG); (c) Third-Harmonic Generation (THG); (d) Difference-Frequency Generation (DFG). Adapted from Ziaee et al.[81] .

material susceptibility. It has been derived in[98,99]. Considering a special case of SFG where $\omega_1 = \omega_2 = \omega_0$, which is the SHG, and the assumption of constant electric field, SHG conversion efficiency can be obtained as:

$$\eta_{SHG} = \frac{I_{2\omega_0}}{I_{\omega_0}} = \frac{2\pi^2(\chi^{(2)})^2 I_{\omega_0} L^2 sinc^2(\frac{\Delta kL}{2})}{\lambda^2 \epsilon_0 c^3 n_{\omega_0}^2 n_{2\omega_0}} \tag{3.14}$$

where the L is the length of the medium crystal and the $k = \frac{n}{c}\omega$ is the wavenumber. $I_{\omega_0}$is the power density, ϵ_0 is the vacuum permittivity, and $n_{n\omega}$ is the optical index of the medium at $n\omega$.

The efficiency increases with pump intensity, limited only by the crystal's damage threshold. It also depends on the spatial overlap of the interacting fields and is maximized under the phase-matching condition ($\Delta k = 0$). As the fundamental wave propagates, its intensity and thus the efficiency of the generated wave decreases. Efficient conversion requires the fundamental and generated waves to remain in phase, but chromatic dispersion typically causes phase mismatch. This can be mitigated using birefringent crystals, which provide different refractive indices for different polarizations, maintaining phase velocity matching between frequencies.

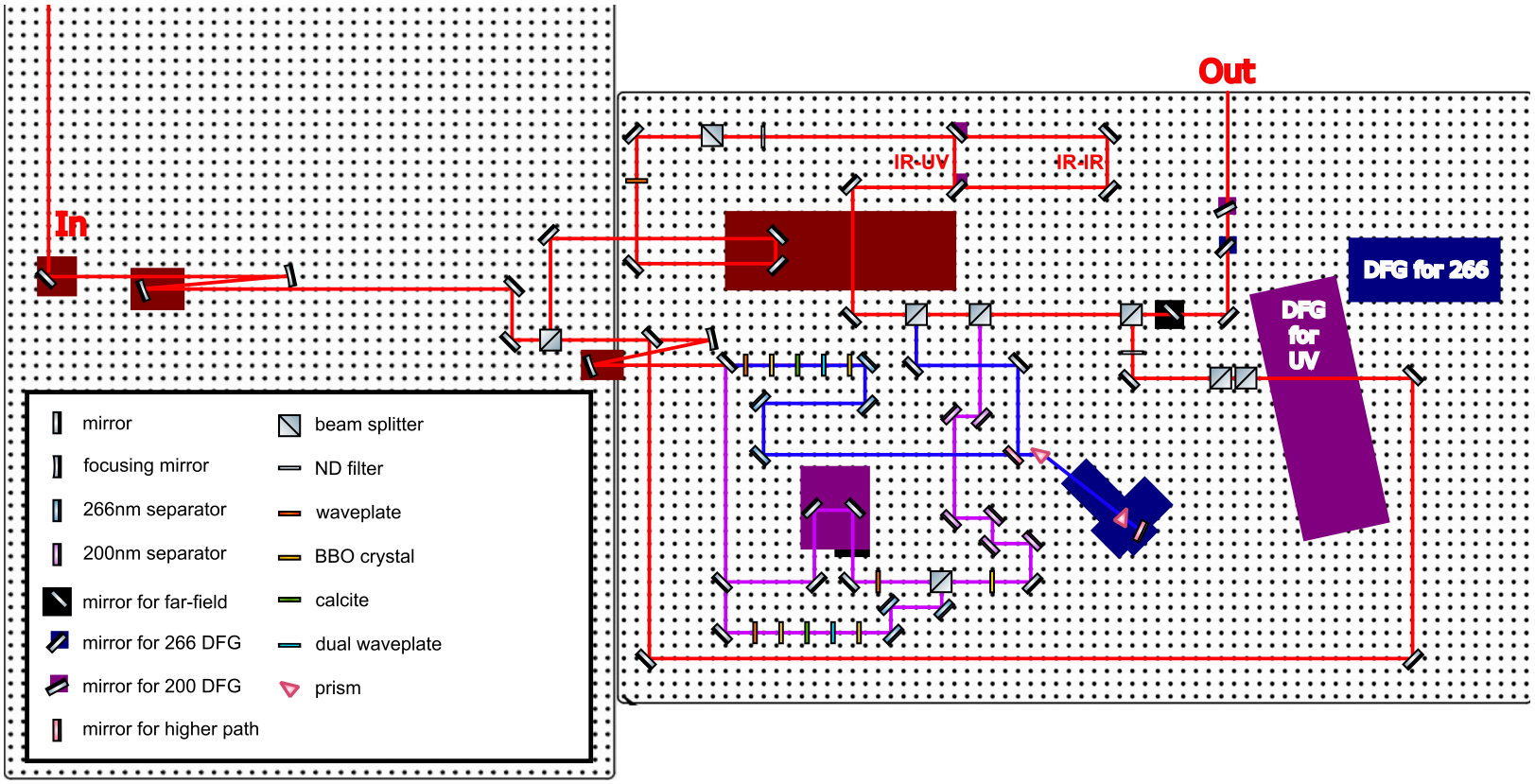

Figure 3.8: ***Diagram of the PULSAR COLTRIMS optical arrangement.*** *The red lines indicate the IR beam path, blue corresponds to the third harmonic generation (THG) beam at 266 nm, and purple represents the fourth harmonic generation (FHG) beam at 200 nm. Figure courtesy of Sanduni Kudagama and Tu Thanh Nguyen (Kansas State University)*

Harmonic generation

From Fig. 3.8, which is the layout of our optical beam path, the SHG pulse is produced in the very first step for the later THG or FHG with sum-frequency generation.

Third Harmonic Generation (THG)

In our experiments, we use a typed-I BBO Crystal with thickness of 150 μm for the high harmonic generation. After SHG pulse is generated in the BBO crystal medium, there is a time delay[100,101] between the fundamental PULSAR output pulse and the second harmonic pulses. For normal incidence of the pulses passing through the medium as we perform in

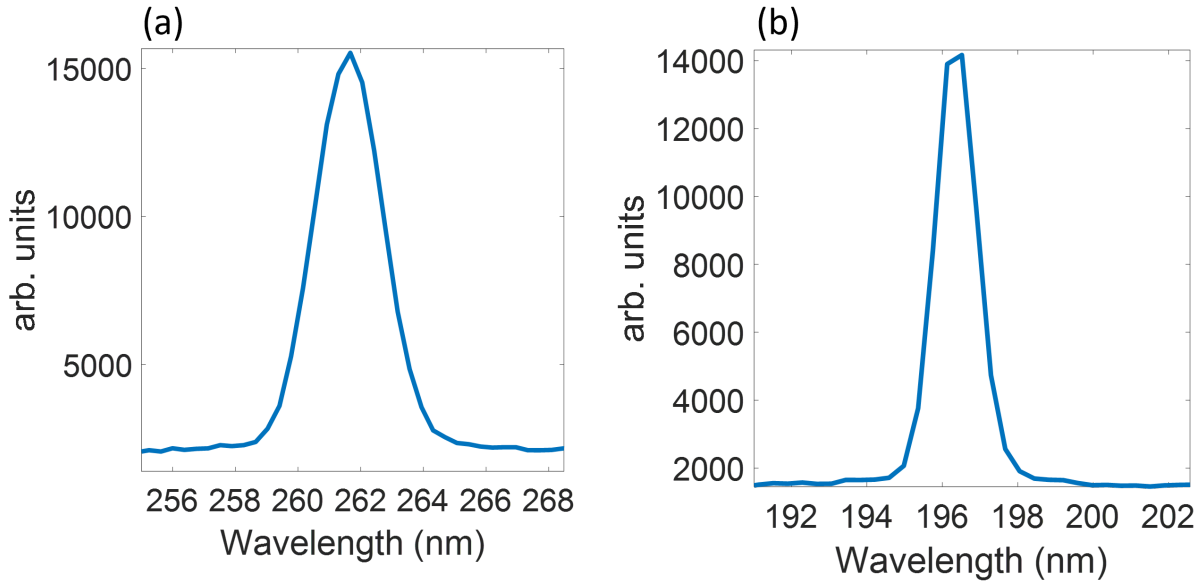

Figure 3.9: ***THG and FHG spectra.***
Spectra of measured (a) THG and (b) FHG from experiment using an Ocean Optics FLAME-S-XR1-ES spectrometer.

our experiments, we have 30fs time difference. As we show from Fig. 3.8, we use calcite crystal with 2mm thickness for adjusting this time delay. To obtain the final output third harmonic beam with parallel (P-polarized) polarization, a dual half-wave plate is used to adjust the fundamental IR pulses by 90 degrees without changing the polarization of the second harmonic beam. With multiple 200nm separators, as shown in the Fig. 3.9(b), the resulting third harmonic beam is separated from the fundamental and the second harmonic beam for generation. The conversion efficiency measured in our experiments is around $2\% - 3\%$. The measured spectrum of the THG beam is shown in Fig. 3.9 (a).

Fourth Harmonic Generation (FHG)

To generate the fourth harmonic of the Ti:Sapphire fundamental beam, we choose to mix the fundamental and the third harmonic in a nonlinear crystal for generation instead of an immediate doubling of the second harmonic using two SHG stages. As the second method needs careful crystal selection to ensure phase matching for both SHG stages and the final

FHG stage and might have lower conversion efficiency due to weaker 2ω intensity or phase mismatch, we use the second method which gives potentially higher conversion efficiency as opposed to losing some energy during the first SHG using another method.

We used a 50 μm type-I BBO crystal for fourth harmonic generation as another two commercially available crystals which are also transparent and near 200 nm have some limitations. Lithium Triborate (LBO), another commonly used crystal, has a small nonlinear coefficient which requires higher input pulse intensity, and potassium pentaborate tetrahydrate (KB5) is relatively fragile and has low thermal stability. We generate the fourth harmonic by mixing two S-polarized (perpendicular to optics table) beams shown from Fig. 3.8, with angle phase matching and the measured spectrum of FHG beam shown in Fig. 3.9(b).

3.2.5 Pulse compression

CPA systems, when experiencing significant temporal broadening during propagation due to group velocity dispersion (GVD) and higher-order dispersion, results in larger pulse duration pulses. Longer pulses lead to a lower peak intensity which is not suitable for ultrafast measurement due to lower temporal resolution. To counteract this broadening, pulse compression techniques are employed to temporally shorten the pulse, ideally recovering its transform-limited duration, the shortest possible pulse duration for a given spectral bandwidth.

The electric field of an ultrashort pulse can also be fully described in the time domain as:

$$E(t) = A(t)e^{-i\phi(t)} \tag{3.15}$$

where the $A(t)$ is the time-dependent amplitude (intensity envelope), and $\phi(t)$ is the time-dependent phase. The relationship between spectral phase and pulse duration can be understood through the Fourier transform of the pulse electric field. A Fourier transform-limited

(FTL) pulse has a flat spectral phase, while any deviation leads to temporal broadening. The accumulated spectral phase can be expanded as a Taylor series:

$$\phi(\omega) = \phi_0 + \frac{\partial\phi}{\partial\omega}|_{\omega=\omega_0}(\omega-\omega_0) + \frac{1}{2}\frac{\partial^2\phi}{\partial\omega^2}|_{\omega=\omega_0}(\omega-\omega_0)^2 + \frac{1}{6}\frac{\partial^3\phi}{\partial\omega^3}|_{\omega=\omega_0}(\omega-\omega_0)^3 + \dots \quad (3.16)$$

Here, the second derivative $\frac{\partial^2\phi}{\partial\omega^2}$ represents GVD, and higher derivatives represent higher-order dispersion. Effective pulse compression systems aim to flatten this spectral phase to recover the shortest pulse duration achievable for the bandwidth. When a short laser pulse passes through a medium, its different frequency components travel at different group velocities, leading to pulse broadening. In normal dispersion, longer wavelengths (red) travel faster than shorter ones (blue), causing the red components to lead and the blue to trail. The opposite effect is known as anomalous dispersion.

The quadratic term $\frac{\partial^2\phi}{\partial\omega^2}$ in the spectral phase represents linear chirp, caused by group delay dispersion (GDD) which is the total dispersion accumulated by a pulse after traveling through a material of finite length, so it's the integrated effect of GVD over that length. When GDD is positive in normal dispersion and leads to pulse stretching, it must be compensated by introducing negative GDD. The third-order term $\frac{\partial^3\phi}{\partial\omega^3}$ corresponds to third-order dispersion (TOD), which can cause intensity ringing near the pulse edges when different spectral components arrive at different times. The sign of TOD determines whether the ringing appears at the leading or trailing edge. Higher-order dispersion terms also affect ultrashort pulses, while the constant phase ϕ_0 and first derivative $\frac{\partial\phi}{\partial\omega}$ do not.

It is worth noting that as pulse durations decrease, higher-order dispersion terms become increasingly significant and must be carefully managed. For example, third-order dispersion (TOD) plays a critical role in 30 fs pulses, while for pulses approaching 10 fs, fourth-order dispersion (FOD) also needs to be considered and compensated.

To compensate for dispersion and compress ultrashort pulses, several types of optical compressors are commonly used, including prism pairs, grating pairs, and chirped mirrors. Each type offers different advantages depending on the pulse characteristics. Various

nonlinear techniques have been developed for pulse compression, utilizing nonlinear interactions such as self-phase modulation in optical fibers[102], and spectral broadening through electro-optic phase modulators combined with pulse shaping[103]. However, a detailed discussion of these methods lies beyond the scope of this work. Instead, we provide a brief overview of commonly used linear dispersion compensation techniques, including chirped mirrors, diffraction grating pairs, and, in particular, the prism-pair compressor employed in our experiments. In our experiments, we used a prism-based compressor, which is well-suited for managing group velocity dispersion in the femtosecond regime while maintaining high throughput and minimal loss. Following compression, the pulse duration was further verified through cross-correlation measurements based on difference frequency generation (DFG), providing temporal characterization of the compressed pulses.

Prism compressor

Like gratings, prisms are used to introduce angular dispersion and are commonly used as a dispersion compensation technique[104,105,106,107]. Prism pairs offer relatively low optical losses compared to diffraction gratings, making them a favorable choice for compensating and controlling dispersion in ultrafast pulse propagation through various media. However, a significant limitation of prism compressors is their narrow angular dispersion bandwidth. As a result, achieving higher group delay dispersion (GDD) compensation typically requires increased separation between the prisms, which is an approach that may be impractical in compact or spatially constrained setups. Furthermore, although angular dispersion is the fundamental mechanism enabling pulse compression in prism-based systems, it inherently introduces spatial chirp and pulse front tilt, both of which can degrade the temporal and spatial quality of the pulse[108] and are therefore generally undesirable.

The optical layout of the prism compressor is shown in Fig. 3.10. For compression and compensation, angular diffraction-based pulse compressors require four identical dispersive elements. The first element introduces angular and spatial dispersion, while the

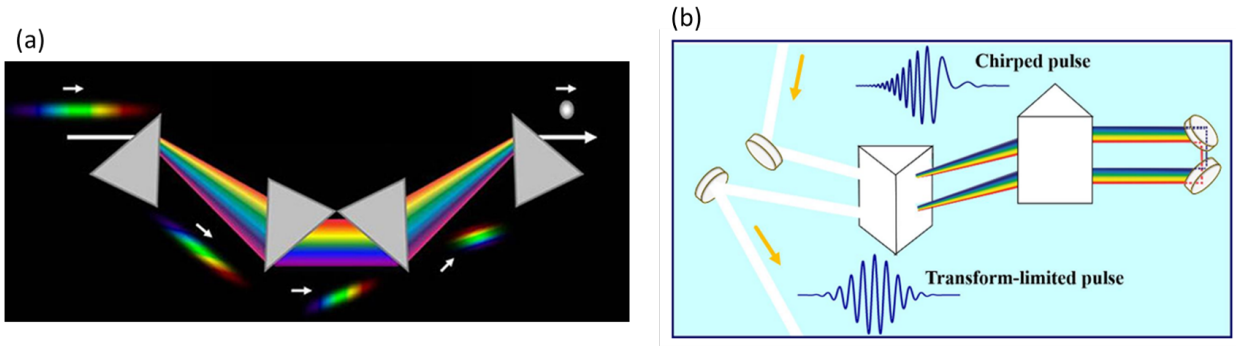

Figure 3.10: ***Schematic of prism compressors.***
(a) The conventional four-prism pulse-compressor adapted from Fork et al.[104] *and (b) a prism-pair compressor in a folded geometry adapted from Martinez et al.*[108] *which is used in our experiment.*

second compensates for the angular dispersion. To eliminate both angular and spatial dispersion, an additional identical pair of elements is required. In this configuration, redder (IR, infrared) wavelengths traverse longer optical paths than bluer (UV, ultraviolet) ones by passing through thicker regions of the second and third components, allowing the shorter wavelengths to catch up temporally. When properly aligned, this setup yields negative group delay dispersion (GDD) without introducing spatial temporal distortions such as pulse-front tilt.[107], where the pulse's arrival time varies across the transverse profile due to a tilt between the pulse front and the direction of propagation.

To determine the required group delay dispersion (GDD) for chirp compensation, we follow the method in Ref.[108], using an unfolded four-prism geometry as in Fig. 3.10(a). The prisms are aligned at the minimum deviation condition, where the beam travels parallel to the prism base, ensuring symmetric incidence and exit angles. This symmetry allows GDD tuning by adjusting the inter-prism distance without altering the output beam direction. Translating a prism perpendicular to the connecting line further adjusts material dispersion. At minimum deviation, the incident and exit angles approach Brewster's angle, minimizing reflection losses for p-polarized light. Gordon and Fork[104,109] demonstrated geometrically that the group delay dispersion (GDD) is proportional to the second derivative of the optical path length with respect to wavelength $P(\lambda)$:

$$GDD_{prism} = \frac{\lambda^3}{2\pi c^3}\frac{\partial^2 P}{\partial \lambda^2} \tag{3.17}$$

With the given optical path $P = 2l\cos\beta$ where the β denotes the angular deviation of the dispersed beam after the first prism, and l represents the distance between the apices of the two prisms. Thus, the calculation of the group delay dispersion (GDD) introduced by the prism compressor can be expressed in terms of the derivatives of the optical path length P as follows:

$$GDD_{prism} \approx \frac{\lambda^3}{2\pi c^3}[-4l[2(\frac{\partial n}{\partial \lambda})^2 + 4(\frac{\partial^2 n}{\partial \lambda^2})(r_0)]] \tag{3.18}$$

Here, r_0 denotes the beam diameter. The resulting expression comprises two distinct terms: a negative term associated with the separation between the two prisms, and a positive term related to the optical path length within the dispersive medium.

The amount of GDD introduced by the prism compressor can be tuned by adjusting the distance l between the two prisms. By applying the Sellmeier equation[110] and computing the derivatives of the refractive index for the prism material, the GDD expression can be reduced to a first-order inequality. To achieve negative GDD, the condition $GDD < 0$ must be satisfied, allowing l to be determined accordingly. This separation is estimated based on the cumulative dispersion introduced by other optical components in the setup. Increasing l enhances the negative GVD imparted by the prisms, thereby compensating for the positive dispersion accumulated elsewhere in the system.

Various prism compressor configurations have been proposed, including four-prism, double-prism, and single-prism setups, all based on a common geometry where the beam traverses the dispersive medium four times to correct both temporal and spatial chirp. Each configuration has trade-offs. The four-prism setup allows a wide GDD tuning range but requires significant space and precise control of prism separations and angles. Any change in input wavelength necessitates synchronized rotation of all four prisms to maintain equal incidence angles. A more compact alternative involves replacing the final two prisms with a

periscope, folding the beam back through the first two prisms, simplifying alignment and tuning. For the experiments in this work, we implemented a prism-pair compressor as shown in Fig. 3.10(b). Although single-prism designs offer easier alignment and use a corner cube for GDD tuning, we opted against this approach due to the difficulty in sourcing low-loss corner cubes.

In the UV-induced Coulomb explosion imaging of thiophenone, we use a third-harmonic-generated 266nm UV beam to induce the ring conversion dynamics. For compressing the UV beam, we employ the prism compressor which is implemented in a folded geometry utilizing a pair of calcium fluoride (CaF_2) prisms, cut at Brewster's angle to optimize transmission at the third-harmonic UV wavelength. The separation distance between the prisms was determined based on estimated dispersion contributions from various transmissive optical components in the beam path. A pair of calcium fluoride (CaF_2) prisms was selected over fused silica due to its lower material dispersion in the ultraviolet regime, thereby minimizing the introduction of higher-order dispersion terms. Pulse duration characterization, both before and after compression, was carried out using a cross-correlation frequency-resolved optical gating (XFROG) technique. This method involved difference frequency generation (DFG) between the UV and NIR pulses to retrieve the temporal profile of the UV pulses.

Pulse characterization

The durations of the uncompressed and compressed UV pulses were characterized using an XFROG-type measurement based on cross-correlation between the NIR and UV pulses via difference frequency generation (DFG). The NIR pulse duration was independently measured using a FROG setup and optimized to 28 fs. The fundamental (NIR) and third harmonic (UV) beams were mixed in a BBO crystal identical to that used in the third harmonic generation stage. A computer-controlled delay stage adjusted the NIR path length to introduce a variable time delay between the pulses. The resulting cross-correlation signal, observed as a second harmonic yield, was recorded as a function of delay using an Ocean

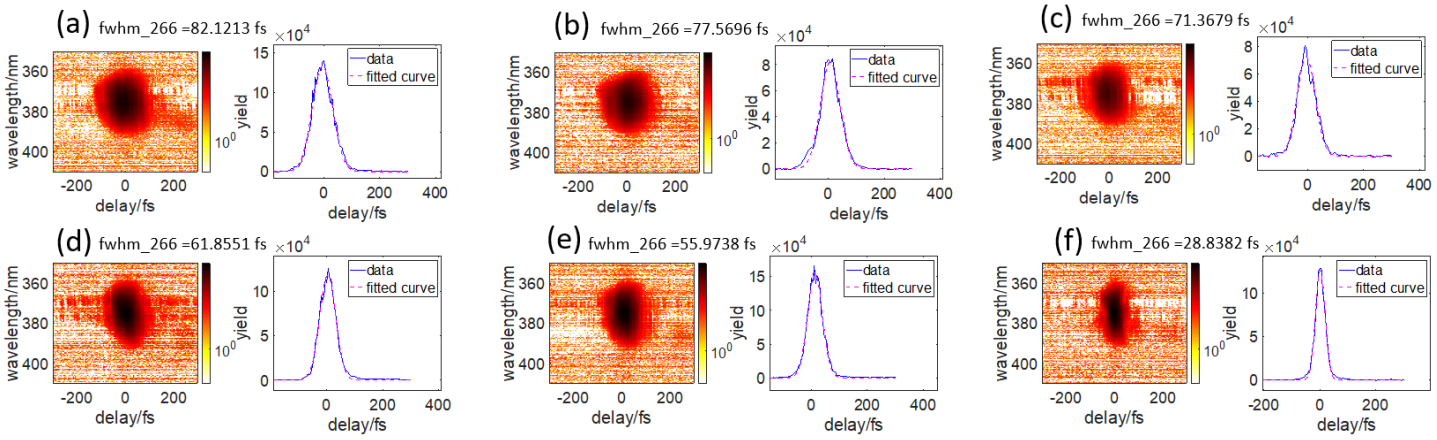

Figure 3.11: ***XFROG traces measured at fixed delay stage position.***
XFROG traces of third harmonic pulses recorded at fixed stage position $X = 13$, while tuning the angle between the two prisms for pulse compression.

Optics FLAME-S-XR1-ES spectrometer. Maximum signal intensity marked the temporal overlap of the pulses. This signal served two purposes: confirming pulse compression and providing a time-zero reference for subsequent time-resolved molecular experiments.

The 400nm cross-correlation signal from the XFROG trace, shown in Fig. B.1 in Appendix B.1, was used to characterize and optimize the prism-pair compressor in order to achieve the shortest possible third-harmonic pulse. The minimum calculated pulse duration for the 266 nm THG pulse was obtained when the prism position was near $X = -13$ (arbitrary unit for the prisms distance). The uncompressed UV pulse had a duration of approximately 131 fs, measured using thin nonlinear crystals to minimize pulse broadening while prioritizing fidelity over conversion efficiency. After tuning the prism compressor, the pulse duration was reduced to 28.8 fs after tuning, approaching the transform-limited duration of 28 fs, estimated assuming a Gaussian pulse envelope and the measured spectral bandwidth. The corresponding cross-correlation traces for the uncompressed and compressed pulses are shown in Fig. 3.11. To further assess the performance of the prism compressor, we re-scanned the delay stage around the point of optimal temporal overlap, using finer adjustments to the prism angles to enhance the temporal resolution of the XFROG trace, as illustrated in Fig. 3.11.

3.3 COLd Target Recoil Ion Momentum Spectrometer (COLTRIMS)

COLd Target Recoil Ion Momentum Spectroscopy (COLTRIMS) is a powerful momentum imaging tool for ions that relies on using internally cold (and well-localized) targets provided by a collimated supersonic gas jet[16]. Conventional atomic and molecular spectroscopy typically investigates light–matter interactions as a function of wavelength to determine the composition and physical properties of atoms and molecules in various phases. In contrast, momentum spectroscopy focuses on measuring the momenta of particles resulting from photoionization or photo-fragmentation, providing complementary insights to traditional spectroscopic techniques. When full 2D or 3D momentum distributions of fragments are obtained, the method is often referred to as momentum imaging. These techniques primarily detect charged products which are ions and/or electrons, although methods for neutral particle detection also exist[111,112,113]. In their most complete form, momentum imaging setups can measure full 3D momentum vectors of multiple ions and electrons in coincidence, and are commonly referred as reaction microscopes (REMI)[17].

Fig. 3.12 shows a typical layout of COLTRIMS. A collimated supersonic jet of cold atoms or molecules intersects with a projectile beam — in this work, a laser pulse or a pair of pulses — in the center of an ultra-high vacuum chamber. In our experiments, we can reach base pressure as low as 10^{-10} to 10^{-11} torr. The intersection of the laser and molecular beams defines the interaction region. The chamber is equipped with an electrostatic spectrometer and a pair of time- and position-sensitive detectors for ions and electrons. A set of closely spaced spectrometer electrodes generates a uniform electric field that accelerates the resulting ions and electrons toward opposing detectors while simultaneously shielding them from external fields. In the work reported throughout this thesis, only the ion detector was used.

Each ion fragment's time-of-flight (TOF) and hitting position on the detector are recorded. The TOF is referenced to a trigger signal typically from a photodiode monitoring the laser

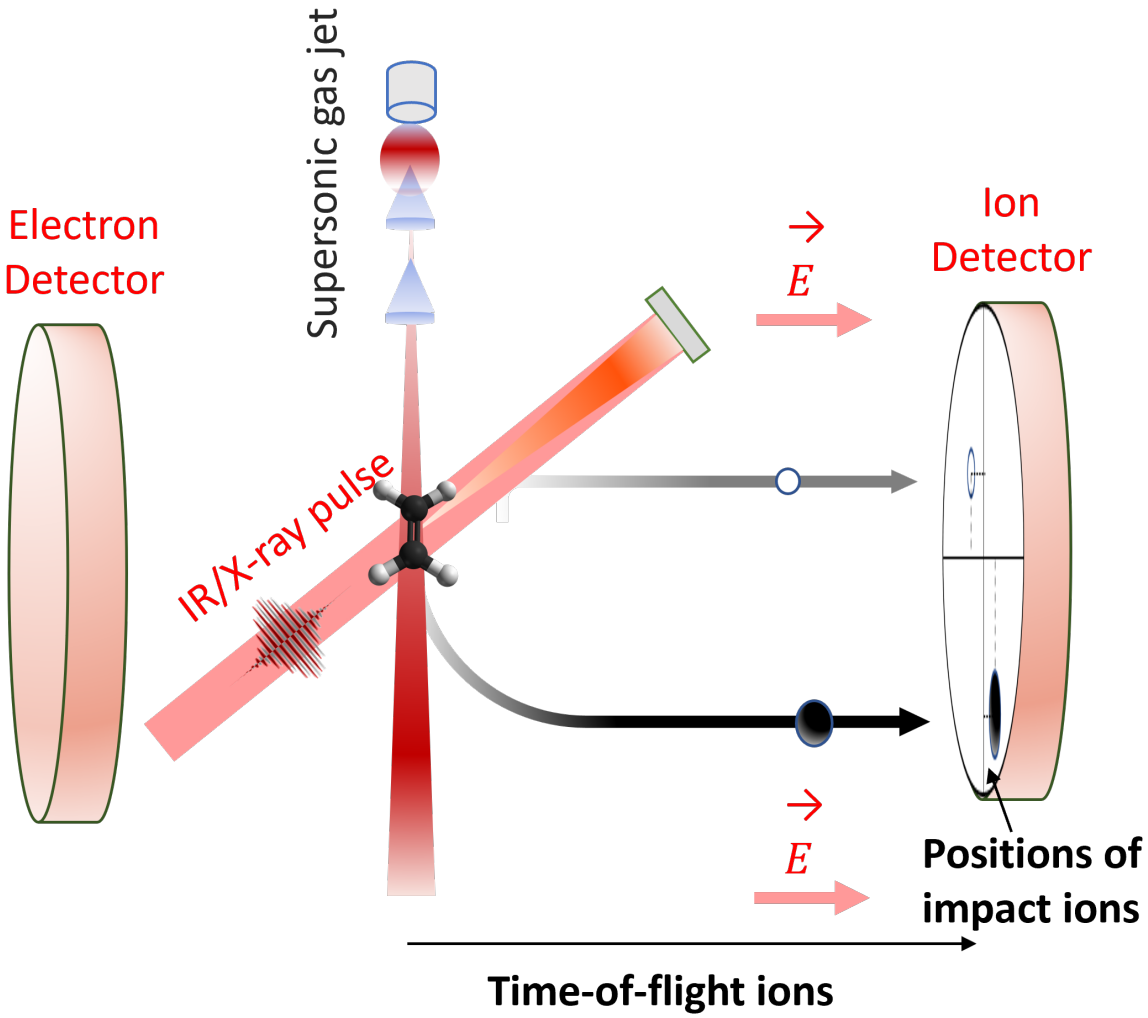

Figure 3.12: ***Scheme of a reaction microscope.***
The molecules are delivered into the interaction region in a supersonic gas jet. The intense IR/X-ray pulse hits one of the molecules, creating multiple ions and electrons. Those are guided towards two time- and position-sensitive detectors on opposite sides of a spectrometer by static electric and magnetic fields. In this way, 3D momenta of all recorded particles can be obtained, making it possible to reconstruct the molecular structure by momentum conservation.

pulse providing precise timing of the interaction. The TOF spectrum reveals both the mass-to-charge ratio of the ions (enabling species identification) and the component of their initial momentum along the spectrometer axis. The transverse momentum components are reconstructed from the detected hitting positions, allowing full three-dimensional momentum vector determination for each particle.

3.3.1 Supersonic gas jet

The supersonic gas jet system consists of a nozzle (with a diameter of 30 μm) for JRML experiments and 200 μm for the EuXFEL setup) followed downstream by skimmers, apertures, and slits, which form differential pumping stages that progressively reduce the gas load along the flow path. The target gas beam reaches the interaction chamber and is subsequently evacuated via a catcher compartment. The nozzle connects a high-pressure gas reservoir (ranging from a few to several tens of bars) to a low-pressure region, driving the gas to expand rapidly. This expansion exceeds the speed of sound, thus forming a supersonic jet. The flow can be approximated by an adiabatic expansion of an ideal gas.

Through this expansion, the gas enthalpy, which is the comprising compression and internal energy, is converted into the translational kinetic energy of the molecular beam:

$$k_B T_0 + \frac{f k_B T_0}{2} = \frac{1}{2} m V_{jet}^2 \tag{3.19}$$

where T_0 is the initial gas temperature before expansion, k_B is the Boltzmann constant, f is the number of degrees of freedom of injecting atom or molecule, and m is the mass of it. The heat capacity ratio can be written as:

$$\gamma = 1 + \frac{2}{f} \tag{3.20}$$

In the ideal case, the jet velocity can be estimated under the assumption that the gas

temperature T after expansion approaches zero. In practice, T remains finite, and the achievable jet temperature is characterized by the ratio $S = \frac{V_{jet}}{V_{thermal}}$. The speed ratio S depends on the nozzle diameter d, the initial gas temperature T_0, and the stagnation pressure P_0 prior to expansion. Given S and T_0, the jet temperature T can be estimated using:

$$T = \frac{\gamma}{\gamma - 1} \frac{T_0}{S^2} \tag{3.21}$$

As the pressure beyond the nozzle is not zero, the expansion becomes less ideal further downstream due to the interactions with residual background gas. However, the central core of the jet, located near the nozzle, remains largely unaffected and undergoes near-free expansion, resulting in lower temperatures. A skimmer positioned at an optimal distance downstream selects this cold central portion before the expansion degrades. Additional skimmers, apertures, and slits can be placed along the beam path to further collimate the jet and isolate its coldest part. In the interaction region, this setup yields a well-collimated gas jet with temperatures as low as tens of mK, a diameter of approximately $1mm$, and a target density on the order $10^8 - 10^{11}$ particles per cm^3, depending on the distance between the nozzle and the interaction region.

For the experiments conducted in this study, the nozzle was heated to increase the vapor pressure of the sample thiophenone. The vapor pressure of thiophenone exhibits a strong temperature dependence. Due to its inherently low volatility, thiophenone has a very low vapor pressure at room temperature, necessitating thermal heating of the nozzle to achieve sufficient molecular density for interaction.

3.3.2 Spectrometer and detectors

Spectrometer

A homogeneous electric field configuration is generated using a stack of equally spaced ring-shaped electrodes, connected via identical resistors. A voltage gradient is applied by setting

a high voltage at one end and a low voltage at the other, resulting in a uniform potential drop along the axis. This configuration produces a nearly homogeneous electric field within the interaction region, ideal for precise momentum reconstruction. In some spectrometers, this homogeneous region is followed by a field-free drift region. The combination of these two regions enables fulfillment of the time-focusing condition, where particles of the same species and identical initial velocity but originating from different positions along the spectrometer axis arrive at the detector simultaneously. This improves the temporal resolution of the time-of-flight (TOF) measurement and enhances mass resolution without compromising momentum reconstruction accuracy.

The spectrometer voltage and length can be tuned to ensure full 4π solid-angle acceptance and optimal resolution for detecting all reaction products. In general, increasing the extraction voltage or shortening the spectrometer length allows for the detection of faster fragments but at the cost of reduced momentum resolution due to increased field-induced broadening and shorter time-of-flight.

Ions are guided by the electric field toward the detector at one end of the spectrometer. Electrons can be directed to the opposite detector using the same electric field; however, due to their much smaller mass and consequently higher initial velocities, achieving full 4π collection efficiency using only the electric field is challenging. To overcome this, a homogeneous magnetic field, generated by a pair of Helmholtz coils and aligned parallel to the electric field, is introduced. This magnetic field forces electrons into helical trajectories along the spectrometer axis, enabling the collection of electrons with significant transverse velocities that would otherwise escape detection. The spiral radius is proportional to the electron's transverse velocity and inversely proportional to the magnetic field strength. Therefore, increasing the magnetic field enhances the acceptance of higher-energy electrons by confining their trajectories within the detector area.

There are non-homogeneous settings for the velocity map imaging (VMI) where the electric field acts as an electrostatic lens, focusing particles with identical initial velocities

but originating from different positions within the interaction region onto the same point on the detector. However, spectrometers are typically designed for either a homogeneous field or a VMI configuration, but both field geometries can be realized using a single spectrometer equipped with a sufficient number of appropriately positioned electrodes[114].

Detectors

In COLTRIMS experiments, charged particles are typically detected using a combination of microchannel plates (MCPs)[115] and a delay-line anode (DLA), which is also employed in this work.

As a single charged particle does not generate a measurable signal on its own, signal amplification is achieved using a triple-stack MCP assembly. Each MCP[116,117,118]is a porous glass plate, approximately 80 mm in diameter and 1–1.5 mm thick, containing thousands of microscopic channels, typically 4 to 12 μm in diameter for the front plate and up to 25 μm for the back plates. When a charged particle strikes the front MCP, it generates secondary electrons. These electrons are accelerated through the channels by an applied electric field, initiating an electron cascade that amplifies the signal. This impact–emission–acceleration process is repeated multiple times along the channel. To ensure efficient electron multiplication, the channels are tilted at a bias angle around 10° relative to the surface normal, preventing particles from passing through without interacting with the channel walls. The resulting electron avalanche produces a measurable pulse, which is used for time-of-flight (TOF) determination.

A DLA consists of two or three wires wound helically around an insulating support, with each wire oriented in a distinct winding direction. Each signal wire is paired with a parallel reference wire, and the differential signal between them is processed by a differential amplifier to suppress noise and enhance signal quality. A bias voltage (typically 20–50 V) is applied to the signal wires relative to the reference wires, ensuring preferential collection of the electron cloud from the MCP onto the signal wires. Once collected, the signal propagates along the

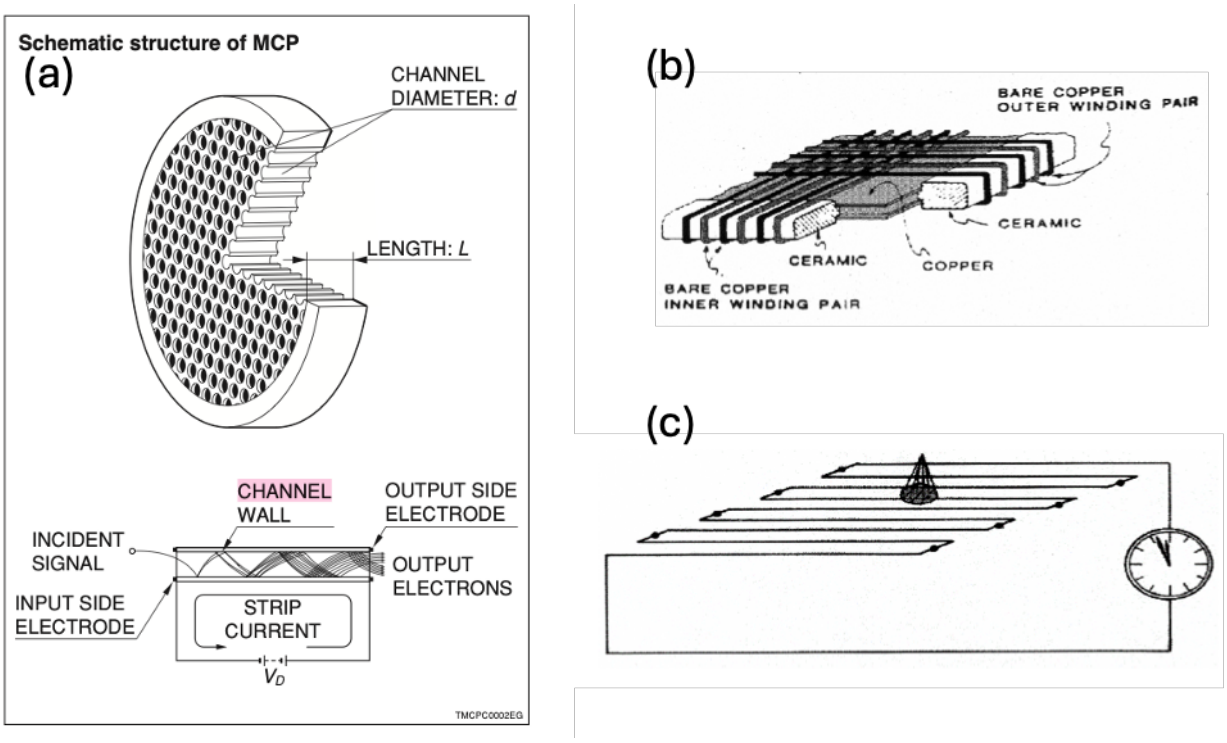

Figure 3.13: ***Scheme of MCP detector.***
(a) Schematic structure of a MCP[115] *(b) structure and (c) operation principle of Delay line anode*[119].

wire, and its arrival time t_1 and t_2 at both ends are recorded. The particle's position is then determined from the time difference $\Delta t = t_1 - t_2$, which encodes spatial information based on the signal propagation delay. The incident particle hit position P is given by[120]:

$$P = \frac{v_{group}}{2D_{1mm}}\Delta t + O \tag{3.22}$$

The v_{group} is the signal group velocity, which is close to the speed of light. The distance D_{1mm} corresponds to the signal propagation length along the wire required to resolve a 1mm displacement in the helical winding direction, and the O is an arbitrary offset factor.

In this study, we employed a QUAD delay line anode (QUAD-DLA) which is a type of position-sensitive detector readout system that enhances spatial resolution and count rate capability by using four helical delay line wires instead of the conventional two or three. We can obtain the incident particle position (X_{pos},Y_{pos})

$$\begin{aligned} X_{pos} &= \frac{v^x_{group}}{2D_{1mm}}\Delta t_x + O_x \\ Y_{pos} &= \frac{v^y_{group}}{2D_{1mm}}\Delta t_y + O_y \end{aligned} \tag{3.23}$$

where the v^i_{group}, D^i_{1mm},Δt_i and O_i $(i = x, y)$ are the same as eq. 3.22 for specified propagating direction. A hexagonal delay-line anode (HEX-DLA) is another type of readout structure frequently used in COLTRIMS setups, offering improved spatial resolution and symmetry through its threefold, 120° offset wire configuration.

3.4 Data acquisition and processing for photoion measurements

The data collected in this study were recorded using the NSCL SpecTcl DAQ system[121]. The reconstruction of ion momenta resulting from the interaction constitutes an initial value

problem, where the goal is to determine the initial velocities of the fragments generated in the interaction with the laser based on their subsequent trajectories in known electromagnetic fields.

The ion time-of-flight (TOF) values and corresponding hit positions recorded for each laser shot are used to reconstruct the full 3D momentum vectors of the detected ions. All secondary observables, such as kinetic energy release (KER) and absolute and relative emission angles, are derived from these momentum vectors[121].

In the JRML PULSAR COLTRIMS setup, the laser propagates along the x-axis, the supersonic gas jet along the y-axis, and the spectrometer axis, with homogeneous electric fields, is aligned along the z-axis. The interaction point, where the laser intersects the target beam, defines the origin of the z-axis (z_0). The detector center defines the transverse coordinate origin (x_0, y_0). The ion detector is aligned parallel to the (x, y)-plane, perpendicular to the spectrometer axis, making the transverse ion motion effectively field-free. In contrast, ion motion along the z-axis is governed by constant acceleration. In these measurements, laser polarization was kept parallel to the spectrometer (i.e., z) axis. At the European XFEL, the spectrometer axis is vertical and the X-ray beam polarization is horizontal, such that it is perpendicular to the TOF axis and parallel to the molecular beam propagation direction.

According to Newton's second law, the momentum components of an ion with mass m and charge q, flying a distance of l_i from the interaction region to the detector, are given by:

$$\begin{aligned} p_x &= m \cdot \frac{x - x_0}{\Delta t} \\ p_y &= m \cdot \frac{y - y_0}{\Delta t} \\ p_z &= m \cdot \frac{l_i}{\Delta t} - \frac{qE\Delta t}{2} \end{aligned} \tag{3.24}$$

where $\Delta t = t_1 - t_0$, t_1 is the time-of-flight (TOF), and t_0 is the interaction time offset that accounts for the delay between the actual laser–molecule interaction and the arrival of the photodiode signal at the DAQ system, which is used to trigger data acquisition. This

offset includes both the intrinsic timing difference and additional delays introduced by the electronic components in the signal path. E is the strength of the homogeneous electric field, and (x, y) are the detected incident positions on the ion detector as X_{pos} and Y_{pos}.

Having reconstructed the momentum vectors of the ion species generated in the laser and molecule interaction, we proceed to calculate their kinetic energy distributions, total kinetic energy release (KER), and emission directions. In coincidence analysis, the individual momentum vectors are further constrained by the condition of momentum conservation, enabling identification of correlated fragmentation channels.

Charged particles travel to the detector according to Newton's Second Law. Based on the spectrometer configuration, their initial momenta resulting from the interaction can be reconstructed using the measured time-of-flight t and hit positions (x, y) which is shown in Fig. 3.14. The specific method for momentum reconstruction depends on the field geometry of the spectrometer and whether the particle is an ion or an electron. Once the momentum components (P_x, P_y, P_z) are determined for a particle of mass m, the kinetic energy E is calculated as:

To identify two-body fragmentation channels, we use the standard photoion-photoion coincidence (PIPICO) map, as shown in Fig. 3.15. For analyzing three-body fragmentation channels in the measured coincidence data, we utilize an advanced version of the PIPICO method, where the time-of-flight (TOF) of the first detected ion (TOF1) is plotted along the horizontal axis, and the sum of the TOFs of the second and third ions (TOF2 + TOF3), commonly referred to as Tri-PICO, is plotted along the vertical axis, as shown in Fig. 3.16. The position information from the detector can be transformed into the momentum distribution of the detected ions.

$$E = \frac{P_x^2 + P_y^2 + P_z^2}{2m} \tag{3.25}$$

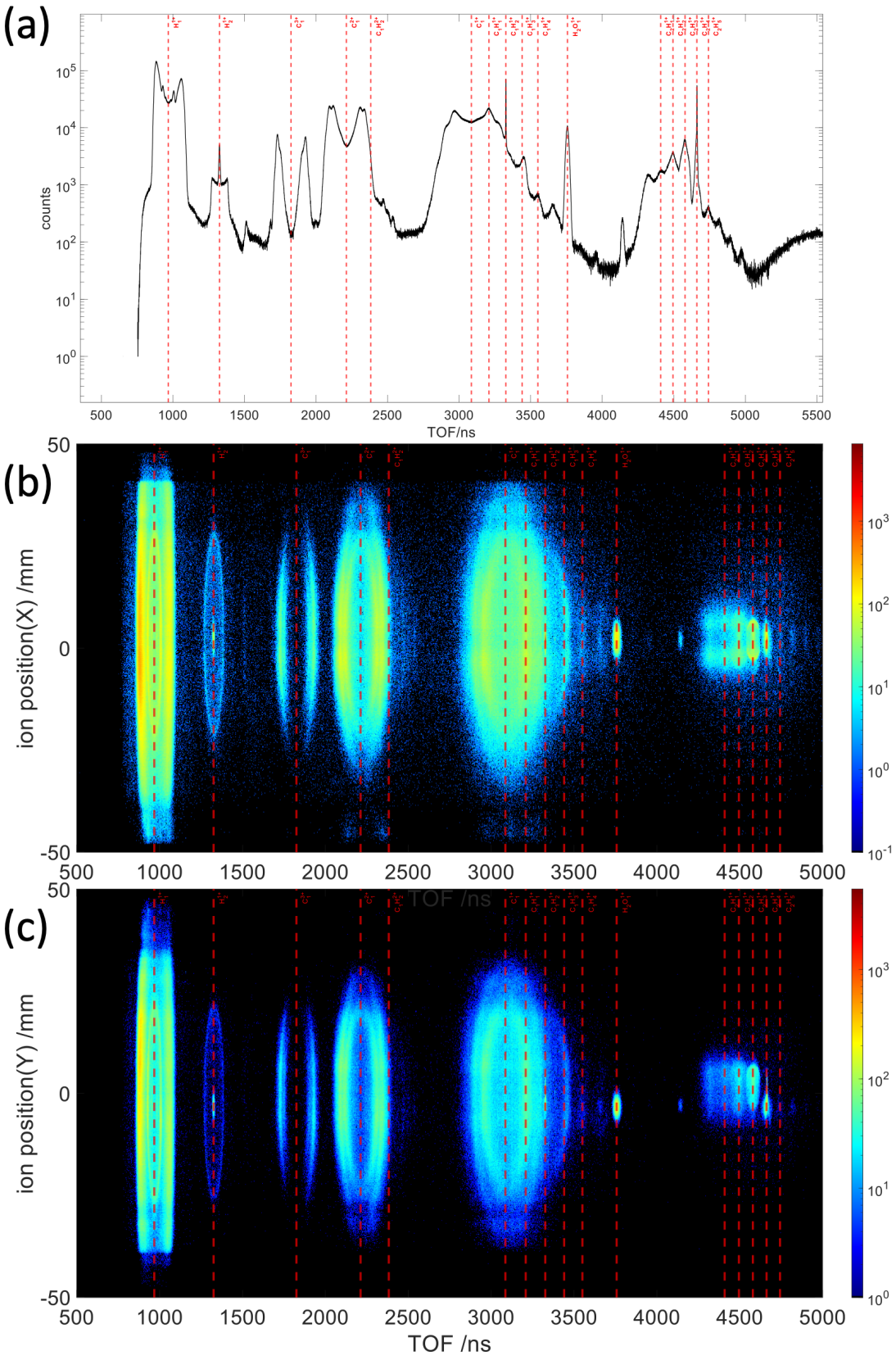

Figure 3.14: ***Measured TOF spectra of ethylene.***

Experimental data of (a) time-of-flight (TOF) spectrum , (b) TOF vs. detector X_{pos}, and (c) TOF vs. detector Y_{pos} of ethylene.

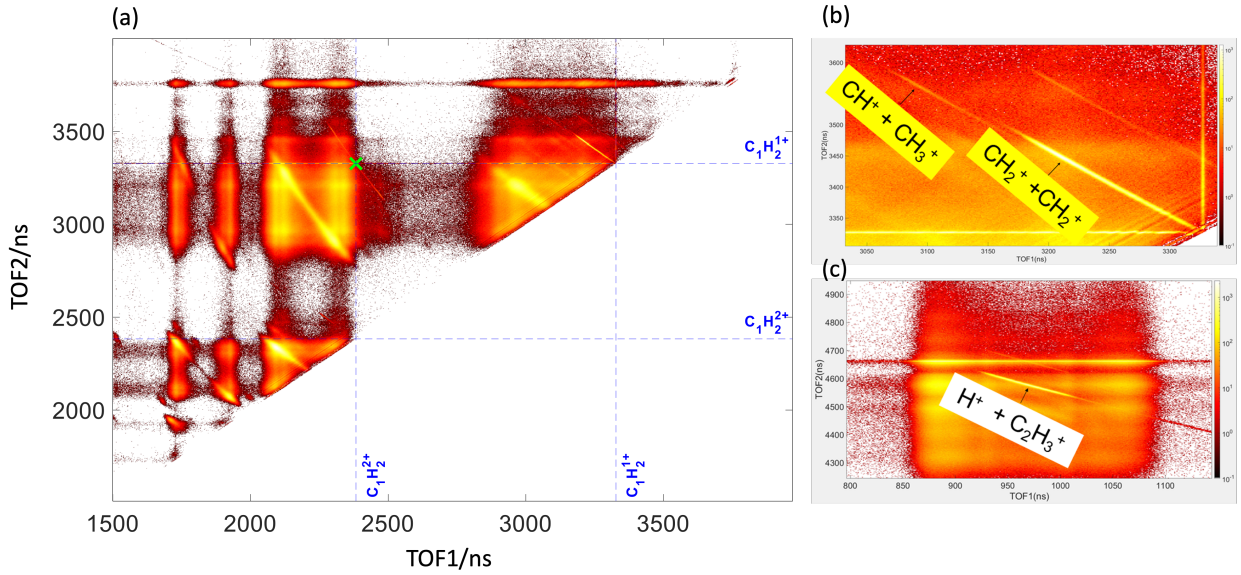

Figure 3.15: ***Photoion-photoion coincidence (PIPICO) maps of different channels of ethylene.***
Plotted experimental data of ethylene, zoomed in on specific two-body fragmentation channels: (a) $CH_2^{2+} + CH_2^+$*, (b)* $CH_2^+ + CH_2^+$*, and (c)* $C_2H_3^+ + H^+$*.*

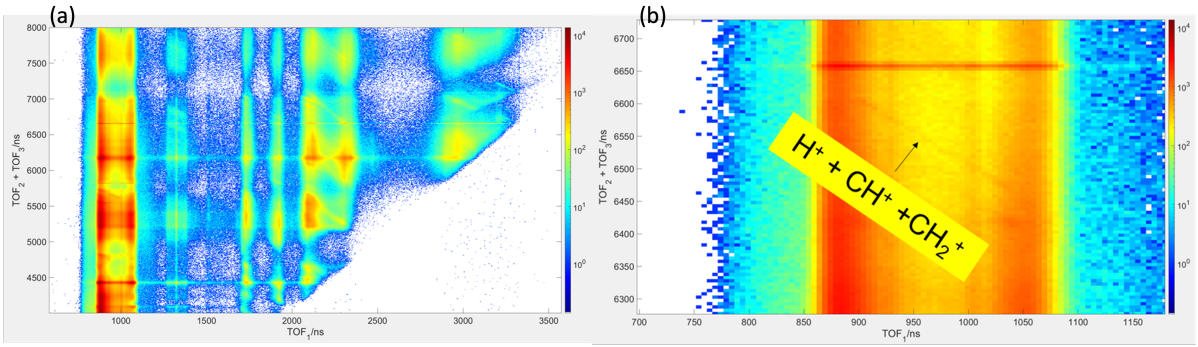

Figure 3.16: ***Full Photoion-photoion-photoion coincidence (Tri-PICO) maps of ethylene.***
(a) Tri-PICO map of experimental data of ethylene, and (b) zoomed in on specific three-body fragmentation channel: $H^+ + CH^+ + CH_2^+$*.*

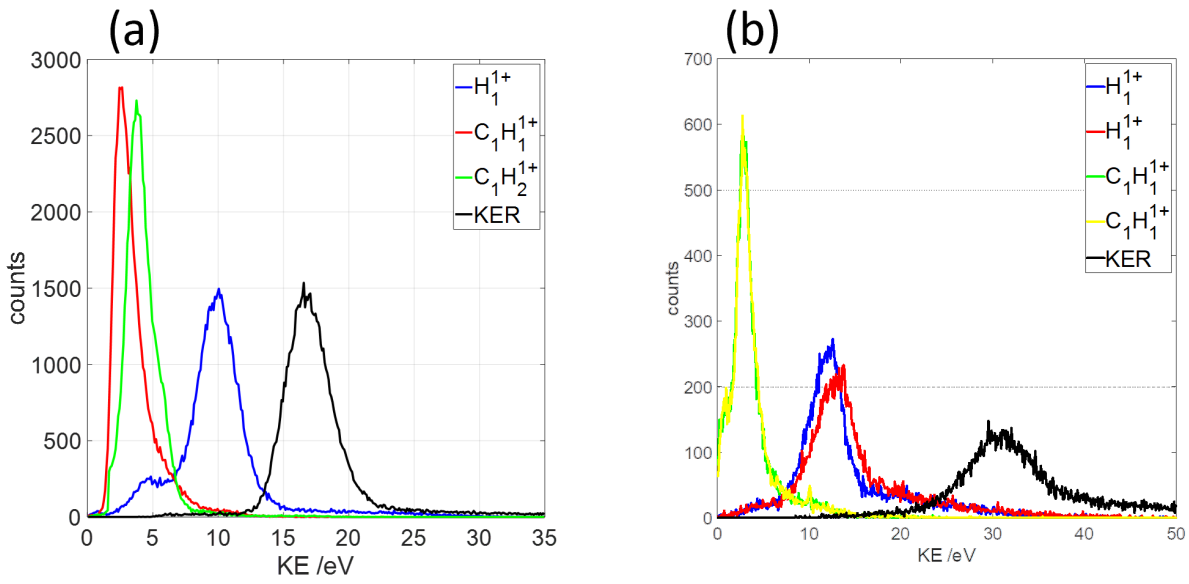

Figure 3.17: ***Kinetic energy release (KER) of (a) three- and (b) four-body fragmentation of ethylene from experiment.***
Experimental data of (a) three- and (b) four-body breakup of ethylene. The details of separating the fragmentation pathways are introduced in Chapter 4. The superscript on each ion fragment label indicates the charge state, while the subscript denotes the number of atoms in that fragment.

3.4.1 Coulomb explosion imaging: data representations

Using the measured information of the detected ions, the three-dimensional momentum components (P_x, P_y, P_z) can be reconstructed, providing the same type of data obtained from the simulations. Consequently, the experimental results can be presented in the same formats discussed in Section 2.3.2, allowing for direct and meaningful comparison.

Kinetic energy release

By using eq. 3.25 for kinetic energy calculation, we can obtain both the kinetic energies of individual ions as well as total kinetic energy release (KER) for a specific channel. For example, Fig. 3.17 illustrates these KE / KER spectra for three-body (a) and four-body (b) fragmentation of ethylene (C_2H_4) molecule into singly charged fragments, all of which have been detected. Further discussion of these data can be found in Chapter 4.

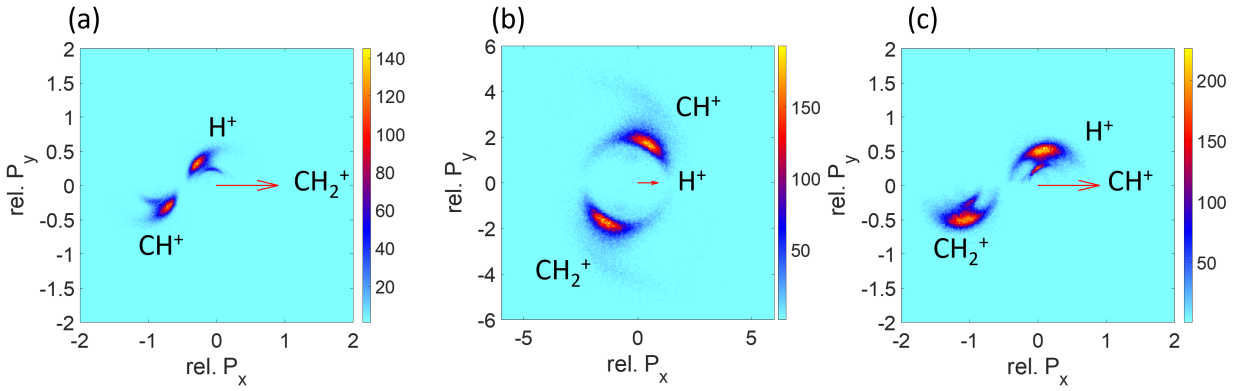

Figure 3.18: ***Exemplary Newton diagrams of the three-body fragmentation of ethylene from experimental data.***
(a)–(c) Relative Newton diagrams of the $H^+ + CH^+ + CH_2^+$ *fragmentation channel measured in coincidence.*
(a) The momentum of CH_2^+ *is normalized to 1 and oriented along the* P_x *axis (orange arrow); the relative momenta of* H^+ *and* CH^+ *fragment ions are plotted in the upper and lower halves, respectively.*
(b) The momentum of H^+ *is normalized to 1 along the* P_x *axis; the relative momenta of* CH^+ *and* CH_2^+ *are plotted in the upper and lower halves.*
(c) The momentum of CH^+ *is normalized to 1 along the* P_x *axis; the relative momenta of* H^+ *and* CH_2^+ *are plotted in the upper and lower halves. The details of these Newton diagrams are introduced in the Chapter 4.*

Newton diagrams and momentum distribution in 3D

As described in Section 2.3.2, we analyze the four-body complete fragmentation channel where H^+, H^+, CH^+, and CH^+ ions are detected in each event. The momentum distribution of the first detected CH^+ ion is used to define the x-axis of the molecular frame, and along the momentum of the second detected H^+ ion together is used to define the molecular plane. This coordinate system allows for direct comparison with the Newton diagrams from the Coulomb explosion simulations shown in Fig. 2.7(b) and (c).

As a further example, for the experimental data, we can also visualize the raw momentum distribution of the four-body complete fragmentation channel of ethylene, in which H^+, H^+, CH^+, and CH^+ ions are detected. The resulting raw data (without representation using Newton diagrams in the molecular frame) in 3D are shown in Fig. 3.19. However, in contrast to the raw Coulomb explosion simulation results where the fragment momenta closely mimic

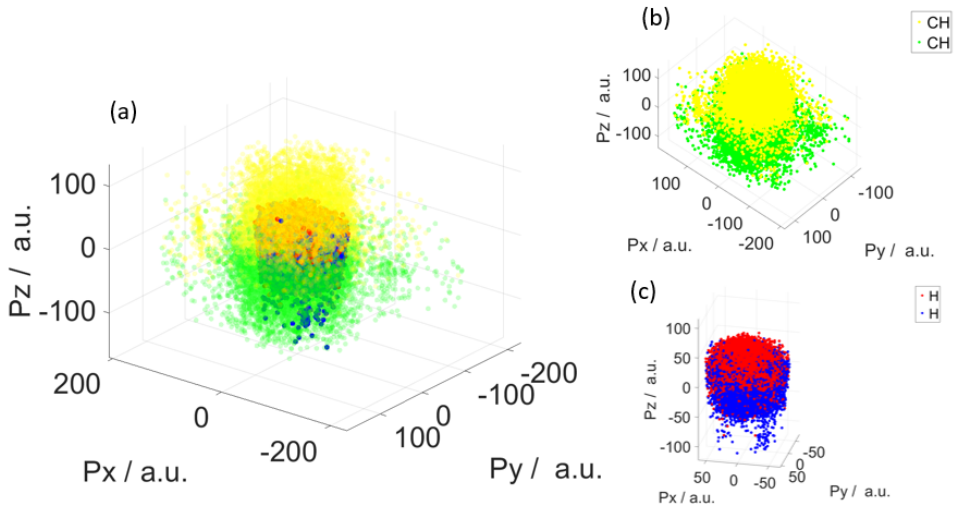

Figure 3.19: ***Raw 3D momentum distribution of the four-body complete fragmentation data of ethylene with H^+, H^+, CH^+, and CH^+ detected.***
(a) all four ion fragments are shown; (b) only CH^+, CH^+ momentum distributions are shown; (c) only H^+, H^+ momentum distributions are shown. Here, 'raw' refers to data that are not represented using Newton diagrams in the molecular frame.

the molecular geometry, as illustrated in Fig. 2.8, the experimental momentum distributions are recorded in the laboratory frame. In this frame, the ion trajectories are largely defined by the lab-frame spatial orientation of the molecule and by the laser polarization direction, oriented along the P_z axis (the TOF axis). As a result, the raw momentum distributions do not reflect the internal molecular structure. To interpret the fragmentation dynamics in the context of the molecular frame, we must transform the data into the molecular frame (normally, we use the momentum distribution of two ion fragments defining the molecular plane), which allow for a more accurate representation of the breakup geometry and enable direct comparison with simulations.

Similar to what is discussed in Section 2.3.2 for the CES output, the raw experimental momentum distributions can be visualized in several different ways, including generalized 3D Newton diagrams and spherical coordinate representation in terms of polar and azimuthal angles with respect to the molecular plane determined from the data. Further discussion of

these possible data representations for ethylene is presented in Chapter 4.

Chapter 4

Coulomb explosion imaging of ethylene with intense laser pulses

All experiments, data analysis and Coulomb explosion simulations presented in this chapter were conducted by the author. Theoretical modeling of the potential energy surfaces for triply and quadruply charged ethylene, which are shown in the Appendix A and are used here for scaling of the results of Coulomb explosion simulations, was carried out by Prof. Loren Greenman and Dr. Paresh Modak (Kansas State University).

As discussed in Chapters 1 and 2, laser-induced Coulomb explosion imaging (CEI) represents a promising approach for probing ultrafast molecular dynamics. It is equally sensitive to light and heavy atoms, can be efficiently used to disentangle competing reaction pathways or characterize minor reaction channels, and, if used as a probe in a pump–probe experiment, can achieve sub-10 fs temporal resolution. However, a successful application of this technique to polyatomic systems relevant to chemistry requires a detailed understanding of the fragmentation processes involved in the formation of Coulomb explosion patterns and the final-state observables. Some of the known issues here are the dynamics that the molecule undergoes during the ionizing pulse and the presence of sequential fragmentation

channels, resulting in a fragmentation pattern reflecting the post-pulse rotational dynamics rather than the initial geometry of the molecule[18,19]. Moreover, CEI can be used to exploit different breakup channels, a variety of final charge-state combinations, and the coincident detection of several ionic fragments. Therefore, data representation and the optimal choice of specific observables needed to characterize the dynamics of interest become an important and complicated issue. Although most of the earlier CEI studies relied on non-coincident ion measurements or involved the coincident detection of all produced ions, recently, a new CEI mode, which exploits the coincident detection of three or four created ions has been shown to be very effective[122,54,52,123,53]. However, no direct comparative analysis of such an 'incomplete' CEI mode and a more conventional 'complete' scheme, where all created ions are detected, has been reported so far. In this chapter, some of these issues are addressed using the example of multiple ionization and Coulomb explosion of an ethylene molecule by intense, femtosecond near-infrared laser pulses,

Ethylene (C_2H_4), a fundamental unsaturated hydrocarbon, plays a significant role in photochemistry and photosynthesis[124], and its fragmentation by various light sources or by charged particle impact has been extensively studied both experimentally and theoretically[125,126,127,128,129,130,131,132,133]. For example, Xie et al.[125] utilized intense femtosecond laser pulses to explore and control the fragmentation behavior of ethylene molecules. Gaire et al.[130] conducted kinetically complete measurements of direct photo-double ionization of ethylene near threshold using synchrotron radiation and revealing dissociation pathways involving both the electronic ground and excited states of the ethylene dication. They further applied coincident measurements of Auger electrons and fragment ions to study the fragmentation dynamics in more detail[131]. Wang et al.[127] investigated the fragmentation processes of ${C_2H_4}^{2+}$ under 300 eV electron impact, analyzing both two-body and three-body dissociation channels. Ethylene has also been chosen as a prototypical molecule for time-resolved photochemistry studies involving carbon–carbon double bonds[132,130]. Van Tilborg et al.[132] investigated EUV-pump-induced dynamics in the excited ethylene cation (${C_2H_4}^{2+}$),

leading to the observation of a transient ethylidene configuration ($HC{-}CH_3{}^+$). Ethylene represents an attractive model system for CEI of polyatomic molecules because of its relative simplicity, accessibility for theory, and its planar geometry in the ground state of the neutral molecule. At the same time, it has enough complexity to study different multi-particle breakup channels, in particular, those involving one or more of the four hydrogen atoms, whose detection is one of the important capabilities of the CEI technique. Earlier ionization studies of ethylene have primarily focused on low charge states of the molecule and considered two-body or three-body fragmentation pathways. In this work, we present a systematic analysis of three- and four-body molecular breakup, focusing on the 'complete' channels, where we detect all ionic fragments created, and complement it with the analysis of several 'incomplete' channels, where we detect three, four, or five ions from the C_2H_4 molecule that is 'fully atomized', i.e., breaks up into six atomic ions.

The experiments discussed in this chapter have been carried out at several different peak intensities of the laser, ranging from 1.1×10^{15} W/cm^2 to 2.5×10^{15} W/cm^2. While the measured ion charge state distributions and the branching ratios of different breakup channels exhibit a pronounced dependence on the peak intensity value, no significant difference has been observed in the correlated few-particle momentum distributions or in the kinetic energy spectra for specific fragmentation channels as a function of intensities. Therefore, all experimental results presented in this chapter are shown for the same peak laser intensity, 1.3×10^{15} W/cm^2, chosen to achieve the optimal experimental count rate and signal-to-noise ratio for the channels of interest.

4.1 Three-body fragmentation in $C_2H_4{}^{3+}$

We first consider the three-body breakup of the ethylene molecule ionized to the triply charged state. Since, for this channel, we detect all three resulting ions (H^+, CH^+, and $CH_2{}^+$), we will refer to it as a "complete" three-body channel. Fig. 4.1 illustrates the

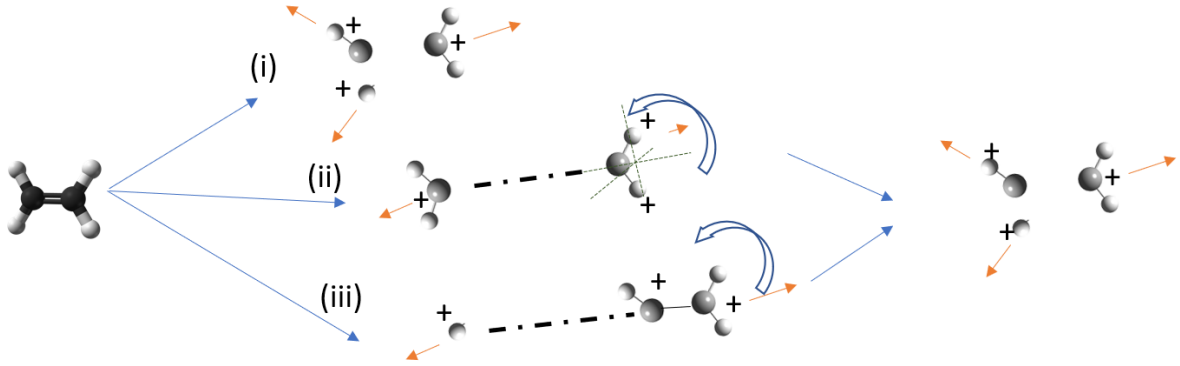

Figure 4.1: ***Illustration of possible fragmentation scenarios for the three-body fragmentation channel of triply-charged ethylene.***
$C_2H_4 \rightarrow H^+ + CH^+ + CH_2^+$ via
(i) Concerted breakup: $C_2H_4 \rightarrow H^+ + CH^+ + CH_2^+$
(ii) Sequential breakup: $C_2H_4 \rightarrow H^+ + C_2H_3^{2+} \rightarrow H^+ + CH^+ + CH_2^+$
(iii) Sequential breakup: $C_2H_4 \rightarrow CH_2^+ + CH_2^{2+} \rightarrow H^+ + CH^+ + CH_2^+$

possible fragmentation pathways leading to this final state. In addition to the concerted fragmentation pathway, which is the one that would enable CEI of the initial molecular geometry, there are two possible sequential pathways involving the production of intermediate metastable dications.

As discussed in Sections 2.3.2 , 2.3.4, and 3.4, to characterize few-body molecular fragmentation, we employ measured or simulated correlated momentum patterns (Newton diagrams) as well as kinetic energy distributions (KEDs) of individual ionic fragments and the total kinetic energy release (KER). Fig. 4.2 shows the experimental Newton diagrams for the $H^+ + CH^+ + CH_2^+$ channel, using CH_2^+ (a) or H^+ (b) momenta to define the positive x direction (plotted as the unit vector pointing to the $+x$). Both distributions exhibit a very complex structure, suggesting the coexistence of several interwoven reaction pathways. The crosses in both panels mark the most intense part of the distributions, while the dashed and dotted lines indicate semicircular structures, characteristic of sequential fragmentation channels[18,19]. The measured KEDs of the individual ions and the total KER spectrum for this channel are shown in Fig. 4.3(a). While the KEDs for both heavier fragments exhibit rather smooth, slightly asymmetric spectra, the proton KED shows a distinct two-peak

structure, with the main peak centered around 10 eV, and a weaker shoulder slightly below 5 eV.

Fig. 4.3(b) depicts simulated KEDs and KER spectra for the same fragmentation channel. The basic assumptions behind the Coulomb explosion simulations (CES) are described in detail in Section 2.3.3. Here, the simulation was performed assuming the concerted breakup of the molecule, with the initial conditions sampled by the Wigner distribution of the ground-state ethylene molecules at 60 K (This is assumed to be the nominal vibrational temperature of molecular beam[58] and the simulation performed for ethylene at 300 K also shows only a slightly increased of out-of-plane width in the distribution of geometries) optimized at the B3LYP/aug-cc-pVDZ level of theory using geometries generated using Newton X[57] software. Charges were assumed to be localized at the center of mass of each fragment, and the inter-fragment Coulombic repulsion was calculated accordingly. While the relation between the simulated KEDs of the individual fragments coarsely resemble the experimental data (in particular, the CH_2^+ KEDs are slightly higher than those for CH^+), neither the asymmetry for heavier fragments nor the two-fold structure of the proton KED is reproduced. Furthermore, compared to the experimental data, all calculated distributions are shifted to higher energy values. This discrepancy is well-known, with the main reasons being the stretching of molecular bonds during the ionizing pulse and the non-Coulombic nature of the final-state potential energy surfaces (PESs). Later in this chapter, we will use the calculated PESs for triply-charged ethylene to bring the results of the CES closer to the experimental values.

Since the Newton diagrams in Fig. 4.2 indicate the presence of several competing pathways, potentially involving some sequential fragmentation channels, we employ recently developed Native frame analysis framework[18,19] to separate the concerted and sequential breakup channels. As discussed in more detail in Section 2.3.4, within this framework, sequential fragmentation is identified as a uniform angular distribution due to the rotation of the intermediate molecular ion in the fragmentation plane. Following the procedure out-

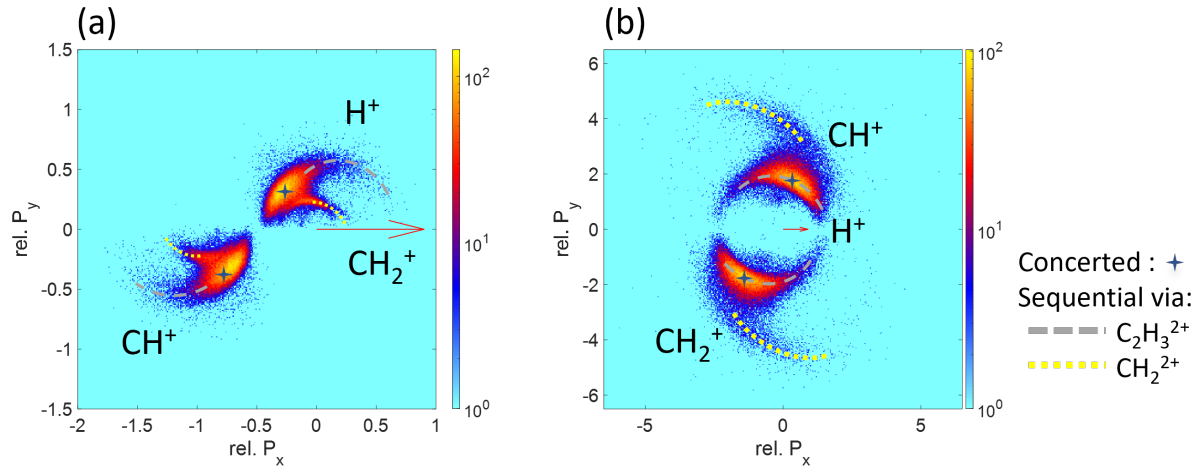

Figure 4.2: ***Experimental Newton diagrams for ethylene three-body breakup into H^+ + CH^+ + $CH_2{}^+$ fragments.***
In (a), the momentum of $CH_2{}^+$ is normalized to 1 pointing to the P_x axis (orange arrow) and relative momenta of H^+ and CH^+ fragment ions are plotted in the upper and lower half, respectively. In (b), the momentum of H^+ is normalized to 1 pointing to the P_x axis (orange arrow), and the relative momenta of CH^+ and $CH_2{}^+$ fragment ions are plotted in the upper and lower half, respectively. Crosses, dashed and dotted lines in both panels mark three distinct structures discussed in text and their tentative assignments.

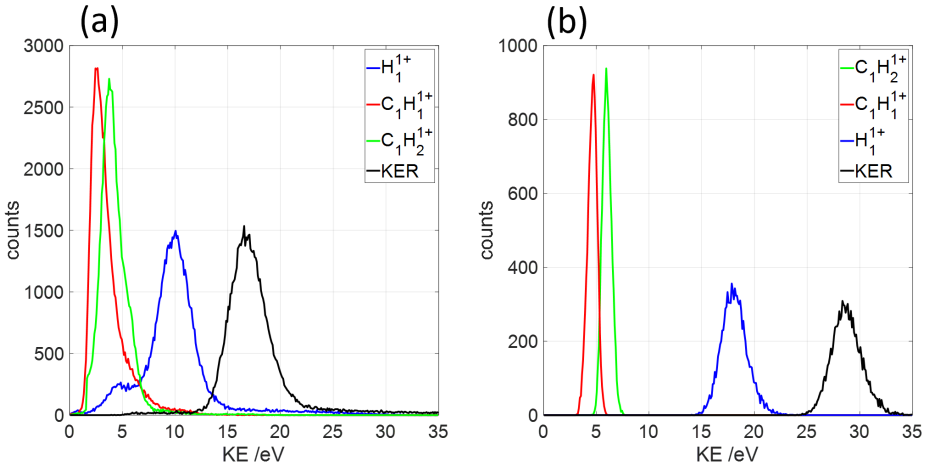

Figure 4.3: ***Measured and simulated kinetic energy distributions of three-body fragmentation of ethylene.***
(a) The measured KE distributions of the H^+ (blue), CH^+ (red) and $CH_2{}^+$ (green) ions and the total KER of the H^+ + CH^+ + $CH_2{}^+$ channel (black). (b) Same as (a) but simulated assuming the concerted breakup.

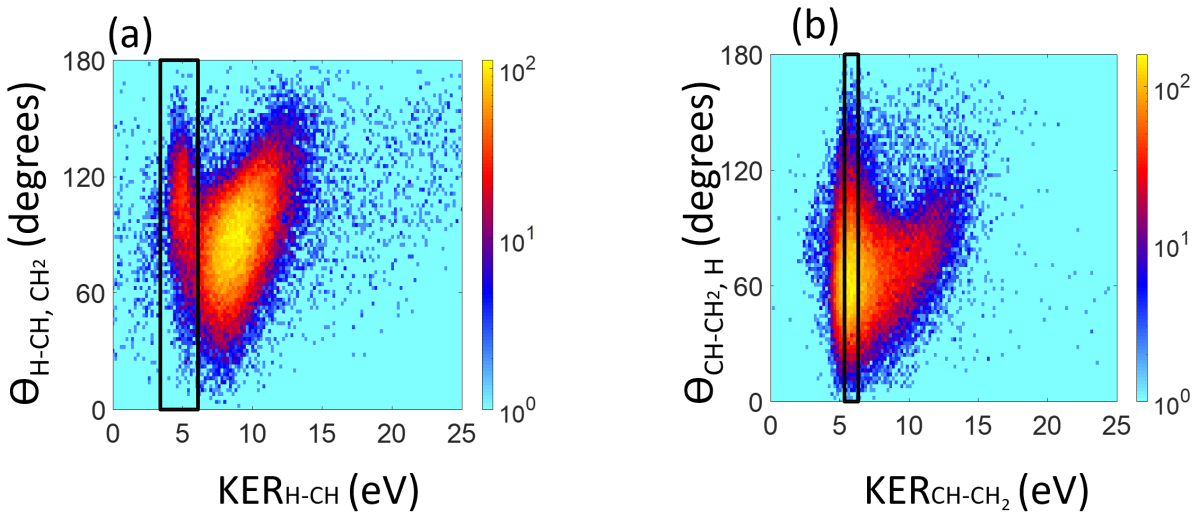

Figure 4.4: ***Native frame analysis of three-body fragmentation of ethylene from experimental data.***
(a) The yield of the H^+ + CH^+ + ${CH_2}^+$ fragmentation channel plotted assuming sequential breakup via CH_2^+ + ${CH_2}^{2+}$ intermediate: $N(KER_{\mathrm{H-CH}},\ \Theta_{\mathrm{H-CH},\ \mathrm{CH_2}})$. (b) The same yield plotted assuming sequential breakup via H^+ + ${C_2H_3}^{2+}$ intermediate: $N(KER_{\mathrm{CH-CH_2}},\ \Theta_{\mathrm{CH-CH_2},\ \mathrm{H}})$. Black rectangles in each panel mark the areas potentially associated with the corresponding sequential fragmentation channel.

lined in Ref.[19], in Fig. 4.4, we plot the angle between the relative momenta of the first and the second breakup step as a function of the second-step KER, calculated assuming two different sequential breakup pathways sketched in Fig. 4.1. Although no regions with truly uniform angular distributions can be observed, each panel contains a vertical feature that can potentially be associated with sequential fragmentation (marked by black rectangles). To identify and separate the contributions from the concerted and sequential breakup channels, we apply the Native frame analysis to the simulated CE data reflecting the three scenarios sketched in Fig. 4.1.

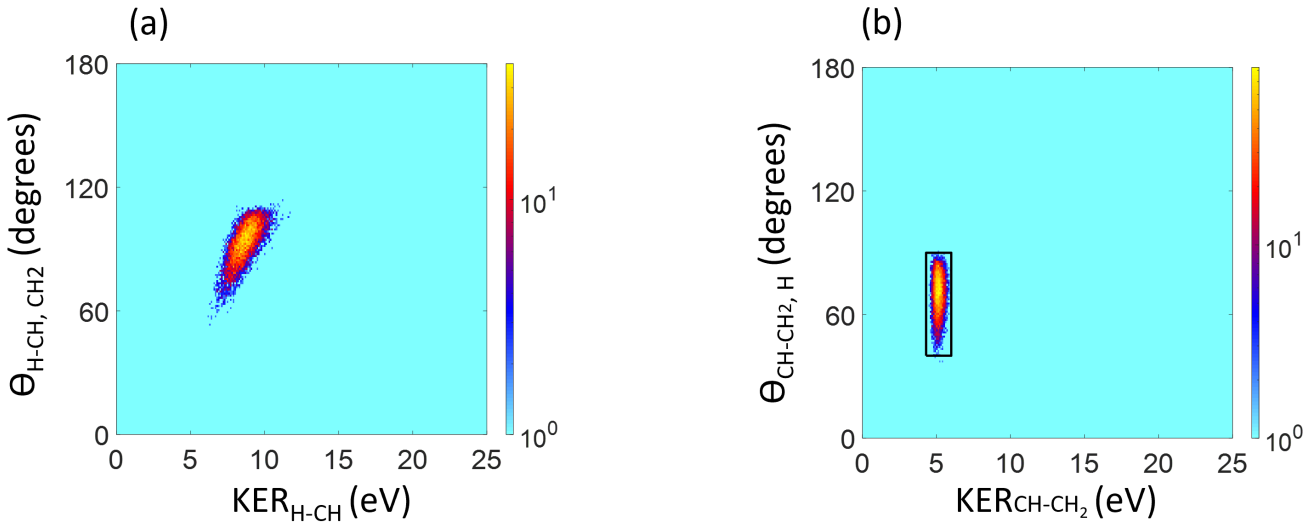

Figure 4.5: ***Native frame analysis from the simulated three-body concerted breakup of ethylene.***
The outcome of the CES is plotted in two different ways to match the data shown in Fig. 4.4. (a) $N(KER_{\mathrm{H-CH}},\ \Theta_{\mathrm{H-CH}},\ _{\mathrm{CH_2}})$. *(b)* $N(KER_{\mathrm{CH-CH_2}},\ \Theta_{\mathrm{CH-CH_2}},\ _{\mathrm{H}})$. *Black box marks the gate used for separating the experimental data for concerted breakup channel.*

4.1.1 Three-body concerted breakup

The concerted pathway of the complete fragmentation channel $H^+ + CH^+ + CH_2^+$ in the measured three-body coincidence data is expected to lie within a localized area of the Newton diagram and in the specific range of the relative angles $\Theta_{\mathrm{H-CH,CH_2}}$ and $\Theta_{\mathrm{CH-CH_2,H}}$. To identify this angular range, we simulate the corresponding observables within the concerted breakup scenario. Since this CES 'as is' significantly overestimates the experimental KE values (see Fig. 4.3), we use the theoretically modeled (non-Coulombic) final-state PES to achieve a better match with the experiment. The calculated PESs of the triply charged ethylene molecule were provided by P. Modak and L. Greenman (see Appendix A for details). While the full simulation of the molecular dynamics on the triply-charged PES is beyond the scope of this work, we use the PES to scale the outcome of the CES. Specifically, we define the scaling factor by comparing the total KER resulting from the CES and the Franck-Condon energy of the triply-charged molecule in its ground state, and use it to derive the appropriate

scaling factors for all velocities, momenta and energies involved in the simulation. While the KER simulated in this manner (14.8 eV) is slightly lower than the peak of the experimental KER distribution (16.5 eV), the simulated Newton maps and Native frame observables provide much better guidance than the unscaled CES, which centers at the KER value of 28 eV (see Fig. 4.3(b)).

The native frame observables for the concerted breakup are plotted in Fig. 4.5. As expected, the results are well localized in both (a) $N(\mathrm{KER}_{\mathrm{H-CH}},\ \Theta_{\mathrm{H-CH},\ \mathrm{CH_2}})$ and (b) $N(\mathrm{KER}_{\mathrm{CH-CH_2}},\ \Theta_{\mathrm{CH-CH_2,H}})$ representations. For the latter, the angle $\Theta_{\mathrm{CH-CH_2,H}}$ is found to lie between 40° and 90°, and the corresponding KER of the $CH^+ + CH_2^+$ pair ranges from 4.3 to 6.0 eV. By applying gates on these angular ranges and KER window (marked by a black rectangle) to the experimental data of Fig. 4.4(b), we isolate the concerted breakup events from the full dataset. In Fig. 4.6, we plot the experimental Newton diagrams (a,b) and KEDs (c) for those selected events, and compare them with the simulated results (d-f). For the Newton diagrams, the simulation matches the selected data pretty well and coincides with the most intense region of the full dataset, marked by the crosses in Fig. 4.2, thus confirming that concerted fragmentation plays an important role for the selected three-body breakup channel. Compared with the CES results (Fig. 4.6(d,e)), the relative momentum distributions in the Newton plots of the experimental data (Fig. 4.6(a,b)) appear slightly broader. This broadening can be caused by the imperfect selection of the $N(\mathrm{KER}_{\mathrm{CH-CH_2}},\ \Theta_{\mathrm{CH-CH_2,H}})$ range in the experimental gating, insufficiency of the thermal spread introduced by the 60 K Wigner distribution used to generate the ground-state ethylene geometries[134] or, more likely, by the uncertainty caused by the dynamics during the triple ionization process.

The KE / KER distributions in panels (c) and (f) closely resemble each other, with the experimental spectra not showing the asymmetries or two-peak structure visible in the full dataset (see Fig. 4.3(a)). As discussed above, the experimental KER peaks at slightly higher value (16.5 eV) than the theoretically calculated KER (used to scale the CES results).

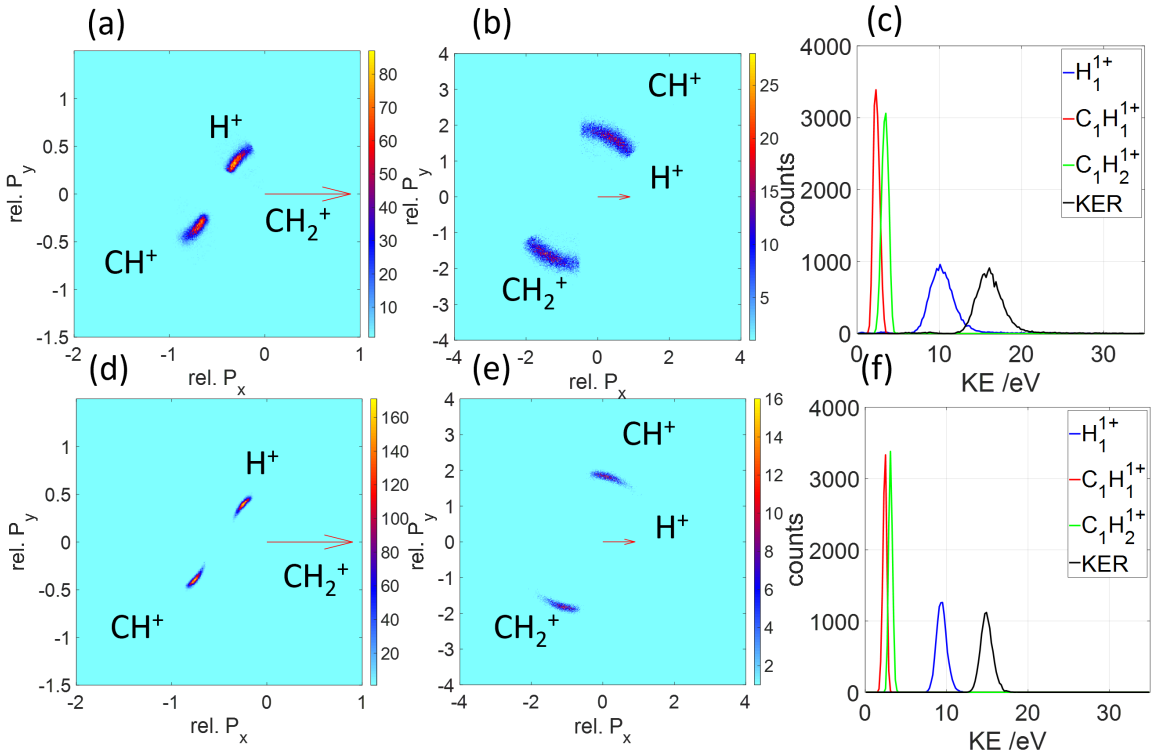

Figure 4.6: ***Concerted three-body breakup events selected from the experimental data of ethylene compared with CES predictions.***
(a-c) Separated concerted breakup events from experimental data. (d-f) CES of concerted breakup channel. (a,b,d,e): normalized Newton diagrams; (c,f) Kinetic energy spectra. The CES results are scaled to match the calculated KER (obtained from calculated potential energy surface) value of 14.8 eV.

This might be caused by the deviations from a simplified vertical ionization model and by potential contributions from the higher-lying PESs of the triply charged molecule, which could result in a higher KER value than the ground-state PES.

4.1.2 Three-body sequential fragmentation channel via $CH_2^+ + CH_2^{2+}$ intermediate

The presence of ring-like structures in the experimental Newton diagrams of Fig. 4.2 as well as vertical features visible in the Native frame plots in Fig. 4.5 suggest that sequential fragmentation also contributes to the $H^+ + CH^+ + CH_2^+$ breakup channel. Since both potential sequential channels illustrated in Fig. 4.1 involve the two-body dissociation of $C_2H_4^{3+}$ producing either CH_2^{2+} or $C_2H_3^{2+}$ metastable doubly-charged intermediate as the first step, we firstly examine whether some of these dications resulting from triple ionization survive long enough to reach the ion detector. To verify this, we explore the corresponding regions of the photoion-photoion coincidence (PIPICO) spectrum shown in Fig. 3.15. As illustrated in Fig. 4.7, we do observe signatures of both (a) $H^+ + C_2H_3^{2+}$ and (c) $CH_2^+ + CH_2^{2+}$ two-body fragmentation channels. Their measured and simulated KE / KER distributions are shown in Fig. 4.7 (b) and (d), respectively. The CES for these two two-body channels are performed under similar assumptions and using the same initial conditions as the three-body concerted simulation discussed above. Similar to the three-body case, the CES without scaling to the calculated final states severely overestimates the experimental KE / KER values for both channels. Using the same procedure as discussed above for the concerted three-body CES, we scale the CES for each of the two-body channels to the theoretically modeled KER values, using the difference between the Franck-Condon energy and the asymptotic energy values in the (b) $H^+ + C_2H_3^{2+}$ and (d) $CH_2^+ + CH_2^{2+}$ limits (see Appendix A.1.3 for details). As can be seen in Fig. 4.7 (b) and (d), for both channels, the scaled CES matches the experimental data very well. Below, we will employ these scaled CES results to model the first steps in the respective sequential fragmentation channels.

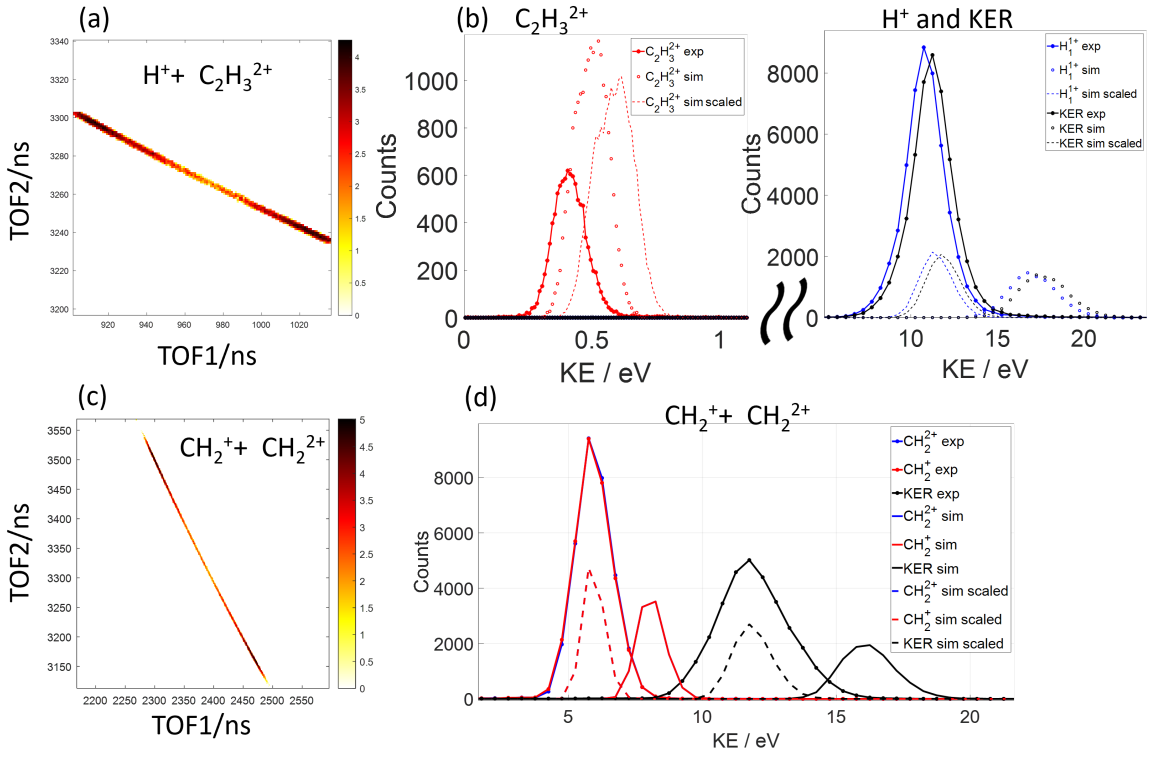

Figure 4.7: ***Two-body fragmentation of*** $C_2H_4^{3+}$**.**

(a) and (c) show the regions of the PIPICO map for $H^+ + C_2H_3^{2+}$ *and* $CH_2^+ + CH_2^{2+}$ *channels, respectively. (b) and (d) display the corresponding kinetic energy release (KER) distributions from experiment (labeled as 'exp'), overlaid with simulated two-body Coulomb explosion simulated kinetic energy distributions (labeled as 'sim'). Scaled CES KER distributions are also included for comparison (labeled as 'sim scaled').*

In order to examine whether each of the two-body channels discussed above indeed represents an intermediate step in the sequential three-body fragmentation as sketched in Fig. 4.1 (in other words, whether a non-negligible fraction of the dications involved breaks up before reaching the detectors), we perform the CES for the respective sequential channels, following the procedure developed in Ref[55]. The modeling of the sequential breakup differs from that of the concerted breakup, as the process is decomposed into two distinct steps. Specifically, we perform two successive two-body CESs, with each step independently scaled to match the theoretical KER value obtained from quantum chemistry calculations. In the first step, a two-body fragmentation (either of the two channels considered in Fig. 4.7) produces an intermediate metastable doubly-charged ion. The two fragments are assumed to move apart for 50 ps with the velocities given by the scaled KER values. Since we do not know the lifetime of the metastable states involved, the 50 ps value was chosen to exceed the expected rotational period of the intermediate dication and to ensure that the Coulomb repulsion from the ion ejected in the first step is negligible. After 50 ps, the intermediate dication undergoes a second Coulomb explosion producing two singly-charged fragments. Here, we assume a fully random orientation of the second breakup direction with respect to the first ejected ion. Such a two-step simulation approach enables us to model the kinematic signatures associated with sequential fragmentation.

First, we focus on the pathway with $CH_2^+ + CH_2^{2+}$ fragmentation as a first step. To model the first step, a two-body CES is performed by assigning charges of +2 and +1 to the two CH_2 fragments, respectively. The outcome of this CES is scaled down to match the KER value predicted by the quantum chemistry calculation carried out by P. Modak and L. Greenman. The latter value is deduced from the PES discussed in the previous section for concerted breakup by stretching the C–C bond to its asymptotic limit (see Appendix A for details). Here, the theoretically predicted KER for the first step (11.7 eV) matches well the experimental KER shown in Fig. 4.7(d). The resulting 3D momentum vectors and the fragment velocities are scaled by applying the square root of the KER ratio. These vector

momenta at 50 ps time are added to the outcome of the independent CES for the second step, the breakup of CH_2^{2+} into $CH_2^+ + H^+$. In the second step, to mimic rotational motion during sequential breakup, the CH_2^{2+} fragment is assumed to have a random orientation with respect to the dissociation direction of the first step. We tested several rotational scenarios (detailed in Appendix A.1.3) and found that the best agreement with experimental data is achieved when the intermediate fragment undergoes rotation about a random axis passing through the center of mass of CH_2^{2+}. This scenario was used for the modeling results shown in this section. To scale the CES outcome for the second step, we use the calculated energy difference between the asymptotic limit for the first step (with only the C–C bond stretched) and the configuration where, in addition, the C–H bond in the CH_2^{2+} dication is also stretched to the asymptotic limit. Remarkably, the corresponding KER value (4.751 eV) matches well the vertical feature of the Native frame second-step KER as shown in Fig. 4.8(a) for the same sequential fragmentation scenario (see Fig. 4.4(a)).

As a second step, we perform the Native frame analysis of the simulated data for this channel. The corresponding $N(\mathrm{KER}_{\mathrm{H-CH}},\ \Theta_{\mathrm{H-CH},\ \mathrm{CH_2}})$ distribution is shown in Fig. 4.8(a) and manifests a characteristic vertical line at the expected second-step KER. For comparison, in Fig. 4.8(b), we plot the same simulated results analyzed under the (wrong) assumption that the sequential breakup proceeds via $H^+ + C_2H_3^{2+}$ intermediate. As can be expected, the corresponding distribution looks very different and does not show any signatures of a sequential process. While the CES results in Fig. 4.8(a) matches the corresponding vertical feature in the experimental data (Fig. 4.4(a)) in $\mathrm{KER}_{\mathrm{H-CH}}$, its angular range in the experimental data is somewhat narrower than in CES. We attribute this discrepancy to the finite detection efficiency of the ion detector for the events where all three fragments are emitted along the same axis. We use the gate around the vertical feature in Fig. 4.8(a) to isolate the contributions of the sequential breakup via CH_2^{2+} in the experimental data.

The resulting Newton diagrams and KE / KER distributions for these isolated events are shown in Fig. 4.9 (a-c), in comparison with the similar graphs obtained from the CES

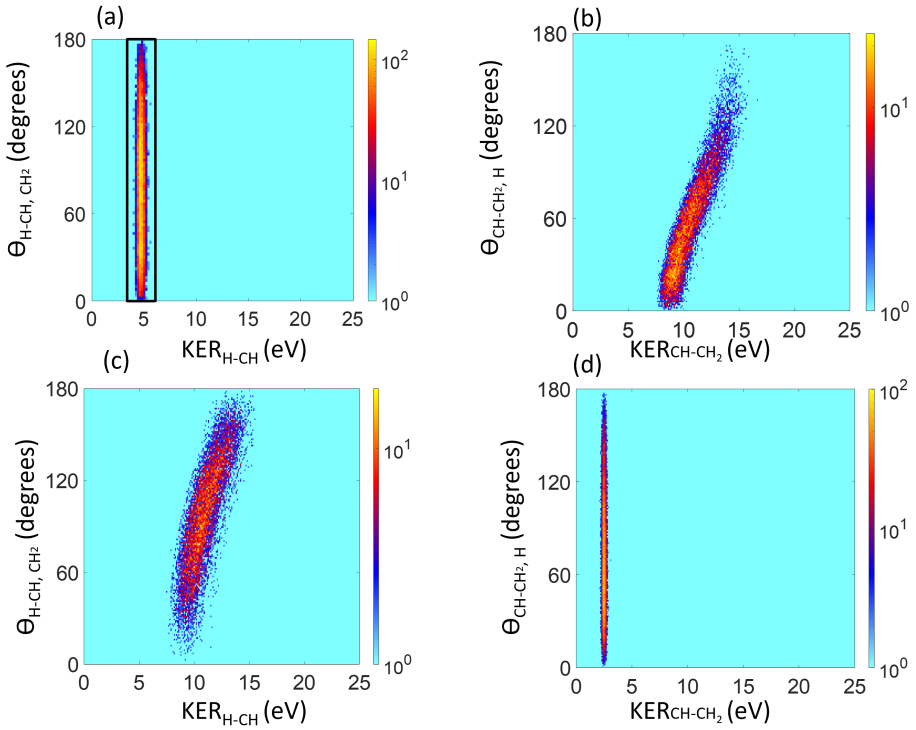

Figure 4.8: ***Native frame analysis of Coulomb explosion simulation of ethylene.*** *(a)* $N(KER_{\mathrm{H-CH}},\ \Theta_{\mathrm{H-CH},\ \mathrm{CH_2}})$ *distribution for the CES of sequential breakup via* $CH_2^+ + CH_2^{2+}$. *(b)* $N(KER_{\mathrm{CH-CH_2}},\ \Theta_{\mathrm{CH-CH_2},\ \mathrm{H}})$ *for the CES of sequential breakup via* $CH_2^+ + CH_2^{2+}$. *(c)* $N(KER_{\mathrm{H-CH}},\ \Theta_{\mathrm{H-CH},\ \mathrm{CH_2}})$ *distribution for the CES of sequential breakup via* $H^+ + C_2H_3^{2+}$. *(d)* $N(KER_{\mathrm{CH-CH_2}},\ \Theta_{\mathrm{CH-CH_2},\ \mathrm{H}})$ *for the CES of sequential breakup via* $H^+ + C_2H_3^{2+}$.

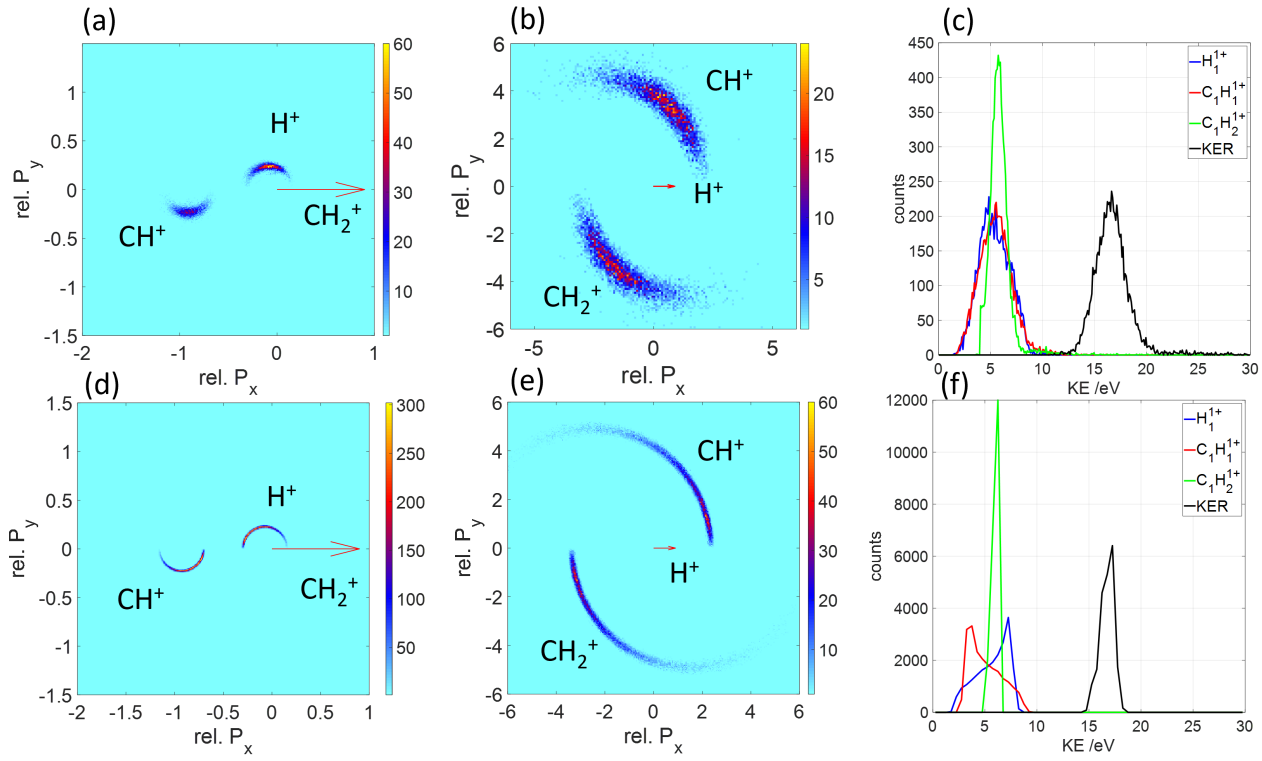

Figure 4.9: ***Three-body sequential fragmentation of ethylene via*** $CH_2^{2+} + CH_2^+$***: simulation and experimental Analysis.***
(a-c) Separated $CH_2^{2+} + CH_2^+$ *sequential breakup events from experimental data. (d-f) CES of the same sequential breakup channel. Panels (a,b) and (d,e) show the normalized Newton diagrams, whereas (c,f) display the KEDs from the experimental data and CES, respectively.*

for this channel Fig. 4.9 (d-f). Both the experimental data and the simulated results clearly show that this sequential pathway is responsible for one of the semi-circular structures in the experimental Newton maps of Fig. 4.2, as well as for the low-energy peak in the proton KED (Fig. 4.3(a)). While, as discussed in the previous section for concerted breakup, the features in the Newton plots and KEDs of the experimental data are somewhat broader than in the CES, overall, the simulation provides a good description of all characteristic features for this channel.

4.1.3 Three-body sequential fragmentation channel via $H^+ + C_2H_3{}^{2+}$ intermediate

To analyze potential contributions of the sequential fragmentation via $H^+ + C_2H_3^{2+}$ intermediate state, we first simulate this process using the logic similar to what we applied in the previous section. In the first step, the CES of $H^+ + C_2H_3{}^{2+}$ two-body breakup is performed. Here, the charge of +2 is placed at the center of mass of the C_2H_3 fragment and another +1 charge is given to the H atom. As described for the other sequential channel, the outcome of this CES is also scaled down to match the KER predicted by the quantum chemistry calculation. Here, to estimate the expected KER for the first step, the C–C bond is kept intact, and one C–H bond is stretched to its asymptotic limit (see Appendix A for details). The resulting theoretical KER (11.941 eV) is slightly higher than the experimental peak KER value for the corresponding two-body channel (11.4 eV, see Fig. 4.7(b)), but is close enough to provide a reasonable scaling factor for CES. After propagating this scaled CES for 50 ps, the second-step CES, the two-body fragmentation of $C_2H_3^{2+}$ into $H^+ + CH^+$ is performed, assuming that the dication undergoes random rotation about its center of mass before its Coulomb explosion. At the instant of the second breakup, the +2 charge is redistributed to the centers of mass of the resulting fragments. The outcome of this second-step CES is again scaled to match the theoretically predicted KER value. The latter amounts to 2.53 eV (see Appendix A for details).

The results of the Native frame analysis of this two-step sequential CES are shown in Fig. 4.8(d) and appear as a well-localized vertical band expected for sequential fragmentation. The same CES data analyzed assuming the sequential breakup via a 'wrong' intermediate step ($CH_2{}^{2+} + CH_2{}^{+}$) (Fig. 4.8(c)) do not show this characteristic behavior. While the corresponding experimental Native frame plot (Fig. 4.4(b)) manifests a qualitatively similar vertical band, it lies at significantly higher KER_{CH-CH_2} values than the theoretical prediction in Fig. 4.8(d). Therefore, we cannot use the theoretical prediction to select potential contributions from this sequential channel to the experimental data. Instead, we

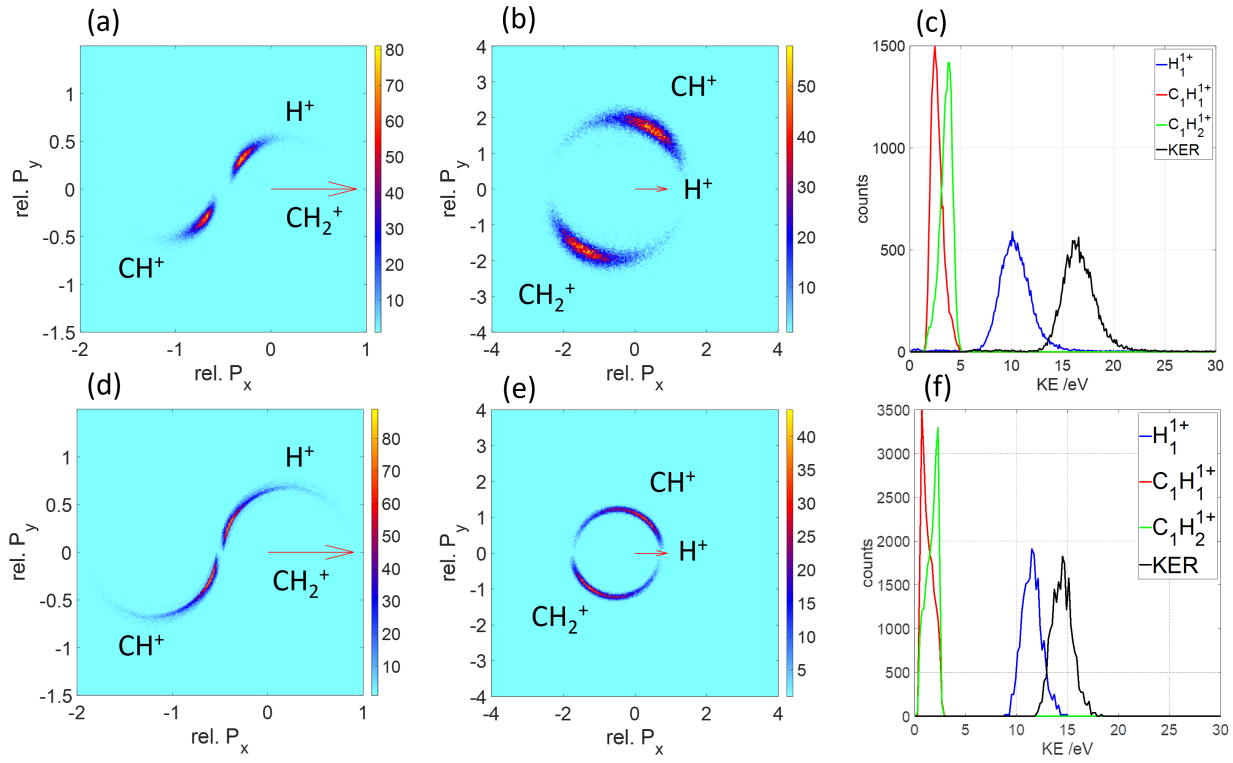

Figure 4.10: ***Three-body sequential fragmentation of ethylene via H^+ + $C_2H_3{}^{2+}$: simulation and experimental analysis.***
(a-c) Separated H^+ + $C_2H_3{}^{2+}$ sequential breakup events from experimental data. (d-f) Coulomb explosion simulation of sequential breakup channel via H^+ + $C_2H_3{}^{2+}$. (a)(b) and (d)(e) are the relative normalized Newton diagrams. (c) and (f) are the kinetic energy distributions from experimental data and Coulomb explosion simulation respectively.

select a rectangular gate on the vertical feature visible in the experimental data shown in Fig. 4.4(b), even though it partly overlaps with the concerted breakup contribution (see Fig. 4.5).

The Newton diagrams and KE / KER distributions for the events within this gate are plotted in Fig. 4.10(a,b), and (c), respectively. They are compared with the CES results for the sequential fragmentation via $H^+ + C_2H_3^{2+}$ shown in Fig. 4.10(d-f). Despite the significant difference in KER_{CH-CH_2}, the shape of the simulated Newton diagrams resembles the experimental ones, suggesting that a sequential process involving initial proton ejection plays a role here. However, both the magnitude of the relative momenta in Newton diagrams

and the KE values differ significantly between theory and experiment. Part of this discrepancy comes from the mismatch in the second-step KER. Its predicted value of 2.523 eV does appear to be lower than the characteristic energies of similar two-body breakup processes. For comparison, the experimental KER distribution for the dominant two-body CE channel in doubly-charged ethylene ($CH_2^+ + CH_2^{2+}$) peaks slightly above 6 eV. So it is not unlikely that the observed discrepancy either results from some issues with the PES modeling in the asymptotic region or it is due to the fact that the intermediate $C_2H_3^{2+}$ dication is not produced in its ground state, as assumed in the calculation.

However, note that the second-step discrepancy alone does not fully explain the difference between the theory and experiment. While the experimental proton KED from the channel in question closely resembles that of the concerted breakup (compare Fig. 4.10(c) and Fig. 4.6(c)), the simulated proton KED (Fig. 4.10(f)) as well as the experimental data from the two-body $H^+ + C_2H_3^{2+}$ channel (Fig. 4.7(b)) peak at somewhat higher values. This suggests that the proton motion during the laser pulse itself might play a role in both concerted breakup and the sequential channel involving initial proton ejection. For example, the proton KE can be reduced if the rest of the molecule stays singly charged for most of the pulse and is further ionized in its trailing edge, when the C–H bond that is being cleaved is already stretched. While initial attempts to simulate this type of dynamics have been attempted during this work, its understanding requires more detailed and systematic modeling.

4.2 Four-body fragmentation in $C_2H_4^{4+}$

As the next step, in this section, we consider the four-body fragmentation of the quadruply charged ethylene molecule into four singly charged fragments: $H^+ + H^+ + CH^+ + CH^+$. Since in the analysis presented here all four fragments are detected in coincidence, we again refer to this channel as a 'complete' channel. Compared to the results presented in the

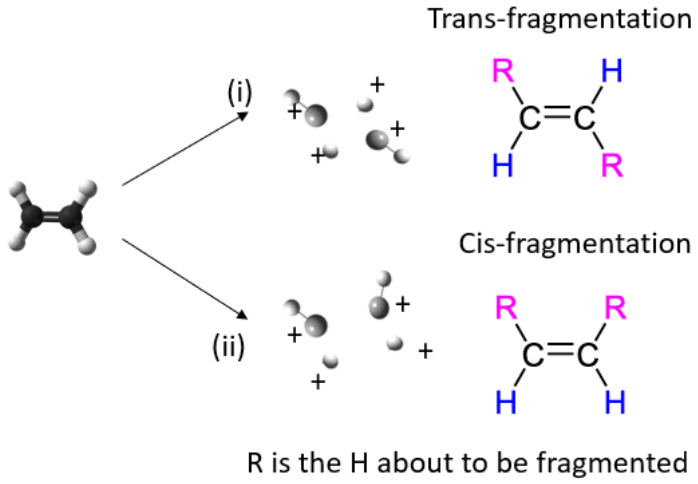

Figure 4.11: ***Schematics of the four-body fragmentation channel of ethylene.*** *$C_2H_4 \rightarrow H^+ + H^+ + CH^+ + CH^+$ via (i) cis-fragmentation and (ii) trans-fragmentation.*

previous section, in four-body fragmentation, a larger variety of pathways leading to the same final state can exist. Besides a variety of potentially contributing sequential channels, even concerted four-body breakup can proceed via two distinctly different mechanisms, as illustrated in Fig. 4.11. In the first scenario, which will be referred as 'trans-fragmentation', in which the two hydrogen atoms detached from the molecule originate from the opposite sides with respect to the C–C bond, whereas in the second one, which we will refer to as 'cis-fragmentation', the two emitted hydrogens are removed from the same side of the C–C bond. While this terminology is borrowed from the definitions of cis- and trans-molecular isomers, neither of the two scenarios considered necessarily involves the creation of the cis- or trans- C_2H_2 intermediate from sequential fragmentation of four-body breakup.

4.2.1 Coulomb explosion simulation for four-body fragmentation

To investigate the dynamics involved in the 'complete' four-body breakup channel, we first perform the CES for each of the scenarios outlined above. Here, we restricted the analysis to

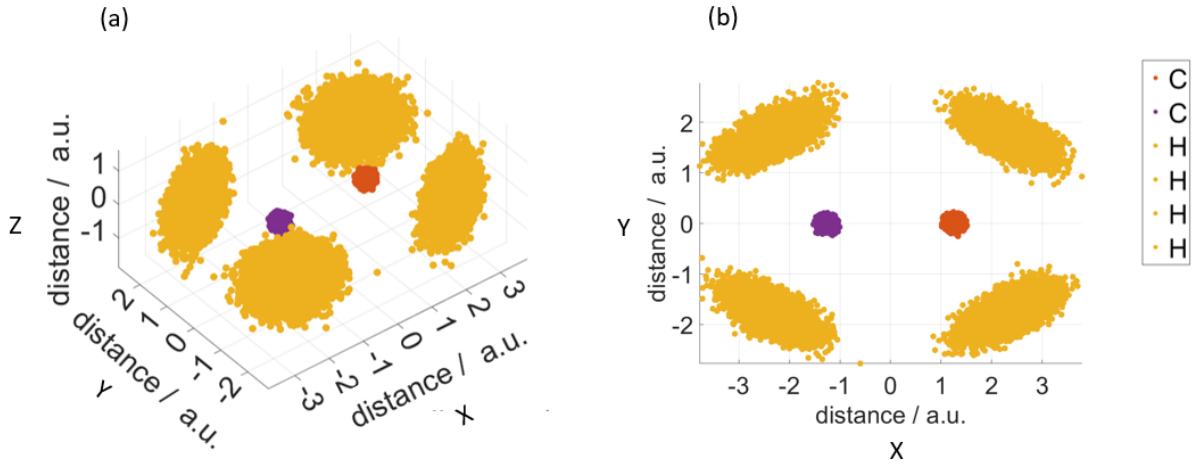

Figure 4.12: ***Ground state geometry of ethylene modeled with Wigner distribution at 60 K.***
(a): 3D representation; (b) in (x, y)-plane view.

concerted fragmentation scenarios, since we did not observe any clear signatures of sequential channels in the corresponding experimental data. The distribution of nuclei positions used for CES (modeled by Wigner distribution at 60 K, as discussed above) is shown in Fig. 4.12. As before, the CES assumes that the charge is located at the center of mass (COM) of each of the four created ionic fragments. To simulate the four-body trans-fragmentation, the charges are placed on the hydrogen atoms located opposite sides of the C–C bond. In contrast, for cis-fragmentation, the charges are placed on the same side of the C–C bond, reflecting the respective geometric configurations of the breakup. The charge distributions used for cis- and trans-fragmentation simulations are shown in Fig. 4.13(a) and (b), respectively. Fig. 4.13(c) and (d) show the corresponding final sets of asymptotic momenta distributions obtained from the simulation for each scenario. These 'raw' (without being represented using Newton diagram under molecular frame definition) momentum distributions are plotted in the same (x, y)-plane as the molecular geometry shown in Fig. 4.11(b), and display very different patterns for cis- and trans-fragmentation scenarios.

To compare the CES results with the experimental data, in Fig. 4.14 the simulation results are presented using Newton diagrams. While traditionally, this representation is

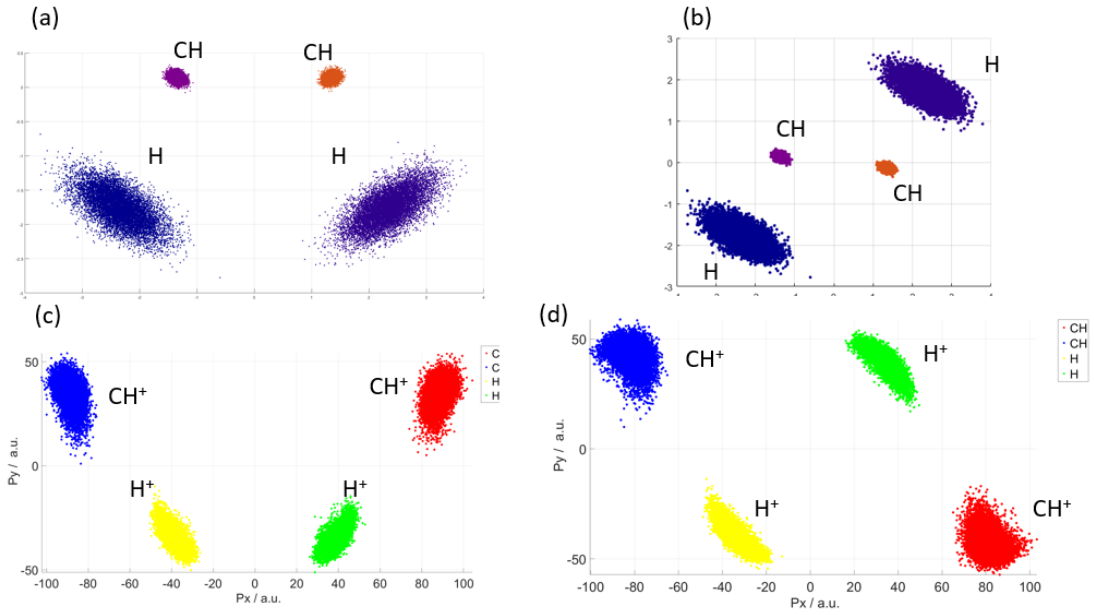

Figure 4.13: ***Charge distributions and simulated momentum distribution from CES of ethylene four-body fragmentation.***
Charge distributions used in the Coulomb explosion simulation for the cis- (a) and trans- (b) four-body fragmentation of ethylene. (c) and (d): Corresponding raw momentum distributions of the final ionic fragments ($H^+ + H^+ + CH^+ + CH^+$) *for the complete cis- and trans-fragmentation obtained from the simulations. Here, 'raw' refers to data that are not represented using Newton diagrams in the molecular frame.*

used to display the data from three-body breakup, it can be easily extended to the multi-body cases[122,135]. Here, similar to the three-body case, the positive x-axis is defined by the normalized momentum unit vector of the first detected CH^+ ion, which, together with the momentum vector of the first detected proton, is used to define the (x, y)-plane ('molecular' or 'fragmentation' plane). The momenta of the other detected particles (here, another CH^+ and H^+) are then plotted in this coordinate frame. In contrast to the three-body case, where the momentum conservation requires that all three measured momentum vectors lie in one plane, for the four-body breakup, the components out of the (x, y)-plane could also carry meaningful information. Therefore, for the Newton diagrams presented in this section, also the momentum components in (x, z)- and (y, z)- molecular planes are shown. While all Newton diagrams shown in this section are normalized by the length of the CH^+ momentum vector used to define the x-axis, the non-normalized version of each diagram (containing absolute values of all fragment momenta and, thus, retaining kinetic energy information) can be found in Appendix A.2.

The upper row of Fig. 4.14 shows (x, y)-, (x, z)-, and (y, z)-plane views of the Newton maps obtained from the CES of trans-fragmentation, whereas the bottom row displays the same plots for the CES of cis-fragmentation. For each plane, the simulated momentum distributions are clearly different for both scenarios, and can be traced towards the charge and momentum distributions shown in Fig. 4.13. Specifically, for trans-fragmentation, the CH^+ ions are emitted nearly back to back and the protons have opposite signs of their y-momentum component. In contrast, for cis-fragmentation, the relative angle between the momentum vectors of the CH^+ ions is noticeably smaller than 180°, and both protons have a positive y-momentum component.

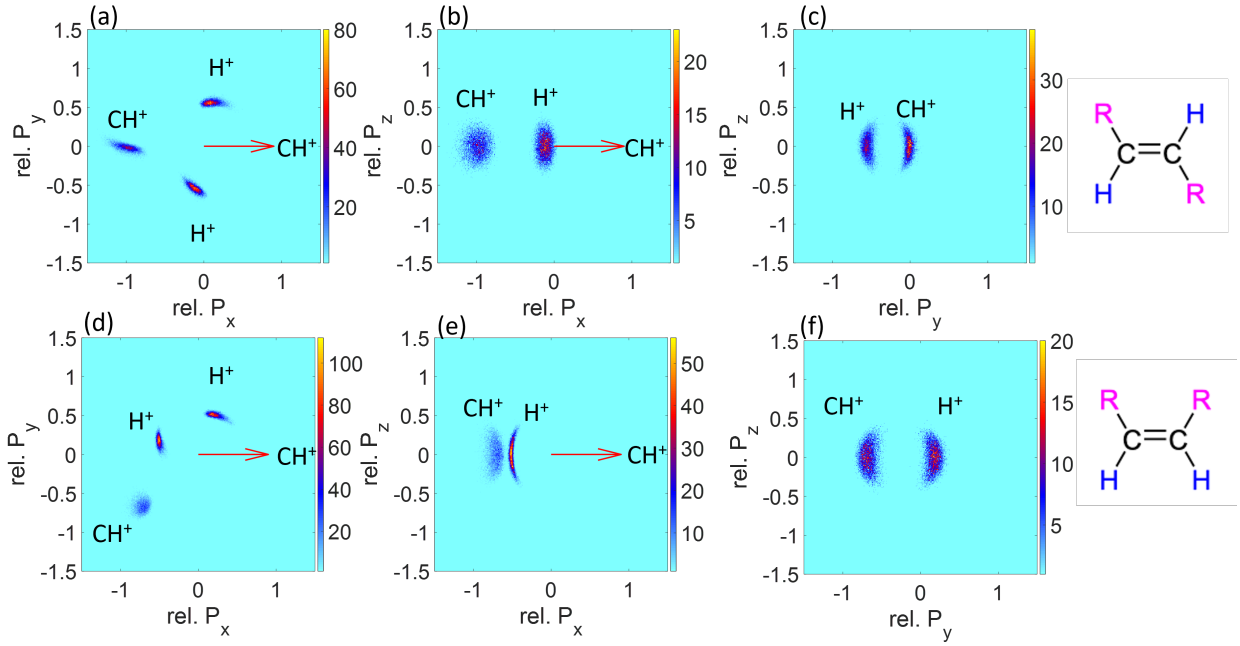

Figure 4.14: ***Normalized Newton diagrams of trans- and cis-fragmentation of four-body breakup of ethylene obtained from CES.***

(a-c) trans-fragmentation;(d-e) cis-fragmentation. (a,d): (x, y)-plane, (b,e): (x, z)-plane, (c,f) (y, z)-plane. Momentum vector of the first detected CH^+ *is used for defining the x-axis and plotted as the orange unit vector. The momentum of one of the* H^+ *ions that is used for defining the (x, y)-plane is shown in (x, y)-representation but is not plotted in the (x, z)- and (y, z)-planes because its z-momentum component is zero after being used to define molecular plane.*

4.2.2 Disentangling signatures of cis- and trans-fragmentation in experimental data

Fig. 4.15 presents the experimental Newton diagrams (a–c) and the corresponding kinetic energy (KE) and kinetic energy release (KER) distributions (d) for the four-body fragmentation channel ($H^+ + H^+ + CH^+ + CH^+$). All experimental data shown in this section were recorded using an increased spectrometer voltage of 4000 V, compared to the 2000 V used in Section 4.1. This adjustment was made to ensure efficient detection of both energetic protons emitted in the four-body breakup channel. The impact of spectrometer voltage on energy acceptance is characterized in Appendix A.2.

Our analysis indicates that the limited angular acceptance at the lower voltage setting has only a minor effect on events from the trans-fragmentation pathway, where the two protons are emitted nearly back-to-back. In contrast, for the cis-fragmentation pathway, the protons are emitted nearly perpendicular to each other. As a result, one proton is more likely to be emitted perpendicular to the spectrometer axis and may miss the detector if its kinetic energy exceeds approximately 12.5 eV. This limitation is effectively resolved by using a higher spectrometer voltage. For reference, the same data set recorded at the lower voltage setting is also shown in Appendix A.2.

Fig. 4.15 includes all the data collected for the $H^+ + H^+ + CH^+ + CH^+$ channel, potentially including contributions from both cis- and trans-fragmentation pathways. The most intense part for each of the three representations of the Newton diagram in panels (a-c) qualitatively resembles the CES results for the trans-fragmentation (Fig. 4.14(a-c)). However, the observed structures are broad, and there are also diffuse counts in-between the main spots. In order to separate contributions from trans- and cis-fragmentation in the experimental data, we gated the experimental data set on the regions where the second CH^+ ion (the one not used to define the x-axis) is expected to appear for each scenario according to the CES results shown in Fig. 4.14(a,d). The corresponding gates are shown in Fig. 4.16(a) as black (trans) and red (cis) ovals. Panels (b-d) and (e-g) of the same figure show the

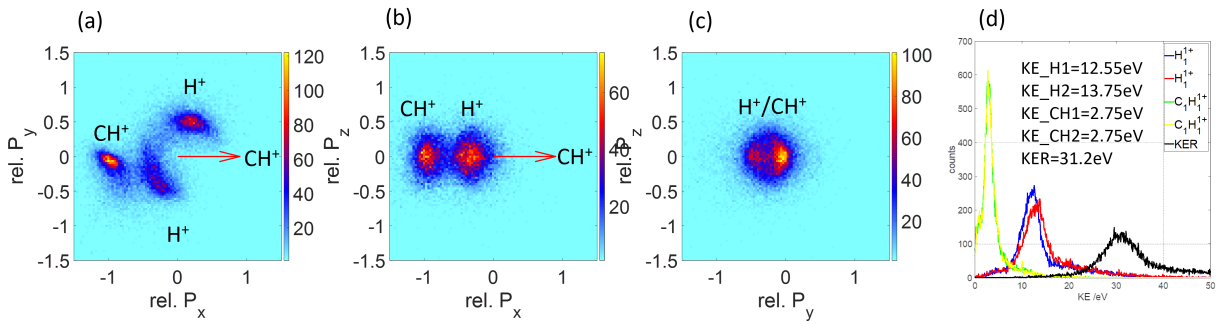

Figure 4.15: ***Experimental Newton diagrams for four-body complete fragmentation of ethylene.***
(a): (x, y)-plane; (b): (x, z)-plane; (c): (y, z)-plane. Momentum distribution of CH^+ *is used for defining the x-axis plotted as the orange unit vector together with one* H^+ *momentum for defining the molecular plane which is not plotted in the (x, z)- and (y, z)-plane. (d) Measured KER of the complete four-body fragmentation channel. The superscript on each ion fragment label indicates the charge state, while the subscript denotes the number of atoms in that fragment.*

Newton diagrams for the events gated on the expected trans- and cis-fragmentation, respectively. The observed structures in each row are sharper and better localized than in Fig. 4.15. The data for cis- and trans-fragmentation gates exhibit very different patterns for each of the three planes shown and qualitatively resemble the simulated Newton diagrams for the corresponding scenarios shown in Fig. 4.14.

Fig. 4.17 compares the measured and simulated KE of the individual ion fragments, as well as the total KER, for both trans- and cis-fragmentation pathways. In contrast to the Newton diagrams shown in Figs. 4.15, 4.16, the KE and KER distributions for both experiment and simulation show little difference for cis- and trans-fragmentation and, thus, cannot be used to discriminate between the two scenarios. While the experimental KE and KER spectra for isolated trans- and cis- fragmentation pathways in Fig. 4.17(d-f) closely resemble the integrated KE / KER spectrum shown in Fig. 4.14(d), the CES (Fig. 4.17(a-c)) yields much higher KE / KER values. As discussed in the previous section, this is a typical issue for CEI experiments, where the CES often overestimates the measured KED because of the dynamics during the ionization process and the non-Coulombic final state. Since at this time we do not have a reliable PES for quadruply charged ethylene,

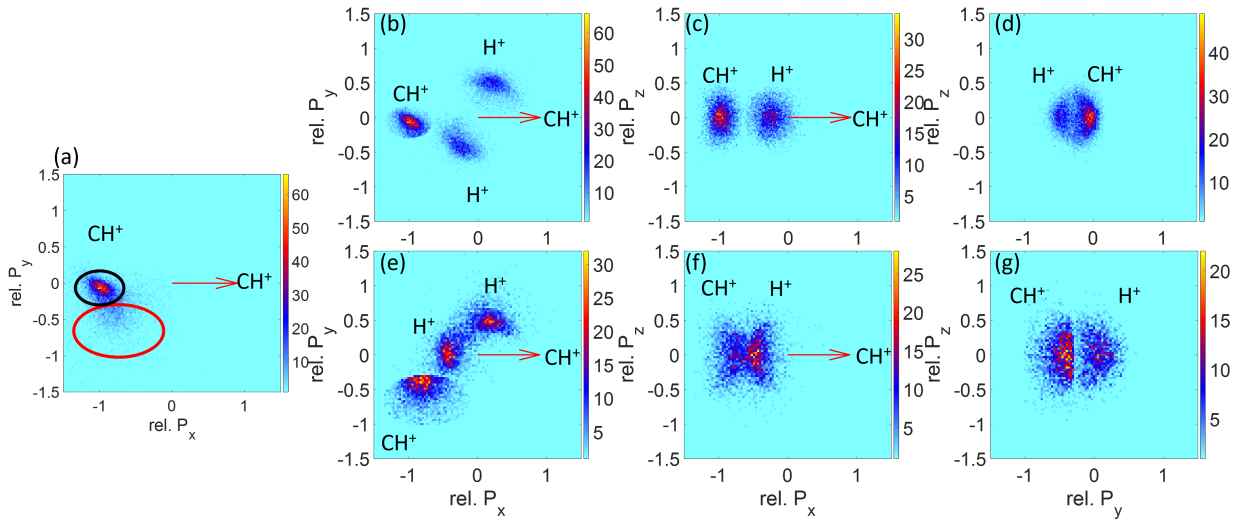

Figure 4.16: ***Experimental separation of the contributions from trans- and cis-fragmentation of four-body breakup of ethylene.***
(a) The Newton diagram contains CH^+ ions only. Black and red ovals show gates used to select trans- and cis-fragmentation events, respectively. (b-d) Newton diagrams for trans-fragmentation (black oval in (a)); (e-g) Newton diagrams for cis-fragmentation (red oval in (a)). (b,e): (x, y)-plane; (c,f) (x, z)-plane; (d,g): (y, z)-plane.

we cannot apply the scaling procedure developed in the previous section for three-body breakup. Nevertheless, even such non-scaled simulation provides very useful insights if relative (normalized) momentum correlation maps (Newton diagrams) are considered.

The analysis presented here in principle enables quantitative determination of the branching ratio of trans- and cis-fragmentation. While precise determination of this quantity is hindered by the uncertainties in relative detection efficiency for both configurations, the data of Fig. 4.16(a) suggest that trans-fragmentation occurs approximately twice as often as cis-fragmentation. A likely reason for this is that the trans-fragmentation is expected to be lower in energy than cis-fragmentation, as shown in the Fig. A.25 of Appendix A.2 .

The discussion in this section focuses on four-body concerted breakup channels for both trans- and cis-fragmentation. Although we do not see any clear manifestations of sequential processes in the experimental data shown in Figs. 4.14 and 4.16, we cannot exclude some minor contributions from such channels. Their separation and identification would require

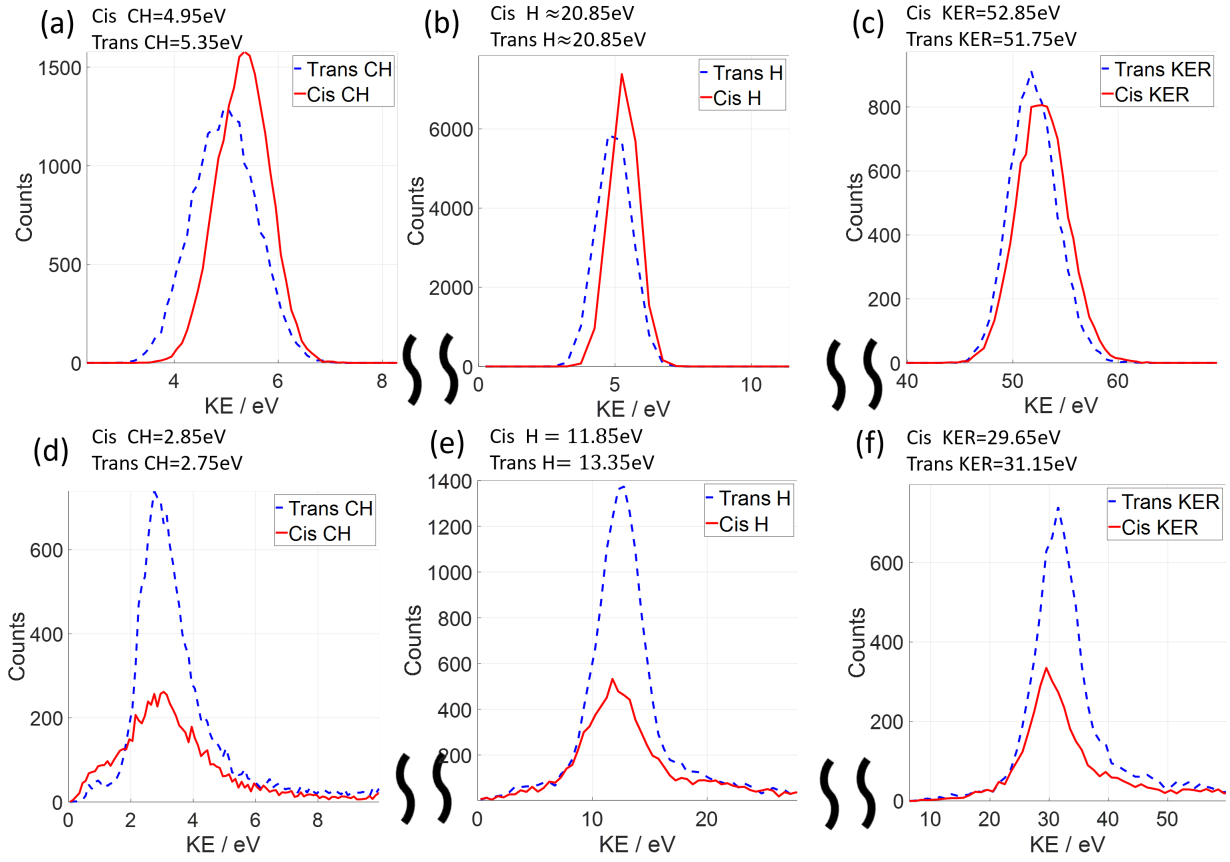

Figure 4.17: ***Comparison of KER for cis- and trans-fragmentation of four-body breakup of ethylene: CES simulation vs. experimental data.***
(a-c) are the simulated KER for cis- and trans-fragmentation pathways while (d-e) are the KER distributions from four-body experimental data. (a) and (d) show the kinetic energy distributions zoomed in on the CH^+ *region. (b) and (e) show the kinetic energy distributions zoomed in on the* H^+ *region. (c) and (f) show the zoomed-in total kinetic energy release (KER). Peaks of each curve are shown above each KE distribution panel.*

more elaborate analysis, extending the Native frame analysis framework to the four-body case. Some initial work in this direction is currently in progress (Prof. Itzik Ben-Itzhak, private communication).

4.2.3 Modified Newton diagrams for more intuitive representation of four-body breakup

While conventional Newton diagrams extended to the case of four-body breakup as discussed above, provide many useful insights into both molecular geometry and fragmentation dynamics, enabling, in particular, experimental separation of cis- and trans-fragmentation, their ability to visualize the initial geometry of the molecule is limited by the fact that one of the fragment's momenta is confined to the x-axis, and the second one lies in (x, y)-molecular plane thus has zero momentum distribution in z-direction. In order to achieve a more intuitive representation of the four-body breakup, we further develop the procedure introduced in Refs[135,136], where the molecular frame of reference is defined by combinations of momentum vectors of ion fragments. This representation allows for an adequate visualization of the measured molecular-frame momentum distributions for all detected ionic fragments.

Fig. 4.18(a) illustrates the selection of the momentum vectors used to define the molecular frame for trans-fragmentation in a conventional way, using individual fragment momenta (a), and in the generalized version, which exploits the pairwise difference of the vector momenta of the two CH^+ ions and two protons (b). This definition provides an adequate representation of the trans-type breakup process. However, as can be seen from Fig. 4.18(c), for cis-fragmentation, the vector difference of the two proton momenta breakup direction would be, on average, parallel to the CH-CH direction and, thus, cannot be efficiently used to define the (x, y)-plane. To circumvent this, cis-fragmentation can be represented by using the vector sum of the two proton momenta instead of their difference, as illustrated in Fig. 4.18(d). If the same frame definition is used for the trans-fragmentation case, though,

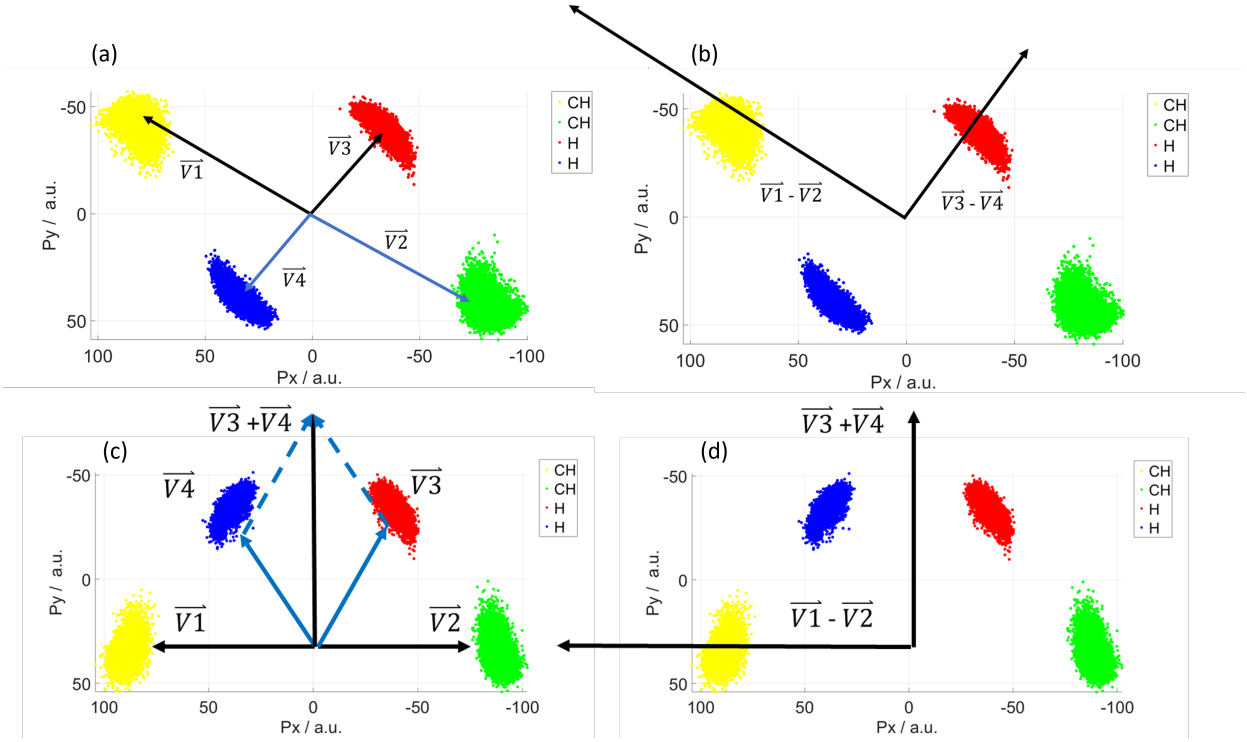

Figure 4.18: ***Vectors used for defining the*** (x, y)***-momentum plane in Newton diagrams from CES of four-body breakup of ethylene.***
$\vec{V}_i$ denotes the symbolic representation of the ion fragment momentum vectors. (a) Traditional method for defining Newton diagrams for trans-fragmentation, where $\vec{V}_1$ (or $\vec{V}_2$) and $\vec{V}_3$ (or $\vec{V}_4$) are used as reference vectors. (b) Alternative method for defining the momentum plane, where the vectors $\vec{V}_1 - \vec{V}_2$ and $\vec{V}_3 - \vec{V}_4$ are used to define the (x, y)-momentum plane in Newton diagrams of trans-fragmentation. (c) The momenta vectors used for cis-fragmentation Newton diagrams definition. (d) Modified method for defining the momentum plane, where the vectors $\vec{V}_1 - \vec{V}_2$ and $\vec{V}_3 + \vec{V}_4$ are used to define the (x, y)-momentum plane in Newton diagrams of cis-fragmentation.

the vector sum of the two proton momenta would be very close to zero and, thus, will not provide a good vector for the (x, y)-plane definition.

While the modified Newton diagrams offer a nice way to present the CES results for cis- and trans-fragmentation, a question arises: if we mistakenly represent the experimental data using a molecular momentum plane better suited for the opposite fragmentation pathway (e.g., plotting cis-fragmentation data using the trans-fragmentation frame), would we still be able to distinguish between cis- and trans-fragmentation processes? To explore this, in Fig. 4.19(a,b), we present the Newton diagrams of the CES results for trans- (a) and cis- (b) fragmentation, respectively, each is analyzed in the appropriate reference frame (i.e., using proton momentum difference for trans- and their momentum sum for cis-). Fig. 4.19(c,d) shows the corresponding analysis of the experimental data, separated into trans- (c) and cis- (d) data sets using the gates shown in Fig. 4.16(a). These plots closely resemble the corresponding simulations and can be intuitively related to the initial geometries and charge distributions sketched in Figs. 4.12 and 4.13. In Fig. 4.19(e,f) and (g,h), we present the same diagrams obtained using the 'wrong' reference frame in the CES and experimental analysis, respectively. While the simulation still matches the corresponding experimental results pretty well, overall, the patterns obtained in this way bear little resemblance to the geometry of the molecule.

Therefore, the analysis of different data representations presented here demonstrates that generalized Newton diagrams relying on pairwise momentum differences or sums of the detected fragments provide a very intuitive way to relate the measured momentum correlation patterns; the exact frame definition must be linked to a specific fragmentation pathway to ensure meaningful results. Overall, the results presented in this section indicate that both cis- and trans-fragmentation pathways are present in the strong-field-induced four-body breakup of ethylene, demonstrating that CEI patterns are sensitive not only to different molecular structures but also to different fragmentation dynamics leading to these patterns.

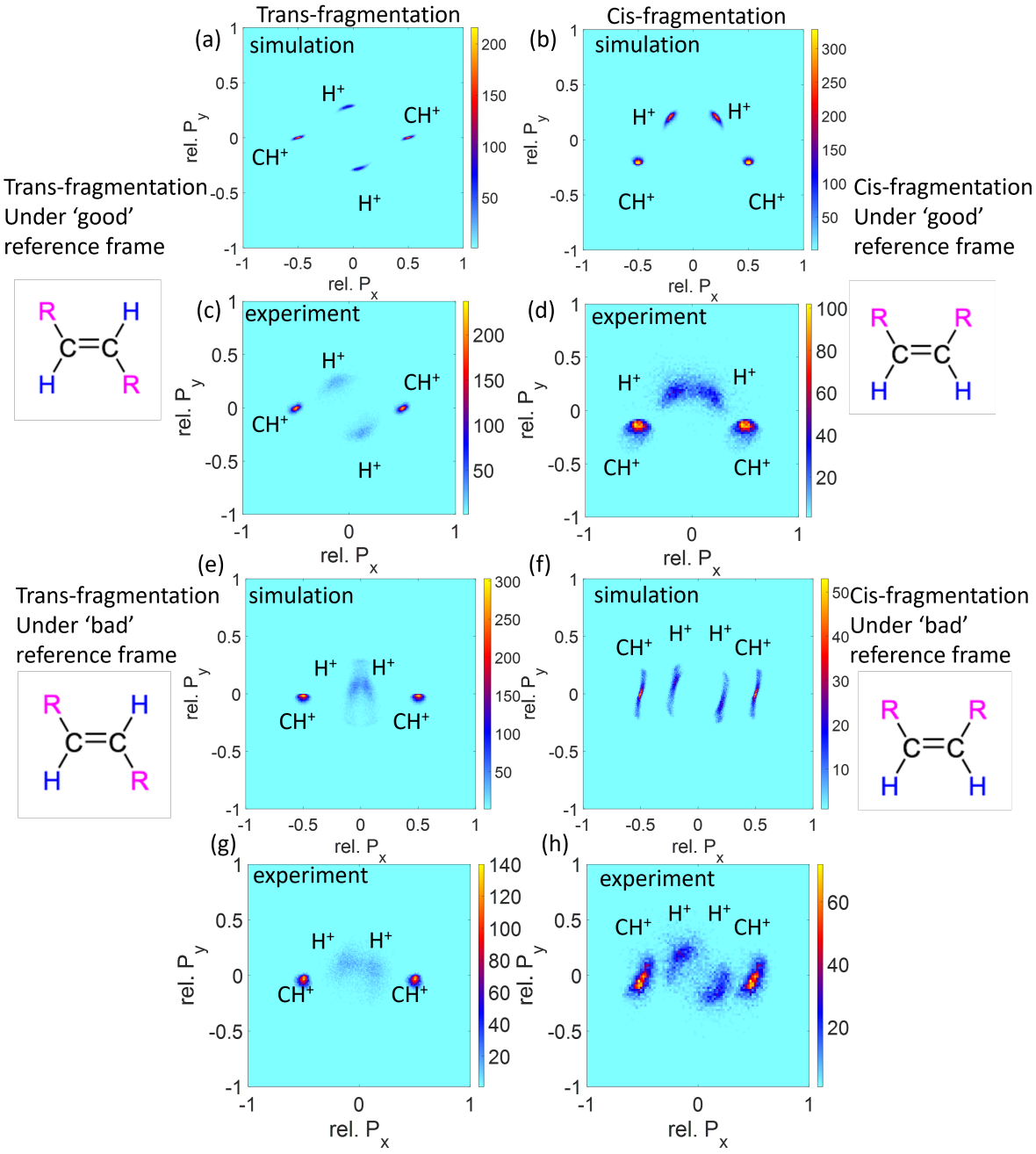

Figure 4.19: ***Comparison of measured and simulated modified Newton diagrams of complete four-body trans- and cis-fragmentation of ethylene using different molecular frame definitions.***
(a), (c), (e), and (g): trans-fragmentation; (b), (d), (f), and (h): cis-fragmentation. (a), (b), (e), and (f) are from the CES, while (c), (d), (g), and (h) are from the experimental data. (x, y)-plane Newton diagrams of trans- and cis-fragmentation are shown using two different molecular plane definitions: (a) and (c) display trans-fragmentation using the definition from Fig. 4.18(b); (e) and (g) show trans-fragmentation using the definition from Fig. 4.18(d); (b) and (d) show cis-fragmentation using the definition from Fig. 4.18(d); (f) and (h) show cis-fragmentation using the definition from Fig. 4.18(b).

4.3 Fragmentation of multiply charged ethylene into six atomic ions

The studies of three- and four-body fragmentation of ethylene presented in the previous sections relied on the coincident detection of all created ions. It was long thought that such 'complete' coincidence measurement is required for an efficient CEI experiment in the coincident mode. In particular, this approach allows for unique determination of the total charge state of the molecule and enables efficient discrimination against the background (false coincidence contributions) by enforcing momentum conservation between the detected fragments. Alternative approaches relied on various non-coincidental measurement schemes, sometimes involving laser alignment of molecules (see[137] and references therein) or employed covariance mapping[138,139]. However, recent CEI measurements at the European XFEL[122,53] and with optical lasers[54,52] demonstrated that detecting a subset (like 3, 4, or 5) of all created molecular ions in coincidence can provide very detailed structural information on a larger molecule provided that it is completely fragmented into individual atomic ions. In this section, we explore the advantages and limitations of this approach for ethylene fragmentation into six atomic ions.

Schematics of the experiments and simulations discussed in this section are illustrated in Fig. 4.20. Following multiple ionization by the laser, the molecules break up into six atomic ions, few of which are detected in the experiment. To minimize the effect of different charge states on the fragmentation dynamics, here we only focus on the singly charged ions. Therefore, all CESs discussed here assume a six-fold ionization of the molecule. For the experimental results, there is some uncertainty in the total charge state since not all of the created ions are detected. This can result in underestimating the total charge of the molecule if only one carbon ion is detected, or to its overestimation if some of the hydrogen atoms remain neutral.

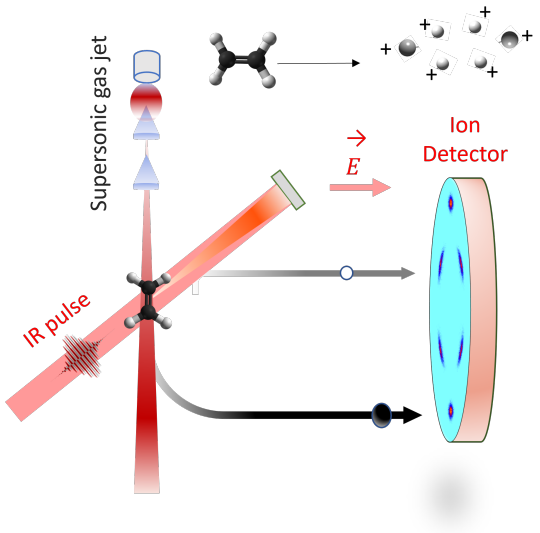

Figure 4.20: ***Sketch of the experimental setup and intuitive representation of the six-body fragmentation of ethylene.***

Figure consists information of incomplete three-, four-, and five- body fragmentation channels with missing ions (H^+/C^+) of ethylene measured in coincidence: $C_2H_4 \rightarrow H^+ + H^+ + H^+ + H^+ + C^+ + C^+$.

4.3.1 Coulomb explosion simulation for six-body complete fragmentation of ethylene

As an initial step, CES of six-body breakup into singly charged atomic ions were employed to guide the analysis. As before, the simulation assumed instantaneous ionization to the final charge state (+6) and purely Coulombic nature of the corresponding PES. As discussed in the previous sections, the distribution of initial geometries for the neutral ground-state ethylene was sampled by Wigner distribution at 60 K. Here, a single charge was placed at the position of each nucleus upon ionization.

To construct conventional and generalized Newton diagrams from the CES results, the atoms in the molecule are labeled with numbers from 1 to 6, with 1-4 assigned to hydrogen and 5,6 - carbon atoms. Their respective momentum vectors are denoted $\vec{V}_1$ - $\vec{V}_6$, as shown in Fig. 4.21(a). In this three-dimensional momentum space, the distributions of the

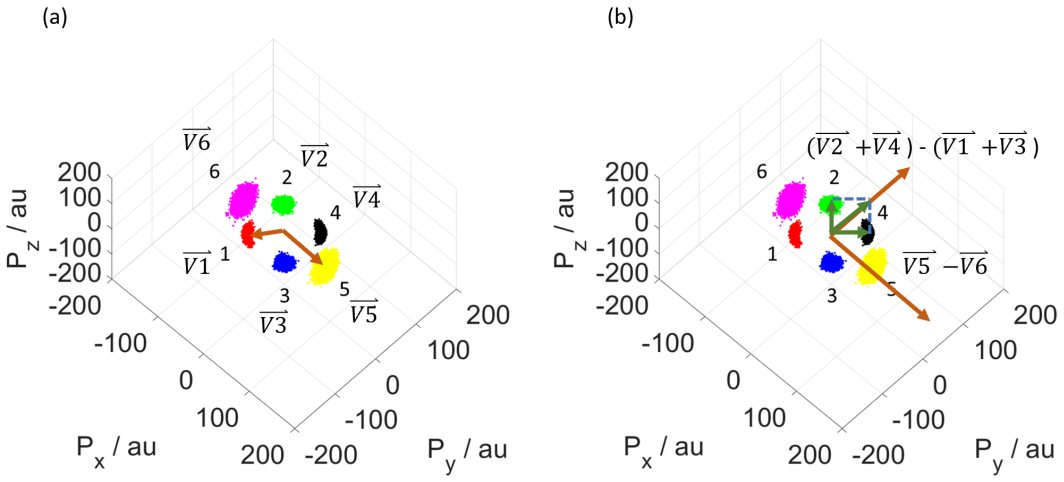

Figure 4.21: ***Vectors used for defining the*** (x, y)***-momentum plane in Newton diagrams from CES of six-body complete fragmentation of ethylene.***
$\vec{V}_i$ denotes the symbolic representation of the ion fragment momentum vectors. (a) Traditional method for defining Newton diagrams, where $\vec{V}_5$ and $\vec{V}_1$ are used as reference vectors. (b) Alternative method for defining the momentum plane, where the vectors $\vec{V}_5 - \vec{V}_6$ and $(\vec{V}_2 + \vec{V}_4)$ - $(\vec{V}_1 + \vec{V}_3)$ are used to define the Newton diagrams (x, y)-momentum plane.

ion fragments following Coulomb explosion are represented by different color-coded regions. For standard Newton diagrams, the momentum vector of one C^+ ion ($\vec{V}_5$) is used to define the positive x-axis, and, in combination with the momentum vector of one proton ($\vec{V}_1$), these two vectors define the (x, y)-momentum plane. The corresponding simulated momentum distributions in (x, y)-, (x, z)-, and (y, z)-planes are shown in Fig. 4.22(a), (b), and (c), respectively. However, the drawback of this representation is that the z-momentum component of the proton used to define the (x, y)-plane would be 0 in this molecular frame. Correspondingly, that proton is not plotted in Fig. 4.22(b,c). To address this limitation and to visualize all three momentum components of each proton, in Fig. 4.22(d-f), the same data are plotted using the difference between the two proton momentum vectors $\vec{V}_4$ - $\vec{V}_1$ to define the (x, y)-plane, together with carbon ion momentum ($\vec{V}_5$).

To achieve an even more illustrative representation in a generalized Newton diagram, conceptually similar to the one used for Fig. 4.19 we subsequently define the x-axis of the (x, y)-momentum plane using the difference vector $\vec{V}_5 - \vec{V}_6$ instead of a single carbon ion.

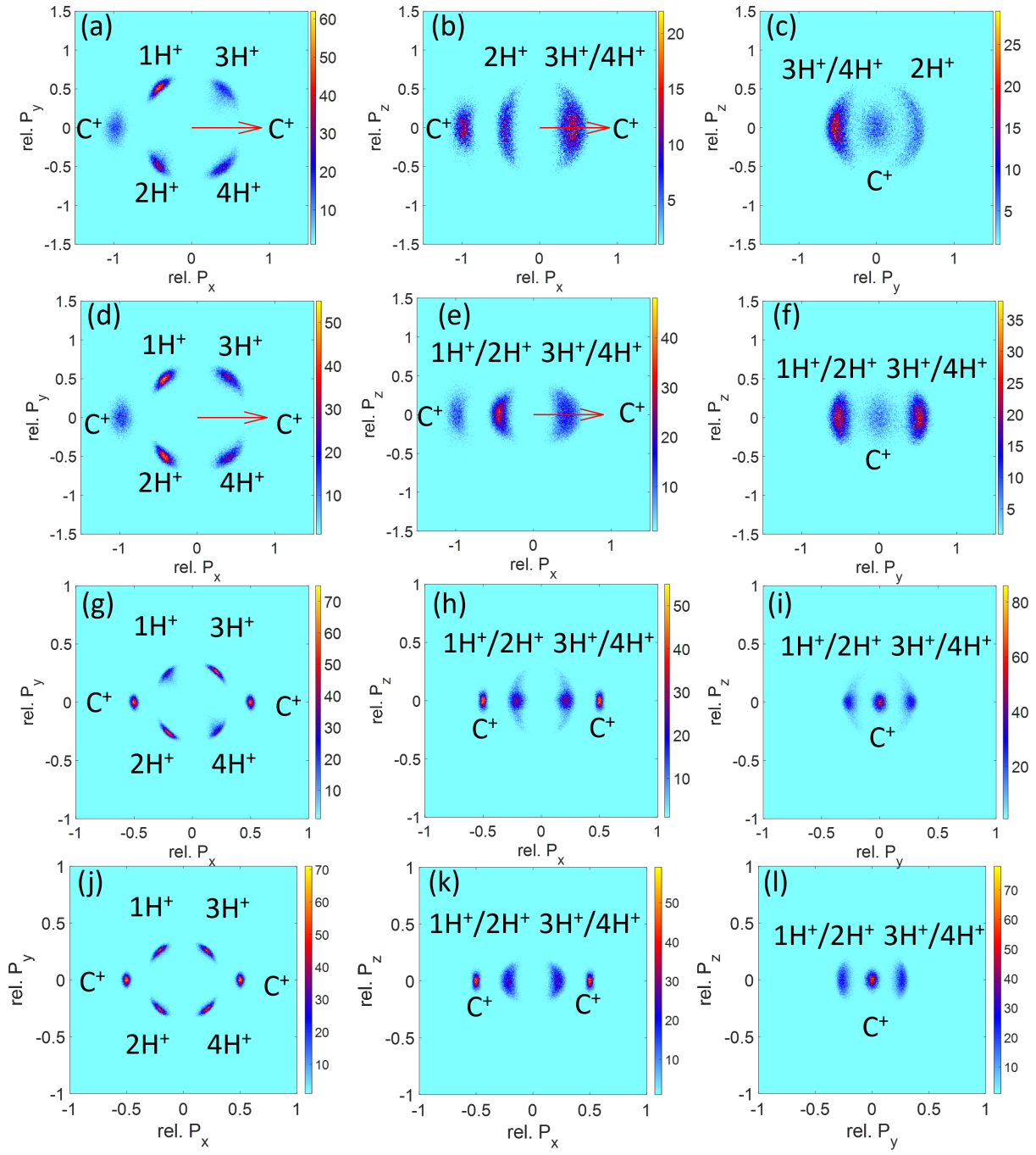

Figure 4.22: ***Newton diagrams of six-body complete fragmentation of ethylene from Coulomb explosion simulation.***

The relative Newton diagram in (x,y)-, (x,z)-, and (y,z)- momentum plane, where the (x,y)-plane are defined by (a-c) using $\vec{V}_5$ (one C^+) and $\vec{V}_1$ (one H^+) as reference vectors; (d-f) using $\vec{V}_5$ and $\vec{V}_4$ - $\vec{V}_1$ as reference vectors; (g-i) using $\vec{V}_5 - \vec{V}_6$ and $\vec{V}_4$ - $\vec{V}_1$ as reference vectors; (j-l) using $\vec{V}_5 - \vec{V}_6$ and $(\vec{V}_2 + \vec{V}_4)$ - $(\vec{V}_1 + \vec{V}_3)$ as reference vectors. Vectors definitions are shown in Fig. 4.21(a)

We still have several options to construct a second vector to be used for the (x, y)-plane definition, combining pairwise vector sum or differences of the proton momenta. Fig. 4.22(d-f) shows the projections of the 3D momentum distributions under a reference frame where $\vec{V}_4$ - $\vec{V}_1$ is used together with $\vec{V}_5 - \vec{V}_6$ to define (x, y)-plane. Finally, as sketched in Fig. 4.21(b), we can combine all four proton momentum vectors to define the (x, y)-plane. The corresponding Newton diagrams, where the x-axis is still aligned with the $\vec{V}_5 - \vec{V}_6$ difference vector and the (x, y)-plane is defined by the momenta of all four protons: $(\vec{V}_2 + \vec{V}_4)$ - $(\vec{V}_1 + \vec{V}_3)$, are shown in Fig. 4.22(g-i).

By constructing Newton diagrams in this manner, we can effectively display the full momentum distribution of all six ion fragments within a single map. Guided by these simulation results, we can compare with the experimental data. However, in a typical experiment, only a subset of the six generated ions is detected. Therefore, a comparison will strongly depend on what fragments are detected. If only one C^+ ion is detected, the experimental results can be compared using the conventional Newton diagram method, whereas a single C^+ ion momentum is needed to define the x-axis (as shown in the upper row of Fig. 4.22). However, if two C^+ ions are detected in coincidence, the generalized approach illustrated in the middle or bottom row of Fig. 4.22 can be applied, depending on how many protons are detected.

While the projections of the 3D momentum distributions onto (x, y)-, (x, z)-, and (y, z)-planes discussed above contain all 3D information obtained from the simulation or the experiment, visualizing the 3 structures or separating out-of-plane contributions in this representation can be challenging. To improve the visualization of the 3D distributions, we adopt an complementary approach that enables all proton momenta to be displayed within a single map. This method is particularly useful for molecular systems where protons (or other fragments) momentum vectors overlap significantly in the (x, y)-momentum plane of traditional Newton diagram but have significant out-of-plane components.

As illustrated in Fig. 4.23(a), the black vector represents an out-of-plane momentum

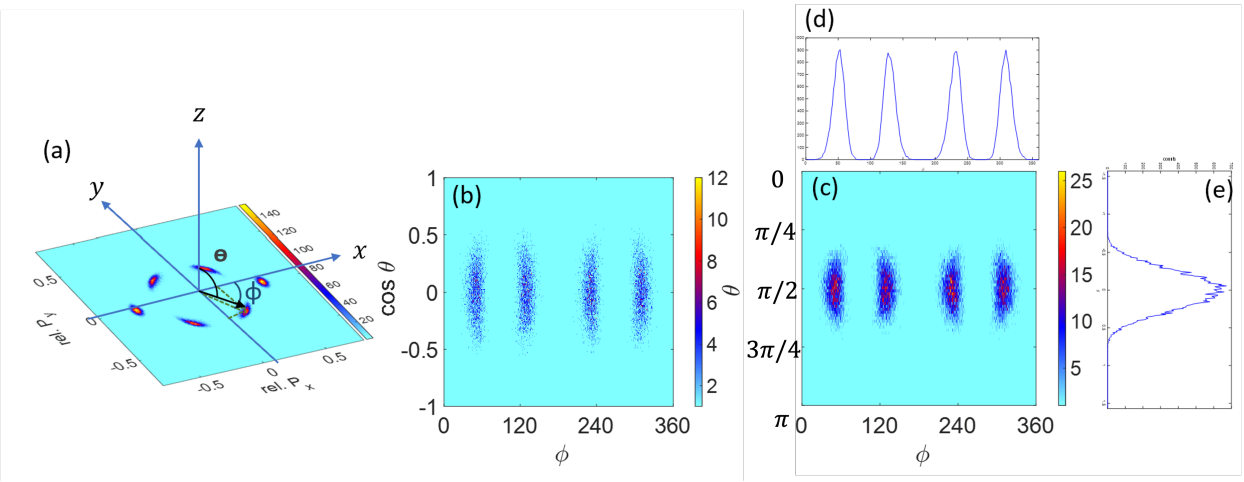

Figure 4.23: ***Correlated angular distributions obtained from the CES of six-body complete fragmentation of ethylene in spherical coordinate representation.***

(a) Schematic representation of the azimuthal angle ϕ and polar angle θ definitions relative to the molecular reference frame. The azimuthal angle ϕ is defined as the angle between the positive x-axis and the projection of the momentum vector onto the (x, y)-plane. The polar angle θ is defined as the angle between the momentum vector and the positive z-axis. (b) H^+ angular distribution plotted with the y-axis as $\cos\theta$; (c) H^+ angular distribution plotted with the y-axis as θ; (d) one-dimensional projection of the angular distribution onto ϕ; (e) one-dimensional projection of the angular distribution onto θ.

vector. The azimuthal angle ϕ is defined as the angle between the positive x-axis and the projection of the momentum vector onto the (x, y)-plane. The polar angle θ is defined as the angle between the positive z-axis and the momentum vector itself. This approach transforms the Cartesian coordinates representation of the momentum distribution into a spherical coordinate system. The resulting angular distributions in this spherical representation obtained from the same simulated 6-body data set as Newton diagrams above are shown in Fig. 4.23(b) and (c). Typically, there are two common approaches to presenting the data: plotting the y-axis as the polar angle θ, as shown in Fig. 4.23(c), or plotting the cosine of the polar angle $\cos\theta$ on the y-axis, as shown in Fig. 4.23(b). In addition, to enable a more quantitative comparison, we projected the two-dimensional spherical momentum distribution from Fig. 4.23(c) onto the x- and y-axes, thus extracting the one-dimensional θ (as shown in Fig. 4.23(e)) and ϕ (as shown in Fig. 4.23(d)) distributions.

4.3.2 Characterizing ethylene fragmentation into six atomic ions with incomplete coincident measurements

Building upon the detailed insights provided by the six-body Coulomb explosion simulations, we now proceed to analyze the experimental data obtained from the corresponding measurements. This comparison between simulation and experiment enables a deeper understanding of the fragmentation dynamics of the ethylene molecule and allows us to assess the reliability and limitations of the simulation model. However, because of the limited detection efficiency of the detection system used, it is challenging to detect all six created ions in coincidence in a single fragmentation events. Furthermore, limitations in energy acceptance of the particles emitted perpendicular to the spectrometer axis discussed in Section 4.2 make it challenging to detect all four H^+ fragments in coincidence. In practice, the collected data often miss one or more H^+ and/or one C^+ fragment. As a result, complete six-body fragmentation events are rarely detected. In this work, the attempt to collect all six particles was unsuccessful: the resulting 6-fold coincidence spectrum contained only a few

events and did not manifest any clear feature reflecting momentum conservation between the detected particles, indicating dominance by false coincidences. Therefore, to characterize the complete breakup of ethylene, we focused on the events in which only a subset (3,4, or 5) atomic ions were detected in coincidence. As before, to restrict the amount of possibilities considered, the analysis is restricted to the events with singly charged carbon ions.

We firstly consider the events in which only one C^+ ion has been detected. The corresponding Newton diagrams for this set of channels are shown in Fig. 4.24. There, the first row (panels a-c) displays the results for triple-coincidence events where two protons have been detected together with a carbon ion. The middle row (panels d-f) shows the results for three protons ($H^+ + H^+ + H^+ + C^+$ ions detected in coincidence), whereas the bottom row (panels g-i) corresponds to the events where one carbon ion and all four protons have been detected. In all panels, the C^+ momentum vector defines the positive $x-$direction, and its magnitude is used for normalization, In panels (a-f), the difference between the momentum vectors of the first and the last detected proton is used to determine the (x, y)-plane together with the C^+. In panels (g-i), where all four protons are detected, all four of their momentum vectors are combined to define the (x, y)-plane as explained in Fig. 4.21(b) and the corresponding discussion.

Each graph in the (x, y)-plane (left column) shows four distinct spots for detected protons. Note that even if not all protons are detected (as in the first two rows), in a single fragmentation event one proton can correspond to either of the 1-4 positions labeled in Fig.4.21(a), such that the figures accumulating all the events exhibit four corresponding spots. Although not all six fragments are detected for the data shown in Fig. 4.24, the presence of three or more individual atomic ions suggests that in most of the events the molecule was fully fragmented and, thus, the detected ions likely originate from the complete breakup of the molecules simulated in the previous section. The main uncertainty here is the charge state of the undetected carbon fragment. While it is unlikely to remain neutral

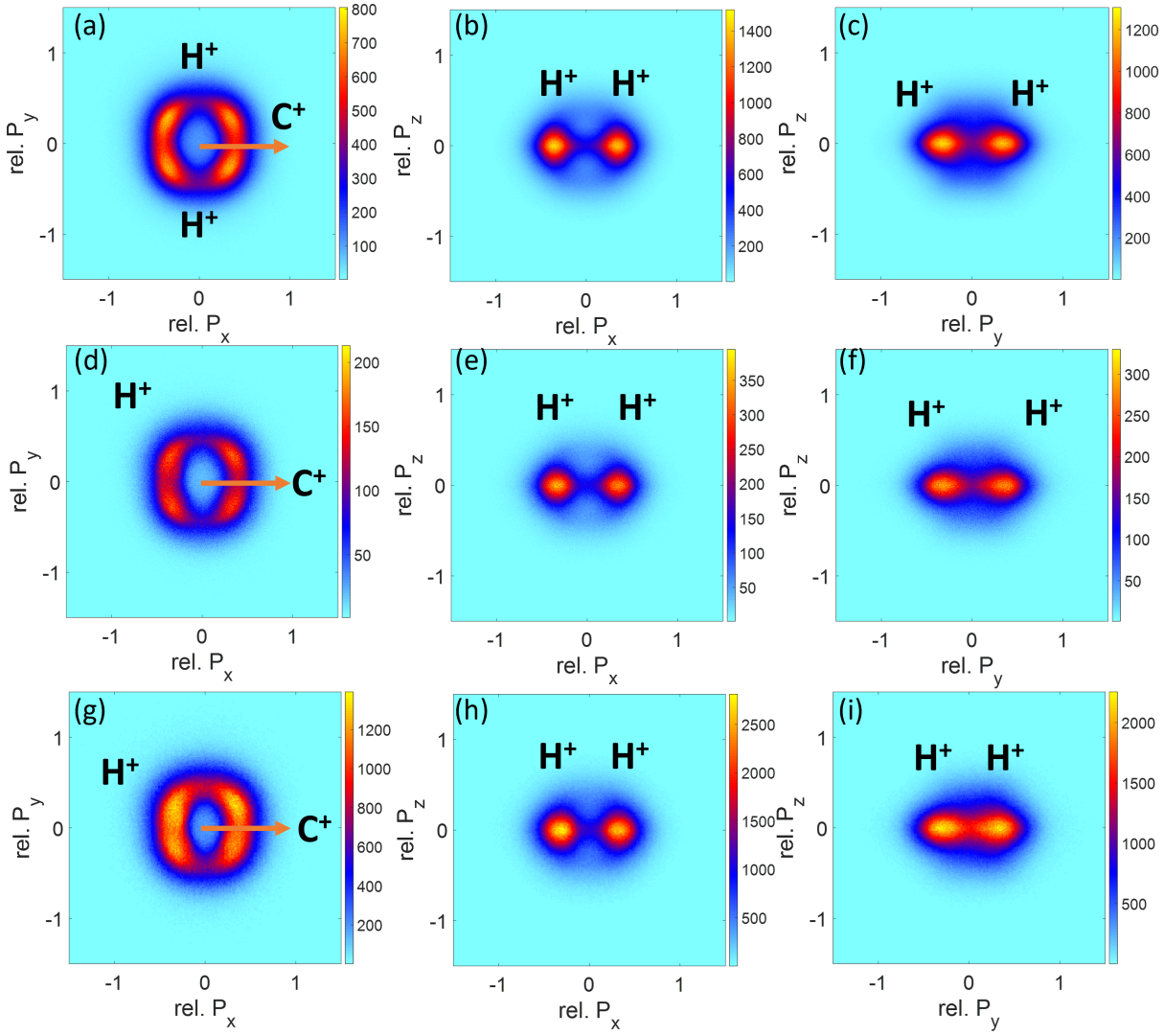

Figure 4.24: ***Experimental data represented using Newton diagrams for three, four- and five-body 'incomplete' channels with one*** C^+ ***ion detected of ethylene.*** *(a–c) Newton diagrams showing the* (x, y)*-,* (x, z)*-, and* (y, z)*-plane momentum distributions for the three-body incomplete* $H^+ + H^+ + C^+$ *channel; (d–f) Same as (a-c) but for the four-body incomplete* $H^+ + H^+ + H^+ + C^+$ *fragmentation channel; (g–i) but for the five-body incomplete* $H^+ + H^+ + H^+ + H^+ + C^+$ *channel. While in (a-f), the difference between the momentum vectors of the first and the last detected proton is used to determine the* (x, y)*-plane together with the* C^+*, in (g-i), the momentum vectors of all four detected protons are combined to define the* (x, y)*-plane (see Fig. 4.21(b)).*

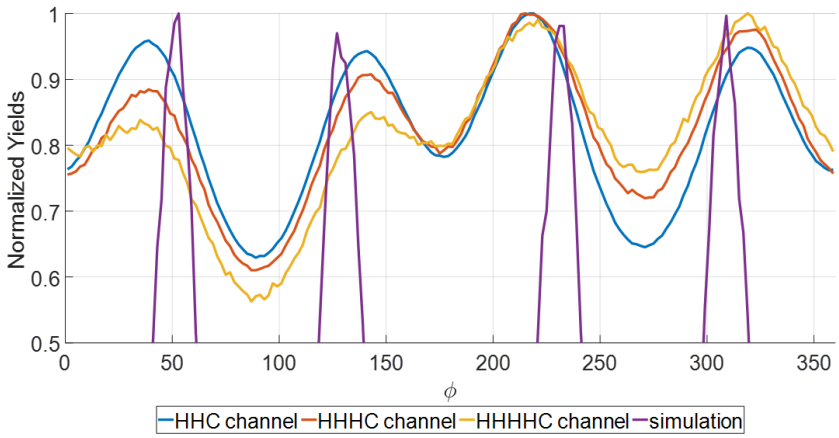

Figure 4.25: ***Normalized angular distribution (ϕ) of H^+ momentum from different incomplete fragmentation channels of ethylene. (1 C^+ detected)***
Blue: three-body channel with H^+, H^+, and C^+ detected; red: four-body channel with H^+, H^+, H^+, and C^+ detected; yellow: five-body channel with H^+, H^+, H^+, H^+, and C^+ detected; purple: Coulomb explosion simulation. The molecular plane is defined using momentum vector of C^+ as the x-axis and the difference of momentum vectors of two H^+. The ϕ angle is defined as shown in Fig. 4.23(a)

with the bare carbon ion and two or more protons created next to it, Fig. 3.14 suggests that doubly-charged C^{2+} ions are produced rather efficiently. Another uncertainty for three- or four-body 'incomplete' channels arises from the possibility of undetected hydrogen(s) remaining neutrals. This is not the case for the bottom row of Fig. 4.24, where all four photons are detected. However, since for the incomplete channels we cannot eliminate false coincidence events by verifying momentum conservation, the increased number of detected protons makes it more likely that at least one of them originates from the background gas fragmentation (water, H_2, or some hydrocarbon contamination).

Despite all limitations mentioned above, the data presented in Fig. 4.24 for protons qualitatively resemble the pattern expected from the CES for the complete six-body breakup plotted in Fig. 4.22. While the patterns for incomplete three-body (top row of Fig. 4.24) and four-body (middle row) breakup visually appear to be very similar to each other, the distribution for the five-body coincidence events (bottom row) looks somewhat smeared

out and manifest light asymmetry. This is most likely due to the increased fraction of background protons and false coincidence events. To better quantify the relation between the three incomplete channels, in Fig. 4.25, we plot the 1D distributions of the azimuthal angle of protons shown in Fig. 4.24 for three- (blue), four- (red), and five-fold (yellow) coincidences. The definition of the azimuthal angle is given in Fig. 4.23(a). Purple curve reflects the corresponding angular distribution obtained from the simulation. Each curve exhibits four clear maxima corresponding to the four protons in the molecule located at different positions with respect to the C−C axis. The peak-to-valley contrast of the three experimental curves varies substantially, reflecting the level of background contributions or false coincidences. Interestingly, this contrast becomes worse with the increasing numbers of the detected protons. One of the reasons why the incomplete channel with only two protons detected shows the best contrast is a limited energy acceptance of our detection systems for the ions emitted perpendicular to the spectrometer axis discussed in Section 4.2. For two protons, they can be emitted nearly back-to-back (as in 'trans-fragmentation' discussed in Section 4.2). In contrast, for three or four protons, at least two of them are emitted from the same side of the C−C axis (as in 'cis-fragmentation' discussed in Section 4.2), such that their momenta are nearly perpendicular to each other. Since, in general, the protons detected in this experiment in the laboratory frame tend to be emitted along the laser polarization direction (see Fig. A.30 in Appendix A.2), which coincides with the spectrometer axis, the one emitted in the perpendicular direction might be lost if its energy is high enough. This worsens the signal-to-noise ratio for channels where three or four protons are detected.

Next, we consider three-, four-, and five-fold coincidence events in which two C^+ ions have been detected. For the three-fold coincidence channel, we consider two versions of a Newton diagram as shown in Fig. 4.26. Panel (a) shows a standard Newton diagram, where one C^+ momentum vector defines the positive x-axis and, together with the momentum vector of a single detected proton, are used to define the (x, y)-molecular plane. Since only one H^+ ion is detected in each event, and its momentum vector is chosen to point into

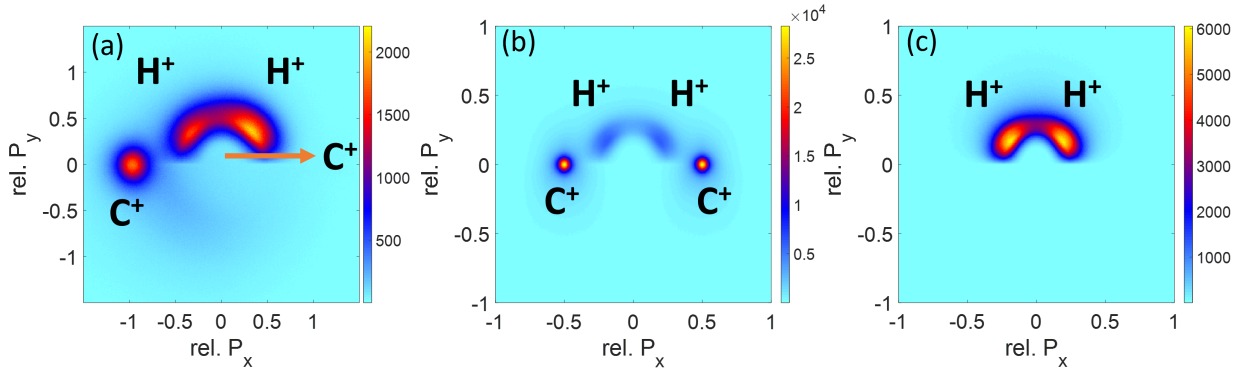

Figure 4.26: ***Newton diagrams for three-body*** $H^+ + C^+ + C^+$ ***channel of ethylene.*** *(a) The momentum vector of the first* C^+ *ion (orange arrow) defines the* x*-axis, and the momentum vector of the only* H^+ *fragment, together with the reference* C^+*, define the* (x, y)*-plane. (b) The difference between of the two (randomized)* C^+ *momentum vectors defines the* x*-axis, enabling both* C^+ *fragments to be presented in a single map. (c) same as (b) but with only the momentum of the* H^+ *fragment shown*

the upper half of the (x, y)-plane, it consistently appears in the upper half of the Newton diagram. Since its z-momentum component is strictly 0, no (x, z)- or (y, z)-projections are shown. Panel (b) displays a modified version of a Newton diagram, where the x-axis is defined by the vector momentum difference of the two carbon ions. Since both of them are identical, the order of both carbons is randomized before constructing their momentum difference. This difference vector together with the momentum vector of the only detected proton are used to define the (x, y)-plane. Panel (c) displays the same Newton map but only showing the proton momentum distribution. These Newton maps match well the prediction of the corresponding CES shown in Fig. 4.22. Thus, despite the limited number of fragments detected, the data presented here still carry information on molecular geometry of ethylene.

Fig. 4.27 displays the experimental Newton diagrams constructed from the four-body (a-c) and five-body (d-f) coincidence data with two C^+ ions detected. For both channels, the positive x-axis is defined by the vector difference between the two randomized C^+ momenta, and the vector difference between the two H^+ momenta was used to define (x, y)-plane. The results for (x, y)-plane are qualitatively similar to the three-body data presented in Fig. 4.26(b,c), with the main difference that in Fig. 4.27, the detection of at least two

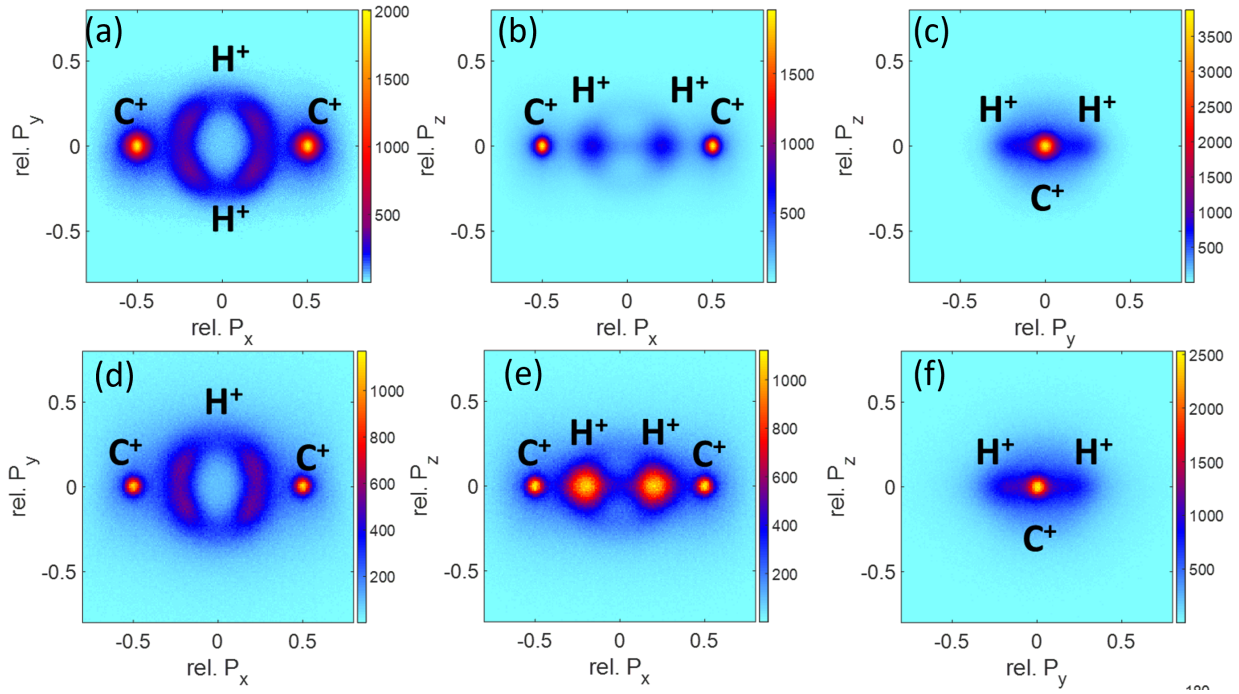

Figure 4.27: ***Newton diagrams for four- and five-body incomplete channels of ethylene with two*** C^+ ***detected.***
(a)–(c) Newton diagrams showing the (x, y)*-,* (x, z)*-, and* (y, z)*-plane momentum distributions for the* $H^+ + H^+ + C^+ + C^+$ *fragmentation channel. (d)–(f) Newton diagrams of the corresponding momentum distributions in the* (x, y)*-,* (x, z)*-, and* (y, z)*-planes for the* $H^+ + H^+ + H^+ + C^+ + C^+$ *fragmentation channel.*

protons allows for (i) visualizing all four hydrogen positions in the molecule since the protons are not restricted to the upper half of (x, y)-plane anymore and (ii) plotting the momentum distribution along z-axis since the z-component of the proton momentum is no longer set to zero.

To quantify the relation between the incomplete channels involving the detection of two carbon ions, in Fig. 4.28 we plot the 1D distributions of the azimuthal angle of protons shown in Fig. 4.26 (three-body, blue line) and Fig. 4.27 (four-body in red line and five-body in yellow line). The definition of the azimuthal angle is given in Fig. 4.23(a). Purple curve reflects the corresponding angular distribution obtained from the simulation in Fig. 4.23. Since the proton data for three-body coincidence in Fig. 4.26 are restricted to the upper half of the (x, y)-plane, the corresponding angular distribution is empty for the angles between

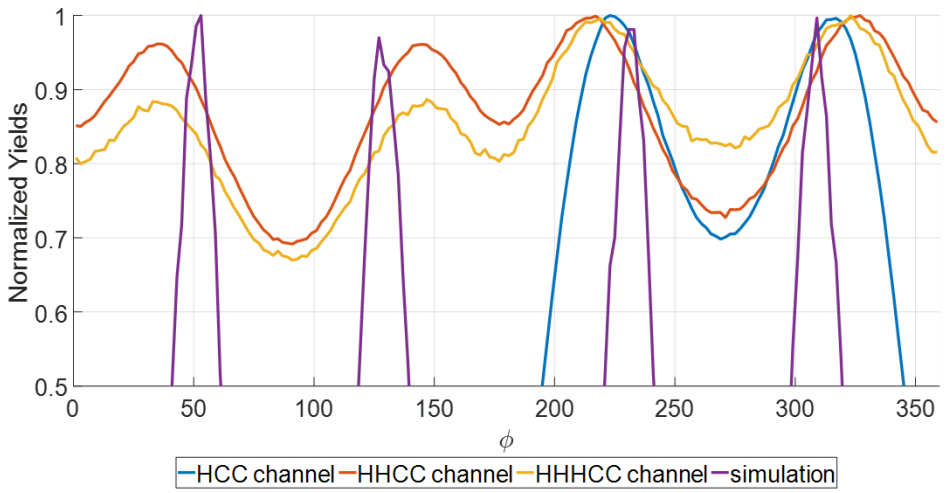

Figure 4.28: ***Normalized angular distribution (ϕ) of H^+ momentum from different incomplete fragmentation channels of ethylene. (2 C^+ detected)***
Blue: three-body channel with H^+, C^+, and C^+ detected; red: four-body channel with H^+, H^+, C^+, and C^+ detected; yellow: five-body channel with H^+, H^+, H^+, C^+, and C^+ detected; purple: Coulomb explosion simulation. The molecular plane is defined using the difference of momentum vectors of 2 randomized C^+ as the x-axis and the the difference of momentum vectors of two H^+. The ϕ angle is defined using Fig. 4.23(a)

0 and 180°. The angular distributions are normalized to their respective maxima. While the distributions for $H^+ + C^+ + C^+$ and $H^+ + H^+ + C^+ + C^+$ channels exhibit comparable peak-to-valley contrast, it becomes somewhat worse for the five-body channel with three protons detected. Likely reasons for this reflect difficulties in detecting three protons in coincidence discussed above in relation to $H^+ + H^+ + H^+ + C^+$ and $H^+ + H^+ + H^+ + H^+ + C^+$ channels.

The results presented in this section show that the incomplete coincidence channels can be efficiently used for ethylene geometry characterization. The best signal-to-noise ratio is achieved for channels where no more than one proton has been detected. Among these, the channel with two protons and both carbon ions detected provides the most complete information on molecular geometry. The channels with three or four protons, which potentially carry even more information, contain larger fractions of background or false coincidence

contamination.

4.3.3 Identifying individual hydrogens in the simulated six-body breakup data

Even though the detection of all six fragments from complete fragmentation of ethylene was not achieved in this work, it is expected to be feasible in the near future. The feasibility of coincidence detection of six or even more fragments in a similar Coulomb explosion imaging experiment on other systems has been recently demonstrated[140]. Therefore, in this section, we present a framework for handling and analyzing such six-body fragmentation data developed using the results on the Coulomb explosion simulations presented in the beginning of this section.

As the initial step, we examine the 'raw' (without being represented using Newton diagrams in the molecular frame) momentum distributions of the ion fragments following Coulomb explosion, as illustrated in Fig. 4.29(a). While here, the contributions from each atom (e.g., as labeled in Fig. 4.21(a)), in real experimental conditions, there is ambiguity in identifying which detected H^+ ion correspond to specific hydrogen atoms in the ethylene molecule. Furthermore, uncertainties arise in determining the correct relation between a specific proton and detected C^+.

To simulate these experimental uncertainties, we first introduce randomization in the ordering of the simulated C^+ momentum vectors. Specifically, while the original P_x, P_y, and P_z components of each ion fragment are preserved, their association with a specific ion hit (e.g., first hit or second hit) is randomized within each event. This is implemented using MATLAB's built-in `randperm`[141] function: for each row (corresponding to a single event), the order of columns representing the momentum vectors is shuffled, but the P_x, P_y, and P_z components for each ion fragment remain grouped together. Their assignment to specific atoms within each ion type is randomized. For example, columns 1 to 3 (across all rows, also referred as the 'first hit' when used for experimental data analysis), which originally

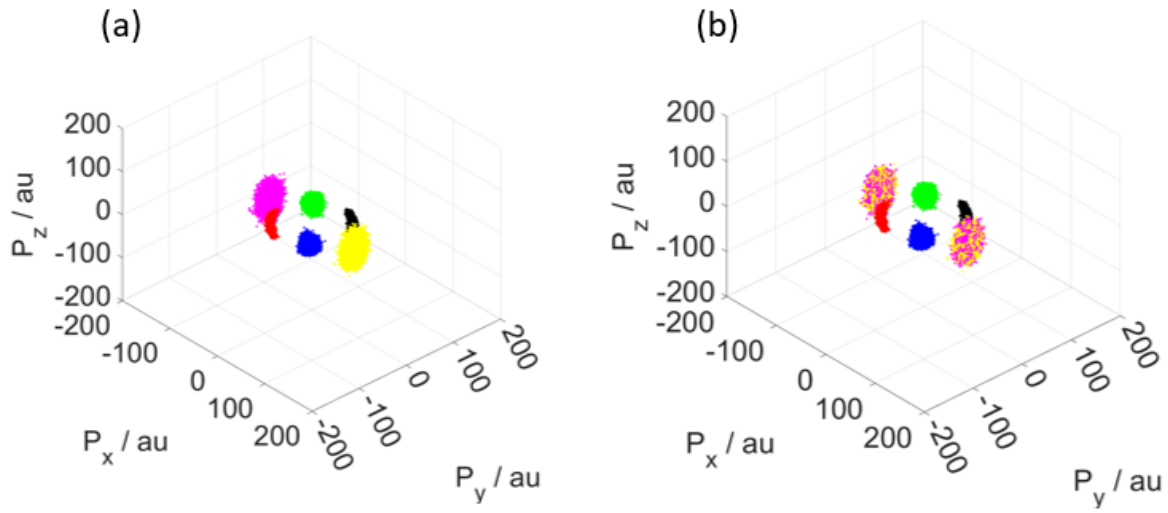

Figure 4.29: ***Three-dimensional momentum distributions of ion fragments from six-body Coulomb explosion of ethylene.***
(a) Raw momentum data from complete six-body fragmentation. (b) Momentum distribution after randomizing the order of the two C^+ ion momentum vectors. Here, 'raw' refers to data that are not represented using Newton diagrams in the molecular frame.

contain the momentum components for one H^+ ion associated with a particular hydrogen atom, may, after randomization, represent the momentum of any hydrogen atom from that molecule. Importantly, since carbon and hydrogen ions can be distinguished in the actual experiment, this randomization is performed only within each ion type and not between them. The resulting distribution is illustrated in Fig. 4.29(b) after randomizing the 'hit order' of C^+.

In the same framework, we also randomize the hit order of the proton momentum vectors from the initial order of raw momentum distribution where each hit of H^+ corresponds to a particular H from the initial geometry, i.e. all first hit of H^+ is corresponding to position 1 shown in Fig. 4.21(a) , as illustrated in Fig. 4.31(a). To better understand the effects of this randomization, we separately plot the momentum distributions associated with each H^+ hit order (first hit, second hit ...), as shown in Fig. 4.31(b–e). After randomization, every H^+ hit in Fig. 4.31(b–e) will include the H^+ from all four positions of H^+ as shown in Fig. 4.21

from initial geometry. However within each geometry, there are still four correlated H^+ momentum from the same molecule using the randomization method mentioned above.

As observed in these plots, each assigned hit of the H^+ ions contains contributions from all four possible hydrogen atoms in the ethylene molecule. However, it is important to note that the randomization is applied only to the internal ordering of hits within each fragmentation events; the information of momentum correlations between the fragments is preserved and can be restored. This procedure mirrors the approach used for handling real experimental data, where fragment identity is uncertain, but the underlying correlation among fragments determine many few-particle observables.

After the randomization, we are confident that this randomized momentum dataset reproduces the same conditions as the real experimental data obtained from complete six-body fragmentation events. The next challenge is to develop a method for 'restoring' the internal correlations between the ion momenta distributions that were obscured by the randomization. Specifically, our goal is to reconstruct a representation of the momentum distribution that reflects the intrinsic structure, similar to the Newton diagram shown in Fig. 4.22.

To achieve this, we seek a strategy to rearrange the H^+ ion hit order in a way that enables recovery of the underlying momentum correlations and allows meaningful visualization of the six-body complete fragmentation. Some efforts in similar direction have been undertaken in[54,142]. First, we revisit Fig. 4.21, where we choose to use the momentum vector difference $\vec{V}_5 - \vec{V}_6$ as the reference axis for rearranging the H^+ ion hit order. Based on the configuration shown in Fig. 4.21, we observe that the angles between $\vec{V}_1$ or $\vec{V}_2$ and $\vec{V}_5 - \vec{V}_6$ are greater than 90°, resulting in negative $\cos\theta$ values. In contrast, the angles between $\vec{V}_3$ or $\vec{V}_4$ and $\vec{V}_5 - \vec{V}_6$ are smaller than 90°, yielding positive $\cos\theta$ values. Using this $\cos\theta$ relative to the C–C bond momentum vector criterion, we can initially classify and reorder the hits into two groups: $\vec{V}_1$, $\vec{V}_2$ as one group and $\vec{V}_3$, $\vec{V}_4$ as the other. However, the precise ordering within each group, specifically, between the first and second hit, and between the third and fourth

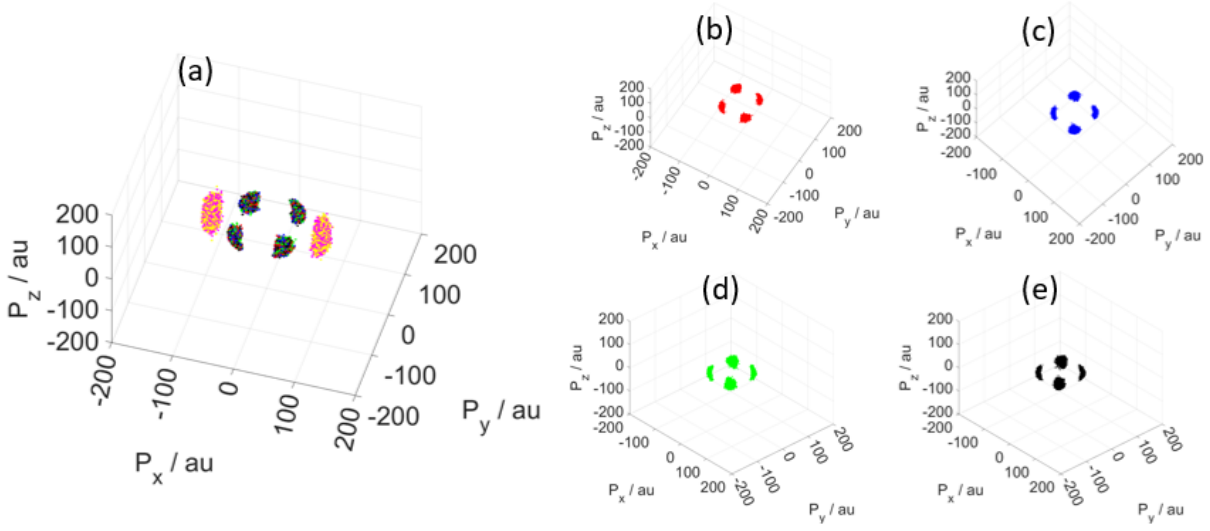

Figure 4.30: ***Three-dimensional momentum distributions of ion fragments from six-body CES of ethylene after randomization.***
(a) Momentum distribution after randomizing the hit order of both the two C^+ *ion momentum vectors and the four* H^+ *ion momentum vectors. (b)–(e) Momentum distributions of the first, second, third, and fourth detected* H^+ *ions*

hit, remains ambiguous at this stage and requires further analysis.

To restore the ion hit order, we proceed by fixing the first hit from last rearrangement step as the first, even though it might be the original second hit before randomization; this minor ambiguity, which reflects the fact that protons 1 and 2 (as well as 3 and 4) in Fig. 4.21(a) are identical with respect to the C−C axis, does not affect the final reconstruction. Once we fix the assignment of the 'first proton', the assignment of all other protons becomes unambiguous. After confirming the first hit, we further refine the sequence by analyzing the angle relationships between the first hit and the subsequent third and fourth hits. From Fig. 4.21, we observe that the relative angle between $\vec{V}_1$ and $\vec{V}_3$ is smaller than that between $\vec{V}_1$ and $\vec{V}_4$. By comparing the $\cos\theta_{13}$ and $\cos\theta_{14}$ values, the hit with the smaller relative angle (larger $\cos\theta$) is assigned as the third hit, while the other is assigned as the fourth hit.

Finally, after this rearrangement procedure, we re-plot the raw momentum distribution of the ion fragments in three dimensions, as shown in Fig. 4.31(a). In this raw distribution,

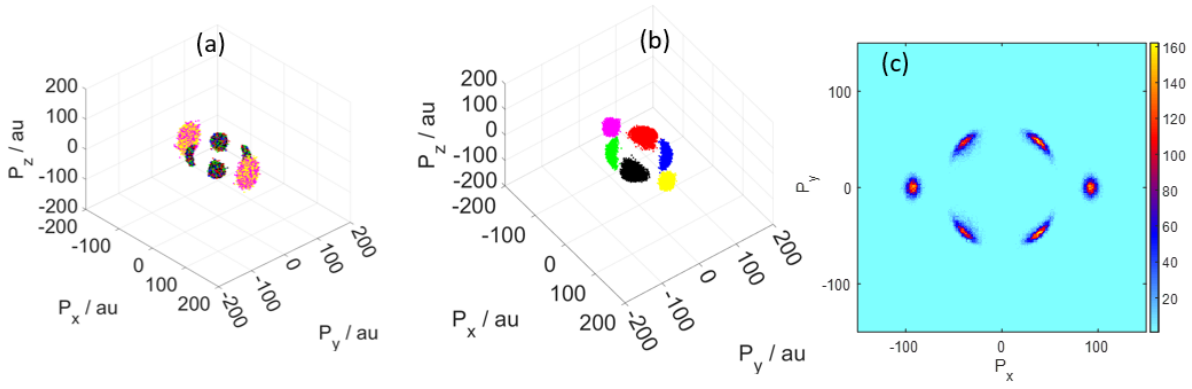

Figure 4.31: ***Three-dimensional momentum distributions of ion fragments from six-body CES of ethylene after order rearrangement.***
(a) Final raw momentum distribution after H^+ *hit order rearrangement. (b) Reconstructed 3D momentum distribution after defining the momentum plane using* $\vec{V}_5 - \vec{V}_6$ *as the* x*-axis and* $(\vec{V}_2 + \vec{V}_4) - (\vec{V}_1 + \vec{V}_3)$ *to define the* (x, y)*-plane. (c) Corresponding Newton diagram projected onto the* (x, y)*-plane using the same plane definition as in (b), illustrating the recovered correlation between ion fragments.*

a degree of randomization remains visible, primarily due to the unresolved randomization of the carbon ion hits.

However, by redefining the momentum plane using $\vec{V}_5 - \vec{V}_6$ as the x-axis and the vector difference $(\vec{V}_2 + \vec{V}_4) - (\vec{V}_1 + \vec{V}_3)$ to define the (x, y)-momentum plane, we can reproduce the momentum distribution in a well-defined coordinate system, as shown in Fig. 4.31(b). With this coordinate system, the intrinsic correlations between ion fragments originating from the same ethylene molecule are recovered, revealing a much clearer internal structure and emission pattern. This representation also provides a highly illustrative visualization of the ethylene molecular geometry. Additionally, the corresponding Newton diagram constructed from this rearranged dataset is shown in Fig. 4.31(c), further illustrating the recovered momentum correlations.

This analysis approach has been developed for static Coulomb explosion imaging, where the molecular geometry remains unchanged during the interaction. Under these conditions, this method provides an effective solution to the ion hit order ambiguity that arises in real experiments, especially in cases where multiple identical ions (e.g., several protons) are

detected within a single laser shot. In contrast, pump–probe experiments involve a pump pulse that can initiate photoinduced molecular dynamics, leading to structural changes within the molecule during the delay time. Correspondingly, the specifics of the event sorting routine presented here will need to be adapted to a particular pump–probe configuration.

4.4 Conclusion

In conclusion, we conducted a detailed systematic study of the few-particle dynamics unfolding after multiple ionization of the ethylene (C_2H_4) molecule by intense femtosecond laser pulses. The main goal of this work was to characterize the dynamics relevant to Coulomb explosion imaging of the molecule. We considered 'complete' three- and four-fold fragmentation of triply and quadruply charged ethylene molecule, where all created ionic fragments have been detected, and studied the events resulting from the full 'atomization' (i.e., six-body breakup) of the molecule by analyzing 'incomplete' subsets of three, four, or five ions detected in coincidence.

For three-body breakup, we identified and disentangled three different fragmentation pathways, two of which turned out to be of the sequential nature and, thus, not suitable for CEI. Here, for two out of three major channels a quantitative agreement between theory was achieved due to the availability of realistic PES for the ground state of the triply ionized molecule. For four-body fragmentation, we identified and disentangled the contributions from two different breakup scenarios, trans- and cis- (detaching two hydrogens from the opposite or the same side of the C–C bond, respectively). Finally, for complete six-body fragmentation of the molecule we demonstrated that detecting the subset of the produced ions is sufficient to obtain information about the molecular geometry. However, since for incomplete channels, momentum conservation cannot be applied to discriminate against background contributions or false coincidences, increasing the number of detected ions does not necessarily improve the imaging quality. Thus, detecting all created ions in coincidence

remains an important goal. As a step towards such experiments, we developed a method for analyzing six-fold complete fragmentation data, restoring the identification of each atom from randomized momentum distributions.

Although classical Coulomb explosion simulations employed in this work tend to overestimate the ion momentum magnitudes and kinetic energies, the normalized momentum correlations, visualized through Newton plots, show strong consistency with the experimental results. This demonstrates the robustness and effectiveness of momentum correlation analysis in CEI across three-, four-, and five-body fragmentation channels. The quantitative agreement can be significantly improved if final-state PESs are available. Overall, this work lays important groundwork for extending CEI techniques to time-resolved studies of ultrafast molecular dynamics in ethylene and other complex polyatomic systems.

Chapter 5

UV-induced Coulomb explosion imaging of ring conversion dynamics in 2(5H)-thiophenone

All Coulomb explosion simulations presented in this chapter were conducted by the author. The ground-state geometries for these simulations were generated by Dr. Surjendu Bhattacharyya (now at SLAC National Accelerator Laboratory) using the Newton-X software, while the excited-state geometries were calculated by Dr. Lea M. Ibele (University of Bristol), and organized by Dr. João P. F. Nunes (University of Nebraska-Lincoln). The experiment at the European XFEL was conducted by a large international collaboration (see the list of authors of Ref.[143]) led by Prof. Daniel Rolles (Kansas State University) and Dr. Rebecca Boll (European XFEL). Data analysis for that experiment was carried out by the author and by Dr. Alice Green (now at University of Edinburgh). Table-top experiments at JRML and the corresponding data analysis were performed by the author.

As discussed in Section 2.2, 2(5H)-thiophenone (hereafter referred to as thiophenone), as

a model heterocyclic molecule, has recently been investigated by the researchers at JRML using various experimental techniques. This includes time-resolved photoelectron spectroscopy (TRPES)[8], which provides time-dependent signals from excited-state populations and the formation of photoproducts and the depletion of the ground-state signal. While TRPES offers valuable insights into electronic state dynamics on ultrafast timescales, it provides only limited direct structural information.

To complement this, a large JRML-led collaboration employed ultrafast electron diffraction (UED)[11] to probe the structural dynamics of thiophenone. UED can yield detailed geometric information on photoinduced products in both excited and ground electronic states. However, the temporal resolution of UED is limited.

In this work, we explore the use of Coulomb explosion imaging (CEI) as an alternative approach for investigating ultrafast structural changes in thiophenone, aiming to capture both the spatial and temporal aspects of molecular fragmentation dynamics.

In the first part of this study, we investigated thiophenone using the Cold Target Recoil Ion Momentum Spectroscopy (COLTRIMS) reaction microscope[16,17], operated at the Small Quantum Systems (SQS) instrument of the European XFEL[144]. This experiment provided high-quality static data for three-dimensional proton momentum imaging.

In the second part, we conducted measurements using the PULSAR-COLTRIMS system at the JRML, which enabled the acquisition of time-resolved data on UV-induced ring-opening in thiophenone.

5.1 X-ray induced Coulomb explosion imaging of 2(5H)-thiophenone

This section is based on a submitted manuscript by Green, Chen, et al.[143], in which the two first authors (including the author of this thesis) have contributed equally to the work. At the time of writing this thesis, this manuscript is under review.

5.1.1 Experimental conditions

The experiment at the European XFEL was performed with SASE XFEL pulses at a central photon energy of 2.6 keV, 1.2-1.5 mJ of pulse energy on target, and an estimated pulse of 6 fs (assuming a linear chirp of the X-ray pulse). The XFEL operated at an effective repetition rate of 840 Hz, comprised of pulse trains arriving at 10 Hz, each containing 84 microbunches. The X-ray beam was focused on target to a spot of smaller 5μm diameter (FWHM) by a pair of bendable Kirkpatrick-Baez mirrors.

Vapor of thiophenone was generated by heating an out-of-vacuum reservoir to 50–60°C. A supersonic gas jet was formed using 200 mbar of helium as carrier gas, expanding the mixture into vacuum through a nozzle of 200 μm diameter, and collimating it by three skimmers and a set of adjustable slits. The gas line, nozzle, and the first section of the jet vacuum chamber were also heated to 60℃ to prevent condensation. The base pressure in the interaction chamber was maintained at 1×10^{-11} mbar during operation. Achieving such a low background pressure was key to enabling the identification of coincidences involving H^+ ions with little contamination from false coincidences originating from ionization of background molecules.

With the XFEL pulse parameters used in this experiment, not only single- but also multiple-X-ray photoabsorption can occur. At a photon energy of 2.6 keV, photoabsorption is dominated by sulfur 1s electrons, for which the ionization cross section is 11 times higher than that for oxygen and 36 times higher than that for carbon atoms. The absorption of a single photon at sulfur K-edge results, on average, in the ejection of 4 or 5 electrons because of Auger-Meitner decay cascades[145]. Therefore, even a single-photon absorption could be suitable for generating Coulomb explosion patterns, whereas two or more absorbed photons produce highly-charged states optimal for efficient CEI.

A schematic overview of the experiment and the approach used for defining the Newton diagrams presented in this section is shown in Fig. 5.1(a). This concept is extended to investigate whether the measurement of H^+ ion momenta can be used to extract three-

dimensional structural information for broader classes of organic molecules. Specifically, we report the results of an X-ray-induced Coulomb explosion imaging (CEI) study of gas-phase thiophenone. The molecular structure is shown in Fig. 5.1(b).

The present experimental CEI data for ground-state thiophenone molecules are also compared with predictions obtained from classical Coulomb explosion simulations for two cases: (i) ground-state thiophenone and (ii) various vibrationally excited photoproducts, including ring-opened isomers and internally 'hot' thiophenone (i.e., ground and excited states of thiophenone with a ring-closed molecular structure) molecules formed via internal conversion following UV photoexcitation. These photoproduct geometries were provided by complementary *ab initio* molecular dynamics (AIMD) simulations.

5.1.2 Experimental results compared with Coulomb explosion simulation of ground-state 2(5H)-thiophenone

In thiophenone, all heavy atoms (carbon, oxygen, and sulfur) lie in a common plane, whereas the hydrogen atom positions span three dimensions, with two lying within and two outside the heavy-atom plane. Remarkably, all four hydrogen atoms can be clearly distinguished in the recorded coincident three-dimensional ion momentum distributions, as illustrated in the lower panel of Fig. 5.1(b). On a shot-by-shot basis, we align the momenta of ion fragments detected in coincidence to a common molecular frame, as defined by the colored arrows in the schematic in Fig. 5.1(b). This alignment enables the construction of molecular-frame Coulomb explosion image from a large dataset.

The molecular frame is chosen such that the S^+ ion momentum defines the positive x-axis, and the O^+ ion momentum lies in the (x, y)-plane, subject to the condition $p_y > 0$. A third ion, typically H^+ or C^+, is then plotted within this frame. To facilitate comparison across events, each momentum vector is normalized by the magnitude of the S^+ ion momentum. As a result, all S^+ ions have coordinates $(1, 0, 0)$, all O^+ ions lie within the (x, y)-plane with $p_y > 0$, and all H^+ and C^+ ions are plotted relative to this transformed coordinate system.

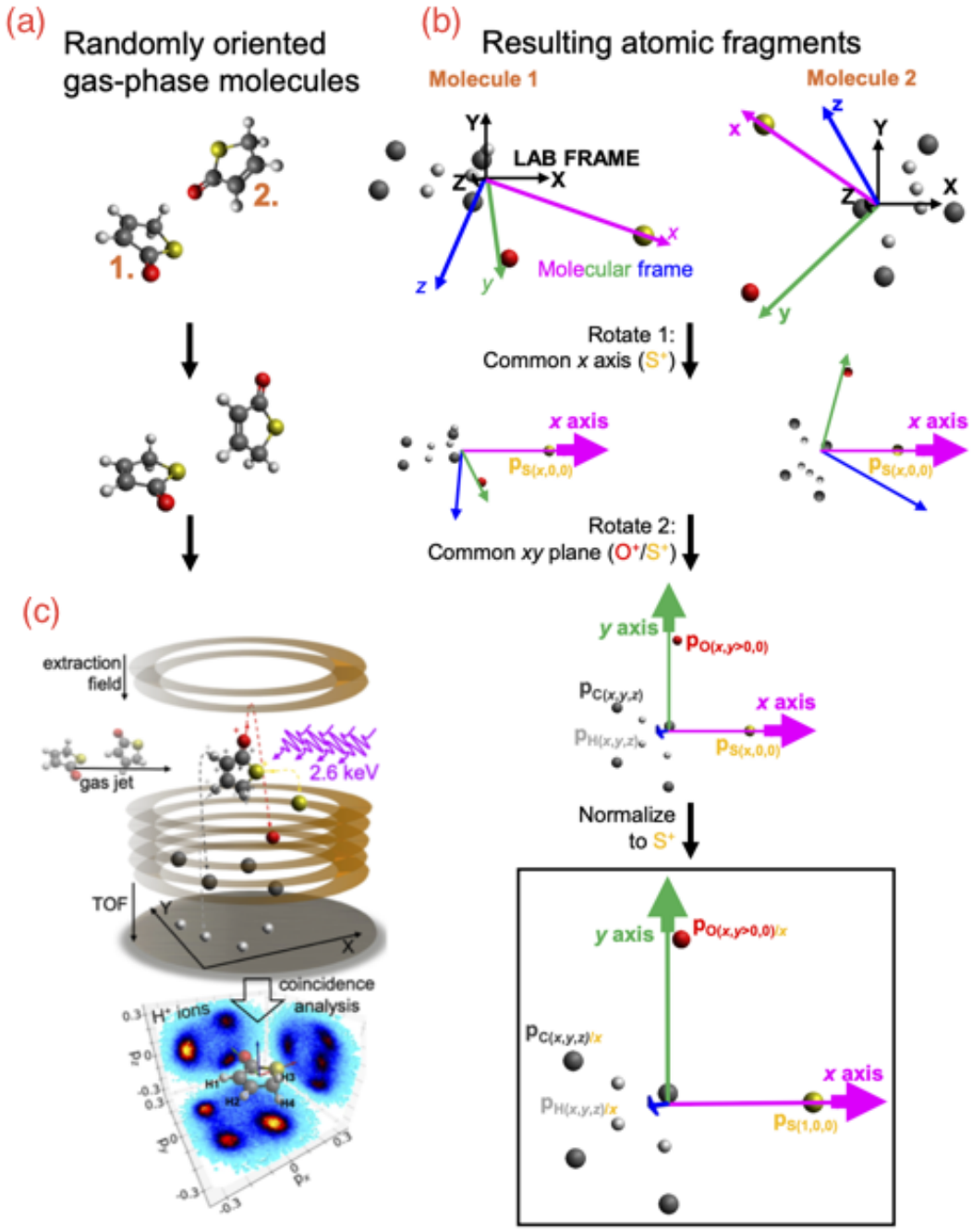

Figure 5.1: ***Schematic of the experimental setup and molecular frame used for presenting Coulomb explosion data of thiophenone.***
(a) Schematic overview of randomly orientated molecule. (b) Schematic overview of the experiment, illustrating the Coulomb explosion of thiophenone (yellow: sulfur, red: oxygen, dark gray: carbon, light gray: hydrogen) molecules induced by intense femtosecond X-ray pulses. The explosion results in the emission of multiple ionic fragments, which are detected in coincidence. From the measured three-dimensional momenta of these ions, the data can be transformed into a molecular frame, as shown in the bottom panel. (c) Schematic overview of the molecular frame definition.

Coincident detection of all ten atomic ions resulting from the complete Coulomb explosion of a thiophenone molecule are extremely rare, primarily due to the limited single-ion detection efficiency, which is typically around 60%. This results in an overall detection efficiency of only $0.6^{10} \approx 0.6\%$ for a full ten-ion coincidence. However, a comprehensive Coulomb explosion image of all ten fragments can be reconstructed statistically by analyzing four-fold coincidence events, in which H^+ and/or C^+ ions are detected in coincidence with O^+ and S^+ ions within the same laser shot.

These comparisons clearly demonstrate the potential of X-ray-induced CEI for tracking the photo-induced structural evolution of organic molecules, including the three-dimensional motion of hydrogen atoms.

For the Coulomb explosion simulations of thiophenone at equilibrium, 10,000 geometries were sampled from a Wigner distribution at a temperature of 60 K, and the explosion dynamics of each geometry were simulated[55]. The equilibrium geometry and normal modes were computed using the DFT-B3LYP/aug-cc-pVDZ level of theory in the GAUSSIAN 09 software package[146]. Wigner sampling was carried out using the NEWTON-X software[57], where finite temperature effects were incorporated via a broadening factor of $\tanh(\hbar\omega/2k_BT)$.

The C^+ momentum distributions (Fig 5.3.(d–f)) do not reflect the molecular structure as directly as the H^+ ions do. The most structurally informative projection is in the (x, y)-plane (as shown in Fig 5.3.(d)), which corresponds to the plane in which all heavy atoms lie in thiophenone. In this projection, each carbon atom can be distinguished, and their positions within the molecular ring can be inferred.

Particular attention is drawn to the feature arising from the C1 atom, which exhibits significantly lower momentum compared to the other C^+ ions, i.e., its distribution lies closer to the origin in the two-dimensional momentum histogram. During the Coulomb explosion, this carbon ion is effectively 'trapped' between the repelling O^+, S^+, and neighboring C^+ ions. The simultaneous Coulomb repulsions from multiple directions result in a lower net momentum, whereas other carbon ions experience more unidirectional repulsive forces and

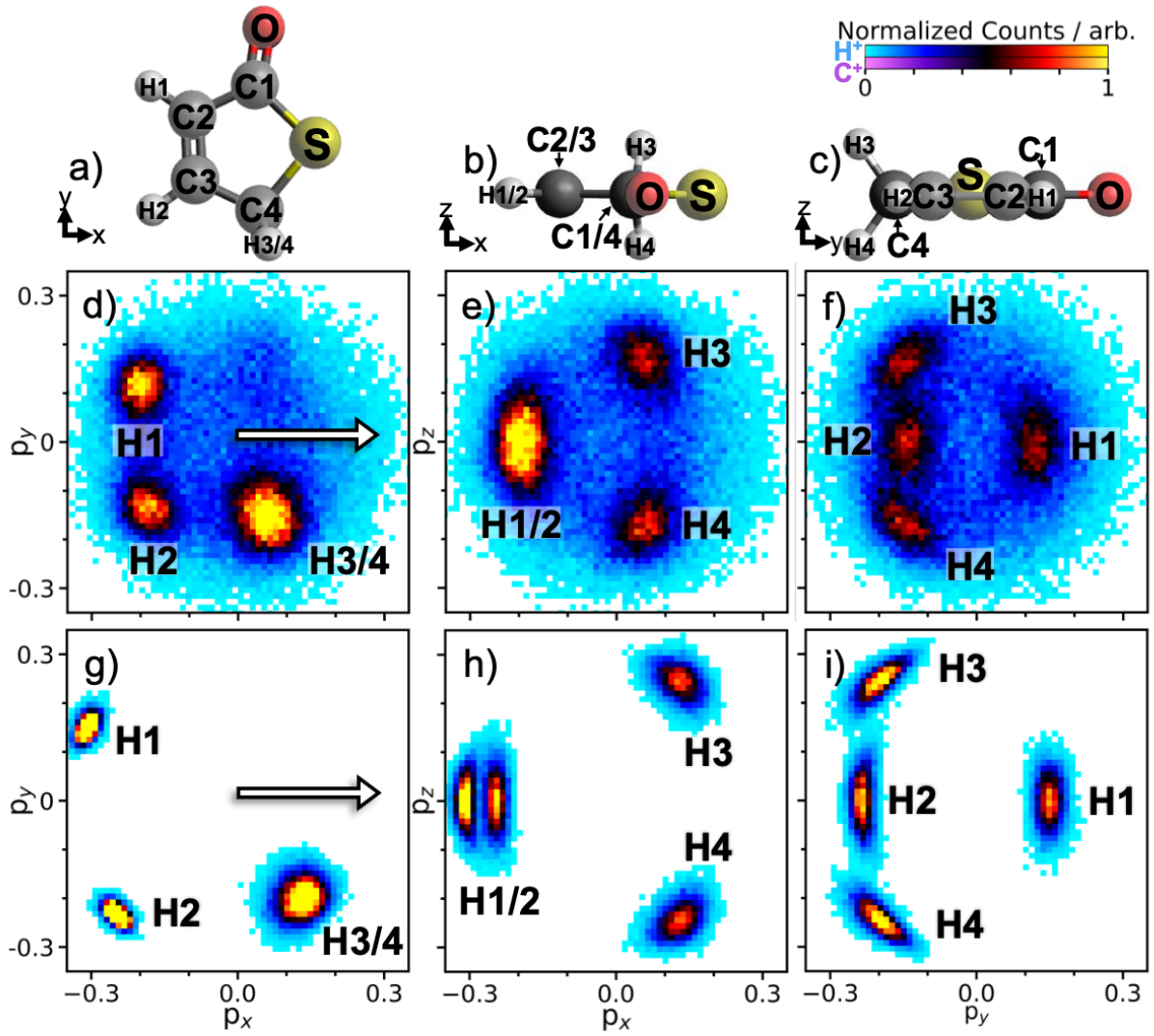

Figure 5.2: ***Comparing the experimental data with Coulomb explosion simulation for ground-state thiophenone:*** H^+***.***
Direct comparison between experimental and simulated Newton diagrams of the normalized coincident momentum distributions of H^+ *ions projected onto the* (x, y)*-,* (x, z)*-, and* (y, z)*-planes. (a)–(c) show ball-and-stick models of the thiophenone molecule viewed along three orthogonal axes. (d)–(f) present the experimental Newton plots, and (g)–(i) show the corresponding simulated Newton plots obtained from classical Coulomb explosion simulations. The simulations were performed on a pool of geometries sampled from a Wigner distribution. All color scales are normalized by the total ion count.*

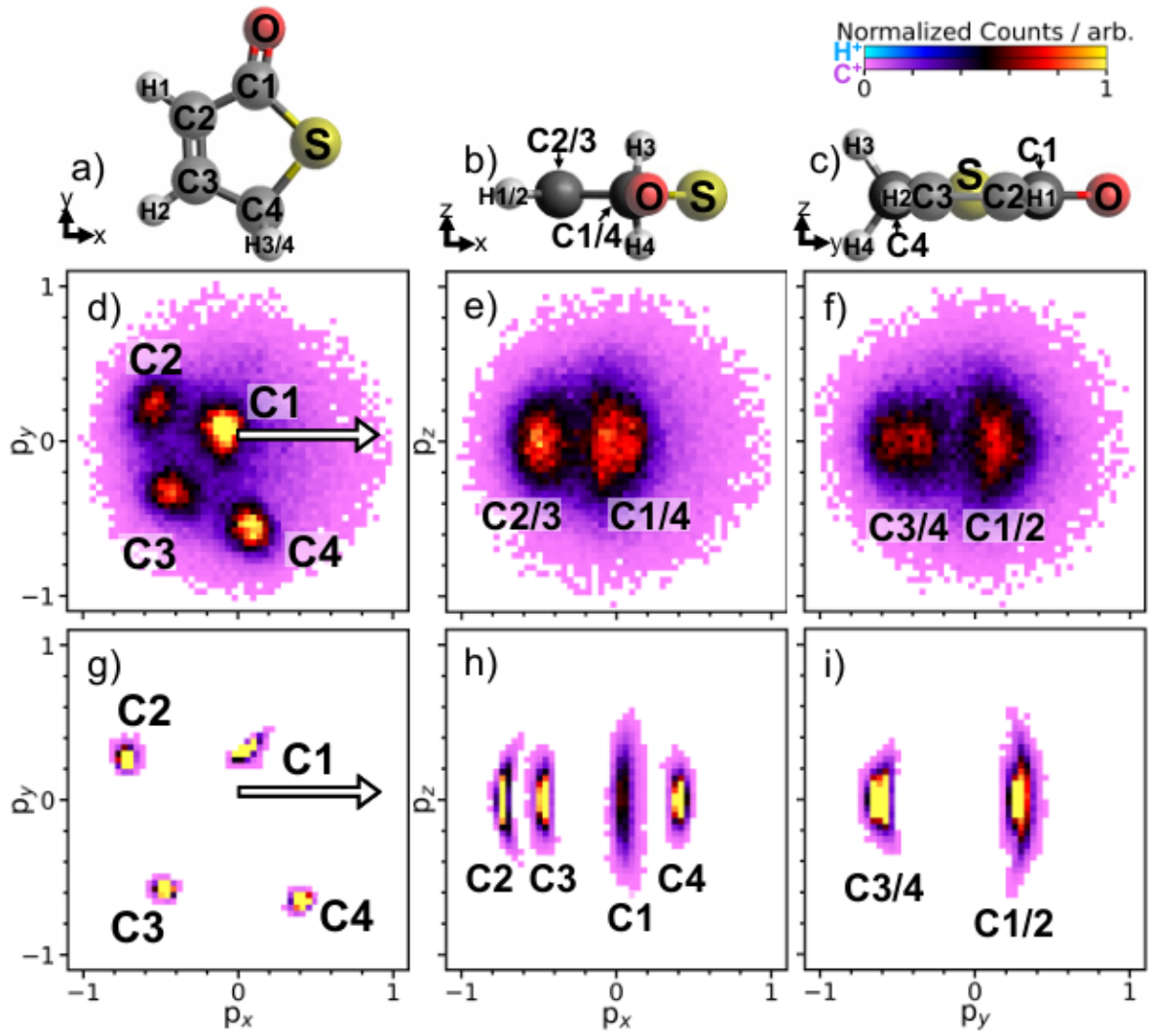

Figure 5.3: ***Comparing the experimental data with Coulomb explosion simulation for ground-state thiophenone:*** C^+***.***
Direct comparison between experimental and simulated Newton diagrams of the normalized coincident momentum distributions of C^+ *ions projected onto the* (x, y)*-,* (x, z)*-, and* (y, z)*-planes. (a–c) show ball-and-stick models of the thiophenone molecule viewed along three orthogonal axes. Panels (d–f) present the experimental Newton plots. Panels (g–i) show the corresponding simulated Newton plots obtained from classical Coulomb explosion simulations. The simulations were performed on a pool of geometries sampled from a Wigner distribution. All color scales are normalized by the total ion count.*

are pushed more strongly away from the molecular center. This also highlights a key advantage of using hydrogen atoms to determine ultrafast changes in three-dimensional molecular structure. Hydrogen atoms typically reside on the periphery of a molecule and are therefore less susceptible to trapping effects caused by surrounding heavy ions. As a result, their final momentum vectors more visually reflect their original positions in the molecule.

Moreover, the low mass of hydrogen enables rapid acceleration and ejection from the poly-cation during the early stages of the Coulomb explosion, occurring before significant structural deformation can take place. This makes hydrogen atoms particularly reliable probes for tracking molecular geometry in time-resolved CEI experiments. However, to further explore the structural information embedded in the present data, we examine alternative methods for representing the coincident three-dimensional momentum distributions. Different representations can emphasize specific features of the Coulomb explosion dynamics captured in these correlated momentum datasets and highlight distinct structural characteristics.

5.1.3 Experimental results under different representations compared with Coulomb explosion simulation

Fig. 5.4 (a) and (b) show three-dimensional iso-surface renderings of the experimental momentum distributions of the H^+ and C^+ ions, respectively. The iso-surfaces are color-coded according to the magnitude of each ion's momentum. For both H^+ and C^+ ions, this representation clearly separates the distributions associated with each atomic site, providing a comprehensive three-dimensional view, while avoiding the challenges associated with visualizing full three-dimensional histograms.

Notably, this representation reveals an increased spread in the out-of-plane (P_z) momentum for the low-momentum (purple-colored) C^+ ions originating from the C1 atom, a feature less evident in the two-dimensional projections shown in Fig. 5.4 (e) and (f). Classical Coulomb explosion simulations of ground-state (cold) thiophenone reproduce this

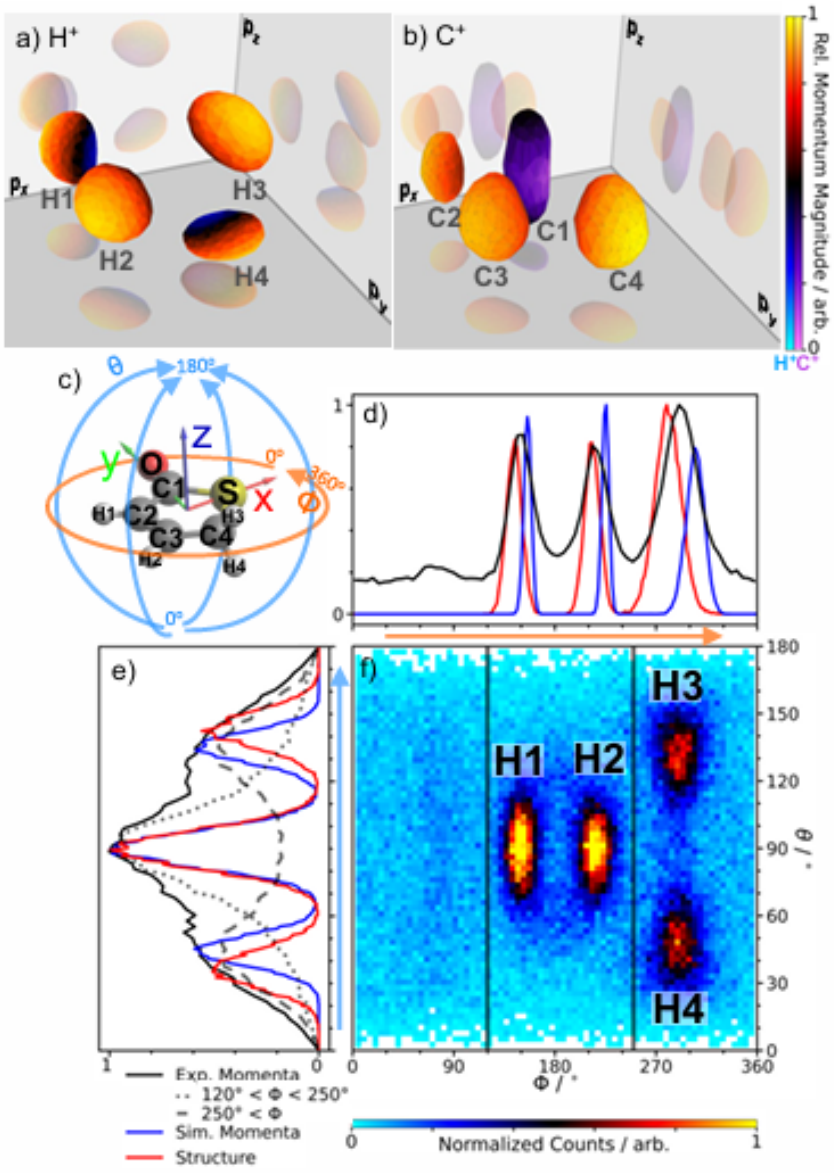

Figure 5.4: ***Different representations of experimental ion momenta of thiophenone.***

(a)–(b) Three-dimensional iso-surfaces of the experimental H^+ *and* C^+ *ion momentum densities in Cartesian coordinates. The color scales represent the (separately normalized) momentum magnitudes of the* H^+ *and* C^+ *ions, respectively. (c) Definition of spherical polar coordinates* (ϕ, θ)*. (f)* H^+ *ion momentum distribution represented in spherical polar coordinates. (d)–(e) One-dimensional projections of panel (f) onto the azimuthal angle* ϕ *and polar angle* θ *(black solid lines), along with two angular slices:* $120° < \phi < 250°$ *(dotted line) and* $\phi > 250°$ *(dashed line). Comparisons to Coulomb explosion simulations (blue lines) and bond angles in the real-space molecular structure (red lines) are also shown.*

observation. However, the Wigner distribution of geometries used in the simulation does not show a significant variation in the initial z-position of the C1 atom. This suggests that the broader p_z momentum spread for the $C1^+$ ion likely arises from its enhanced sensitivity to small deviations in the initial molecular structure prior to Coulomb explosion, in contrast to the other carbon atoms in the ring.

Since much of the structural information encoded in the recorded three-dimensional correlated momentum distributions is related to the angles between different ion momenta, Fig. 5.4(d) and (e) present a comparison between the observed H^+ ejection angles, represented by the polar angle θ and the azimuthal angle ϕ, and the results of Coulomb explosion simulations for cold thiophenone molecules.

In both angular dimensions, the peak positions in the experimental distributions (black lines) show good agreement with the simulated distributions (blue lines). However, the experimental angular distributions are noticeably broader than those predicted by the simulations, likely reflecting experimental uncertainties, initial-state vibrational motion, or residual misalignment effects.

It is important to emphasize that advanced modeling is not required to identify the general structural features of the molecule from experimental momentum correlations. In the present case, we observe a strong correspondence between the measured H^+ momentum distributions and the inter-bond angles in the real-space molecular structure, which was determined and Wigner-sampled as described in the Coulomb explosion simulations section. These bond angles are shown as red lines in Fig. 5.4(d) and (e).

For this comparison, the real-space θ and ϕ angles for each C–H bond vector were computed in a coordinate system defined analogously to the one used for the Coulomb explosion data: the sulfur and oxygen atoms lie in the (x, y)-plane, and the bisector between the two C–S bonds defines the x-axis. Although such a direct mapping between ion ejection angles and bond angles is not generally valid, the present finding highlights that the momenta of the light H^+ ions can serve as reliable reporters of molecular geometry. This is primarily

because H^+ ions tend to be ejected along the axis of the C–H bond from which they originate. In the following section, we explore this approach further by examining the expected changes in the three-dimensional H^+ momentum distributions as the molecular structure evolves following UV-induced electronic excitation. The photochemistry of thiophenone has attracted significant interest, with recent time-resolved experiments investigating the role of ultrafast ring-opening dynamics following UV photoexcitation at wavelengths around 266 nm. The subsequent nonadiabatic relaxation to the S_1 and then to the S_0 electronic states is driven by nuclear motion along an S–C bond stretch coordinate. Cleavage of this bond initially produces a ring-opened biradical intermediate, from which multiple rapid isomerization pathways are possible. Using mega-electronvolt ultrafast electron diffraction (UED) in combination with ab initio molecular dynamics (AIMD) simulations, time-resolved product branching ratios during this reaction were determined. A substantial yield (approximately 50%) of a high-energy episulfide (three-membered ring) isomer was confirmed[11].

However, various ring-opened structural variants, which differ primarily in the relative positions of hydrogen atoms, could not be distinguished. Of particular interest are three variants: the initial biradical species formed upon photoexcitation (denoted as P0), a thioaldehyde isomer (2-thioxoethylketene, P1), and a thiol isomer (2-(2-sulfanylethyl) ketene, P2), as shown in Fig. 5.5. Demonstrating that Coulomb explosion imaging (CEI) can resolve these structurally similar isomers is a central objective of the present study.

To explore the feasibility of future time-resolved CEI studies on thiophenone, we coupled classical CEI simulations with outputs from previously reported ab initio molecular dynamics (AIMD) simulations[8], which track the neutral dynamics up to 2 ps following UV photo-excitation. Product structures from the AIMD trajectories were classified into isomeric species, allowing simulation of the corresponding fragment momentum distributions. The relative H^+ momentum distributions for each product are presented in spherical-polar coordinates in Fig. 5.5(b–f), while Fig. 5.5(a) shows the result for unexcited, ground-state thiophenone, which closely resembles the experimental distribution in Fig. 5.4(f) despite the

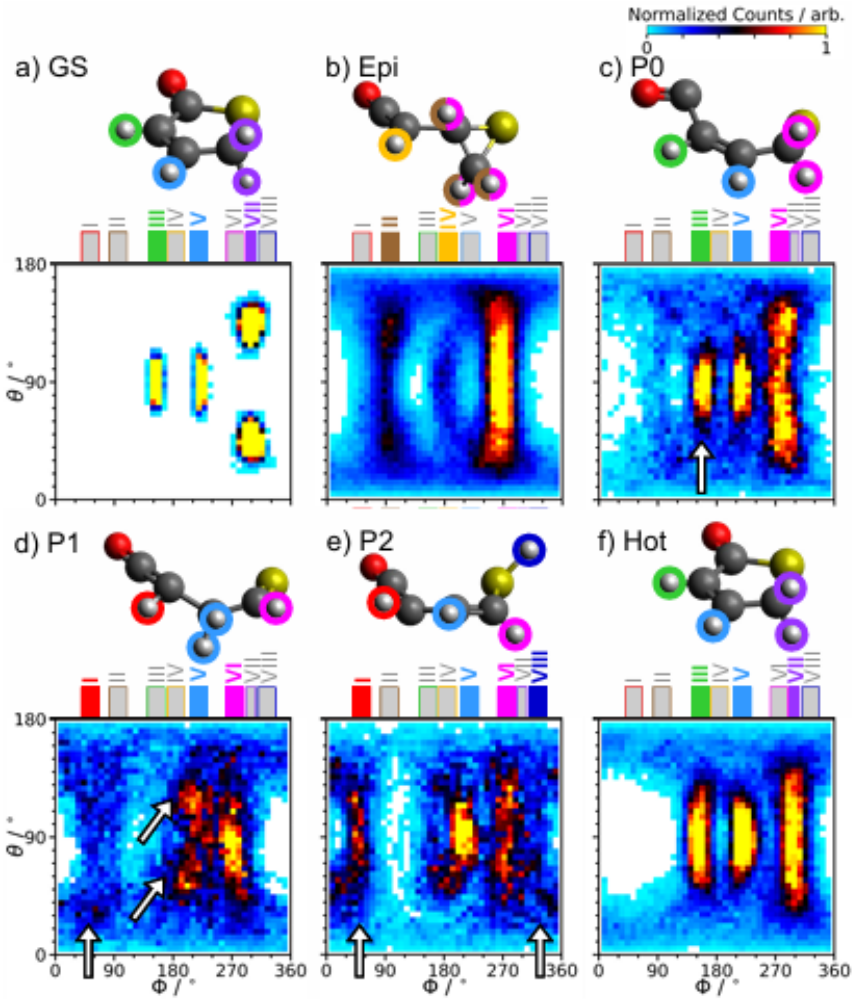

Figure 5.5: ***Three-dimensional*** H^+ ***momentum distributions represented in spherical polar coordinates for various molecular geometries of thiophenone and its photoproduct.***

(a) Cold ground-state thiophenone. (b) Episulfide photoproduct. (c)–(e) Additional vibrationally hot photoproducts of UV-excited thiophenone, labeled P0, P1, and P2, respectively, following prior work[8,11]*. (f) Hot ground-state thiophenone. Representative sketches of the corresponding molecular geometries are shown alongside each distribution. Specific regions of ϕ are labeled (I–VIII) and color-coded above each panel, with the corresponding hydrogen atom also color-coded to match. White arrows indicate regions that exhibit unique signatures compared to the other ring-opened products. The color scale is normalized to the number of coincidence events contributing to each panel.*

simulation's simplicity.

The predicted signal for the high-energy episulfide product (Fig. 5.5(b)) appears in a distinct momentum region, demonstrating CEI's sensitivity to molecular structure. Our focus is on three ring-opened species, P0 (biradical), P1 (thioaldehyde), and P2 (thiol), which differ mainly by hydrogen atom positions and were indistinguishable in previous studies[8,11]. Their H^+ distributions (Fig. 5.5(c-e)) reflect key structural differences. For instance, P1 and P2 exhibit unique features at $\phi \approx 50°$ (region I), corresponding to a hydrogen adjacent to the ketene moiety. Compared to the ground state (GS), P0 shows modest shifts in momentum features due to bond elongation and increased rotational freedom after ring opening.

Overall, the largest differences in predicted H^+ momenta arise from the out-of-plane hydrogen atoms. In the ground state (GS), P0, and P1, two hydrogens attached to the same carbon yield signals in a single ϕ-region but are distinguishable in θ. In contrast, P2, lacking such out-of-plane hydrogens, produces an additional signal near $\phi \approx 330°$ (region VIII), indicating all four hydrogens contribute distinct momentum signatures. These distinctions highlight CEI's capability to resolve subtle structural variations. The molecular frame used here, optimized for visualizing the equilibrium structure of thiophenone, was held fixed across all products for consistency. However, given the complexity of multi-dimensional momentum correlations, identifying optimal molecular frames for specific products remains an open challenge.

In summary, we have demonstrated that X-ray-induced CEI of an organic molecule can yield well-resolved structural information by detecting the three-dimensional momentum vectors of H^+ fragment ions originating from the peripheral hydrogen atoms. By utilizing the structural information carried by these light 'messenger' ions, combined with Coulomb explosion simulations and quantum-mechanical predictions of photo-induced molecular dynamics, this approach offers the potential for direct observation of neutral fragmentation dynamics at the atomic level, with femtosecond temporal resolution.

5.2 Coulomb explosion imaging of UV-induced ring conversion dynamics of 2(5H)-thiophenone using table-top lasers

Although a time-resolved measurement with an ultraviolet pump pulse at 266 nm and a 2.6 keV X-ray probe of was attempted during the European XFEL experiment (as described in the previous section), no clear signatures of ring opening in thiophenone were observed. While analysis for that time-resolved measurement is still underway, we have, in the meantime, conducted a similar pump–probe experiment at JRML, employing intense NIR pulses (from the tabletop setup described in Chapter 3) as the probe. The measurement was guided by the CES discussed in the previous section and by the results of the earlier TR-PES[8] and UED[11] studies. The main goal here was to investigate whether direct signatures of ring opening dynamics in thiophenone upon 266 nm UV excitation could be observed in strong-field-induced CEI patterns and to determine the time scale of this process.

As a first step, we examined whether NIR-induced Coulomb explosion of thiophenone yield well-resolved structural information similar to the XFEL-driven CEI discussed in the previous section. Specifically, we aimed to determine whether the three-dimensional momentum vectors of H^+ and C^+ fragment ions, originating from hydrogen and carbon atoms, could be detected with sufficient resolution to reconstruct fragment momentum correlations using Newton diagrams. This was carried out using four-body (four-fold) coincidence detection events, where H^+ and/or C^+ ions were detected in coincidence with O^+ and S^+ ions from the same laser shot.

Second, we investigated whether UV-induced ring conversion dynamics of thiophenone could be observed through pump–probe measurements. Specifically, we aimed to resolve time-dependent changes in the fragment momentum distributions reflecting ultrafast structural transitions initiated by the UV excitation.

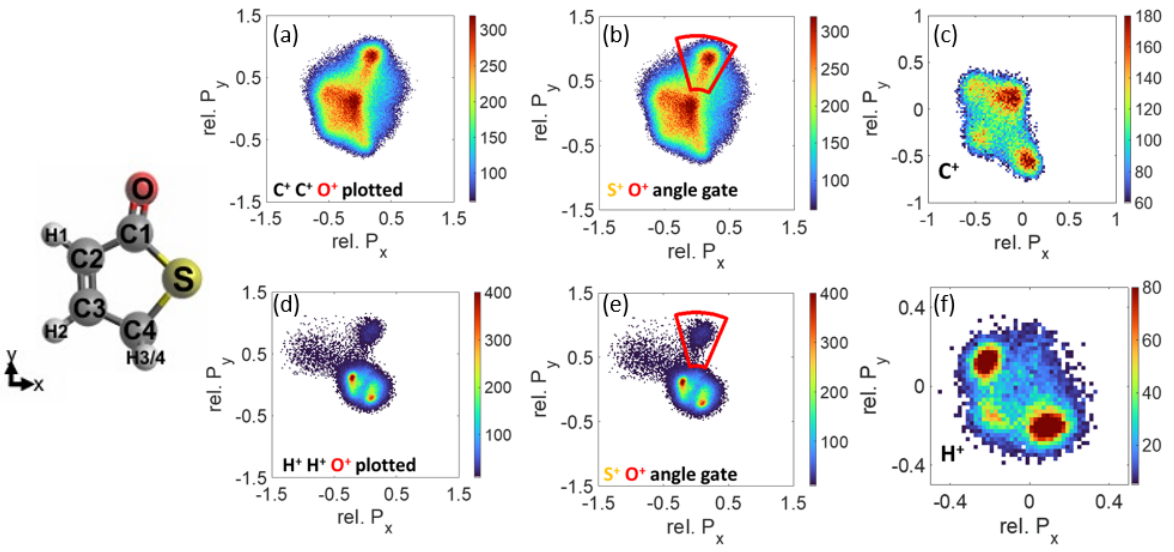

Figure 5.6: ***Newton diagrams of four-body fragmentation channels in*** (x, y)***-plane of thiophenone.***

For all panels, the momentum vector of the S^+ *ion (not shown) defines the* x*-axis of the* (x, y)*-momentum plane, and the* O^+ *ion momentum is used to establish the* (x, y)*-molecular plane. (a-c) Newton diagram of the* $C^+ + C^+ + O^+ + S^+$ *channel. In (a), the relative momentum distribution of the* C^+*,* C^+*, and* O^+ *fragments is shown. Panel (b) shows the same data (a) but with the red arc indicating the momentum gate applied to the* O^+ *momentum distribution, which separates the target contributions from the background. (c) Relative momentum distribution of the two* C^+ *ions from the events selected using the gate shown in (b). (d-f) Newton diagrams of the* $H^+ + H^+ + O^+ + S^+$ *fragmentation channel. (d) The relative momentum distribution of the* H^+*,* H^+ *and* O^+ *ions is plotted. (e) Same as (d) but with the red arc indicating momentum gate applied to the* O^+ *momentum distribution for event selection. (f) Relative momentum distribution of the two* H^+ *ions from events selected using the gate shown in panel (e).*

5.2.1 Static Coulomb explosion imaging of thiophenone with intense NIR pulses

Figs. 5.6(a,c) show the Newton diagrams for the $C^+ + C^+ + O^+ + S^+$ and $H^+ + H^+ + O^+ + S^+$ four-body coincidence data, respectively. While the distribution of carbon ions partially resembles the molecular structure, the proton distribution does not display such a clear pattern and is markedly different from the corresponding data obtained with the XFEL pulses shown in Fig. 5.2(d).

The most likely reason for this difference is the higher background level in the NIR data. In comparison to site-selective X-ray ionization, which efficiently targets sulfur atoms and, thus, target molecules, strong-field NIR ionization is non-selective, with comparable probability to ionize target or background molecules. Because of this and also taking into account significantly higher background pressure in the JRML experiment (1×10^{-10} mbar vs. 1×10^{-11} mbar in the EuXFEL experiment), the NIR pulse introduces significantly more background signal in our CEI experiments. Altogether, these factors make NIR-induced Coulomb explosion imaging (CEI) more susceptible to background noise, whereas site-selective X-ray ionization provides a cleaner and more interpretable signal, making it better suited for high-precision structural studies. This explains the blurrier momentum distribution features observed in the Newton diagrams shown in Fig. 5.6(a) and (d).

Nevertheless, we developed a method to suppress background contributions and isolate the target events originating from molecular fragmentation. For static CEI, the relative angle between the momentum distributions of the O^+ and S^+ ions is expected to fall within a specific range. Using the S^+ momentum vector as a reference direction, we determined, based on equilibrium ground-state thiophenone Coulomb explosion simulations, that the relative angle of the O^+ ion momentum should lie between 59° and 95°. This angular range is slightly broader than the simulated ground equilibrium state of thiophenone which is ranging from 67° and 77°, which reflects a limited number of vibrational states sampled from a 60 K Wigner distribution. In contrast, the real experimental ensemble likely includes a wider spread of vibrational excitations, justifying a more inclusive angular gate. In spherical polar coordinates, this corresponds to the ϕ-angle gating window of the O^+ momentum vector shown in Fig. 5.4(c).

In addition to the angular constraint, we imposed a criterion on the magnitude of the O^+ momentum relative to the S^+ momentum vector, as visualized in the Newton diagrams. We selected events in which this relative momentum falls within the range of 95 to 205 a.u., defining the radius of the red arc-shaped gate illustrated in Fig. 5.6(b) and (e).

The final momentum distributions of the events obtained after applying both angular and radial gating are shown in Fig. 5.6(c) and (f). Compared with the Coulomb explosion simulation results presented in Fig. 5.3(g) and 5.2(g), we observe a good agreement. This demonstrates that the applied gating method successfully discriminates against the background noise while preserving the inherent momentum correlations in the fragmentation pattern. Thus, this approach allows NIR-induced CEI to effectively visualize the molecular geometry and convey structural information with improved clarity.

For better comparison to the CES results from Fig. 5.5, we also represent this dataset in a spherical polar coordinate system, using the events after gating on the O^+ momentum distribution. We also plot the cosine of the polar angle theta for a reference.

From the projection of the azimuthal angle ϕ shown in Fig. 5.7(c), we observe that, even with a same number fold of detection (i.e., four-fold coincidence with S^+ and O^+ detected), the NIR-induced CEI data exhibit slightly reduced resolution compared to X-ray-driven CEI. For clearer comparison, the normalized yield of the second H^+ ion is lower in the NIR case than in both the simulation and the X-ray data shown in Fig. 5.4(d). This observation is further supported by comparing Fig. 5.6(f) with Fig. 5.2(g), where the signal in the lower-left region of the H^+ momentum distribution, which is labeled as H2 is noticeably diminished.

Nevertheless, the results demonstrate that NIR-driven CEI remains a viable technique for structural imaging of thiophenone. The molecular geometry can still be visualized using Newton diagrams, and the final momentum distributions of the proton fragments can be effectively represented in spherical polar coordinates. This indicates that structurally informative proton momentum distributions can be obtained even with a tabletop NIR laser setup, reinforcing the accessibility and utility of CEI for molecular structure determination.

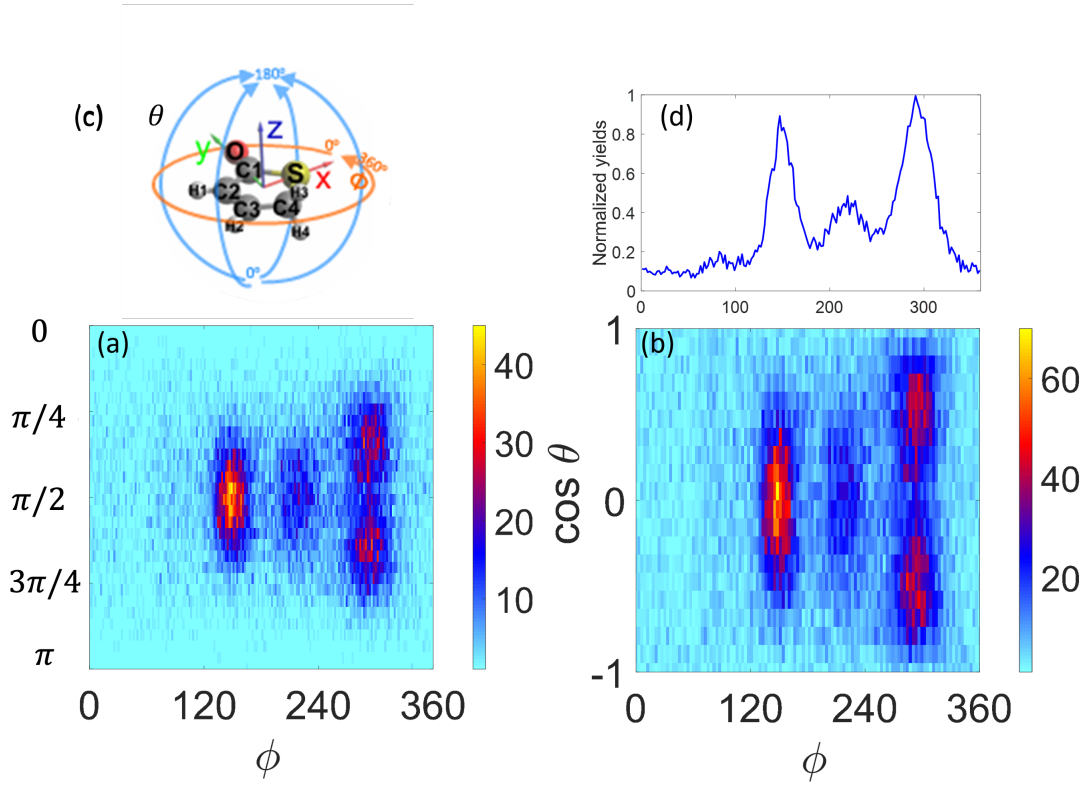

Figure 5.7: ***Three-dimensional*** H^+ ***momentum distributions of thiophenone represented in spherical polar coordinate.***
(a) H^+ *ion yield as a function of polar angle* θ *and azimuthal angle* ϕ*. (b) Same as (a) but plotted as a function of* $cos(\theta)$*. (c) Definition of spherical polar coordinates* (ϕ, θ)*. (d) One-dimensional projection of (a) onto azimuthal angle* ϕ*.*

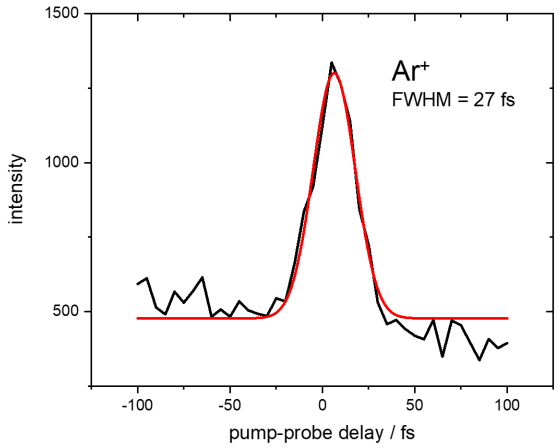

Figure 5.8: ***Cross-correlation of Argon ion as a function of pump–probe delay.*** *The black curve shows the measured Ar^+ yield as a function of pump–probe delay; the red curve is the Gaussian fit with the calculated FWHM of $\simeq$ 27 fs*

5.2.2 UV-induced ring opening of 2(5H)-thiophenone probed with intense NIR pulses

For the time-resolved experiments at JRML, we used near Fourier–transform–limited (FTL) UV pulses at a central wavelength of 262 nm, with pulse characteristics described in Chapter 3, as the pump pulse to induce the ring conversion dynamics. To characterize the *in situ* temporal resolution of this experiment, the cross-correlation of the UV and NIR pulses measured using single ionization of argon is shown in Fig. 5.8. The FWHM of the cross-correlation pattern is measured to be 27 fs, which roughly matches the duration of each pulse. The fact that the measured FWHM of the cross-correlation pattern is significantly shorter than what would be expected from a convolution of the temporal profiles of the UV and NIR pulses reflects the non-linearity of the ionization of Ar by the combined two-color laser field.

Coulomb explosion simulations for different 2(5H)-thiophenone geometries

In this experiment, we focus on four-body fragmentation channels in which both S^+ and O^+ ions were detected. Specifically, we investigated the four-fold coincidence channels corresponding to $C^+ + C^+ + O^+ + S^+$ and $H^+ + C^+ + O^+ + S^+$ as shown in Appendix. B.2. First, we processed the coincidence data using the same filtering method described previously. In this case, our goal was to isolate events beyond those associated with equilibrium ground-state thiophenone and to filter out events corresponding to UV-excited photoproducts. To provide clearer guidance using CES, we generated Newton diagrams constructed from simulated data for different groups of molecular geometries of thiophenone and its photoproducts, with O^+ and C^+ ions plotted in the (x, y)-momentum plane('the molecular plane').

To define the coordinate system, we normalize the S^+ momentum vector and use it as the unit vector along the x-axis. The O^+ momentum vector is also used to define the (x, y)-momentum plane. For clarity and to better highlight the ring structure of thiophenone, we display only the momentum distributions of the C^+ and O^+ fragments.

In Fig. 5.9(a) and (b), we present the Newton diagrams of C^+ and O^+ fragments obtained from CES of cold and hot ground-state thiophenone, respectively. These correspond to the ring-closed structures shown in Fig. 5.5(a) and (f). Additionally, Fig. 5.9(c) shows the Newton diagram generated from CES of UV-excited photoproducts, corresponding to the ring-opened structures shown in Fig. 5.5(c), (d), and (e).

From the Newton diagrams in Fig. 5.9, we observe two prominent features that change upon UV excitation. First, the O^+ momentum distribution band becomes noticeably broader relative to the S^+ momentum distribution as shown in Fig. 5.10(c). Second, the C^+ momentum distribution becomes increasingly diffuse. Notably, in Fig. 5.9(c), the two right-side C^+ momentum distributions as shown in Fig. 5.10(d) appear as a line along the relative P_y axis indicating a significant rearrangement of atomic positions. These changes reflect distortions in the thiophenone molecular ring structure induced by UV excitation and support

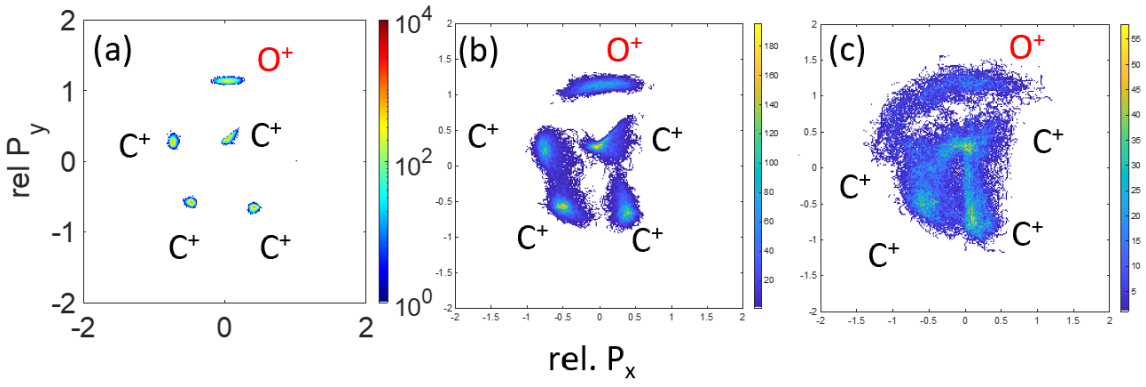

Figure 5.9: ***Newton diagrams of CES results for different groups of molecular geometries of thiophenone.***
(a) Cold ground-state thiophenone; (b) hot ground-state thiophenone; (c) UV-induced thiophenone photoproducts (combined P0, P1, and P2 structures shown in Fig. 5.5(c), (d), and (e)).

the presence of ring-opening dynamics in the excited-state photoproducts.

To better visualize the differences between various groups of molecular geometries, we also project the momentum distributions onto specific coordinate axes. From Fig. 5.9, we first project the ion yields of O^+ onto the azimuthal angle ϕ shown in Fig. 5.9(a), the angle ϕ is defined in Fig. 5.4(c). Since ϕ increases counterclockwise when viewed from the top of the thiophenone molecule, we reverse the angle to maintain a consistent frame of reference. Specifically, the x-axis in this projection is defined as $360° - \phi$, resulting in a clockwise representation of the O^+ momentum distribution. The projected O^+ yields are normalized to the highest peak to facilitate comparison of angular distributions across different geometries.

Second, we project the momentum distributions of the two right-side C^+ ions originating from different molecular geometries onto the relative P_y axis. These distributions are also normalized to unity to allow for direct comparison of structural differences in the C^+ momentum distribution patterns.

As shown in Fig. 5.10(a), the angular distribution of the O^+ momentum relative to the S^+ momentum becomes noticeably broader. With normalized yields, we observe increased

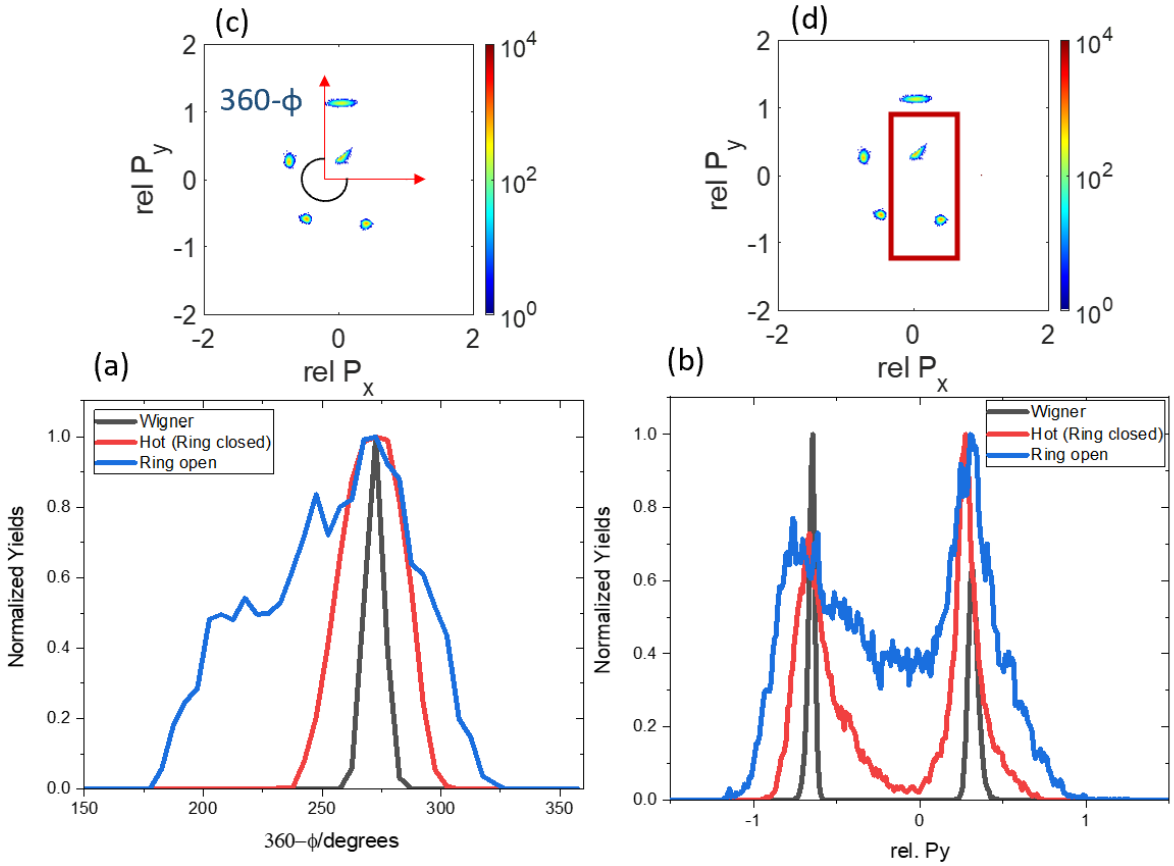

Figure 5.10: ***Projections of the three-dimensional momentum distributions for different groups of molecular geometries of thiophenone.***
(a) Angular projection of O^+ *momentum distribution for different groups of molecular geometries. (b) Projection of* C^+ *momentum along the relative* P_y *coordinate for different groups of molecular geometries. Black: cold ground-state of thiophenone; red: hot thiophenone; blue: UV-induced thiophenone photoproducts. (c) Newton diagram of cold ground-state thiophenone used to illustrate the azimuthal angle distribution* ϕ*. (d) Newton diagram of cold ground-state thiophenone highlighting the selected two* C^+ *momentum distributions used for projection in the red box.*

yields at higher azimuthal angles ϕ for both hot thiophenone and ring-opened thiophenone, compared to cold ground-state species. In Fig. 5.10(b), the yields at lower relative momentum values along the y-axis are also enhanced for the hot and ring-opened species relative to the ground state. These features serve as predictive markers for the UV-induced ring conversion dynamics of thiophenone. By identifying the similar signatures in our experimental data, we aim to extract the corresponding pump–probe signal.

To isolate real molecular fragmentation events from background noise introduced by the NIR probe pulses, we apply an angular filter based on the relative momentum angle between the O^+ and S^+ ions. Specifically, we retain only those events where the angle of the O^+ momentum vector relative to the S^+ vector lies within the range of 180° to 300° in the $(360° - \phi)$ frame. This corresponds to selecting events where the azimuthal angle ϕ lies between 60° and 180°.

Experimental results

In the discussion of time-resolved experimental data, we mainly focus on $C^+ + C^+ + O^+ + S^+$ coincidence events and show the experimental plots for this channel. Very similar conclusions can be drawn from the data for $H^+ + C^+ + O^+ + S^+$ channel, which are shown in Appendix. B.2.

For the $C^+ + C^+ + O^+ + S^+$ four-fold coincidence channel, we apply an angular filter on the O^+ momentum distribution to suppress background contributions. The filtered data are then used to generate UV-pump / NIR-probe Newton diagrams at various pump–probe delays.

In Fig. 5.11, panels (a–e) correspond to delays where the UV pulse arrives early. The $C^+ + C^+$ momentum distributions in these panels appear significantly blurred, which we attribute to the onset of UV-induced ring conversion dynamics in thiophenone. This feature is consistent with the CES shown in Fig. 5.9(b) and (c), where the C^+ momentum distribution is also diffuse due to distortions in the molecular ring structure.

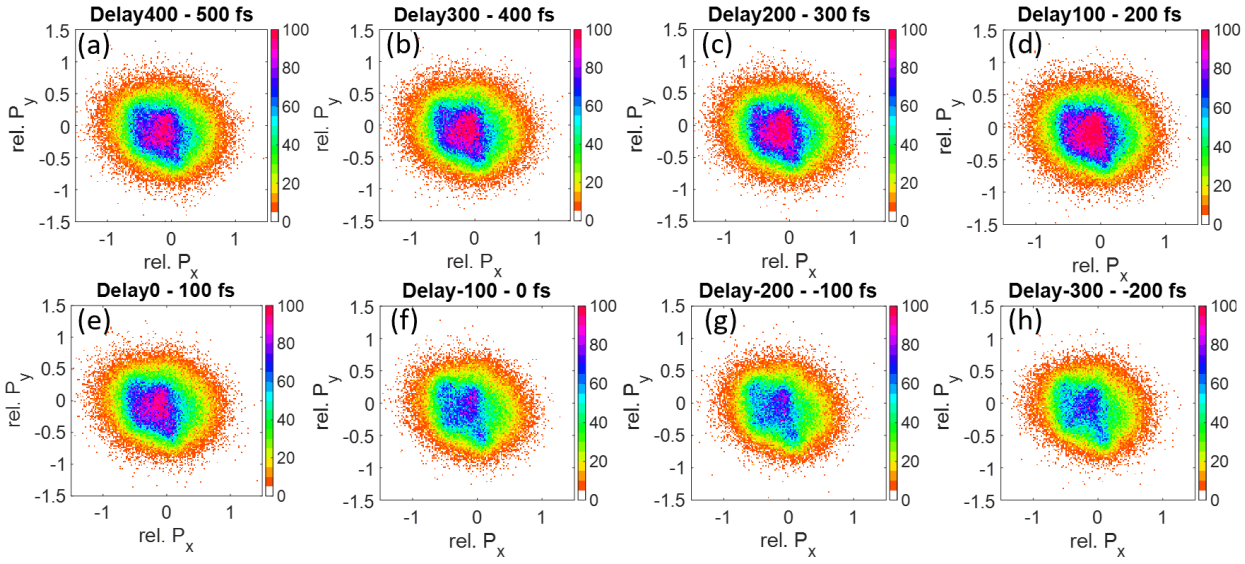

Figure 5.11: ***Newton diagrams showing*** C^+ ***momentum distributions at different pump–probe delays for*** $C^+ + C^+ + O^+ + S^+$ ***coincidence channel of thiophenone.***
Panels (a-e) correspond to the delays where the UV pump arrives first; in (d-e), the NIR pulse arrives first.

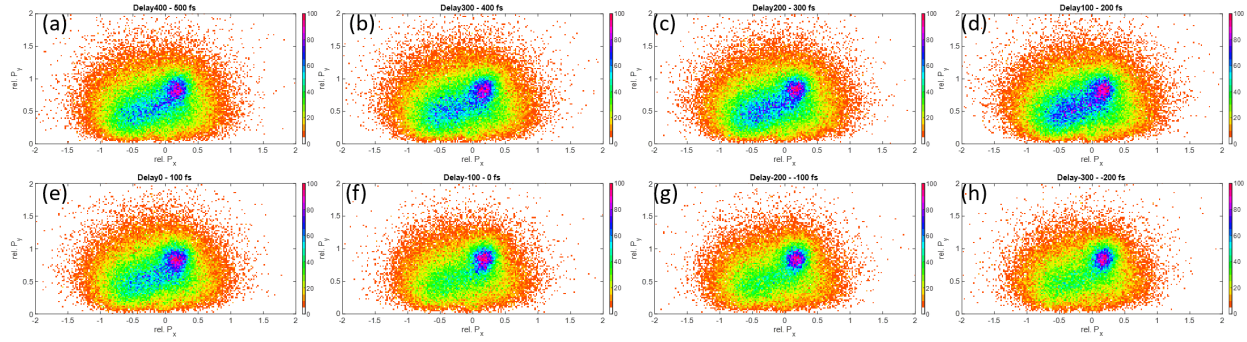

Figure 5.12: ***Newton diagrams of*** O^+ ***momentum distributions of thiophenone at different pump–probe delays for*** $C^+ + C^+ + O^+ + S^+$ ***coincidence channel of thiophenone.***
Panels (a-e) correspond to the delays where the UV pump arrives first; in (d-e), the NIR pulse arrives first.

In contrast, panels (f–h) in Fig. 5.11, corresponding to UV-late / NIR-early delays, show more localized C^+ momentum distributions. This should be expected because here, the NIR probe pulse arrives before the UV pump and, thus, no ring-opening or structural rearrangement processes can occur.

To examine an additional pump–probe signal feature, we plot the Newton diagrams of the relative O^+ momentum distribution, as shown in Fig. 5.12. In panels (a–e), where the UV pulse arrives early, we observe a progressive broadening of the relative O^+ momentum distribution band. In contrast, in the UV-late / NIR-early regime, where the intense NIR pulse ionizes the thiophenone molecule before the UV pulse arrives, the distribution of the relative O^+ momentum is well localized.

To quantify the pump–probe signal, we analyze the angular projection of the O^+ momentum distribution, following the same procedure as in Fig. 5.10(a), using yields from the $C^+ + C^+ + O^+ + S^+$ four-fold coincidence channel. The resulting O^+ angular distributions are shown in Fig. 5.13(c) for four different delays. A clear trend is observed: when the UV pulse precedes the NIR pulse, the normalized angular distribution shifts towards smaller angles in the ($360° - \phi$) frame (corresponding to larger ϕ). This behavior is consistent with the simulation results for UV-excited thiophenone presented in Fig. 5.10(a), where similar angular shifts in the relative O^+ momentum distribution were observed.

To further quantify this observed angular shift and investigate the timescale of the ring conversion dynamics, in Fig. 5.13(b), we plot the mean value of the (O^+, S^+) momentum angle as a function of the UV - NIR delay. This value exhibits a clear change between zero and 200 fs, on a time scale longer than the rise of the total yield of this channel observed in Fig. 5.13(a). To confirm this trend, we summed the yields over specific angular regions at each pump–probe delay. Based on the simulations in Fig. 5.10(a), we identified a clear distinction in the relative O^+ angular distributions between cold ground-state thiophenone and the hot or UV-excited (ring-opened) thiophenone. In the $360° - \phi$ frame, cold thiophenone shows a dominant angular distribution between 260° and 295°, while for hot and

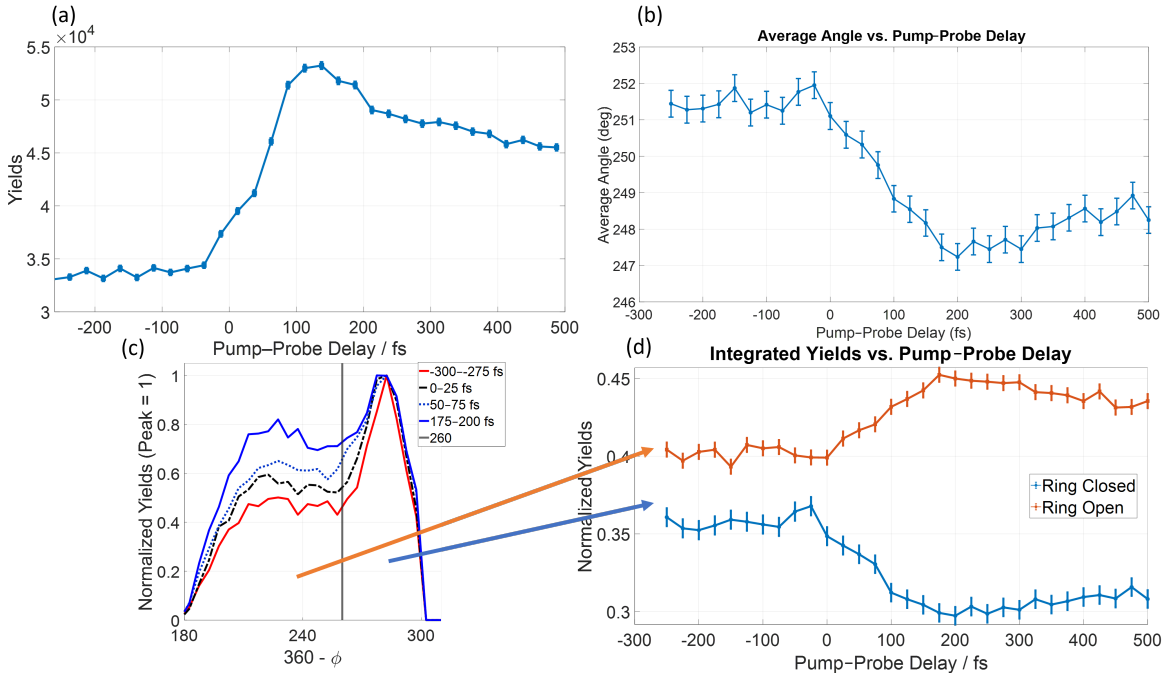

Figure 5.13: ***Delay-dependent yields and angular distributions of*** O^+ ***ions from*** $C^+ + C^+ + O^+ + S^+$ ***coincidence channel of thiophenone.***
(a) Total yield of the $C^+ + C^+ + O^+ + S^+$ *channel as a function of pump–probe delay, using a 25 fs time step. (b) Mean value of the measured angle between* (O^+, S^+) *momenta as a function of pump–probe delay. (c) Normalized distribution of the* (O^+, S^+) *momentum angle at four different delay intervals. The gray line indicates the angle of* $\phi = 260°$ *(marked as a straight black line) used for events separation in (d). (d) Integrated and normalized* O^+ *yield as a function of UV–IR pump–probe delay, grouped by angle: the orange curve corresponds to* $360° - \phi < 260°$ *(*$\phi > 100°$*), tentatively representing ring-open configurations; the blue curve corresponds to* $360° - \phi > 260°$ *(*$\phi < 100°$*), representing ring-closed configurations.*

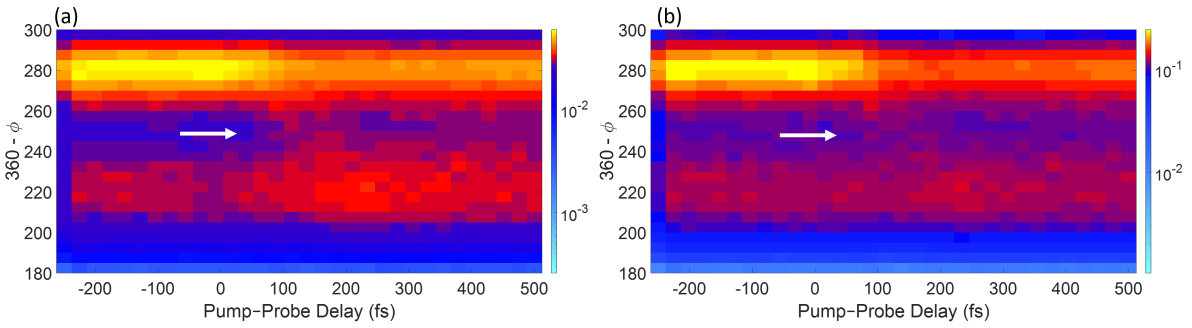

Figure 5.14: ***2D map of delay-dependent*** (O^+, S^+) ***momentum angle for (a)*** $H^+ + C^+ + O^+ + S^+$ ***and (b)*** $C^+ + C^+ + O^+ + S^+$ ***coincidence channels of thiophenone.*** *The white arrows point to the ring-opening transition region*

UV-excited thiophenone, the distribution shifts to angles below 260°. Accordingly, we set 260° shown as a gray line in Fig. 5.13(d) in the $(360° - \phi)$ frame as the boundary: events with angles $< 260°$ are associated with ring-opened structures, and those with angles $> 260°$ correspond to ring-closed geometries. The integrated yields for each region as a function of UV–IR delay are shown in Fig. 5.13(d). The data exhibits the same behavior as the average angle in panel (b), showing a clear ring opening signature between 0 and 200 fs.

These results provide direct experimental evidence that the ring conversion dynamics of thiophenone occur within 200 fs, consistent with previously reported timescales[8,11], but now measured with much better resolution. To provide a more detailed view of the ring-opening step itself, in Fig. 5.14 we plot 2D angle vs. delay distribution for both $H^+ + C^+ + O^+ + S^+$ (a) and $C^+ + C^+ + O^+ + S^+$ (b) channels, In both panels, in addition to the trends observed in the previously, a transition feature connecting the ring-closed and ring-opened angular regions (marked by white arrows) can be clearly observed.

5.2.3 Conclusion

In conclusion, by analyzing two distinct four-fold coincidence channels ($C^+ + C^+ + O^+ + S^+$ and $H^+ + C^+ + O^+ + S^+$), we have consistently observed UV-induced ring opening dynam-

ics in thiophenone within a sub-200 fs timescale. In both channels, angular projections of the O^+ momentum distributions reveal a clear shift from ring-closed to ring-open configurations as the UV pulse precedes the IR probe. These pump–probe effects, supported by the comparisons with Coulomb explosion simulations, are consistent across different detected fragmentation pathways. The agreement between the two independent channels strongly validates the structural sensitivity of pump–probe Coulomb explosion imaging and its utility in capturing ultrafast molecular dynamics with temporal and geometric resolution. These results not only provide direct experimental evidence for the ring-opening process in thiophenone but also underscore the broader potential of CEI in probing photo-induced transformations in complex molecular systems. Moreover, these results confirm the viability of Coulomb explosion imaging with NIR probe pulses as a powerful technique for direct probing of ultrafast ring conversion dynamics in UV-excited molecules.

Chapter 6

Coulomb explosion imaging of ring conversion dynamics in 2,3-dihydrofuran

The work presented in this chapter was inspired and coordinated by Dr. Yusong Liu (SLAC National Accelerator Laboratory). The experiments described here were conducted by the author with strong support from Dr. Liu and the JRML team. Data analysis and Coulomb explosion simulations were carried out by the author, while the time-resolved excited-state geometries used as an input for those simulations were provided by Dr. Ryan Macdonell (Dalhousie University).

As illustrated in the inset in Fig. 6.1, a 2,3-dihydrofuran (2,3-DHF, C_4H_6O) molecule is a five-membered heterocyclic compound consisting of four carbon atoms and one oxygen atom, with a double bond between the second and third carbon positions. It features an enol ether functionality,[147] which imparts high reactivity and makes it a valuable intermediate in organic synthesis[148]. 2,3-DHF can be synthesized via cyclization[149] of 4-hydroxybutanal or

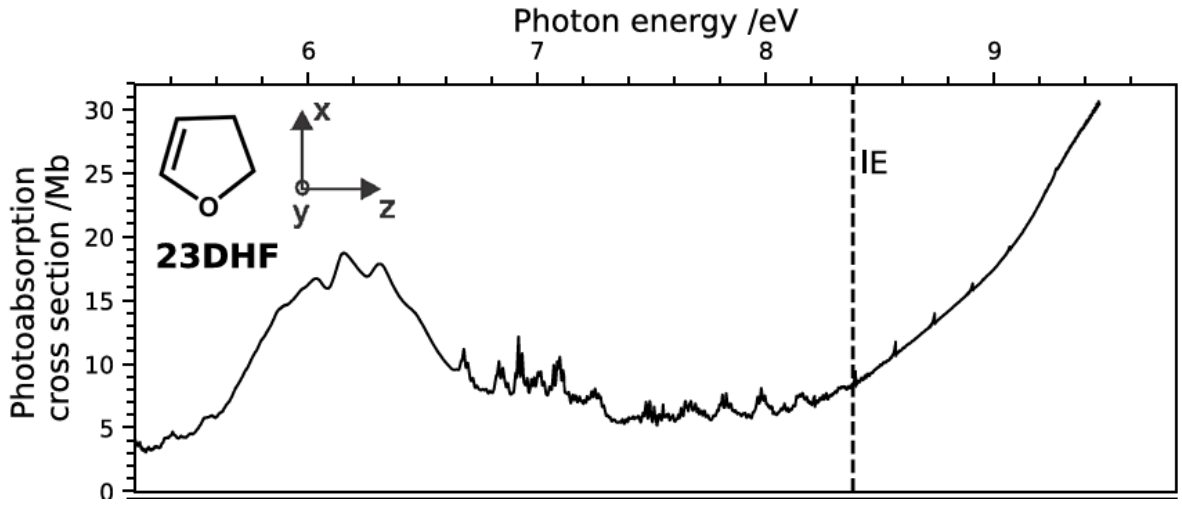

Figure 6.1: ***VUV absorption spectra of 2,3-DHF.***
Figure is adapted from Röder et al.[152].

through catalytic dehydrogenation of 1,4-butanediol using cobalt-based systems[150]. Upon treatment with *n*-butyllithium, it undergoes lithiation to form a 2-lithio derivative, which serves as a versatile building block for further functionalization.

2,3-DHF participates in a variety of cycloaddition reactions, including Diels–Alder processes, often catalyzed by transition metals such as lanthanides or rhodium. These transformations enable the efficient construction of complex molecular architectures, including biologically active molecules such as antitumor agents[150]. Beyond its role in small-molecule synthesis, 2,3-DHF has also been explored in polymer science. A recent study demonstrated a green, metal-free cationic polymerization method for producing poly(2,3-dihydrofuran), a strong, biorenewable, and degradable thermoplastic, highlighting its potential as a sustainable monomer for advanced materials[151].

W. H. Green's 1969 study of the ring-puckering vibration in 2,3-DHF used far-infrared spectroscopy to construct a one-dimensional potential energy curve along the puckering coordinate[153]. The symmetric double-well potential indicated that the molecule adopts a puckered conformation in both the ground and first excited vibrational state.

Building on this, Autrey and Laane[154] combined far-infrared measurements and *ab initio*

MP2/6-31G* calculations to derive a puckering potential with a barrier height of approximately 149 cm^{-1} and a fundamental vibration near 83 cm^{-1}. This confirmed the nonplanar equilibrium geometry and rapid interconversion between puckered forms.

Schalk et al.[155] investigated the excited-state dynamics of furan and its derivatives, including 2,3-DHF, using time-resolved photoelectron spectroscopy combined with theoretical calculations. For 2,3-DHF, they found that photoexcitation primarily leads to a ring-opening pathway facilitated by a dissociative $\pi\sigma^*$ state, serving as the major relaxation mechanism. This behavior parallels the dynamics observed in furan and 2-methylfuran. The study further emphasizes the important role of Rydberg–valence interactions in modulating the photochemical reactivity of these five-membered heterocycles.

The excited-state dynamics of furan and its derivatives are complex due to closely spaced excited states and competing reaction pathways. This study[155] introduced structural modifications to furan to isolate these influences. Partial double-bond saturation or single methylation at the 2-position had minimal impact on dynamics. However, dimethylation at positions 2 and 5 significantly altered behavior, lowering the energy of the 3s Rydberg state and preventing its crossing with valence states along the ring-opening coordinate. This suggests ring-opening is the dominant relaxation pathway in furan systems. The active involvement of Rydberg states, particularly the 3s state in methylated derivatives, underscores the structural dependence of Rydberg–valence state mixing.

Röder et al.[152] investigated the high-resolution VUV absorption spectrum of 2,3-DHF, identifying a broad valence transition from 5.5 to 6.8 eV followed by distinct Rydberg series converging to the ionization energy (see Fig. 6.1). The first absorption bands of 2,3- and 2,5-dihydrofuran (2,3-DHF and 2,5-DHF) both exhibit broad valence transitions from 5.5 to 6.7 eV, corresponding to HOMO $\rightarrow \pi^*$ excitation coupled with Rydberg states. Due to their differing symmetries, subsequent transitions diverge: 2,3-DHF shows only Rydberg transitions with ring-puckering vibrational structure, converging to the ionization energy. The geometry mismatch between the puckered neutral and planar cationic forms of 2,3-DHF

reduces Franck–Condon overlap, resulting in weak absorption between 6.8 and 8.4 eV. These results reveal a complex situation where both valence and Rydberg characters are mixed and likely strongly vibronically coupled, as in furan.

To investigate such UV-induced ring conversion dynamics in furan (C_4H_4O), the JRML group has recently employed time-resolved Coulomb explosion imaging (CEI) with femtosecond near-infrared pulses, which enabled direct tracing the structural changes following UV excitation at 198 nm.[54] By combining experimental CEI data with *ab initio* molecular dynamics and Coulomb explosion simulations, compelling evidence was obtained that in furan, ring opening, which occurs within 100 fs, is a dominant reaction channel[54]. That study also underscored the power of CEI in resolving real-time structural transformations during photochemical reactions.

In this chapter, we present the first steps towards similar studies of the UV-induced ring-conversion dynamics in 2,3-DHF, with a particular focus on a ring puckering pathway[152], where the oxygen atom is displaced out of the molecular plane. This process is initiated by a C–C bond $\pi \rightarrow \pi^*$ transition and involves ethylenic bond twisting, hydrogen rotation, and carbon pyramidalization, all of which can occur on a sub-100 femtosecond timescale. Alternatively, the molecule may undergo ring opening as observed in the furan[54] molecule driven by C–O bond stretching and associated with $\pi\sigma^*$ states. The main goal of this work is to identify, disentangle, and characterize possible contributions of these two reaction pathways.

6.1 Coulomb explosion simulation of 2,3-dihydrofuran fragmentation

Before performing the experiments to investigate the ring-conversion dynamics of 2,3-DHF, we employed detailed Coulomb explosion simulations (CES) for guidance. In addition to using ground-state geometries generated with the Newton-X software[57], we also performed

simulations based on trajectories obtained from *ab initio* multiple spawning (AIMS). These AIMS trajectories, initiated from 20 different nuclear configurations, were used to monitor the UV-triggered structural conversion dynamics of 2,3-DHF in its excited state.

First, we simulate the probe step of the time-resolved experiment: the Coulomb explosion of 2,3-DHF by intense NIR laser pulses. Similar to the results presented in the previous chapters, these CES were performed using ground-state geometries generated with Newton-X software[57], with the initial conditions given by Wigner-distributed geometries of 2,3-DHF at 60 K, optimized at the B3LYP/aug-cc-pVDZ level of theory. Then we distribute a single charge on each atom for Coulomb explosion, as discussed in Section 2.3.2. The resulting CES yields the final momentum distributions for these initial geometries.

Kinetic energy release

Using the momentum distribution of each fragment obtained from the CES, we calculate the kinetic energy (KE) distribution and total kinetic energy release (KER) using eq. 3.25, as shown in Fig. 6.2(a). The molecular geometry is shown in the left panel, with each fragment labeled accordingly; these labels are also used in the KER plots for clarity. The KE distributions of the four C^+ ions are slightly different, with C2 and C4 exhibiting, on average, higher KE than C1 and C3, which can be attributed to differences in the effect of proton repulsion during CE. A zoomed-in view of the C^+ region is provided in the inset of Fig. 6.2(a) for better comparison. From the KED in Fig. 6.2(b), we can see the KED of H^+ fragmented from the C1 is the lowest, due to the lower Coulomb repulsion.

Newton diagrams

As discussed in previous chapters, another useful form of data representation for visualizing molecular fragmentation and relative momentum correlations is provided by the Newton diagrams. While molecules such as thiophenone (C_4H_4OS) naturally provide two distinct marker fragments (O and S) to define molecular plane, 2,3-DHF lacks such features. In

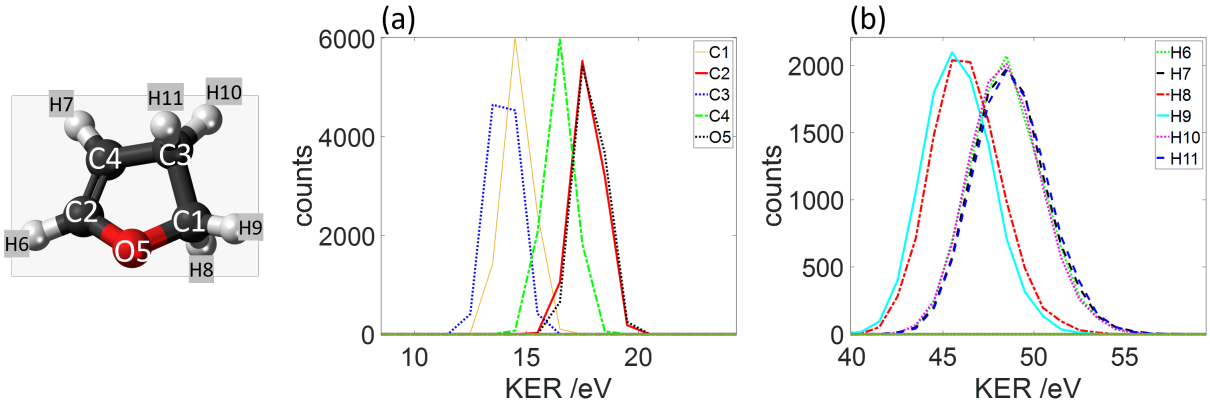

Figure 6.2: ***Simulated KE distributions for 2,3-DHF Coulomb explosions.*** *(a) KED of C^+ and (b) H^+ from Coulomb explosion simulations of ground-state 2,3-DHF.*

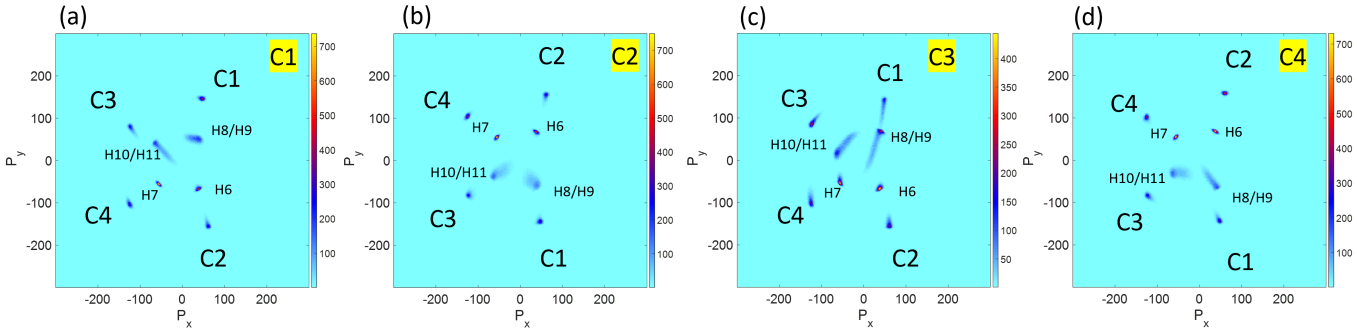

Figure 6.3: ***Newton diagrams from CES of the ground-state 2,3-DHF.*** *The O^+ momentum (not plotted) defines the x-axis, and the momentum of each C^+ fragment is used to define the momentum plane in each panel: (a) C1, (b) C2, (c) C3, and (d) C4.*

the case of 2,3-DHF, we use the momentum vector of the oxygen fragment (P_x, P_y, P_z) to define the x-axis of the Newton diagram. To define the molecular plane (the (x, y)-plane of Newton diagrams), we simulate various scenarios by pairing the oxygen vector with different C^+ fragment momentum distributions, following the procedure introduced in[54]. This approach allows us to extract meaningful spatial momentum correlations from all possible combinations of fragments.

In the Newton diagrams shown in Fig. 6.3, the outer four localized momentum spots correspond to the C^+ ions, while the inner distributions represent the H^+ ions. When using C1 or C3 to define the Newton diagram, their momentum distributions appear in the upper

part of the (x, y)-momentum plane, with C2 and C4 in the lower part. In contrast, when C2 or C4 is used for definition, their distributions appear in the upper part, and C1 and C3 are in the lower part.

Combined with the KEDs shown in Fig. 6.2, which indicate that C2 and C4 have higher kinetic energies than C1 and C3, this observation offers a strategy for analyzing experimental data: by sorting detected C^+ ions according to their kinetic energy, the highest-KE C^+ ions can be used to define the (x, y)-momentum plane and molecular frame.

Angular distribution

We also simulate the relative angular distribution of the ions by transforming the data into spherical coordinates, as introduced previously in Section 2.3.2. One of the C^+ ion momenta is selected to define the (x, y)-momentum plane, corresponding to the $\theta = 0$ plane in spherical coordinates. As a result, the momentum distribution of this reference C^+ appears as a localized point in the polar plots shown in Fig. 6.4. By plotting the angular distribution of H^+ in this transformed coordinate system, we obtain a clearer visualization of its momentum structure compared to the Newton diagrams shown in the (x, y)-momentum plane, allowing us to distinguish between two different "out-of-plane" H^+ ions (H9/H8 or H11/H10) associated with a single C^+ fragment.

6.1.1 Coulomb explosion simulation of excited-state 2,3-dihydrofuran using *ab initio* multiple spawning (AIMS) simulations

In addition to simulating the ground-state geometries of 2,3-DHF generated by Newton-X[57], we also performed CES using the *ab initio* multiple spawning (AIMS) trajectories calculated by Dr. Ryan J. MacDonell (Dalhousie University). For the dynamics simulations, multi-reference configuration interaction singles (MR-CIS) potential energies were computed on-the-fly, employing a 4-electron in 4-orbital (4, 4) complete active space self-consistent field (CASSCF) reference wave functions that were optimized with a 3 electronic state average.

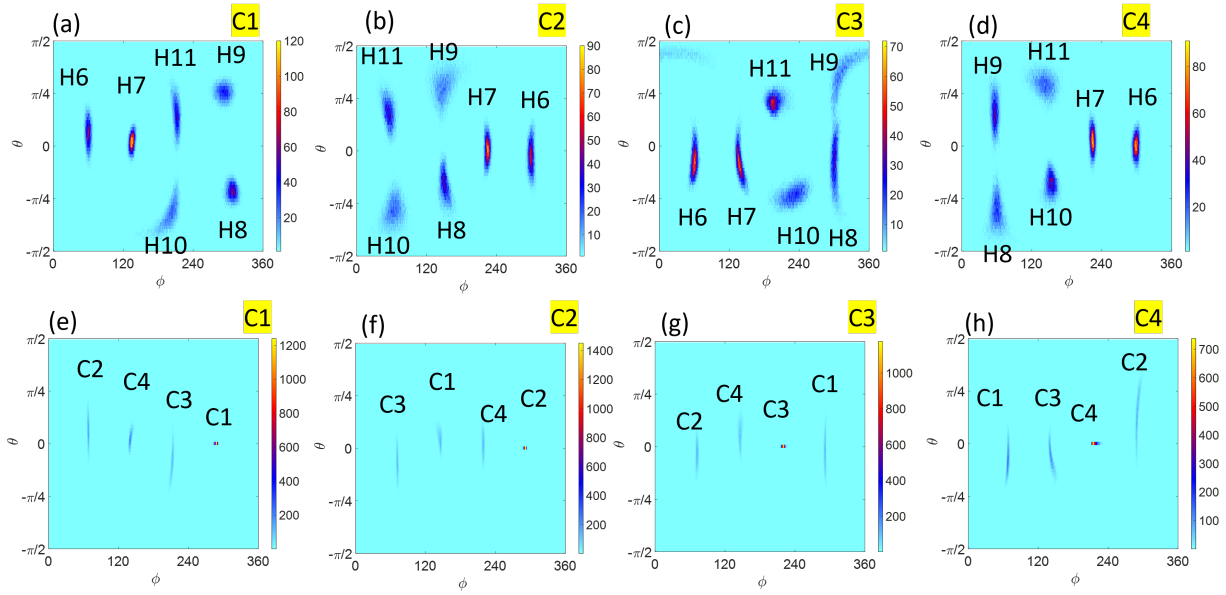

Figure 6.4: ***Three-dimensional momentum distributions of*** H^+ ***(a–d) and*** C^+ ***(e–h) ions from CES of ground-state 2,3-DHF represented in spherical polar coordinates.***

The momentum of O^+ *(not shown) is used to define the* x*-axis of the Cartesian coordinates before transformation into spherical polar coordinates, and the momentum of each* C^+ *fragment is used to define the momentum plane: (a), (e) using C1; (b), (f) using C2; (c), (g) using C3; and (d), (h) using C4.*

AIMS dynamics simulations were initiated from 26 initial conditions sampled from a Wigner distribution of the harmonic ground vibrational state of 2,3-DHF. The AIMS algorithm represents the molecular wavefunction in a basis of multidimensional Gaussian trajectory basis functions (TBFs) evolving on adiabatic electronic states. When a TBF encounters a region of strong coupling, a new basis function is spawned on the coupled electronic state. The TBF centroids evolve according to classical equations of motion, and the coefficient of each TBF evolves according to the time-dependent Schrödinger equation. A total of 1960 trajectories were generated over the course of the simulation.

Separation and categorization of geometries obtained from the simulated trajectories

To facilitate the interpretation of the CES results for the excited-state geometries of 2,3-DHF, we categorize the structures into four distinct groups based on their geometric features: (1) **ring-opened** group, (2) **ring-puckered** group, (3) **ring-closed** (non-puckered) group, and (4) **three-membered ring** group.

To categorize the excited-state geometries of 2,3-DHF extracted from the AIMS calculated trajectories, we apply the following criteria:

1. **Ring-open:** If either the C1–O5 or C2–O5 bond length exceeds 1.8 Å, the geometry is classified as ring-open. Within this group, if any of the following structural conditions are satisfied:

   - C1–C4 $<$ 1.8 Å, C1–C3 $<$ 1.8 Å, and C3–C4 $<$ 1.8 Å,
   - C2–C4 $<$ 1.8 Å, C2–C3 $<$ 1.8 Å, and C3–C4 $<$ 1.8 Å,

   then the geometry is further categorized as a **three-membered ring** group. If neither condition is met, the geometry remains in the **ring-opened** group.

2. **Ring-closing:** If both C1–O5 and C2–O5 distances are less than 1.8 Å, and all three carbon-carbon distances of C1–C3, C3–C4, and C2–C4 are also less than 1.8 Å, the

geometry is considered ring-closed. We further differentiate the puckering using the dihedral angle O–C1–C2–C3 (ranging from 0° to 180°, where 180° corresponds to a fully planar structure and 0° to a fully folded one, though the latter is rare):

- If the dihedral angle is less than 140°, the geometry is classified as **ring-puckered**.
- If the dihedral angle is greater than or equal to 140°, the geometry is classified as **ring-closed (non-puckered)**.

After categorizing the geometries into distinct groups, we perform CES for each group to compare with the experimental patterns, with an ultimate goal to track the corresponding pathways in the UV-induced structural dynamics of 2,3-DHF. We first focus on KE distributions of individual carbon ions, exploring both potential signatures of different geometries and the possibility of exploiting the KE values for identifying a specific carbon atom and using it for orienting the simulated Newton diagrams.

Kinetic energy release

In Fig. 6.5, we present the KE distributions of each carbon ion obtained from the CES of all excited-state geometries of 2,3-DHF combined. The trend in average KE values across trajectories is consistent with the ground-state CES results, where C_2 and C_4 show slightly higher KE compared to C_1 and C_3, mainly because of the two hydrogens attached to these carbon atoms.

With the previously established categorization of the excited-state geometries of 2,3-DHF, as the next step, we evaluate the individual KE distributions obtained from CES for each structural group.

For the **ring-opened** group, illustrated in Fig. 6.6, the left panel shows one representative ring-opened geometry projected onto the (x, y)-plane. Out of a total of 12,167 geometries in this group, 7,272 geometries exhibit ring opening via O–C1 bond extension, 1,614 via O–C2 bond extension, and the remaining structures involve simultaneous extension of

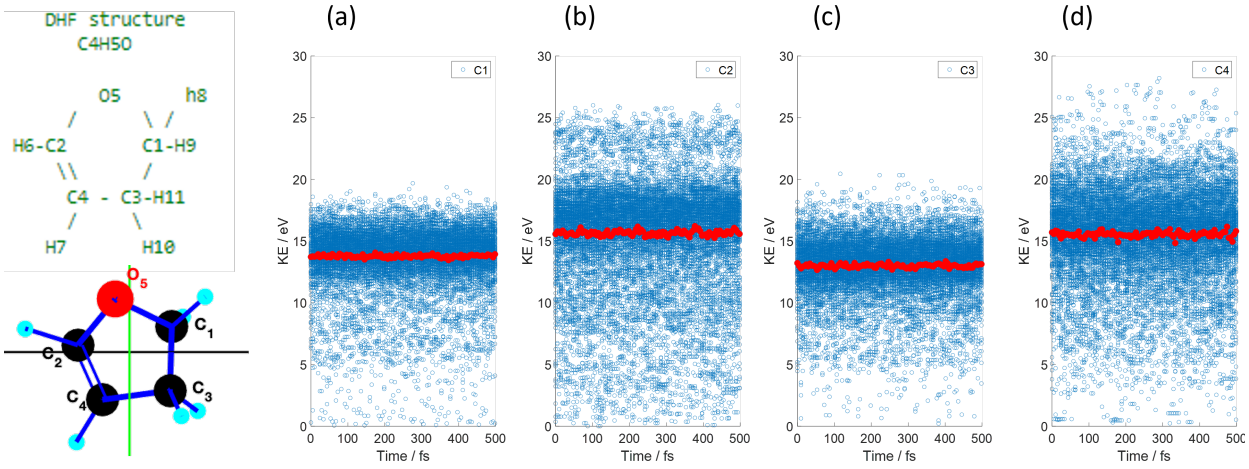

Figure 6.5: ***KE obtained from CES of the AIMS trajectories for all excited-state 2,3-DHF geometries as a function of time for each C^+ fragment.***
(a) C1, (b) C2, (c) C3, and (d) C4. Blue circles represent the KE values of individual geometry from the trajectories, while the red dots represent the average values of the trajectories at each time.

both bonds or additional carbon-carbon bond elongation. In this group, a larger population of low-KE C^+ ions is observed. This trend arises because the ring opening reduces Coulomb repulsion within the carbon ring, resulting in lower KER upon explosion. However, the difference between the individual carbon ions' KEs, which was exploited in[54] for identifying carbon ion positions, is not pronounced, while still correlating with the number of hydrogen atoms attached, similar to the results for the 2,3-DHF ground state shown in Fig. 6.2.

For the **ring-puckered** group, shown in Fig. 6.7, a total of 2,518 geometries are categorized. The left panel shows one representative geometry, where the (x, y)-projection highlights the non-open ring structure, and the xz-projection clearly shows the puckering feature, with the oxygen atom pointing out of the molecular ring plane. In this group, there is a negligible population of low-KE C^+ ions, similar to what is observed for the **ring-closed (non-puckered)** group. The latter consists of 15,245 geometries, as illustrated in Fig. 6.8. While the geometric distinction between these two groups is apparent in the (x, z)-plane projection, the KE distributions are very similar, making it difficult to distinguish between them based on the KE data alone.

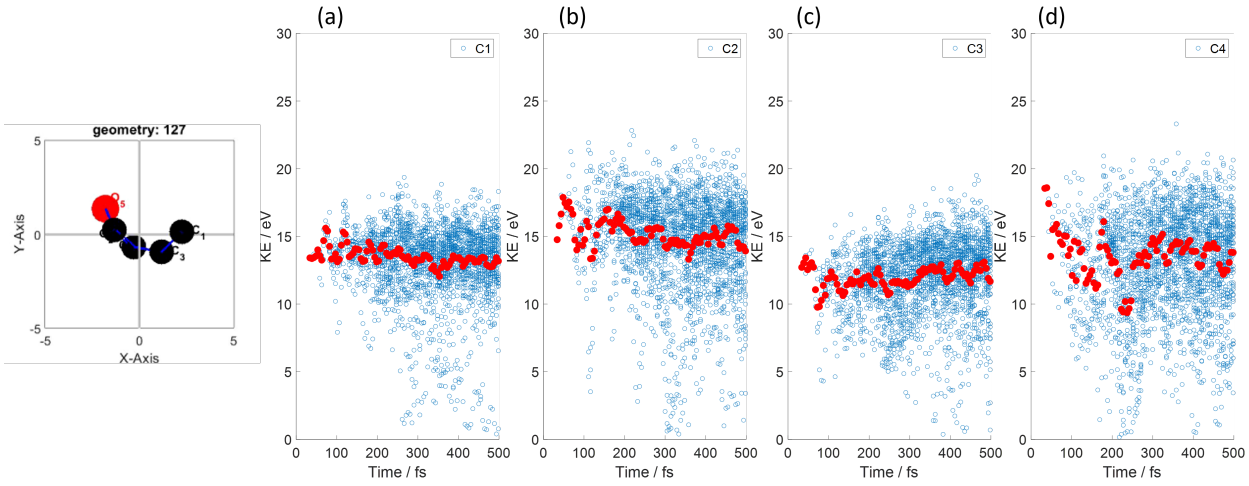

Figure 6.6: *Same as Fig. 6.5 but only for the ring-opened geometries from CES of excited-state 2,3-DHF.*

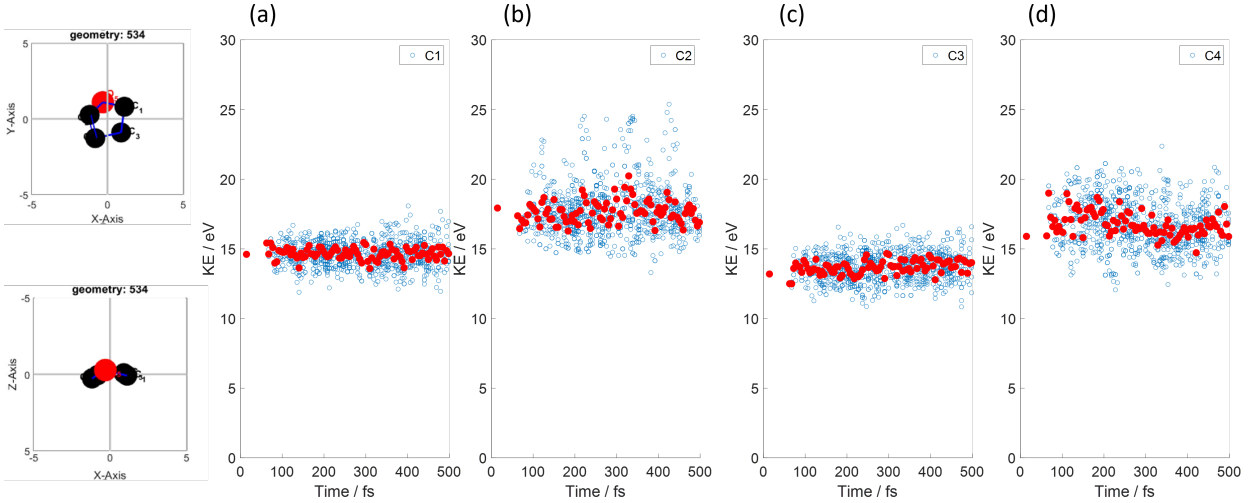

Figure 6.7: *Same as Fig. 6.5 but for the ring-puckered geometries from CES of excited-state 2,3-DHF.*

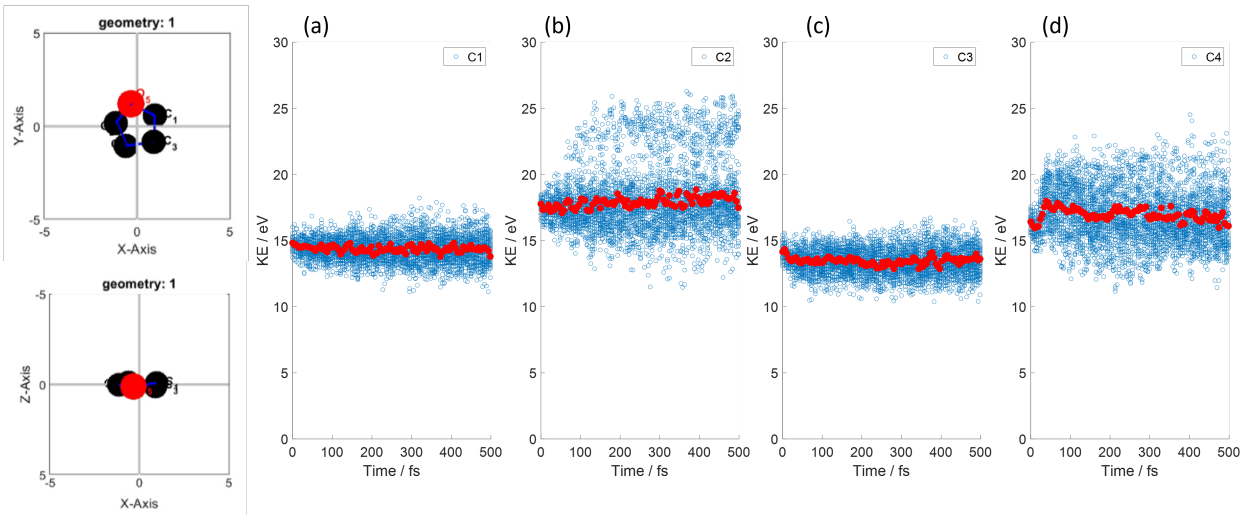

Figure 6.8: ***Same as Fig. 6.5 but for the ring-closed, non-puckered geometries from CES of excited-state 2,3-DHF.***

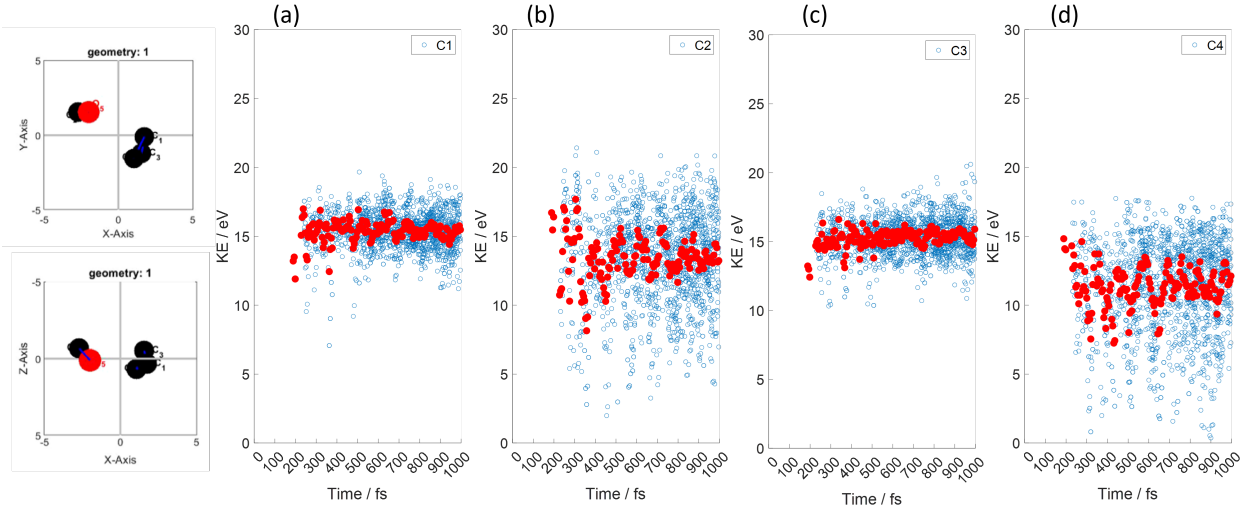

Figure 6.9: ***Same as Fig. 6.5 but for the three-membered ring group from CES of excited-state 2,3-DHF.***

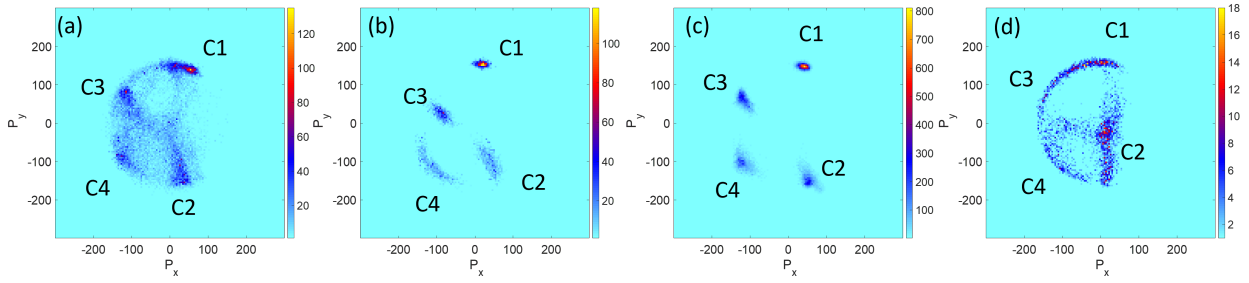

Figure 6.10: ***Newton diagrams obtained from CES based on the AIMS trajectories for different excited-state geometries of 2,3-DHF.***
(a) ring-opened group; (b) ring-puckered; (c) ring-closed (non-puckered) group and (d) ring-closed group.

For the **three-membered ring** group, shown in Fig. 6.9, a total of 1,734 geometries are included. In contrast to the **ring-opened group**, where all carbon ions tend to have rather low KE, the $C1^+$ and $C3^+$ carbon ions in the three-membered ring group display relatively stable, slightly higher KE values. At the same time, the KEs of the other two fragments, which initially had one hydrogen attached to them, are typically lower. This reflects a localized structural rearrangement, where the C–O bond is typically broken at the C2 site, and the C1 and C3 carbon atoms end up on the side of the three-membered ring opposite the oxygen atom.

Newton diagrams and momentum distributions in 3D

As the next step, we consider the simulated Newton diagrams for each categorized geometry group. In these simulations, the momentum vector of O^+ is used to define the x-axis of the molecular momentum plane. Here we use the momentum of the $C1^+$ ion, together with O^+, to define the molecular (x, y)-plane. By comparing the Newton diagrams in the (x, y)-plane for each group, we observe that as the molecular ring structure becomes more distorted (from ring-closed to ring-puckered, ring-opened, and three-membered ring), the corresponding Newton diagram features become increasingly diffuse.

In the CEI experiments, the position of any detected carbon ion within the molecular

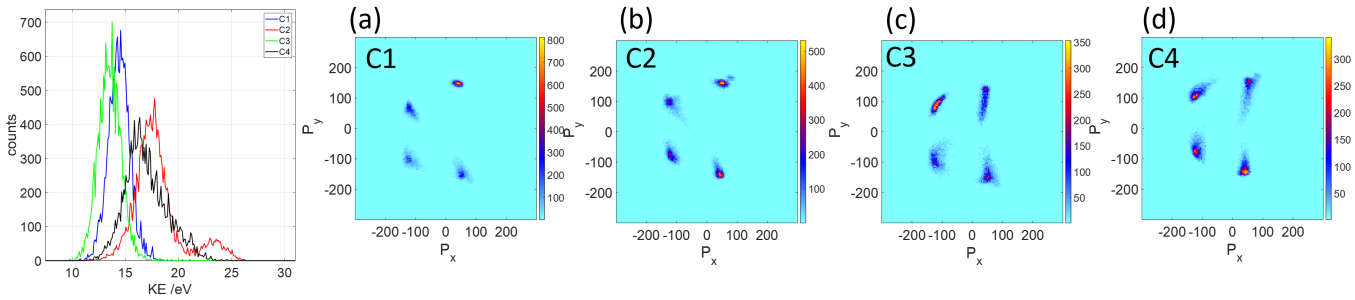

Figure 6.11: ***Newton diagrams obtained from CES of 2,3-DHF based on the AIMS trajectories for the ring-closed (non-puckered) group .***
O^+ momentum (not plotted) defines the positive x-axis and the momentum of different C^+ fragments is used to define the momentum plane: (a) C1, (b) C2, (c) C3, and (d) C4.

ring is initially unknown. To understand how this uncertainty would affect the Newton diagrams, we analyze the simulated patterns where different carbon ions are used to define the molecular plane. In Fig. 6.11, the Newton diagrams, generated from the CES of AIMS trajectories for the ring-closed (non-puckered) group are shown, each using a different carbon ion fragments together with the O^+ momentum vector to define the molecular plane. Among all options, using $C1^+$ (which has neither the highest nor the lowest KE) to define the molecular plane produces the clearest Newton diagram, with the carbon ion momentum distributions appearing most localized. In contrast, using $C3^+$ or $C4^+$, neither of which is adjacent to the oxygen atom in the ring-closed geometry, results in somewhat less distinct Newton diagrams.

The dependence of the Newton diagrams on the choice of the carbon ion used to define the molecular plane is even more pronounced for ring-puckered and ring-opened geometries, as seen in the upper panels of Figs. 6.12 and 6.13, respectively. There, the appearance of the simulated momentum correlation patterns changes significantly depending on which specific carbon is chosen. This reflects a pronounced non-equivalence of individual carbon ions and the non-planar geometries of those configurations.

To avoid averaging over all these patterns in the experiment and to improve guidance in interpreting the experimental data based on the simulated KEs, we organize the ring-

puckered and ring-opened geometry groups according to the KE distributions of the carbon ions, as suggested in Ref[54]. The simulated KE distributions for the ring-puckered and ring-opened groups are presented in the upper left panels of Fig. 6.12 and Fig. 6.13, respectively. Next, for each geometry, we reorder the carbon ions according to their KE, such that C1 always represents the highest-KE carbon and C4 the lowest-KE carbon, as shown in the lower left panels of Figs. 6.12 and 6.13. Using each reordered carbon ion along with the momentum of O^+ to define the molecular plane, we plot the resulting Newton diagrams for the ring-puckered group in Fig. 6.12(e-h). We apply the same procedure to the ring-opened group, as shown in Fig. 6.13(e-h).

By comparing the Newton diagrams before and after the carbon ion rearrangement, we observe that the differences resulting from the choice of reference C^+ used to define the molecular plane are significantly reduced after the rearrangement. This indicates that relying solely on the KE distribution of the C^+ ions to assign carbon positions for 2,3-DHF may be problematic, in contrast to the results obtained[54] for furan. Furthermore, even the distinction between the ring-opened and ring-puckered groups becomes less pronounced. In contrast, both of these groups show clear differences when compared to the ring-closed (non-puckered) group, where there are almost no low-momentum C^+ ions observed in the Newton diagrams, as shown in Fig. 6.10(c).

In addition to Newton diagrams, we can also visualize the simulated (or measured) momentum distributions in 3D using scatter plots for the Px, Py, Pz momenta of each ion fragment, as shown in Fig. 6.14. An interesting feature is observed for the ring-puckered group: the momentum distribution of $C4^+$ exhibits an 'X'-shaped pattern, while $C2^+$ and $C3^+$ show two distinct localized lobes along the z-axis. This characteristic shape arises from the puckered geometry of the molecule, where the oxygen atom points out of the plane. Since the puckering can occur in two directions, which is either 'up' or 'down' relative to the plane of the ring, the resulting momentum distributions reflect both types of geometries, producing double-lobed features along the Pz axis in the $C2^+$, $C3^+$, and $C4^+$ ion momentum

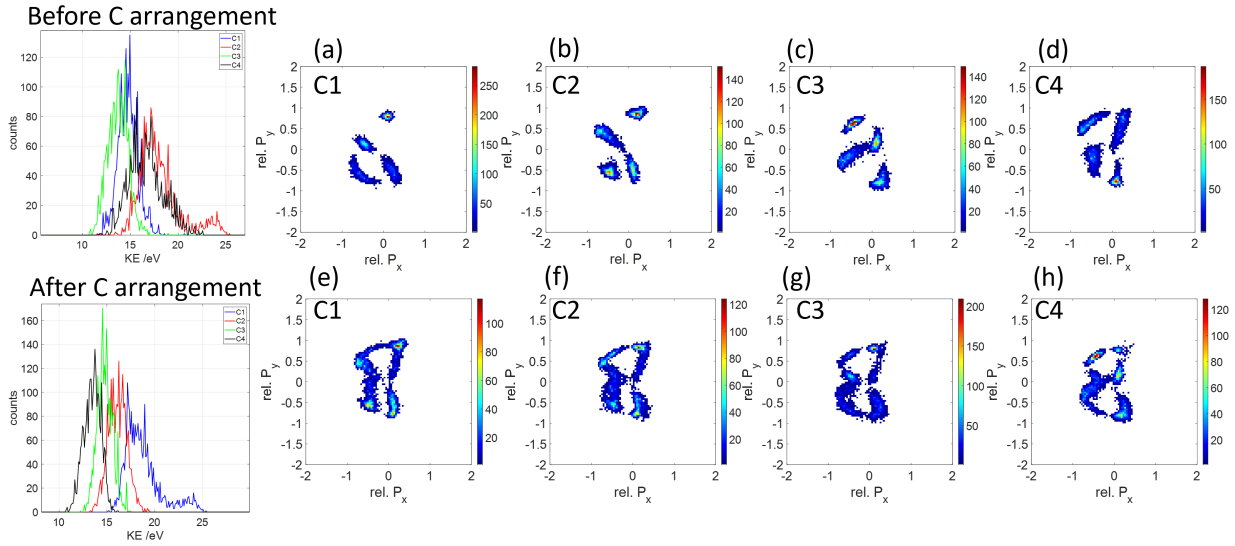

Figure 6.12: ***Newton diagrams obtained from CES of 2,3-DHF based on the AIMS trajectories for the ring-puckered group.***

The upper row shows the Newton diagrams constructed before carbon ion rearrangement using (a) C1, (b) C2, (c) C3, and (d) C4 as the second reference ion (in addition to O^+) for defining the molecular plane. Panels (e-h) show the Newton diagrams after rearranging the carbon ions by their KE, where (e) C1 is the highest KE carbon ion and (h) C4 is the lowest. The molecular plane is defined by O^+ and the corresponding reordered carbon ion.

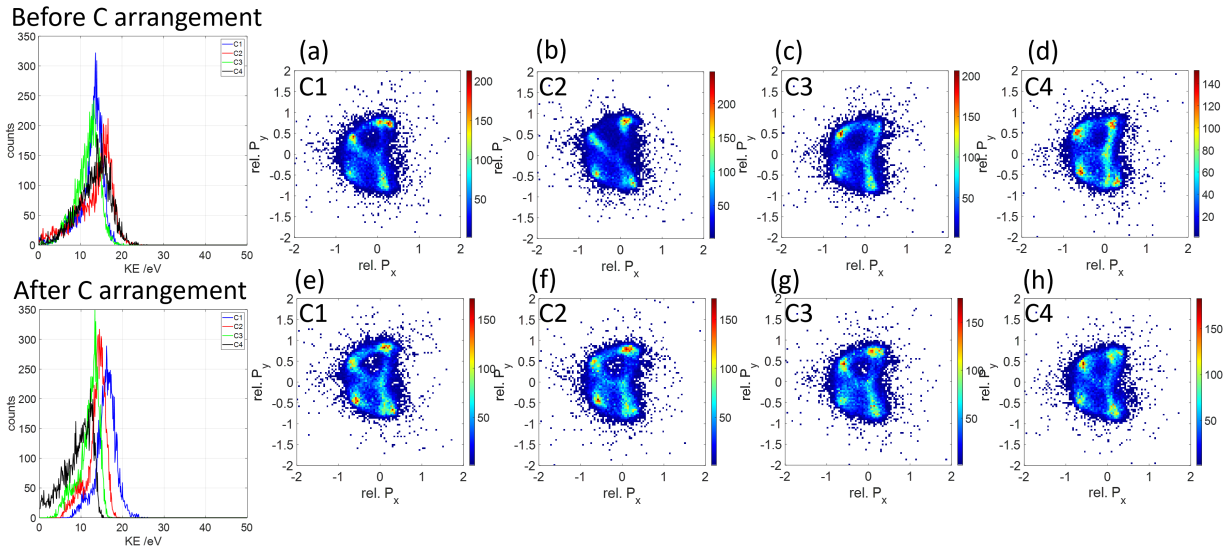

Figure 6.13: ***Same as Fig. 6.12 but for ring-opened group from CES of excited-state 2,3-DHF .***

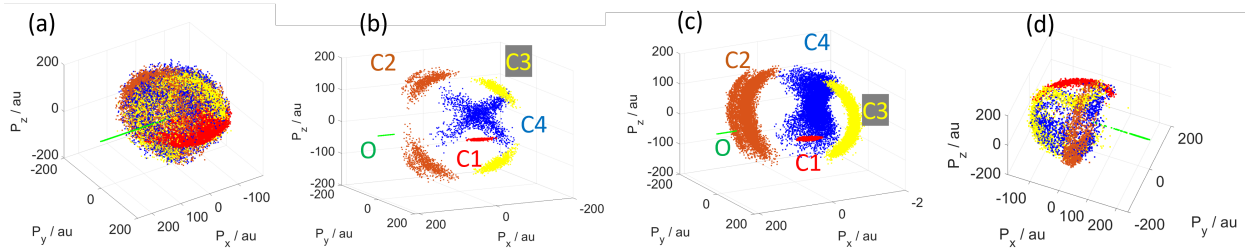

Figure 6.14: ***3D momentum distribution of carbon ions obtained from Coulomb explosion simulations of the AIMS trajectories for excited-state geometries of 2,3-DHF***
Categorized in (a) ring-opened group; (b) ring-puckered group; (c) ring-closed (non-puckered) group and (d) ring-closed group. Red: C1, orange: C2, yellow: C3, blue: C4; green: O.

distributions.

Angular distribution

Another useful way to distinguish between structural groups is to examine the relative angular distribution of ion momenta. As discussed earlier for the static 2,3-DHF CES (as well as for ethylene and 2(5H)-thiophenone in the previous chapters), we transform the momentum distributions obtained from the CES from Cartesian to spherical coordinates to spherical polar coordinates, as shown in Fig. 6.15(a-c). The angular distribution of the $C1^+$ carbon ion is omitted, since it is used to define the molecular plane and therefor shows no spread in polar angle. Under this representation, the characteristic "X"-shaped structure of $C4^+$ and the doubled-lobed features along the polar angle θ axis of $C2^+$ and $C3^+$ become more clearly visible in the ring-puckered group.

A notable feature observed in the angular distributions of carbon ions is the difference in the azimuthal angle ϕ spread among the structural groups as shown in Fig. 6.15(d-f). For the ring-closed group, the ϕ distribution of each carbon ion is relatively narrow and confined within a small ϕ angular range. For the ring-puckered and especially for ring-opened group, the ϕ distributions are significantly broader. Since explicit time information is available from the AIMS simulations, in Fig. 6.16, we also plot the carbon ion azimuthal ϕ angular distribution as a function of time for the different structural groups. For the ring-closed

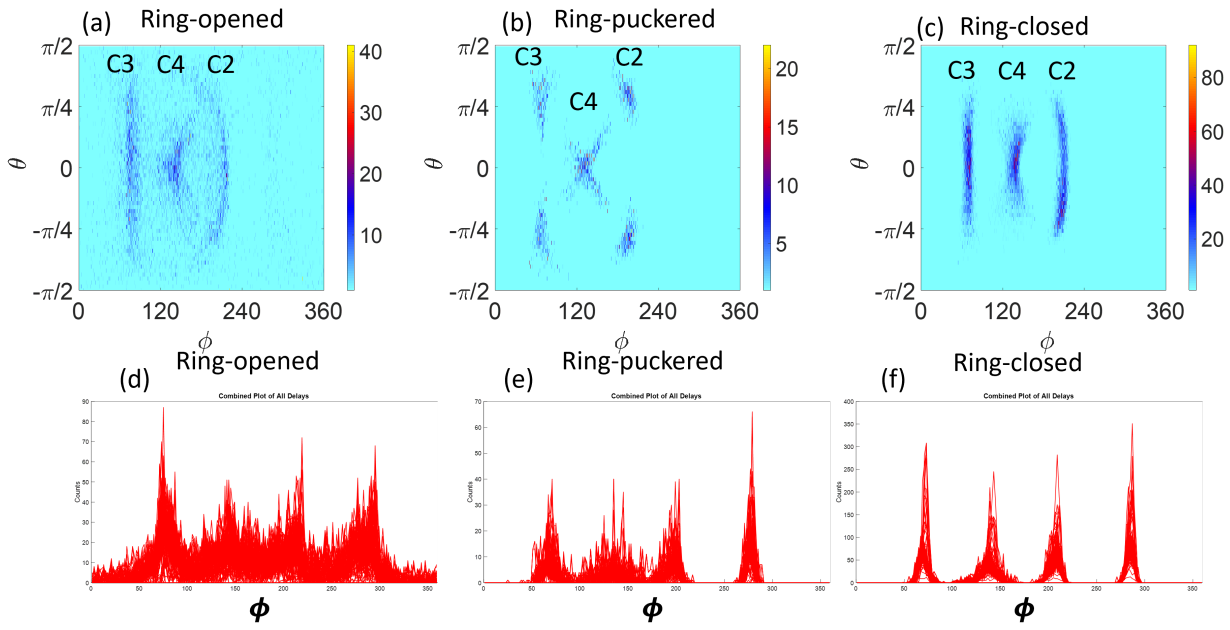

Figure 6.15: ***(a–c) 3D momentum distributions of C^+ ions in spherical polar coordinates from CES of AIMS trajectories for excited-state 2,3-DHF; (d–f) corresponding azimuthal angle distributions.***
(a) and (d): ring-opened group; (b) and (e) ring-puckered group; (c) and (f) ring-closed (non-puckered) group. C1 is omitted in the upper row since it is used to define the (x, y)-plane and, thus, does not have any spread in the polar angle.

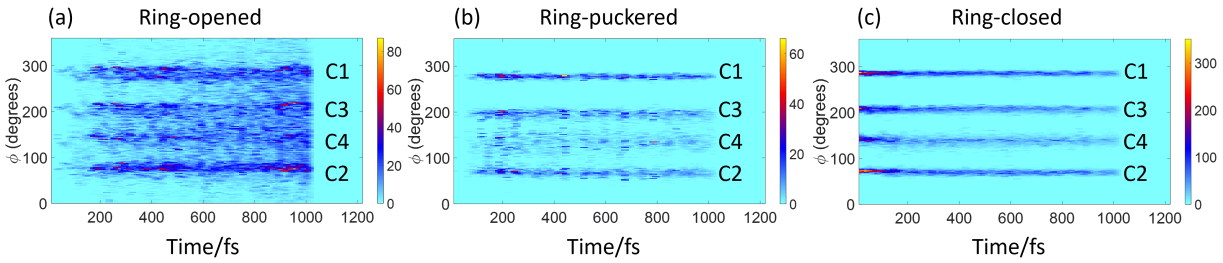

Figure 6.16: ***Azimuthal angle ϕ for carbon ion momenta as a function of time obtained from CES of the AIMS trajectories for excited-state 2,3-DHF***
Azimuthal angle ϕ for carbon ion momenta as a function of time obtained from CES based on the AIMS trajectories for excited-state geometries of 2,3-DHF : (a) ring-opened group; (b) ring-puckered group and (c) ring-closed (non-puckered) group

group, the distribution remains relatively narrow and confined to a small ϕ angle range for each carbon. In contrast, for the ring-opened and ring-puckered groups, the ϕ angular distributions broaden significantly over time, with an especially pronounced increase for the ring-open geometries. This reflects larger structural distortion and increased angular dispersion of the carbon ion momenta as the molecular ring structure evolves with time.

6.2 Coulomb explosion imaging of UV-induced ring conversion dynamics in 2,3-dihydrofuran

For experimental studies of UV-induced dynamics in 2,3-dihydrofuran, we employed a 200 nm pump pulse produced by fourth harmonic generation (FHG) using BBO crystals and the PULSAR setup, as described in Chapter 3. As can be seen from the 2,3-DHF absorption spectra shown in Fig. 6.1, at this wavelength one can expect to initiate rich molecular dynamics. As the first step towards these studies, we examined whether the NIR-induced Coulomb explosion of 2,3-DHF could yield well-resolved structural information.

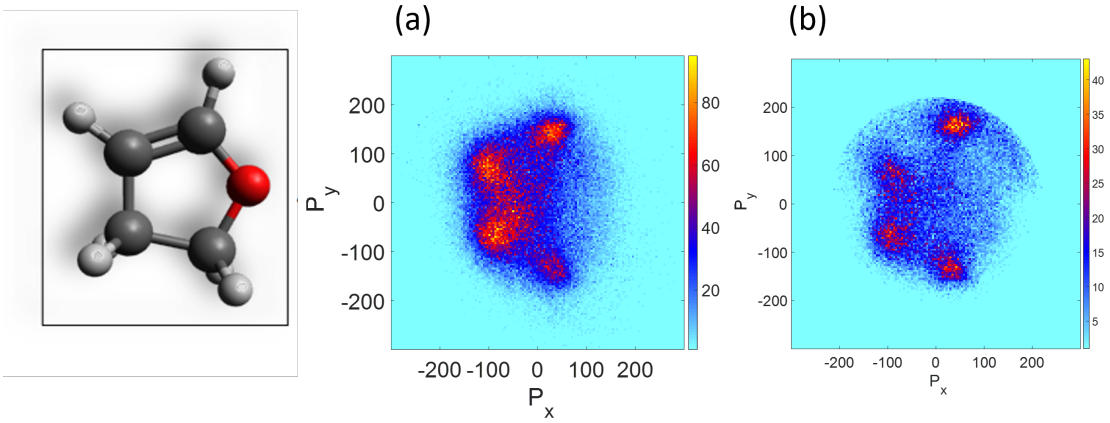

Figure 6.17: ***Non-normalized Newton diagrams of the four- (a) and five-body (b) coincidence channels shown in*** (x, y)***-plane from IR-probed only 2,3-DHF experiment***

6.2.1 Coulomb explosion imaging of 2,3-dihydrofuran with intense NIR pulses

We first employed an intense 790 nm NIR pulse to perform "static" CEI experiment on 2,3-DHF. The duration (28 fs FWHM) and the peak intensity (1.3×10^{15} W/cm^2) of the NIR pulse were the same as used in the experiments on ethylene described in Chapter 4. To visualize the molecular structure, we focused on analyzing the four- or five-body "incomplete" coincidence channels in which the molecule is expected to be fully fragmented, while three or four carbon ions and one oxygen ion are detected. The momentum vector of O^+ was used to define the x-axis of the molecular plane, and the first detected C^+ ion was used to define the (x, y)-molecular plane. This approach yields a clear visualization of the molecular structure, as illustrated in Fig. 6.17.

Compared to the ground-state CES of 2,3-DHF (see Fig. 6.3), the experimental data for both channels contain significantly more background events with low-momentum carbon ions. The distributions of the carbon ion momenta in the simulated Newton diagrams are also more localized compared to the experimental data. While the peaks of the measured KEDs (Fig. 6.18) agree reasonably well with the CES results shown in Fig. 6.2, the momen-

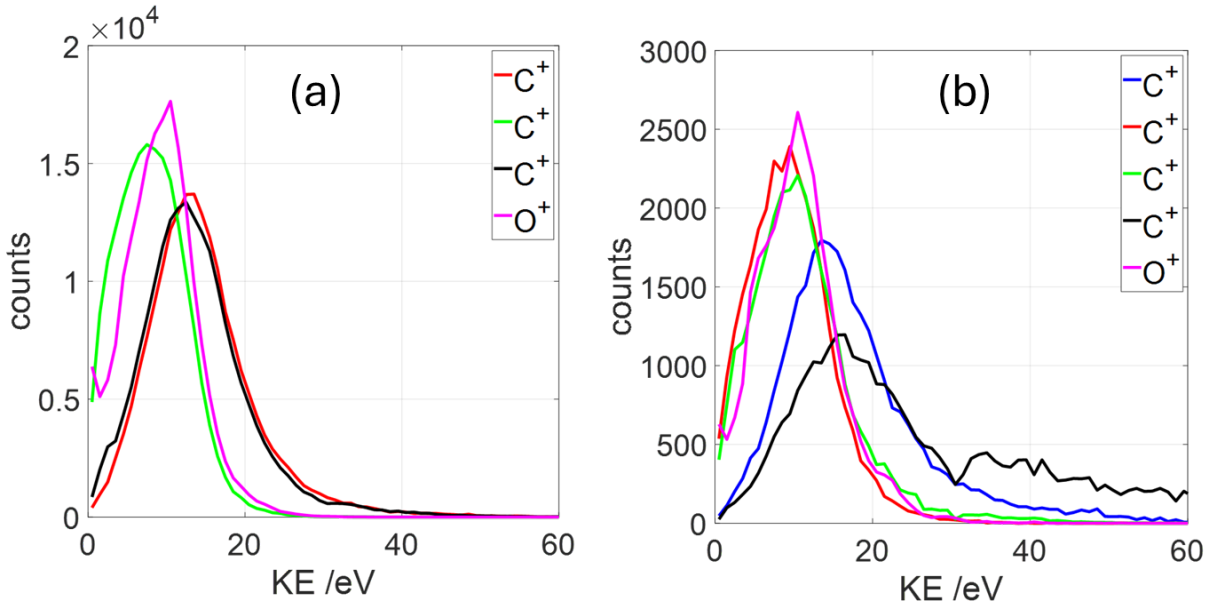

Figure 6.18: ***KEDs of the four-body (a) and five-body (b) coincidence channels of 2,3-DHF from experiment.***
(a): $C^+ + C^+ + C^+ + O^+$ *channel; (b):* $C^+ + C^+ + C^+ + C^+ + O^+$. *Both channels are from the NIR- only measurement*

tum distributions from experiment are significantly broader. Nevertheless, the experimental Newton diagrams shown in Fig. 6.17 clearly reveal the signatures of all four carbon atoms in the molecular ring, establishing a solid foundation for pump–probe experiments in which a UV pulse is used to initiate the ring-conversion dynamics.

6.2.2 UV pump–NIR probe experiment on 2,3-dihydrofuran

As a next step, we employed 100 fs, 200 nm UV pulses obtained via FHG as described in Chapter 3, as the pump pulse to induce ring conversion dynamics in 2,3-DHF. To probe the dynamics, we employed the same NIR pulses as for the NIR only measurements described in the previous section. In this time-resolved experiment, we focus on four-body fragmentation channels in which three C^+ ions and the O^+ ion were detected.

For the results presented here, negative values of the pump–probe delay indicate that the UV pulse arrives earlier than the IR pulse, while positive values correspond to the IR

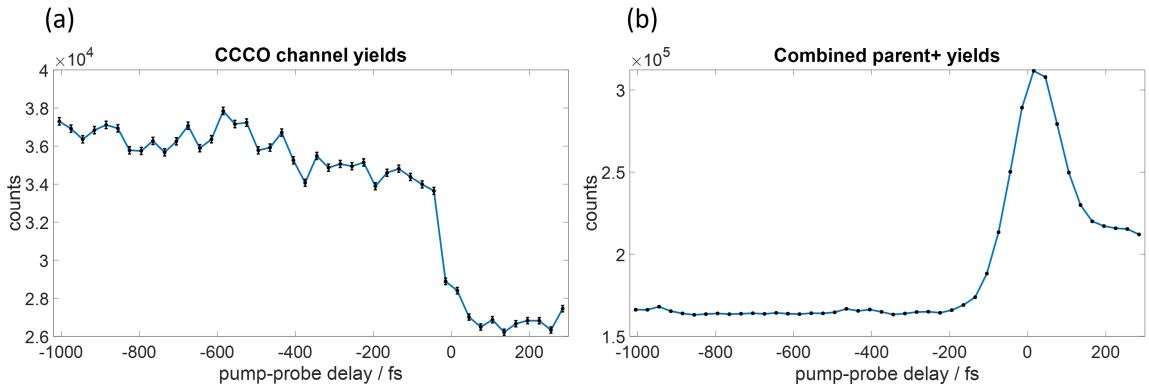

Figure 6.19: ***(a) Delay-dependent yield of four-body coincidence channel:*** $C^+ + C^+ + C^+ + O^+$ ***of 2,3-DHF. (b) Parent ion*** ($C_4H_6O^+$) ***yield as a function of pump–probe delay.***

pulse arriving before the UV pulse. As a first step in analyzing the pump–probe dynamics, we examine the yield of the $C^+ + C^+ + C^+ + O^+$ coincidence channel as a function of pump–probe delay. As shown in Fig. 6.19(a), when the UV pulse arrive before the NIR probe, the yield of the four-body coincident channel increases. As a reference, in Fig. 6.19(b), we plot the delay-dependent parent ion ($C_4H_6O^+$) yield. While the parent ion yield is dominated by the cross-correlation between the UV and NIR pulses, it exhibits the opposite trend, decreasing when the UV pulse arrives before the NIR. Similar behavior for both channels was observed in[54] for furan. The increase in the coincidence channel yield can be rationalized considering the increase in multiple ionization and fragmentation probability because of the energy deposited by absorption of the 200 nm UV photon. Furthermore, multiple ionization can be significantly enhanced if some molecular bonds stretch because of the UV excitation of the molecule[156]. At the same time, the increase in multiple ionization and fragmentation depletes the yield of singly charged, bound parent ions, resulting in the corresponding decrease at neagative delays in Fig. 6.19(b).

Newton diagrams

After extracting the momentum information from the experimental data, we analyze the dependence of the four-body coincidence channel on the delay between the UV pump and NIR probe pulses. In Fig. 6.20, we present the Newton diagrams (normalized to the momentum distribution of the O^+ ion) for six different pump-probe delays, ranging from -1020 fs to $+300$ fs. All diagrams share the same color scale. As before, we use the momentum vector of O^+ to define the positive x-axis of the molecular reference frame, together with the momentum of the first detected C^+ ion to fix the (x, y)-plane. Since the arrival time (and, thus, the detection order) does not depend on the initial carbon position within the ring, this procedure effectively averages the experimental Newton diagram over all representations from CES shown in Figs. 6.11, 6.12 and 6.13. in Fig. 6.20.

By comparing the Newton diagrams at different delays, the most pronounced difference is the increase in the ion yield for UV-excited molecules (i.e., at negative delays, where the UV pump pulse precedes the NIR probe), as already observed in Fig. 6.19(a). Beyond this, it is difficult to clearly identify any effect of the UV pump pulse on the shape of the correlated momentum distributions. While from the 2D plots suggest that more carbon ions with low P_x and P_y momenta are produced when the UV pulse arrives earlier, a quantitative analysis of the 1D momentum projections or the KE distributions does not support this observation beyond the level of statistical error.

Angular distributions

In order to further explore potential signatures of UV-induced dynamics in the measured four-fold coincidence data, we consider the delay dependence of the measured angular distributions of the fragments in the molecular frame. Specifically, Fig. 6.21(a) shows the azimuthal angular distribution ϕ of the carbon ion momentum vectors relative to the O^+ momentum in the four-body coincidence channel ($C^+ + C^+ + C^+ + O^+$) as function of pump-probe delay. Fig. 6.21(b) displays the 1D projections of this distribution onto the azimuthal

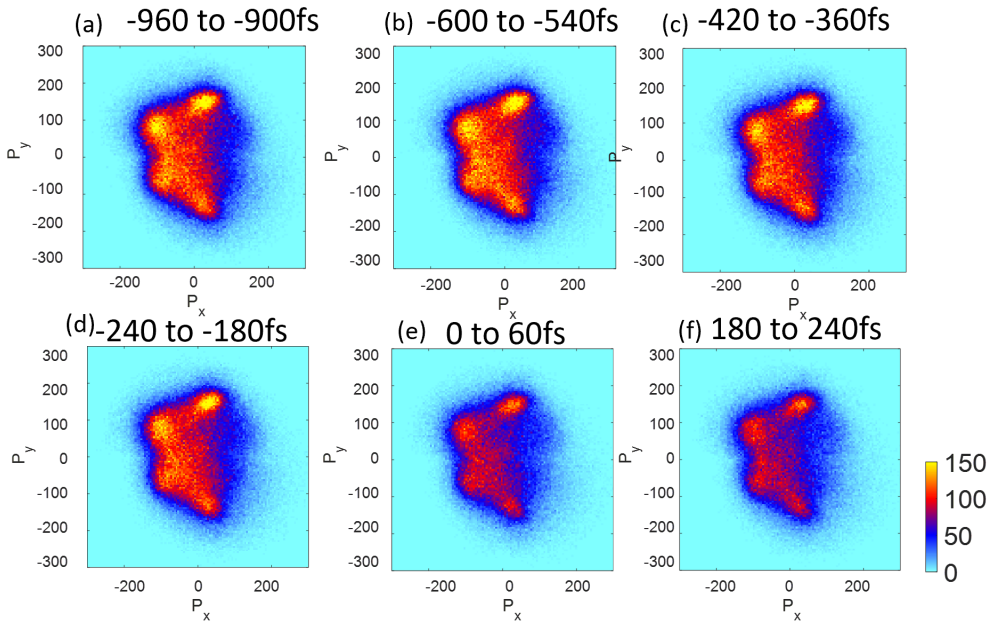

Figure 6.20: ***Newton diagrams of the four-body coincidence channel of 2,3-DHF at different pump–probe delay bins.***
The molecular plane is defined using the momentum vector of O^+ *as the* x*-axis, together with the momentum vector of the first detected* C^+ *ion. Panels correspond to different pump–probe delay ranges: (a)* -960 *to* -900 *fs; (b)* -600 *to* -500 *fs; (c)* -420 *to* -360 *fs; (d)* -240 *to* -180 *fs; (e)* 0 *to* 60 *fs; and (f)* 180 *to* 240 *fs. Both* P_x *and* P_y *are plotted over the range* -300 *to* 300 *a.u. in steps of* 100 *a.u., and the color scale is fixed for all panels shown in the bottom right. Negative delay values indicate that the UV pulse arrives before the IR pulse (UV early, IR late), while positive values indicate that the IR pulse arrives before the UV pulse (UV late, IR early)*

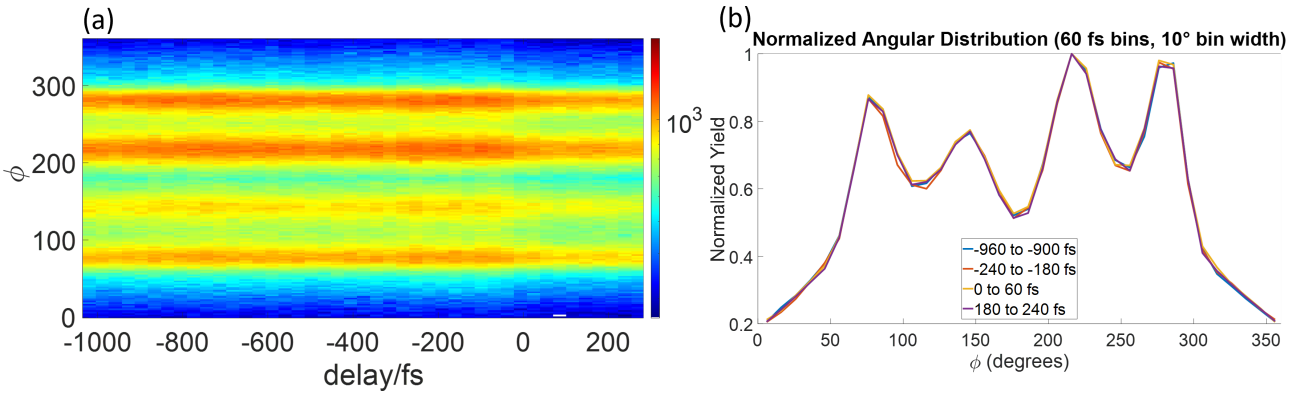

Figure 6.21: ***Angular distribution of the carbon ions from 2,3-DHF experiment as a function of pump–probe delay.***
(a) Azimuthal angular distribution of the three detected C^+ fragments relative to the O^+ momentum vector as a function of pump–probe delay. (b) Corresponding one-dimensional angular distribution projected onto the azimuthal angle ϕ axis at different pump–probe delays: -960 to -900 fs (blue), -240 to -180 fs (red), 0 to 60 fs (orange), and 180 to 240 fs (purple).

angle (ϕ) axis at four different pump–probe delays. These results can be directly compared with the CES results for angular distributions shown in Figs. 6.15 and 6.16. While the experimental data shown in Fig. 6.21(b) resemble the average of the simulated angular distributions for different excited-state geometries of the 2,3-DHF (Fig. 6.15(d-f)), the distributions do not change with the delay beyond the statistical uncertainty. A clear delay dependence that can be observed in Fig. 6.21(a) once again reflects the increase of the four-body coincidence channel yield upon UV excitation but does not reveal any clear change in the measured angular distribution.

6.3 Conclusion and outlook

The results presented in this chapter lay the groundwork for using CEI to study UV-induced ring conversion dynamics in 2,3-dihydrofuran. Coulomb explosion simulations based on the time-dependent geometries obtained using ab initio multiple spawning trajectories demonstrate including different ring-conversion pathways, ring puckering, ring opening, and the

formation of a three-membered ring, can be disentangled and characterized using time-resolved CEI. However, in contrast to our recent study of UV-induced dynamics in furan[54], where sorting the detected carbon ions according to their KE enabled unique identification of individual carbon positions in the ring-open products, for 2,3-DHF, this sorting scheme was shown to be less successful. Consequently, the experimental Newton diagrams used a molecular reference frame determined using a random carbon ion, which still works well for ring-closed geometries, but may introduce ambiguity for imaging ring-opened or ring-puckered structures.

To overcome this limitation, further analysis and data sorting routines, potentially including a combination of fragments' KEs, angles between carbon and oxygen momenta or between different carbon ion momentum vectors, might need to be considered. First steps in this direction are outlined in Ref.[142] for C_7H_8 isomers, which do not contain any unique marker atoms. Furthermore, for 2,3-DHF, where the KE difference between different carbon fragments is largely determined by the number of hydrogen atoms initially attached to them (see Figs. 6.2, 6.5-6.8), the angles between carbon and hydrogen ion momenta may help identify initial carbon positions. However, such analysis will require higher-order coincidence measurements, which would require detecting at least two protons in addition to carbon and oxygen ions considered in this work. Such multi-coincidence measurements will likely become feasible soon[140], especially with the availability of high-repetition-rate laser and XFEL sources.

The initial experimental results presented in this chapter suggest that detailed information about UV-induced ring conversion dynamics in 2,3-DHF could potentially be obtained using CEI driven by intense NIR laser pulses. However, no clear structural information has been extracted from the recorded pump-probe data. The reasons for this remain unclear. First, the pump-probe contrast of the experiment could have been insufficient. While the yields of both the singly charged parent ion and four-body coincidence channel used to characterize molecular geometry show clear delay dependence (see Fig. 6.19), the con-

trast for both channels is about half that observed for the same channels in furan[54], where ring opening dynamics could be clearly visualized. Second, the signal-to-noise ratio of the measured CEI patterns in combination with the lack of reliable routine for identifying initial carbon ion positions could be a limiting factor for identifying contributions from ring opening or ring puckering processes. Thus, further analysis and follow-up experiments with improved signal-to-background ratio are needed to achieve the ultimate goals of this study. Improvements to the experimental setup, including better background pressure in the reaction chamber, employing shorter UV pulses, and increasing the repetition rate of the laser could provide decisive steps forward. Despite current limitations, the initial experimental data and simulation results suggest that 2,3-DHF is a promising model system for observing prototypical ring conversion dynamics.

Chapter 7

Summary and outlook

This dissertation presents a detailed investigation of the applications of Coulomb explosion imaging (CEI) and pump–probe methodologies for probing ultrafast molecular dynamics in three representative systems: ethylene, 2(5H)-thiophenone (thiophenone), and 2,3-dihydrofuran (2,3-DHF). By combining experimental data with classical Coulomb explosion simulations and time-resolved coincidence ion momentum imaging, we explore the fragmentation behavior and structural evolution of these molecules upon ionization and photoexcitation.

In the case of ethylene, we systematically studied complete and incomplete three-, four-, and five-body fragmentation pathways initiated by strong near-infrared laser pulses. Despite the known overestimation of kinetic energies (KEs) in classical simulations, the normalized momentum correlations, visualized through Newton diagrams, show strong agreement with experimental results. This confirms the robustness of CEI in analyzing multi-body fragmentation dynamics and lays a methodological foundation for future time-resolved studies in more complex polyatomic systems. A more quantitative agreement with experiment is achieved if the realistic potential energy surfaces for the final state of the fragmentation are available.

More specifically, we have demonstrated the separation of the concerted and two different

sequential channels for complete three-body breakup of ethylene. We have separated 'cis-' and 'trans-fragmentation' pathways for complete four-body fragmentation and analyzed 3-, 4-, and 5-particle coincidence data obtained from the complete atomization of the molecule. Our results show that the latter breakup pathway would be optimal for CEI; however, for incomplete channels, they contain significant background contributions that increase with the number of detected protons. Complete 6-particle detection for this channel has not been realized in this work and remains a near-future goal, which, based on recent results for other molecules[140], is realistic to achieve.

For thiophenone, we successfully captured sub-200 fs UV-induced ring-opening dynamics using pump–probe CEI. Analysis of two distinct four-body coincidence channels, $C^+ + C^+ + O^+ + S^+$ and $H^+ + C^+ + O^+ + S^+$, revealed consistent changes in angular distributions, particularly in the momentum vector of O^+, indicating transitions from ring-closed to ring-open geometries. A good agreement between these channels and supporting CE simulations validates the structural sensitivity and temporal resolution of the technique for tracking photo-induced chemical transformations. Further analysis of these data might enable more specific photoproduct characterization. We have also shown that even better structural imaging, especially for hydrogen atom positions, can be achieved using XFEL pulses to drive CEI. However, the attempts to directly visualize the ring-opening dynamics in thiophenone have not been successful so far, and the analysis of the time-resolved XFEL data is still underway.

In contrast, the study of 2,3-DHF proved more challenging. Although simulations and experimental CEI data both suggest UV-induced structural evolution, the kinetic energy distributions of the carbon ions are too similar to allow for unambiguous assignment of molecular geometry changes. Unlike prior studies on furan[54], where KE signatures enabled confident identification of ring-opening dynamics, the more uniform KE profile in 2,3-DHF complicates interpretation. Newton diagrams and angular analyses do hint at possible ring-puckering and ring-opening behavior, but further work is needed to confirm these dynamics.

To overcome these limitations, future analyses should integrate angular distributions with Newton diagrams to better distinguish fragment ions in the four-body coincidence channels. Normalization to the number of events per time-delay bin will be critical for quantitatively assessing pump–probe effects. Experimentally, improvements such as shorter-duration UV pulses or the use of free-electron lasers (FELs) could enhance structural sensitivity and signal clarity.

In summary, this work demonstrates the powerful capabilities of CEI in capturing ultrafast structural changes across a range of molecular systems. From benchmarking methodologies in ethylene to directly visualizing UV-induced dynamics in thiophenone and exploring complex fragmentation in 2,3-DHF, these studies collectively highlight both the promise and the challenges of applying CEI to time-resolved molecular imaging. The insights gained here pave the way for more refined techniques in ultrafast spectroscopy and chemical reaction dynamics.

Looking forward, the continued development of CEI combined with ultrafast pump–probe techniques holds great promise for exploring more complex molecular systems and reaction pathways with both spatial and temporal resolution. To advance the current limitations observed in systems like 2,3-DHF, future efforts should focus on enhancing fragment ion discrimination through improved data analysis strategies, and on optimizing experimental parameters, including the use of shorter UV pulses or alternative ionization sources like free-electron lasers (FELs).

Expanding CEI to study transient intermediates in larger organic and bio-relevant molecules will not only deepen our understanding of fundamental photochemical processes, but also open doors for designing photoactive materials, drugs, and molecular devices, guided by real-time structural feedback. Moreover, in view of the extreme complexity and multidimensionality of the CEI data demonstrated in this work, it will be very natural to employ machine learning techniques to sort such data sets, identify and separate different structures, and assess on the level of agreement with theory. First steps recently undertaken in

this direction in Ref.[140], in combination with orders-of-magnitude higher repetition rates of the JRML's new KONZA laser and LCLS-II XFEL facility, make further developments of ultrafast molecular imaging with multi-coincidence Coulomb explosion a very promising research direction.

Bibliography

[1] Elizabeth Mansfield and H. H. Arnason. *History of Modern Art: Painting, Sculpture, Architecture, Photography*. Pearson Education, Upper Saddle River, NJ, 6th edition, 2010.

[2] Bryan F. Ronalds. The beginnings of continuous scientific recording using photography: Sir francis ronalds' contribution. *European Society for the History of Photography*, 9(1):30–37, 2016.

[3] Wilhelm Conrad Röntgen. On a new kind of rays. *Sitzungsberichte der Würzburger Physikalisch-Medizinischen Gesellschaft*, 9:132–141, 1895. English translation available in *Nature*, 1896.

[4] John Francis Hall-Edwards. First surgical use of x-rays (14 february 1896), 1896. URL https://engole.info/john-hall-edwards/.

[5] Albert Londe. X ray of a deformed hand (plaque xxi). In *Nouvelle Iconographie de la Salpétrière*, Tome IX, 1896.

[6] Ahmed H. Zewail. Femtochemistry: atomic-scale dynamics of the chemical bond. *The Journal of Physical Chemistry A*, 104(24):5660–5694, 2000. doi: 10.1021/jp001460h.

[7] Andrew R. Attar, Arnab Bhattacherjee, Chandra D. Pemmaraju, Kerstin Schnorr, Kristina D. Closser, David Prendergast, and Stephen R. Leone. Femtosecond X-ray spectroscopy of an electrocyclic ring-opening reaction. *Science*, 356(6333):54–59, 2017. doi: 10.1126/science.aaf4788. URL https://www.science.org/doi/10.1126/science.aaf4788.

[8] Shashank Pathak, Lea M. Ibele, Rebecca Boll, Carlo Callegari, Alexander Demidovich, Benjamin Erk, Raimund Feifel, Ruaridh Forbes, Michele Di Fraia, Luca Giannessi, Christopher S. Hansen, David M. P. Holland, Rebecca A. Ingle, Robert Mason, Oksana Plekan, Kevin C. Prince, Arnaud Rouzée, Richard J. Squibb, Jan Tross, Michael N. R. Ashfold, Basile F. E. Curchod, and Daniel Rolles. Tracking the Ultraviolet Photochemistry of Thiophenone During and Beyond the Initial Ultrafast Ring Opening. *Nature Chemistry*, 12(9):795–800, 2020. doi: 10.1038/s41557-020-0507-3. URL https://doi.org/10.1038/s41557-020-0507-3.

[9] Benjamin W. Toulson, Mario Borgwardt, Han Wang, Florian Lackner, Adam S. Chatterley, C. D. Pemmaraju, Daniel M. Neumark, Stephen R. Leone, David Prendergast, and Oliver Gessner. Probing ultrafast CBr bond fission in the UV photochemistry of bromoform with core-to-valence transient absorption spectroscopy. *Structural Dynamics*, 6(5):054304, 2019. doi: 10.1063/1.5113798. URL https://doi.org/10.1063/1.5113798.

[10] Michael P. Minitti, Joseph S. Robinson, Jason M. Weber, Ryan A. Seaberg, Daniel A. Zimdars, Jacob J. Boland, Dustin J. Curtis, Thomas J. Lane, Jesse S. Hummert, Michael W. Dunning, Mark F. Greig, Todd J. Martinez, Nora Berrah, Raimund Feifel, Michael Gühr, Marvin H. Nass, David J. Reis, Daniel Rolles, and Philip H. Bucksbaum. Imaging molecular motion: Femtosecond X-ray scattering of an electrocyclic chemical reaction. *Physical Review Letters*, 114(25):255501, 2015. doi: 10.1103/PhysRevLett.114.255501.

[11] João P. F. Nunes, Lea M. Ibele, Shashank Pathak, Andrew R. Attar, Surjendu Bhattacharyya, Rebecca Boll, Kurtis Borne, Martin Centurion, Benjamin Erk, Ming-Fu Lin, Ruaridh J. G. Forbes, Nathan Goff, Christopher S. Hansen, Matthias Hoffmann, David M. P. Holland, Rebecca A. Ingle, Duan Luo, Sri B. Muvva, Alexander H. Reid, Arnaud Rouzée, Artem Rudenko, Sajib K. Saha, Xiaozhe Shen, Anbu S. Venkatacha-

lam, Xijie Wang, Matt R. Ware, Stephen P. Weathersby, Kyle Wilkin, Thomas J. A. Wolf, Yanwei Xiong, Jie Yang, Michael N. R. Ashfold, Daniel Rolles, and Basile F. E. Curchod. Monitoring the evolution of relative product populations at early times during a photochemical reaction. *Journal of the American Chemical Society*, 146(5): 4134–4143, 2024. doi: 10.1021/jacs.3c13046.

[12] Thomas J. A. Wolf, Daniel M. Sanchez, Jie Yang, Robert M. Parrish, João P. F. Nunes, Marco Centurion, Ryan Coffee, James P. Cryan, Michael Gühr, Khaled Hegazy, Alexandre Kirrander, Renkai Li, Jennifer Ruddock, Xijie Shen, Thomas Vecchione, Sean P. Weathersby, Peter M. Weber, Katherine Wilkin, Hyejin Yong, Qiang Zheng, Xijie J. Wang, Michael P. Minitti, and Todd J. Martínez. The photochemical ring-opening of 1,3-cyclohexadiene imaged by ultrafast electron diffraction. *Nature Chemistry*, 11(6):504–509, June 2019. doi: 10.1038/s41557-019-0252-7. URL https://doi.org/10.1038/s41557-019-0252-7.

[13] Cosmin I. Blaga, Junliang Xu, Anthony D. DiChiara, Emily Sistrunk, Kaikai Zhang, Pierre Agostini, Terry A. Miller, Louis F. DiMauro, and C. D. Lin. Imaging ultrafast molecular dynamics with laser-induced electron diffraction. *Nature*, 483(7388):194–197, 2012. doi: 10.1038/nature10820. URL https://www.nature.com/articles/nature10820#citeas.

[14] Gregor Kastirke, Markus Ilchen, Christoph Schober, Markus Weller, Paul Eckart, Marco Martins, Tobias Weber, Thomas Baumann, André Knie, Christoph Schröter, Milutin Dondera, Sadia Bari, Sonia Coriani, Andrew W. Turtle, Robin Santra, Jacek B. Rajewska, Christian Buth, Rolf Treusch, Daniel Rolles, Artem Rudenko, Till Jahnke, and Reinhard Dörner. Photoelectron Diffraction Imaging of a Molecular Breakup Using an X-Ray Free-Electron Laser. *Physical Review X*, 10(2):021052, 2020. doi: 10.1103/PhysRevX.10.021052.

[15] Zeev Vager, Ron Naaman, and Elliot P. Kanter. Coulomb explosion imaging of small molecules. *Science*, 244(4903):426–431, 1989. doi: 10.1126/science.244.4903.426.

[16] Reinhard Dörner, Volker Mergel, Ottmar Jagutzki, Lothar Spielberger, Joachim Ullrich, Reinhard Moshammer, and Hans Schmidt-Böcking. Cold Target Recoil Ion Momentum Spectroscopy: A 'momentum microscope' to view atomic collision dynamics. *Physics Reports*, 330(2–3):95–192, 2000. doi: 10.1016/S0370-1573(99)00109-X.

[17] Joachim Ullrich, Reinhard Moshammer, Alexander Dorn, Reinhard Dörner, Lucas Ph. H. Schmidt, and Hans Schmidt-Böcking. Recoil-ion and electron momentum spectroscopy: Reaction-microscopes. *Reports on Progress in Physics*, 66(9):1463, 2003. doi: 10.1088/0034-4885/66/9/203.

[18] Jyoti Rajput, T. Severt, Ben Berry, Bethany Jochim, Peyman Feizollah, Balram Kaderiya, M. Zohrabi, U. Ablikim, Farzaneh Ziaee, P. Kanaka Raju, D. Rolles, A. Rudenko, K. D. Carnes, B. D. Esry, and I. Ben-Itzhak. Native Frames: Disentangling Sequential from Concerted Three-Body Fragmentation. *Physical Review Letters*, 120(10):103001, 2018. doi: 10.1103/PhysRevLett.120.103001. URL https://journals.aps.org/prl/abstract/10.1103/PhysRevLett.120.103001.

[19] Travis Severt, Jyoti Rajput, Ben Berry, Bethany Jochim, Peyman Feizollah, Balram Kaderiya, Mohammad Zohrabi, Farzaneh Ziaee, Kanaka Raju P., Daniel Rolles, Artem Rudenko, K. Dean Carnes, Brett D. Esry, and Itzik Ben-Itzhak. Native frames: An approach for separating sequential and concerted three-body fragmentation. *Physical Review A*, 110(5):053104, 2024. doi: 10.1103/PhysRevA.110.053104. URL https://journals.aps.org/pra/abstract/10.1103/PhysRevA.110.053104.

[20] David C. Thompson and Juan I. Rodríguez. Chapter 2 - an introduction to quantum chemistry. In Juan I. Rodríguez, Fernando Cortés-Guzmán, and James S. M. Anderson, editors, *Advances in Quantum Chemical Topology Beyond QTAIM*,

pages 21–36. Elsevier, January 2023. ISBN 978-0-323-90891-7. doi: 10.1016/B978-0-323-90891-7.00012-8. URL https://www.sciencedirect.com/science/article/pii/B9780323908917000128.

[21] Frank Jensen. *Introduction to Computational Chemistry*. Wiley, Chichester, West Sussex; Hoboken, NJ; Oxford, 3rd edition, 2017. ISBN 978-1-118-82599-0.

[22] Laurie J. Butler. Chemical reaction dynamics beyond the born-oppenheimer approximation. *Annual Review of Physical Chemistry*, 49(1):125–171, 1998. doi: 10.1146/annurev.physchem.49.1.125. URL http://www.annualreviews.org/doi/pdf/10.1146/annurev.physchem.49.1.125.

[23] Graham A. Worth and Lorenz S. Cederbaum. Beyond Born-Oppenheimer: Molecular Dynamics Through a Conical Intersection. *Annual Review of Physical Chemistry*, 55 (1):127–158, June 2004. ISSN 0066-426X. doi: 10.1146/annurev.physchem.55.091602.094335. URL http://www.annualreviews.org/doi/10.1146/annurev.physchem.55.091602.094335.

[24] LibreTexts Chemistry. Selection rules and transition moment integral, 2020. URL https://chem.libretexts.org/@go/page/1784. Accessed: 2025-06-23.

[25] Wolfgang Becker, Franz Grasbon, Rainer Kopold, Dejan B. Milošević, Gisela G. Paulus, and Herbert Walther. Above-threshold ionization: From classical features to quantum effects. *Advances in Atomic, Molecular, and Optical Physics*, 48:35–98, 2002. doi: 10.1016/S1049-250X(02)80077-1.

[26] Nikolai B. Delone and Valery P. Krainov. Multiphoton processes in atoms. *Physics-Uspekhi*, 37(9):875–910, 1994. doi: 10.1007/978-3-642-97509-7_8.

[27] Pierre V. Auger. Sur l'effet photoélectrique composé. *Journal de Physique et le Radium*, 6(6):205–208, 1925. doi: 10.1051/jphysrad:0192500606020500.

[28] Linda Young, Elliott P. Kanter, Brian Krässig, Yuelin Li, Benedikt Rudek, Michael H. R. Schmitt, Edwin S. Southworth, Linda Fang, Myung-Jin Cho, Christian Bostedt, Joachim D. Bozek, Lou DiMauro, Shih-Ying Chen, Steve R. Leone, Stefan W. Epp, Stephan D. Ludewigt, Till Laarmann, Thomas Möller, Markus Hoener, Lee F. DiMauro, Nora Berrah, Christian Buth, and Robin Santra. Femtosecond electronic response of atoms to ultra-intense X-rays. *Nature*, 466:56–61, 2010. doi: 10.1038/nature09177.

[29] Nora Berrah, Christophe Bostedt, Linda Young, Joachim D. Bozek, Lou DiMauro, Stefan W. Epp, Till Laarmann, Thomas Möller, Markus Hoener, Robin Santra, Elliott P. Kanter, Brian Krässig, and Yuelin Li. Nonlinear processes in the interaction of atoms and molecules with intense EUV and X-ray fields from SASE free electron lasers. *Journal of Modern Optics*, 58(16):1442–1450, 2011. doi: 10.1080/09500340.2011.604333.

[30] Thomas Brabec and Ferenc Krausz. Intense few-cycle laser fields: Frontiers of nonlinear optics. *Reviews of Modern Physics*, 72(2):545–591, 2000. doi: 10.1103/RevModPhys.72.545. URL https://link.aps.org/doi/10.1103/RevModPhys.72.545.

[31] Ferenc Krausz and Misha Ivanov. Attosecond physics. *Reviews of Modern Physics*, 81 (1):163–234, 2009. doi: 10.1103/RevModPhys.81.163.

[32] Pierre Agostini and Louis F. DiMauro. The physics of attosecond light pulses. *Reports on Progress in Physics*, 67(6):813–855, 2004. doi: 10.1088/0034-4885/67/6/R01.

[33] Leonid V. Keldysh. Ionization in the field of a strong electromagnetic wave. *Soviet Physics JETP*, 20:1307–1314, 1965.

[34] Tamar Seideman. On the dynamics of ionization and fragmentation in intense laser fields. *Annual Review of Physical Chemistry*, 56:827–856, 2005. doi: 10.1146/annurev.physchem.56.092503.141258.

[35] Ying H. Jiang, Markus Guehr, Jens Güdde, Norbert Huse, Robert W. Schoenlein, and Philip H. Bucksbaum. Ultrafast extreme ultraviolet induced isomerization of acetylene cations. *Physical Review Letters*, 105(26):263002, 2010. doi: 10.1103/PhysRevLett.105.263002.

[36] Devens Gust, Thomas A. Moore, and Ana L. Moore. Molecular switches controlled by light. *Chem. Commun.*, pages 1169–1178, 2006. doi: 10.1039/B514736K. URL http://dx.doi.org/10.1039/B514736K.

[37] Masahiro Irie, Seiya Kobatake, and Masashi Horichi. Reversible surface morphology changes of a photochromic diarylethene single crystal by photoirradiation. *Science*, 291 (5509):1769–1772, 2001. doi: 10.1126/science.291.5509.1769. URL https://science.sciencemag.org/content/291/5509/1769.

[38] Wolfgang Geppert, Laura Seyfarth, and Regina de Vivie-Riedle. Laser control schemes for molecular switches. *Applied Physics B*, 79(8):987–992, 2004. doi: 10.1007/s00340-004-1636-x.

[39] Rienk Eelkema, Michael M. Pollard, Javier Vicario, Nathalie Katsonis, Blanca Serrano Ramon, Cees W. M. Bastiaansen, Dirk J. Broer, and Ben L. Feringa. Nanomotor rotates microscale objects. *Nature*, 440(7081):163, March 2006. doi: 10.1038/440163a. URL https://doi.org/10.1038/440163a.

[40] Wesley R. Browne and Ben L. Feringa. Making molecular machines work. *Nature Nanotechnology*, 1(1):25–35, October 2006. doi: 10.1038/nnano.2006.45. URL https://doi.org/10.1038/nnano.2006.45.

[41] Klaus L. Kompa and Raphael D. Levine. A molecular logic gate. *Proceedings of the National Academy of Sciences*, 98(2):410–414, 2001. doi: 10.1073/pnas.98.2.410. URL https://www.pnas.org/content/98/2/410.

[42] Hector F. Deluca. History of the discovery of vitamin D and its active metabolites. *BoneKEy Reports*, 3:479, January 2014. doi: 10.1038/bonekey.2013.213. URL https://pubmed.ncbi.nlm.nih.gov/24466410.

[43] Chong-Yu Ruan, Vladimir A. Lobastov, Ramesh Srinivasan, Boyd M. Goodson, Hyotcherl Ihee, and Ahmed H. Zewail. Ultrafast diffraction and structural dynamics: The nature of complex molecules far from equilibrium. *Proceedings of the National Academy of Sciences*, 98(13):7117–7122, 2001. doi: 10.1073/pnas.131192898. URL https://www.pnas.org/content/98/13/7117.

[44] Hyotcherl Ihee, Vladimir A. Lobastov, Udo M. Gomez, Boyd M. Goodson, Ramesh Srinivasan, Chong-Yu Ruan, and Ahmed H. Zewail. Direct imaging of transient molecular structures with ultrafast diffraction. *Science*, 291(5503):458–462, 2001. doi: 10.1126/science.291.5503.458. URL https://science.sciencemag.org/content/291/5503/458.

[45] Narayanan Kuthirummal, Fedor M. Rudakov, Conor L. Evans, and Peter M. Weber. Spectroscopy and femtosecond dynamics of the ring opening reaction of 1,3-cyclohexadiene. *The Journal of Chemical Physics*, 125(13):133307, 2006. doi: 10.1063/1.2345203. URL https://doi.org/10.1063/1.2345203.

[46] Wenji Fu, Wolfgang E. Schmid, and Sergey A. Trushin. Time-resolved dissociative intense-laser field ionization for probing dynamics: Femtosecond photochemical ring opening of 1,3-cyclohexadiene. *The Journal of Chemical Physics*, 112(19):8347–8362, 2000. doi: 10.1063/1.481478. URL https://doi.org/10.1063/1.481478.

[47] Robert B. Woodward and Roald Hoffmann. The conservation of orbital symmetry. *Angewandte Chemie International Edition in English*, 8(11):781–853, 1969. doi: 10.1002/anie.196907811. URL https://onlinelibrary.wiley.com/doi/abs/10.1002/anie.196907811.

[48] Bruce Hudson and Bruce Kohler. Linear polyene electronic structure and spectroscopy. *Annual Review of Physical Chemistry*, 25(1):437–460, 1974. doi: 10.1146/annurev.pc.25.100174.002253. URL https://doi.org/10.1146/annurev.pc.25.100174.002253.

[49] Bruce S. Hudson, Bryan E. Kohler, and Klaus Schulten. Linear polyene electronic structure and potential surfaces. In *Excited States*, volume 6, pages 1–95. Elsevier, 1982. doi: 10.1016/B978-0-12-227206-6.50006-5. URL https://www.sciencedirect.com/science/article/pii/B9780122272066500065.

[50] Daniel Murdock, Stephanie J. Harris, Joel Luke, Michael P. Grubb, Andrew J. Orr-Ewing, and Michael N. R. Ashfold. Transient UV Pump–IR Probe Investigation of Heterocyclic Ring-Opening Dynamics in the Solution Phase: The Role Played by $n\pi^*$ States in the Photoinduced Reactions of Thiophenone and Furanone. *The Journal of Physical Chemistry A*, 123(30):6523–6533, 2019. doi: 10.1021/acs.jpca.9b04314.

[51] Sanghamitra Deb and Peter M. Weber. The Ultrafast Pathway of Photon-Induced Electrocyclic Ring-Opening Reactions: The Case of 1,3-Cyclohexadiene. *Annual Review of Physical Chemistry*, 62(1):193–213, 2011. doi: 10.1146/annurev.physchem.012809.103350. URL https://doi.org/10.1146/annurev.physchem.012809.103350.

[52] Huynh Van Sa Lam, Anbu Selvam Venkatachalam, Surjendu Bhattacharyya, Keyu Chen, Kurtis Borne, Enliang Wang, Rebecca Boll, Till Jahnke, Vinod Kumarappan, Artem Rudenko, and Daniel Rolles. Differentiating Three-Dimensional Molecular Structures Using Laser-Induced Coulomb Explosion Imaging. *Physical Review Letters*, 132(12):123201, 2024. doi: 10.1103/PhysRevLett.132.123201. URL https://journals.aps.org/prl/abstract/10.1103/PhysRevLett.132.123201.

[53] Till Jahnke, Sebastian Mai, Surjendu Bhattacharyya, Keyu Chen, Rebecca Boll, Maria Elena Castellani, Simon Dold, Ulrike Frühling, Alice E. Green, Markus Ilchen,

Rebecca Ingle, Gregor Kastirke, Huynh Van Sa Lam, Fabiano Lever, Dennis Mayer, Tommaso Mazza, Terence Mullins, Yevheniy Ovcharenko, Björn Senfftleben, Florian Trinter, Atia-Tul-Noor, Sergey Usenko, Anbu Selvam Venkatachalam, Artem Rudenko, Daniel Rolles, Michael Meyer, Heide Ibrahim, and Markus Gühr. Direct observation of ultrafast symmetry reduction during internal conversion of 2-thiouracil using Coulomb explosion imaging. *Nature Communications*, 16(2074), 2025. doi: 10.1038/s41467-025-57083-3. URL https://www.nature.com/articles/s41467-025-57083-3.

[54] Enliang Wang, Surjendu Bhattacharyya, Keyu Chen, Kurtis Borne, Farzaneh Ziaee, Shashank Pathak, Huynh Van Sa Lam, Anbu Selvam Venkatachalam, Xiangjun Chen, Rebecca Boll, Till Jahnke, Artem Rudenko, and Daniel Rolles. Time-Resolved Coulomb Explosion Imaging Unveils Ultrafast Ring Opening of Furan. *arXiv preprint*, 2023. URL https://arxiv.org/abs/2311.05099.

[55] Surjendu Bhattacharyya, Kurtis Borne, Farzaneh Ziaee, Shashank Pathak, Enliang Wang, Anbu Selvam Venkatachalam, Huynh Van Sa Lam, Keyu Chen, Rebecca Boll, Till Jahnke, Artem Rudenko, and Daniel Rolles. Strong-Field-Induced Coulomb Explosion Imaging of Tribromomethane. *The Journal of Physical Chemistry Letters*, 13 (25):58455853, 2022. doi: 10.1021/acs.jpclett.2c01007. URL https://pubs.acs.org/doi/full/10.

[56] Travis Severt, Zachary L. Streeter, Wael Iskandar, Kirk A. Larsen, Averell Gatton, Daniel Trabert, Bethany Jochim, Brandon Griffin, Elio G. Champenois, Matthew M. Brister, Dylan Reedy, Demitri Call, Richard Strom, Allen L. Landers, Reinhard Dörner, Joshua B. Williams, Daniel S. Slaughter, Robert R. Lucchese, Thorsten Weber, C. William McCurdy, and Itzik Ben-Itzhak. Step-by-step state-selective tracking of fragmentation dynamics of water dications by momentum imaging. *Nature*

Communications, 13:5146, 2022. doi: 10.1038/s41467-022-32836-6. URL https://www.nature.com/articles/s41467-022-32836-6.

[57] Mario Barbatti, Martina Bondanza, Rachel Crespo-Otero, Benjamin Demoulin, Pavlo O. Dral, Giovanni Granucci, Fabiano Kossoski, Hans Lischka, Benedetta Mennucci, Sudip Mukherjee, Michele Pederzoli, Maurizio Persico, Marcelo Pinheiro Jr, Jiří Pittner, Felix Plasser, Emiliano Sangiogo Gil, and Lazar Stojanovic. Newton-X Platform: New Software Developments for Surface Hopping and Nuclear Ensembles. *Journal of Chemical Theory and Computation*, 18(11):6851–6867, 2022. doi: 10.1021/acs.jctc.2c00804.

[58] Surjendu Bhattacharyya, Kurtis Borne, Farzaneh Ziaee, Shashank Pathak, Enliang Wang, Anbu Selvam Venkatachalam, Xiang Li, Nathan Marshall, Kevin D. Carnes, Charles W. Fehrenbach, Travis Severt, Itzik Ben-Itzhak, Artem Rudenko, and Daniel Rolles. Strong-Field-Induced Coulomb Explosion Imaging of Tribromomethane. *The Journal of Physical Chemistry Letters*, 13(25):5845–5853, 2022. doi: 10.1021/acs.jpclett.2c01007. URL https://doi.org/10.1021/acs.jpclett.2c01007. PMID: 35727076.

[59] Carl Runge. *Über die numerische Auflösung von Differentialgleichungen*, volume 3. Jahresbericht der Deutschen Mathematiker-Vereinigung, 1895.

[60] John C. Butcher. *Numerical Methods for Ordinary Differential Equations*. John Wiley & Sons, 2nd edition, 2008. ISBN 978-0470753751.

[61] The MathWorks, Inc. *MATLAB Version 9.14 (R2023a): Ordinary Differential Equation Solvers*. The MathWorks, Inc., Natick, Massachusetts, 2023. URL https://www.mathworks.com/help/matlab/ordinary-differential-equations.html.

[62] Hans Steinwedel, Hans-Joachim Andrä, and Werner Dreizler. Über die zerlegung von molekülionen beim stoß mit elektronen. *Discussions of the Faraday Society*,

33:149–157, 1962. doi: 10.1039/DF9623300149. URL https://doi.org/10.1039/DF9623300149.

[63] Xinhua Ren, Andrew M. Summers, Pavani Raju, Alireza Vajdi, Vikram Makhija, Cole W. Fehrenbach, Nathaniel G. Kling, Kevin J. Betsch, Zhaoxuan Wang, Matthias F. Kling, K. Dean Carnes, Itzik Ben-Itzhak, Carlos Trallero-Herrero, and Vinod Kumarappan. Single-shot carrier-envelope-phase tagging using an f–2f interferometer and a phase meter: A comparison. *Journal of Optics*, 19(12):124017, 2017. doi: 10.1088/2040-8986/aa9865. URL https://iopscience.iop.org/article/10.1088/2040-8986/aa9865.

[64] John M. J. Madey. Stimulated Emission of Bremsstrahlung in a Periodic Magnetic Field. *Journal of Applied Physics*, 42(5):1906–1913, 1971. doi: 10.1063/1.1660466. URL https://aip.scitation.org/doi/10.1063/1.1660466.

[65] David A. G. Deacon, Lawrence R. Elias, John M. J. Madey, George J. Ramian, Henry A. Schwettman, and Thomas I. Smith. First operation of a free-electron laser. *Physical Review Letters*, 38(16):892–894, 1977. doi: 10.1103/PhysRevLett.38.892. URL https://link.aps.org/doi/10.1103/PhysRevLett.38.892.

[66] James P. Cryan, Taran Driver, Joseph Duris, Zhaoheng Guo, Siqi Li, Jordan T. O'Neal, and Agostino Marinelli. The Development of Attosecond XFELs for Understanding Ultrafast Electron Motion. In *Advances in Atomic, Molecular, and Optical Physics*, volume 71, pages 1–64. Elsevier, 2022. ISBN 978-0-323-98843-8. doi: 10.1016/bs.aamop.2022.05.001. URL https://linkinghub.elsevier.com/retrieve/pii/S1049250X22000015.

[67] Joseph Duris, Siqi Li, Taran Driver, Elio G. Champenois, James P. MacArthur, Alberto A. Lutman, Zhen Zhang, Philipp Rosenberger, Jeff W. Aldrich, Ryan Coffee, Giacomo Coslovich, Franz-Josef Decker, James M. Glownia, Gregor Hartmann, Wolfram Helml, Andrei Kamalov, Jonas Knurr, Jacek Krzywinski, Ming-Fu Lin, Megan

Nantel, Adi Natan, Jordan O'Neal, Niranjan Shivaram, Peter Walter, Anna Wang, James J. Welch, Thomas J. A. Wolf, Joseph Z. Xu, Matthias F. Kling, Philip H. Bucksbaum, Alexander Zholents, Zhirong Huang, James P. Cryan, and Agostino Marinelli. Tunable isolated attosecond X-ray pulses with gigawatt peak power from a free-electron laser. *Nature Photonics*, 14:30–36, 2020. doi: 10.1038/s41566-019-0549-5. URL https://www.nature.com/articles/s41566-019-0549-5.

[68] Artem Rudenko, Lorenz Inhester, Kazuki Hanasaki, Xiang Li, Sam R. Robatjazi, Benjamin Erk, Rebecca Boll, Kohei Toyota, Yiming Hao, Oriol Vendrell, Clément Bomme, Eugene Savelyev, Benedikt Rudek, Laurent Foucar, Stephen H. Southworth, Carsten S. Lehmann, Brian Kraessig, Thomas Marchenko, Marc Simon, Kenji Ueda, Kevin R. Ferguson, Michael Bucher, Thomas Gorkhover, Sébastien Carron, Rodrigo Alonso-Mori, Josef E. Koglin, Julio Correa, Gregory J. Williams, Sébastien Boutet, Linda Young, Christoph Bostedt, Sang-Kil Son, Robin Santra, and Daniel Rolles. Femtosecond response of polyatomic molecules to ultra-intense hard X-rays. *Nature*, 546(7656):129–132, 2017. doi: 10.1038/nature22373. URL https://www.nature.com/articles/nature22373.

[69] Christoph Bostedt, Sébastien Boutet, David M. Fritz, Zhentang Huang, Hae Ja Lee, Henrik T. Lemke, Axel Robert, William F. Schlotter, Joshua J. Turner, and Gregory J. Williams. Linac Coherent Light Source: The First Five Years. *Reviews of Modern Physics*, 88:015007, 2016. doi: 10.1103/RevModPhys.88.015007. URL https://link.aps.org/doi/10.1103/RevModPhys.88.015007.

[70] European XFEL. Accelerator – European XFEL, 2024. URL https://www.xfel.eu/facility/accelerator/index_eng.html. Accessed: 2025-05-18.

[71] Claudio Pellegrini, Agostino Marinelli, and Sven Reiche. The physics of X-ray free-electron lasers. *Reviews of Modern Physics*, 88(1):015006, 2016. doi: 10.1103/

RevModPhys.88.015006. URL https://link.aps.org/doi/10.1103/RevModPhys.88.015006.

[72] Zhirong Huang and Kwang-Je Kim. Review of X-ray free-electron laser theory. *Physical Review Special Topics - Accelerators and Beams*, 10(3):034801, 2007. doi: 10.1103/PhysRevSTAB.10.034801. URL https://journals.aps.org/prab/abstract/10.1103/PhysRevSTAB.10.034801.

[73] Emanuele Allaria, Roberto Appio, Luca Badano, William A. Barletta, Sergio Bassanese, Sandra G. Biedron, Alessandro Borga, Emanuele Busetto, Daniele Castronovo, Paolo Cinquegrana, Silvano Cleva, Davide Cocco, Massimo Cornacchia, Paolo Craievich, Iacopo Cudin, Giovanni D'Auria, Marco Dal Forno, Maria B. Danailov, Riccardo De Monte, Gianluca De Ninno, Paolo Delgiusto, Alexander Demidovich, Sandro Di Mitri, Bruno Diviacco, Andrea Fabris, Roberto Fabris, William Fawley, Mauro Ferianis, Emanuele Ferrari, Silvia Ferry, Lars Froehlich, Paolo Furlan, Giovanni Gaio, Fabio Gelmetti, Luca Giannessi, Marco Giannini, Riccardo Gobessi, Rumen Ivanov, Evangelos Karantzoulis, Marco Lonza, Andrea Lutman, Benoît Mahieu, Michele Milloch, Stephen V. Milton, Mauro Musardo, Ivan Nikolov, Stefano Noe, Filippo Parmigiani, Giuseppe Penco, Massimo Petronio, Luca Pivetta, Marco Predonzani, Federico Rossi, Lorenzo Rumiz, Alessandro Salom, Claudio Scafuri, Claudio Serpico, Paolo Sigalotti, Silvio Spampinati, Carlo Spezzani, Mario Svandrlik, Corrado Svetina, Stefano Tazzari, Marco Trovo, Raffaele Umer, Andrea Vascotto, Mauro Veronese, Raffaele Visintini, Marco Zaccaria, Daniele Zangrando, and Marco Zangrando. Highly coherent and stable pulses from the FERMI seeded free-electron laser in the extreme ultraviolet. *Nature Photonics*, 6(10):699–704, 2012. doi: 10.1038/nphoton.2012.233. URL https://www.nature.com/articles/nphoton.2012.233.

[74] Marco Zangrando, Andrea Abrami, Dan Bacescu, Iacopo Cudin, Claudio Fava, Fabio Frassetto, Alessandro Galimberti, Roberto Godnig, Diego Giuressi, Luca Poletto,

Lorenzo Rumiz, Renato Sergo, Corrado Svetina, and Davide Cocco. The photon analysis, delivery, and reduction system at the FERMI at Elettra free electron laser user facility. *Review of Scientific Instruments*, 80(11):113110, November 2009. ISSN 0034-6748. doi: 10.1063/1.3262502. URL https://doi.org/10.1063/1.3262502.

[75] Pieter Kruit and Francis H. Read. Magnetic field paralleliser for 2 electron-spectrometer and electron-image magnifier. *Journal of Physics E: Scientific Instruments*, 16(4):313–324, April 1983. ISSN 0022-3735. doi: 10.1088/0022-3735/16/4/016. URL https://iopscience.iop.org/article/10.1088/0022-3735/16/4/016.

[76] Paul Radcliffe, Sven Düsterer, Armin Azima, Wei-Bo Li, Ernst Plönjes, Holger Redlin, Jürgen Feldhaus, Piergiorgio Nicolosi, Luca Poletto, Jean Dardis, Juan P. Gutierrez, Paul Hough, Kevin D. Kavanagh, Eugene T. Kennedy, Humberto Luna, Patrick Yeates, John T. Costello, Alain Delyseries, Caroline L. S. Lewis, Didier Glijer, Daniel Cubaynes, and Michael Meyer. An experiment for two-color photoionization using high intensity extreme-UV free electron and near-IR laser pulses. *Nuclear Instruments and Methods in Physics Research Section A: Accelerators, Spectrometers, Detectors and Associated Equipment*, 583(2-3):516–525, December 2007. ISSN 0168-9002. doi: 10.1016/j.nima.2007.09.014.

[77] Michael Mucke, Markus Förstel, Tobias Lischke, Thomas Arion, Anthony M. Bradshaw, and Uwe Hergenhahn. Performance of a short "magnetic bottle" electron spectrometer. *Review of Scientific Instruments*, 83(6):063106, 2012. doi: 10.1063/1.4729256. URL https://pubs.aip.org/rsi/article/83/6/063106/354251/Performance-of-a-short-magnetic-bottle-electron.

[78] Yuri V. Shvyd'ko and Ryan R. Lindberg. Spatiotemporal response of crystals in x-ray bragg diffraction. *Physical Review Special Topics - Accelerators and Beams*, 15(10):100702, 2012. doi: 10.1103/PhysRevSTAB.15.100702.

[79] Ryan R. Lindberg and Yuri V. Shvyd'ko. Time dependence of Bragg forward scattering and self-seeding of hard X-ray free-electron lasers. *Physical Review Special Topics - Accelerators and Beams*, 15(5):050706, 2012. doi: 10.1103/PhysRevSTAB.15.050706.

[80] Jochen Amann, William Berg, Volker Blank, Franz-Josef Decker, Yuantao Ding, Paul Emma, Yiping Feng, Josef Frisch, David Fritz, Jerry Hastings, Zhentang Huang, Jacek Krzywinski, Ryan Lindberg, Henrik Loos, Andrea Lutman, Heinz-Dieter Nuhn, Daniel Ratner, Jaroslaw Rzepiela, Deming Shu, Yuri Shvyd'ko, Silvio Spampinati, Sergei Stoupin, Sergei Terentyev, Emil Trakhtenberg, David Walz, John Welch, Juhao Wu, Alexander Zholents, and Diling Zhu. Demonstration of self-seeding in a hard-X-ray free-electron laser. *Nature Photonics*, 6:693–698, 2012. doi: 10.1038/nphoton.2012.180. URL https://www.nature.com/articles/nphoton.2012.180.

[81] Farzaneh Ziaee. *Imaging Nuclear Motion During the Photofragmentation of Halomethane Molecules Triggered by Ultraviolet Light*. Ph.d. dissertation, Kansas State University, 2022. URL https://hdl.handle.net/2097/42116.

[82] Jeffrey H. Posthumus. The dynamics of small molecules in intense laser fields. *Reports on Progress in Physics*, 67(5):623–665, 2004. doi: 10.1088/0034-4885/67/5/R01. URL https://iopscience.iop.org/article/10.1088/0034-4885/67/5/R01.

[83] Jean-Claude Diels and Wolfgang Rudolph. *Ultrashort Laser Pulse Phenomena*. Academic Press, 2nd edition, 2006. ISBN 9780122154935. URL https://www.sciencedirect.com/book/9780122154935/ultrashort-laser-pulse-phenomena.

[84] John C. H. Spence and Henry N. Chapman. X-ray lasers for structural and dynamic biology. *Reports on Progress in Physics*, 75(10):102601, 2012. doi: 10.1088/0034-4885/75/10/102601. URL https://iopscience.iop.org/article/10.1088/0034-4885/75/10/102601.

[85] Michel Piché. Beam reshaping and self-mode-locking in nonlinear laser resonators. *Optics Communications*, 86(2):156–160, 1991. doi: 10.1016/0030-4018(91)90552-O.

[86] Zenghu Chang. *Fundamentals of Attosecond Optics*. CRC Press, 2016. ISBN 9781498722735.

[87] Mohammad Zohrabi. *Quantum Control of Molecular Fragmentation in Strong Laser Fields*. Ph.d. dissertation, Kansas State University, 2014. URL http://hdl.handle.net/2097/18401.

[88] Eugene Hecht and Alfred Zajac. Optics. *American Journal of Physics*, 42(10):921–922, October 1974. doi: 10.1119/1.1987895. URL https://pubs.aip.org/aapt/ajp/article/42/10/921/1038204/Optics.

[89] Robert Goldstein. Pockels Cell Primer. *Laser Focus*, 34(1):21–26, 1968.

[90] Rick Trebino. *Frequency-Resolved Optical Gating: The Measurement of Ultrashort Laser Pulses*. Springer, 2000. ISBN 978-0-306-46493-2. doi: 10.1007/978-1-4615-1181-6. URL https://link.springer.com/book/10.1007/978-1-4615-1181-6.

[91] Tsz Chun Wong and Rick Trebino. Single-frame measurement of complex laser pulses tens of picoseconds long using pulse-front tilt in cross-correlation frequency-resolved optical gating. *Journal of the Optical Society of America B*, 30(11):2781–2786, 2013. doi: 10.1364/JOSAB.30.002781. URL https://opg.optica.org/josab/abstract.cfm?uri=josab-30-11-2781.

[92] Rick Trebino and Daniel J. Kane. Using phase retrieval to measure the intensity and phase of ultrashort pulses: frequency-resolved optical gating. *Journal of the Optical Society of America A*, 10(5):1101–1111, 1993. doi: 10.1364/JOSAA.10.001101. URL https://opg.optica.org/josaa/abstract.cfm?uri=josaa-10-5-1101.

[93] John N. Sweetser, David N. Fittinghoff, and Rick Trebino. Transient-grating frequency-resolved optical gating. *Optics Letters*, 22(8):519–521, 1997. doi: 10.1364/OL.22.000519. URL https://opg.optica.org/ol/abstract.cfm?uri=ol-22-8-519.

[94] Daniel J. Kane and Rick Trebino. Characterization of arbitrary femtosecond pulses using frequency-resolved optical gating. *IEEE Journal of Quantum Electronics*, 29(2): 571–579, 1993. doi: 10.1109/3.199311. URL https://doi.org/10.1109/3.199311.

[95] Kevin W. DeLong, Rick Trebino, James Hunter, and William E. White. Frequency-resolved optical gating with the use of second-harmonic generation. *Journal of the Optical Society of America B*, 11(11):2206–2215, 1994. doi: 10.1364/JOSAB.11.002206. URL https://opg.optica.org/josab/abstract.cfm?uri=josab-11-11-2206.

[96] Daniel J. Kane. Real-time measurement of ultrashort laser pulses using principal component generalized projections. *IEEE Journal of Selected Topics in Quantum Electronics*, 4(2):278–284, 1998. doi: 10.1109/2944.686733. URL https://doi.org/10.1109/2944.686733.

[97] Stefan Linden, Harald Giessen, and Jürgen Kuhl. XFROG — A New Method for Amplitude and Phase Characterization of Weak Ultrashort Pulses. *physica status solidi (b)*, 206(1):119–124, 1998. doi: 10.1002/(SICI)1521-3951(199803)206:1⟨119::AID-PSSB119⟩3.0.CO;2-X. URL https://onlinelibrary.wiley.com/doi/abs/10.1002/(SICI)1521-3951(199803)206:1<119::AID-PSSB119>3.0.CO;2-X.

[98] Robert W. Boyd. *Nonlinear Optics*. Academic Press, 2nd edition, 2003. ISBN 978-0121216801. URL https://www.sciencedirect.com/book/9780121216801/nonlinear-optics.

[99] Geoffrey New. *Introduction to Nonlinear Optics*. Cambridge University Press, 2011. ISBN 9780521877015. doi: 10.1017/CBO9780511975851. URL

https://www.cambridge.org/core/books/introduction-to-nonlinear-optics/B8F0632EDF25919CC10293D9EBFD1B9F.

[100] Kurt Nassau. Handbook of Non-Linear Optical Crystals. *Materials Research Bulletin*, 27(11), 1992. doi: 10.1016/0025-5408(92)90102-6.

[101] John Lekner. Reflection and refraction by uniaxial crystals. *Journal of Physics: Condensed Matter*, 3(32):6121–6133, August 1991. doi: 10.1088/0953-8984/3/32/017.

[102] Shu-Yu Chen, Yu-Chen Liu, Hsiu-Yuan Wu, Chi-Kung Ni, and Yuan T. Lee. I_2 molecular elimination in single-photon dissociation of CH_2I_2 at 248 nm by using cavity ring-down absorption spectroscopy. *The Journal of Chemical Physics*, 134(3):034315, 2011. doi: 10.1063/1.3523571.

[103] Takeshi Kobayashi, Hiroshi Yao, Koji Amano, Yoshio Fukushima, Akira Morimoto, and Toshio Sueta. Optical pulse compression using high-frequency electrooptic phase modulation. *IEEE Journal of Quantum Electronics*, 24(2):382–387, 1988. doi: 10.1109/3.135.

[104] Raymond L. Fork, Oscar E. Martinez, and James P. Gordon. Negative dispersion using pairs of prisms. *Optics Letters*, 9(5):150–152, 1984. doi: 10.1364/OL.9.000150.

[105] Claude Froehly, Bernard Colombeau, and Michel Vampouille. II. Shaping and Analysis of Picosecond Light Pulses. In Emil Wolf, editor, *Progress in Optics*, volume 20, pages 63–153. Elsevier, 1983. doi: 10.1016/S0079-6638(08)70277-4.

[106] Serkan Akturk, Xuejian Gu, Patrick Gabolde, and Rick Trebino. The general theory of first-order spatio-temporal distortions of Gaussian pulses and beams. *Optics Express*, 13(21):8642–8661, 2005. doi: 10.1364/OPEX.13.008642.

[107] Vikas K. Chauhan, Jonathan Cohen, Paul M. Vaughan, Peter Bowlan, and Rick Trebino. Distortion-free single-prism/grating ultrashort laser pulse compressor. *IEEE*

Journal of Quantum Electronics, 46(12):1726–1731, 2010. doi: 10.1109/JQE.2010.2063017.

[108] Oscar E. Martinez, James P. Gordon, and Raymond L. Fork. Negative group-velocity dispersion using refraction. *Journal of the Optical Society of America A*, 1(10):1003–1006, 1984. doi: 10.1364/JOSAA.1.001003.

[109] James P. Gordon and Raymond L. Fork. Optical resonator with negative dispersion. *Optics Letters*, 9(5):153–155, 1984. doi: 10.1364/OL.9.000153.

[110] Ingemar H. Malitson. Interspecimen comparison of the refractive index of fused silica. *Journal of the Optical Society of America*, 55(10):1205–1209, 1965. doi: 10.1364/JOSA.55.001205. URL https://opg.optica.org/abstract.cfm?URI=josa-55-10-1205.

[111] Brandon Berry, Daniel J. Haxton, Thilo Weber, Ali Belkacem, Duncan J. Wilcox, and Randall R. Jones. Note: Determining the detection efficiency of excited neutral atoms by a microchannel plate detector. *Review of Scientific Instruments*, 86(4):046103, April 2015. doi: 10.1063/1.4916953.

[112] Itzik Ben-Itzhak, Brett D. Esry, Hongxia Miao, Pengqi Wang, Joachim Ullrich, Thomas Jahnke, Reinhard Dörner, Ali S. Alnaser, Xiao-Min Tong, Chandra M. Maharjan, Benjamin Ulrich, André C. L. Staudte, and Charles L. Cocke. Dissociation and ionization of H_2^+ by ultrashort intense laser pulses probed by coincidence 3D momentum imaging. *Physical Review Letters*, 95(7):073002, August 2005. doi: 10.1103/PhysRevLett.95.073002.

[113] Itzik Ben-Itzhak. Fragmentation of molecular-ion beams in intense ultrashort laser pulses. In *Fragmentation Processes: Topics in Atomic and Molecular Physics*, pages 72–97. Cambridge University Press, Cambridge, 2012. doi: 10.1017/CBO9781139017572.004.

[114] Timur Osipov, Christoph Bostedt, Jean-Claude Castagna, Kevin R. Ferguson, Michael Bucher, Sergio C. Montero, Michael L. Swiggers, Rami Obaid, Daniel Rolles, Artem Rudenko, Joachim D. Bozek, and Nora Berrah. The LAMP instrument at the Linac Coherent Light Source free-electron laser. *Review of Scientific Instruments*, 89:035112, 2018. doi: 10.1063/1.5017727. URL https://aip.scitation.org/doi/10.1063/1.5017727.

[115] Hamamatsu Photonics. *MCP (MicroChannel Plate) and MCP Assembly*, n.d. URL https://www.hamamatsu.com/resources/pdf/etd/MCP_TMCP0002E.pdf. TMCP0002E.

[116] Joseph L. Wiza. *Microchannel Plate Detectors*, volume 162. Elsevier, 1979. doi: 10.1016/0029-554X(79)90734-1. Classic foundational review of MCP design and applications.

[117] George W. Fraser. The detection of X-rays and particles with microchannel plates. *Nuclear Instruments and Methods*, 187:581–593, 1981. doi: 10.1016/0029-554X(81)90695-1.

[118] Photek Ltd. *Microchannel Plate Handbook*. 2019. URL https://www.photek.com/wp-content/uploads/2019/01/Photek-MCP-Handbook.pdf. Manufacturer handbook with technical details on MCP geometry and performance.

[119] Stephen E. Sobottka and Michael B. Williams. Position-sensitive detector with delay-line readout. *IEEE Transactions on Nuclear Science*, 35(1):348–351, Feb 1988. doi: 10.1109/23.12507.

[120] Xiang Li. *Ultrafast Dynamics in Molecular Systems Probed by Coulomb Explosion Imaging*. Ph.d. dissertation, Kansas State University, Manhattan, KS, 2019. URL https://jrm.phys.ksu.edu/theses.html.

[121] SpecTcl Home Page. https://docs.nscl.msu.edu/daq/spectcl/, note = Accessed: May 22, 2025.

[122] Rebecca Boll, Julia M. Schäfer, Benoît Richard, Kilian Fehre, Gregor Kastirke, Zoltan Jurek, Markus S. Schöffler, Malik M. Abdullah, Nils Anders, Thomas M. Baumann, Sebastian Eckart, Benjamin Erk, Alberto De Fanis, Reinhard Dörner, Sven Grundmann, Patrik Grychtol, Alexander Hartung, Max Hofmann, Markus Ilchen, Ludger Inhester, Christian Janke, Rui Jin, Max Kircher, Katharina Kubicek, Maksim Kunitski, Xiang Li, Tommaso Mazza, Severin Meister, Niklas Melzer, Jacobo Montano, Valerija Music, Giammarco Nalin, Yevheniy Ovcharenko, Christopher Passow, Andreas Pier, Nils Rennhack, Jonas Rist, Daniel E. Rivas, Daniel Rolles, Ilme Schlichting, Lothar Ph. H. Schmidt, Philipp Schmidt, Juliane Siebert, Nico Strenger, Daniel Trabert, Florian Trinter, Isabel Vela-Perez, Rene Wagner, Peter Walter, Miriam Weller, Pawel Ziolkowski, Sang-Kil Son, Artem Rudenko, Michael Meyer, Robin Santra, and Till Jahnke. X-ray multiphoton-induced Coulomb explosion images complex single molecules. *Nature Physics*, 18(4):423–428, 2022. doi: 10.1038/s41567-022-01507-0. URL https://www.nature.com/articles/s41567-022-01507-0.

[123] Hang Yuan, Yue Gao, Bo Yang, Shaofei Gu, Hong Lin, Dalong Guo, Junliang Liu, Shaofeng Zhang, Xinwen Ma, and Shenyue Xu. Coulomb Explosion Imaging of Complex Molecules Using Highly Charged Ions. *Phys. Rev. Lett.*, 133:193002, Nov 2024. doi: 10.1103/PhysRevLett.133.193002. URL https://link.aps.org/doi/10.1103/PhysRevLett.133.193002.

[124] Eric Brenya, Esha Dutta, Brittani Herron, Lauren H Walden, Daniel M Roberts, and Brad M Binder. Ethylene-mediated metabolic priming increases photosynthesis and metabolism to enhance plant growth and stress tolerance. *PNAS Nexus*, 2(7): pgad216, 07 2023. ISSN 2752-6542. doi: 10.1093/pnasnexus/pgad216. URL https://doi.org/10.1093/pnasnexus/pgad216.

[125] Xinhua Xie, Stefan Roither, Markus Schöffler, Erik Lötstedt, Daniil Kartashov, Li Zhang, Gerhard G. Paulus, Atsushi Iwasaki, Andrius Baltuška, Kaoru Yamanouchi, and Markus Kitzler. Electronic Predetermination of Ethylene Fragmentation Dynamics. *Phys. Rev. X*, 4:021005, Apr 2014. doi: 10.1103/PhysRevX.4.021005. URL https://link.aps.org/doi/10.1103/PhysRevX.4.021005.

[126] Huailiang Xu, Tomoya Okino, Katsunori Nakai, Kaoru Yamanouchi, Stefan Roither, Xinhua Xie, Daniil Kartashov, Markus Schöffler, Andrius Baltuska, and Markus Kitzler. Hydrogen migration and C–C bond breaking in 1,3-butadiene in intense laser fields studied by coincidence momentum imaging. *Chemical Physics Letters*, 484(4):119–123, 2010. ISSN 0009-2614. doi: https://doi.org/10.1016/j.cplett.2009.11.008. URL https://www.sciencedirect.com/science/article/pii/S0009261409014146.

[127] Bo Wang, Long Wei, Yu Zhang, Wandong Yu, Yaming Zou, Li Chen, and Baoren Wei. Fragmentation of $C_2H_4^{2+}$ produced by 300 eV electron impact. *Journal of Physics B: Atomic, Molecular and Optical Physics*, 53(15):155205, jun 2020. doi: 10.1088/1361-6455/ab91e5. URL https://dx.doi.org/10.1088/1361-6455/ab91e5.

[128] Nadja Endstrasser, Fabio Zappa, Andreas Mauracher, Alexander Bacher, Stefan Feil, Donald K. Bohme, Peter Scheier, Michael Probst, and Tilmann D. Märk. Absolute partial cross sections and kinetic energy analysis for the electron impact ionization of ethylene. *International Journal of Mass Spectrometry*, 280(1):65–71, 2009. ISSN 1387-3806. doi: https://doi.org/10.1016/j.ijms.2008.08.004. URL https://www.sciencedirect.com/science/article/pii/S1387380608003126. Ion-molecule and ion-surface interactions: A special issue honoring Zdenek Herman on the occasion of his 75th birthday.

[129] Lívia Sigaud and E. C. Montenegro. Absolute cross sections for ethylene-dication production by electron impact. *Physical Review A*, 95:012704, January 2017. doi: 10.

1103/PhysRevA.95.012704. URL https://link.aps.org/doi/10.1103/PhysRevA.95.012704.

[130] Binod Gaire, Sang Youn Lee, Daniel J. Haxton, Paul M. Pelz, Irina Bocharova, Florian P. Sturm, Niklas Gehrken, Marcus Honig, Markus Pitzer, Daniel Metz, Hyun-Kyung Kim, Markus Schöffler, Reinhard Dörner, Holger Gassert, Sebastian Zeller, Jens Voigtsberger, Wei Cao, Mohammad Zohrabi, Joshua Williams, Austin Gatton, Dalton Reedy, Christopher Nook, Thomas Müller, Arthur L. Landers, Charles L. Cocke, Itzik Ben-Itzhak, Thomas Jahnke, Ali Belkacem, and Thorsten Weber. Photo-double-ionization of ethylene and acetylene near threshold. *Physical Review A*, 89:013403, January 2014. doi: 10.1103/PhysRevA.89.013403. URL https://link.aps.org/doi/10.1103/PhysRevA.89.013403.

[131] Binod Gaire, Daniel J. Haxton, Florian P. Sturm, Joshua Williams, Austin Gatton, Irina Bocharova, Niklas Gehrken, Markus Schöffler, Holger Gassert, Sebastian Zeller, Jens Voigtsberger, Thomas Jahnke, Mohammad Zohrabi, Dalton Reedy, Christopher Nook, Arthur L. Landers, Ali Belkacem, Charles L. Cocke, Itzik Ben-Itzhak, Reinhard Dörner, and Thorsten Weber. Auger decay and subsequent fragmentation pathways of ethylene following K-shell ionization. *Physical Review A*, 92:013408, July 2015. doi: 10.1103/PhysRevA.92.013408. URL https://link.aps.org/doi/10.1103/PhysRevA.92.013408.

[132] Jeroen van Tilborg, Thomas K. Allison, Trevor W. Wright, Michael P. Hertlein, Roger W. Falcone, Yi Liu, Hamed Merdji, and Ali Belkacem. Femtosecond isomerization dynamics in the ethylene cation measured in an EUV-pump NIR-probe configuration. *Journal of Physics B: Atomic, Molecular and Optical Physics*, 42(8): 081002, April 2009. doi: 10.1088/0953-4075/42/8/081002. URL https://dx.doi.org/10.1088/0953-4075/42/8/081002.

[133] Ying Hu Jiang, Artem Rudenko, Markus Kübel, Oliver Herrwerth, Laurent Fou-

car, Markus Kurka, Karsten U. Kühnel, Alexander Senftleben, Matthias F. Kling, Florian P. Sturm, Jeroen van Tilborg, Ali Belkacem, Kazuki Motomura, Akihiro Yamada, Kenji Ueda, Sven Düsterer, Rolf Treusch, Christoph D. Schröter, Reinhard Moshammer, and Joachim Ullrich. Time-resolved XUV-induced isomerization and H_3^+ formation in $C_2H_4^+$ cation. *Journal of Physics: Conference Series*, 388 (3):032014, November 2012. doi: 10.1088/1742-6596/388/3/032014. URL https://dx.doi.org/10.1088/1742-6596/388/3/032014.

[134] Rachel Crespo-Otero, Baptiste Demoulin, Pavlo O. Dral, Giovanni Granucci, Fábris Kossoski, Hans Lischka, Benedetta Mennucci, Saikat Mukherjee, Marek Pederzoli, Maurizio Persico, Max Pinheiro Jr., Jiří Pittner, Felix Plasser, Eduarda Sangiogo Gil, Ljiljana Stojanovic, Mario Barbatti, and Mattia Bondanza. Newton-x platform: New software developments for surface hopping and nuclear ensembles. *Journal of Chemical Theory and Computation*, 18(11):6851–6865, 2022. doi: 10.1021/acs.jctc.2c00804.

[135] Xiang Li, Artem Rudenko, Markus S. Schöffler, Nils Anders, Thomas M. Baumann, Sebastian Eckart, Benjamin Erk, Andrea De Fanis, Katharina Fehre, Reinhard Dörner, Laurent Foucar, Sebastian Grundmann, Piotr Grychtol, Alexander Hartung, Michael Hofmann, Michael Ilchen, Christian Janke, Georg Kastirke, Matthias Kircher, Karol Kubicek, Marko Kunitski, Tommaso Mazza, Stefan Meister, Niklas Melzer, Juan Montano, Vjekoslav Music, Giuseppe Nalin, Yaroslav Ovcharenko, Christian Passow, Andrea Pier, Nils Rennhack, Johannes Rist, Daniel E. Rivas, Ilme Schlichting, Lucas Ph. H. Schmidt, Philipp Schmidt, Jan Siebert, Nicole Strenger, David Trabert, Florian Trinter, Irene Vela-Perez, Robin Wagner, Peter Walter, Matthias Weller, Pawel Ziolkowski, Achim Czasch, Daniel Rolles, Michael Meyer, Thomas Jahnke, and Rebecca Boll. Coulomb explosion imaging of small polyatomic molecules with ultrashort X-ray pulses. *Physical Review Research*, 4:013029, January 2022. doi: 10.1103/PhysRevResearch.4.013029. URL https://link.aps.org/doi/10.1103/PhysRevResearch.4.013029.

[136] Huynh Van Sa Lam, Van-Hung Hoang, Anbu Selvam Venkatachalam, Surjendu Bhattacharyya, Keyu Chen, Sina Jacob, Sanduni Kudagama, Tu Thanh Nguyen, Daniel Rolles, Uwe Thumm, Artem Rudenko, and Vinod Kumarappan. Simultaneous imaging of vibrational, rotational, and electronic wave-packet dynamics in a triatomic molecule. *Phys. Rev. A*, 111:L061101, Jun 2025. doi: 10.1103/1yd8-786g. URL https://link.aps.org/doi/10.1103/1yd8-786g.

[137] Constant A. Schouder, Adam S. Chatterley, James D. Pickering, and Henrik Stapelfeldt. Laser-Induced Coulomb Explosion Imaging of Aligned Molecules and Molecular Dimers. *Annual Review of Physical Chemistry*, 73(Volume 73, 2022):323–347, 2022. ISSN 1545-1593. doi: https://doi.org/10.1146/annurev-physchem-090419-053627. URL https://www.annualreviews.org/content/journals/10.1146/annurev-physchem-090419-053627.

[138] Leszek J Frasinski. Covariance mapping techniques. *Journal of Physics B: Atomic, Molecular and Optical Physics*, 49(15):152004, jul 2016. doi: 10.1088/0953-4075/49/15/152004. URL https://dx.doi.org/10.1088/0953-4075/49/15/152004.

[139] Chuan Cheng, Leszek J. Frasinski, Gönen ç Moğol, Felix Allum, Andrew J. Howard, Daniel Rolles, Philip H. Bucksbaum, Mark Brouard, Ruaridh Forbes, and Thomas Weinacht. Multiparticle Cumulant Mapping for Coulomb Explosion Imaging. *Phys. Rev. Lett.*, 130:093001, Mar 2023. doi: 10.1103/PhysRevLett.130.093001. URL https://link.aps.org/doi/10.1103/PhysRevLett.130.093001.

[140] Anbu Selvam Venkatachalam, Loren Greenman, Joshua Stallbaumer, Artem Rudenko, Daniel Rolles, and Huynh Van Sa Lam. Exploiting correlations in multi-coincidence Coulomb explosion patterns for differentiating molecular structures using machine learning. Manuscript submitted for publication, 2025.

[141] *MATLAB version 24.1.0 (R2024a)*. The MathWorks, Inc., Natick, Massachusetts,

2024. randperm function. Available at: https://www.mathworks.com/help/matlab/ref/randperm.html.

[142] Kurtis Borne. *Probing the Structure and Dynamics of Complex Hydrocarbons with Ionizing Radiation from Free-Electron Lasers*. Ph.d. dissertation, Kansas State University, Manhattan, KS, USA, 2024. URL https://jrm.phys.ksu.edu/theses.html.

[143] Alice E. Green, Keyu Chen, Surjendu Bhattacharyya, Felix Allum, Sergey Usenko, Michael N. R. Ashfold, Thomas M. Baumann, Kurtis D. Borne, Mark Brouard, Michael Burt, Basile F. E. Curchod, Benjamin Erk, Ruaridh J. G. Forbes, Lea M. Ibele, Rebecca A. Ingle, Huynh Van Sa Lam, Xiang Li, Kang Lin, Tommaso Mazza, Joseph W. McManus, Michael Meyer, Terrence Mullins, João P. F. Nunes, Daniel Rivas, Aljoscha Roerig, Arnaud Rouzée, Philipp Schmidt, John Searles, Björn Senfftleben, Henrik Stapelfeldt, Rico Mayro P. Tanyag, Florian Trinter, Anbu Selvam Venkatachalam, Enliang Wang, Emily M. Warne, Peter M. Weber, Thomas Wolf, Till Jahnke, Artem Rudenko, Rebecca Boll, and Daniel Rolles. Visualizing the three-dimensional arrangement of hydrogen atoms in organic molecules by Coulomb explosion imaging. *Submitted*, 2025. Manuscript submitted for publication. Dated: February 7, 2025.

[144] Wolfgang Decking, Sargis Abeghyan, Pavel Abramian, Alexander Abramsky, Antonio Aguirre, Christian Albrecht, Philippe Alou, Massimo Altarelli, Philipp Altmann, Karen Amyan, and et al. A MHz-repetition-rate hard X-ray free-electron laser driven by a superconducting linear accelerator. *Nature Photonics*, 14:391–397, 2020. doi: 10.1038/s41566-020-0607-z.

[145] Terry A. Ferrett, David W. Lindle, Philip A. Heimann, Hans G. Kerkhoff, Ulrich E. Becker, and David A. Shirley. Sulfur 1s core-level photoionization of SF_6. *Physical Review A*, 34:1916–1930, September 1986. doi: 10.1103/PhysRevA.34.1916. URL https://link.aps.org/doi/10.1103/PhysRevA.34.1916.

[146] Michael J. Frisch, Geoffrey W. Trucks, H. Bernhard Schlegel, Gustavo E. Scuseria, Michael A. Robb, John R. Cheeseman, Giovanni Scalmani, Vincenzo Barone, Benedetta Mennucci, Gregory A. Petersson, Hiroshi Nakatsuji, Maurizio Caricato, Xue Li, Hrant P. Hratchian, Anatoly F. Izmaylov, Jacopo Bloino, Gaofan Zheng, Jose Luis Sonnenberg, Masahiko Hada, Masahiro Ehara, Kazuyuki Toyota, Ryo Fukuda, Jun Hasegawa, Masanori Ishida, Takashi Nakajima, Yasuhiro Honda, Osamu Kitao, Hiroshi Nakai, Tom Vreven, John A. Montgomery Jr., Javier E. Peralta, Fabrizio Ogliaro, Michael Bearpark, John J. Heyd, Emrah Brothers, Konstantin N. Kudin, Viktor N. Staroverov, Rika Kobayashi, Joseph Normand, Krishnan Raghavachari, Andreas Rendell, Jeffrey C. Burant, Sanjay S. Iyengar, Jacopo Tomasi, Maurizio Cossi, Nicola Rega, James M. Millam, Matthias Klene, James E. Knox, James B. Cross, Vannoy Bakken, Claudio Adamo, Jorge Jaramillo, Richard Gomperts, Robert E. Stratmann, Oleg Yazyev, Andrew J. Austin, Roberto Cammi, Cecilia Pomelli, Jason W. Ochterski, Richard L. Martin, Keiji Morokuma, Vladimir G. Zakrzewski, Gregory A. Voth, Pablo Salvador, John J. Dannenberg, Stefan Dapprich, Andrew D. Daniels, Ödön Farkas, James B. Foresman, Jorge V. Ortiz, Jerzy Cioslowski, and Douglas J. Fox. Gaussian 09, revision a.1, 2009.

[147] Michael P. Doyle, Michael A. McKervey, and Tong Ye. Cyclopropanation of 2,3-dihydrofuran. In Paul Knochel and Gary A. Molander, editors, *Comprehensive Organic Synthesis II*, volume 4, chapter 4.20.4.1.4.9.8, pages 953–954. Elsevier, 2014. doi: 10.1016/B978-0-08-097743-0.00432-3. URL https://www.sciencedirect.com/referencework/9780080977430/comprehensive-organic-synthesis. Accessed May 29, 2025.

[148] Fumiyuki Ozawa, Akira Kubo, and Tamio Hayashi. Catalytic asymmetric arylation of 2,3-dihydrofuran with aryl triflates. *Journal of the American Chemical Society*, 113 (4):1417–1419, 1991. doi: 10.1021/ja00004a007.

[149] Alexander Domling. Multicomponent reactions. In Alan R. Katritzky, Christopher A. Ramsden, Eric F.V. Scriven, and Richard J.K. Taylor, editors, *Comprehensive Heterocyclic Chemistry III*, volume 3, chapter 3.07.3.4, pages 587–620. Elsevier, 2008. doi: 10.1016/B978-008044992-0.00090-4. URL https://www.sciencedirect.com/referencework/9780080449920/comprehensive-heterocyclic-chemistry-iii. Accessed May 29, 2025.

[150] ScienceDirect Topics. 2,3-dihydrofuran. https://www.sciencedirect.com/topics/chemistry/2-3-dihydrofuran, 2022. Accessed May 29, 2025.

[151] Cheng Zhu, Yu Zhang, Shuang Wang, Xue Wang, Jiajia Zhang, Jiahui Wang, Xiaoyu Li, Ning Ma, Jinbo Zhu, and Deyue Yan. Green, metal-free cationic polymerization of 2,3-dihydrofuran to a strong, biorenewable, and degradable polymer. *Journal of the American Chemical Society*, 144(37):17064–17072, 2022. doi: 10.1021/jacs.2c06103. URL https://doi.org/10.1021/jacs.2c06103.

[152] Anja Röder, Nelson de Oliveira, Floriane Grollau, and Jean-Michel Mestdagh. High-resolution vacuum ultraviolet absorption spectra of 2,3- and 2,5-dihydrofuran. *The Journal of Chemical Physics*, 153(13):134303, 2020. doi: 10.1063/5.0015835. URL https://pubs.aip.org/aip/jcp/article/153/13/134303/199493.

[153] William H. Green. Ring-puckering vibration of 2,3-dihydrofuran. *The Journal of Chemical Physics*, 50(4):1619–1621, 1969. doi: 10.1063/1.1671224.

[154] David Autrey and Joseph Laane. Far-infrared spectra, *ab initio* calculations, and the ring-puckering potential energy function of 2,3-dihydrofuran. *The Journal of Physical Chemistry A*, 105(27):6894–6899, 2001. doi: 10.1021/jp010571c.

[155] Oliver Schalk, Tian Geng, Tony Hansson, and Richard D. Thomas. The ring-opening channel and the influence of rydberg states on the excited state dynamics of furan and

its derivatives. *The Journal of Chemical Physics*, 149(8):084303, 2018. doi: 10.1063/1.5040331. URL https://doi.org/10.1063/1.5040331.

[156] Stefan Roither, Xinhua Xie, Daniil Kartashov, Li Zhang, Markus Schöffler, Huailiang Xu, Atsushi Iwasaki, Tomoya Okino, Kaoru Yamanouchi, Andrius Baltuska, and Markus Kitzler. High Energy Proton Ejection from Hydrocarbon Molecules Driven by Highly Efficient Field Ionization. *Phys. Rev. Lett.*, 106(16):163001, 2011. doi: 10.1103/PhysRevLett.106.163001.

[157] Hans-Joachim Werner and Peter J. Knowles. An efficient internally contracted multiconfiguration–reference configuration interaction method. *The Journal of Chemical Physics*, 89(9):5803–5814, 1988. doi: 10.1063/1.455556.

[158] Björn O. Roos, Peter R. Taylor, and Per E. M. Sigbahn. A complete active space SCF method (CASSCF) using a density matrix formulated super-CI approach. *Chemical Physics*, 48(2):157–173, 1980. doi: 10.1016/0301-0104(80)80045-0.

[159] Thom H. Dunning. Gaussian basis sets for use in correlated molecular calculations. i. the atoms boron through neon and hydrogen. *The Journal of Chemical Physics*, 90 (2):1007–1023, 1989. doi: 10.1063/1.456153.

[160] Hans-Joachim Werner, Peter J. Knowles, Gerald Knizia, Frederick R. Manby, and Matthias Schütz. Molpro: A general-purpose quantum chemistry program package. *WIREs Computational Molecular Science*, 2(2):242–253, 2012. doi: 10.1002/wcms.82.

Appendix A

Coulomb explosion imaging of three-body and four-body complete fragmentation of ethylene

This Appendix includes content related to Chapter. 4.

A.1 Coulomb explosion imaging of three-body complete fragmentation of ethylene

A.1.1 Theoretical calculations provided

For the theoretical calculations as shown in Fig. A.1, which were done by Prof. Loren Greenman and Dr. Paresh Modak. They calculated a two-dimensional potential energy surface for the breakup of $C_2H_4^{3+}$ into CH^+, CH_2^+, and H^+ fragments. The relevant C–H and C–C bond lengths were systematically varied without reoptimizing the remaining internal coordinates. The energies were computed at the contracted MRCI level of theory[157], based on a CASSCF(4,8) calculation[158] and using the cc-pVTZ basis set[159] in the MOLPRO

software package[160]. These potential energy curves were compared to Coulomb curves extrapolated to large bond lengths. The effects of geometry optimization, active space size, and state-averaged excited-state treatments were also considered, but are not shown. For the

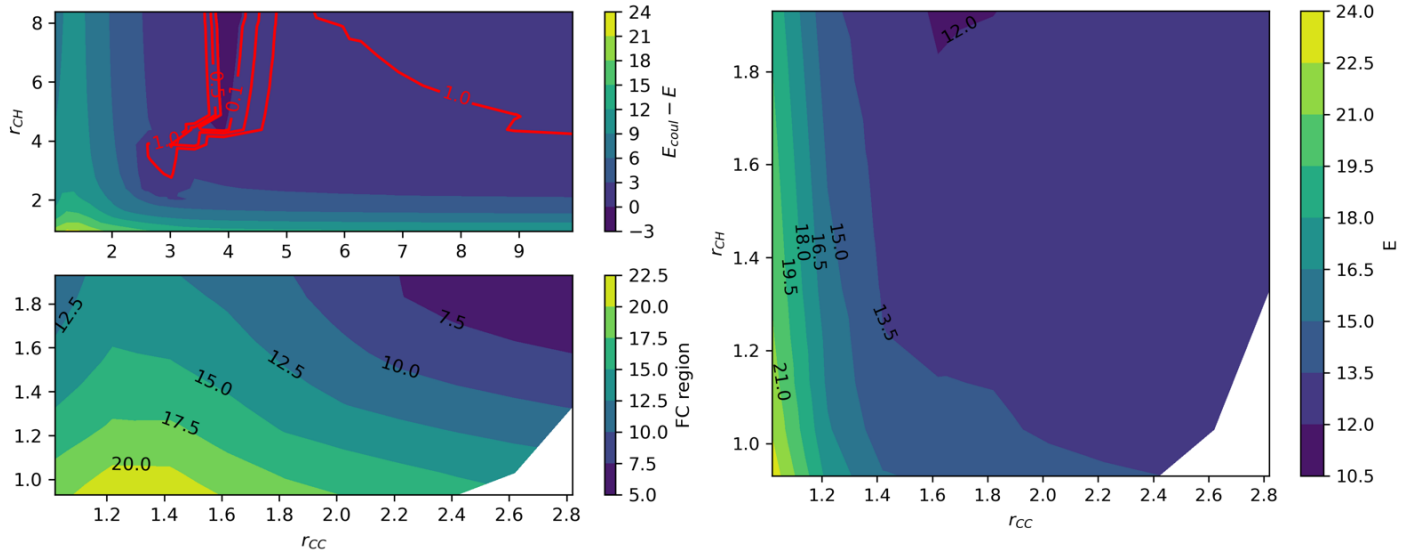

Figure A.1: *Theory Calculation of potential energy surface of triply-charged ethylene obtained from Dr. Paresh Modak and Prof. Loren Greenman.*

The first plot shows the Coulomb energy overlaid on the actual potential energy surface (PES), including both a full view and a close-up of the Franck–Condon (FC) region. The second plot displays the PES alone, focused on the FC region.

relaxation energy calculations, which were carried out by Dr. Paresh Modak, the methods he used are described below:

To assess the impact of geometry relaxation on the electronic structure of the multiply charged ethylene molecule, multic-onfigurational self-consistent field (CASSCF) calculations were performed by our collaborator. The calculations employed the augmented correlation-consistent polarized valence triple-zeta (aug-cc-pVTZ) basis set and a complete active space (CAS) comprising five electrons in five orbitals, denoted as CAS(5,5). The energies of four electronic states—ground state (GS) and three excited states (Ex1, Ex2, Ex3)—were evaluated under different geometrical constraints.

Case 1: Fixed r_{CH} at Franck–Condon (FC), $r_{CC} \to \infty$ In this case, the C–H bond length (r_{CH}) was fixed at its Franck–Condon (FC) value, while the C–C bond (r_{CC}) was set to an asymptotically large value of 16.42 Å. The relaxation energy, defined as the difference between the unrelaxed and relaxed geometries for each state, was computed:

State	GS	Ex1	Ex2	Ex3
Relaxation Energy (eV)	1.961	1.113	1.922	0.546

Case 2: $r_{CH} = 8.38$ Å, $r_{CC} = 16.67$ Å Here, both the C–H and C–C bonds were fixed at asymptotically large separations. The corresponding relaxation energies for the four states were much smaller, indicating minimal structural relaxation at large interatomic distances:

State	GS	Ex1	Ex2	Ex3
Relaxation Energy (eV)	0.014	0.051	0.057	0.002

Case 3: Fixed r_{CC} at FC, $r_{CH} = 16.15$ Å In this configuration, the C–C bond was kept at its Franck–Condon value while r_{CH} was extended to a large value. The calculated relaxation energies are as follows:

State	GS	Ex1	Ex2	Ex3
Relaxation Energy (eV)	0.478	1.200	0.672	0.860

These calculations provide insight into how geometry relaxation influences the electronic structure across different molecular configurations. In particular, the significant energy differences observed in Cases 1 and 3 reflect the localized nature of the electronic states when only one bond is dissociated, while Case 2 suggests nearly negligible relaxation when the molecule is fully dissociated.

A.1.2 Concerted breakup and experimental data

We show the three-body experimental data in Fig. A.2, and we plot the non-normalized Newton diagrams of experimental data shown in Fig. A.3. Fig. A.4 shows the separated

concerted breakup experimental data compared with Coulomb explosion simulation using the non-normalized Newton diagrams and KERs. Fig. A.5 (a) shows the gate used for the separated concerted breakup experimental data.

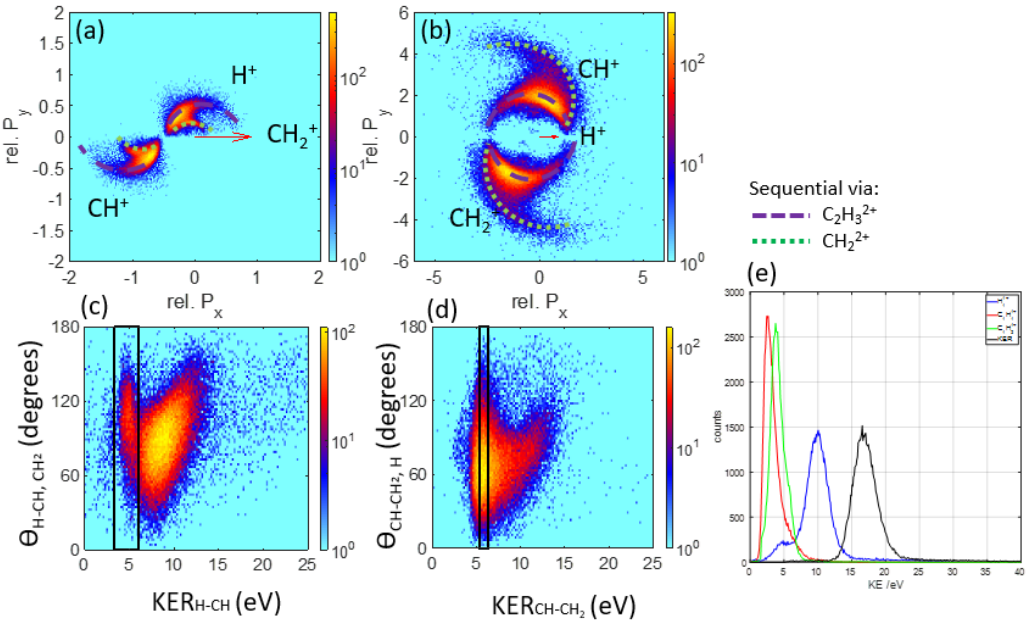

Figure A.2: *Native frame analysis of ethylene experimental data of three-body fragmentation.*

All events of the H^+ + CH^+ + $CH_2{}^+$ fragmentation channel are plotted as (a-b) Newton diagrams measured in coincidence. For (a), the momentum of $CH_2{}^+$ is normalized to 1, pointing to the P_x axis (orange arrow),and the relative momenta of H^+ and CH^+ fragment ions are plotted in the upper and lower half. For (b), the momentum of H^+ is normalized to 1, pointing to the P_x axis (orange arrow), and the relative momenta of CH^+ and $CH_2{}^+$ fragment ions are plotted in the upper and lower half. (c). $N(KER_{H-CH}, \Theta_{H-CH}, {}_{CH_2})$ and the black box is marked to be the sequential breakup via CH^+ + $CH_2{}^+$ fragmentation (d). $N(KER_{CH-CH_2}, \Theta_{CH-CH_2}, {}_{H})$ distributions for three-body fragmentation channel H^+ + CH^+ + $CH_2{}^+$ The black box is marked to be the sequential breakup via H^+ + $C_2H_3{}^{2+}$ (e). Kinetic energy distribution of each fragment ion detected H^+, CH^+, $CH_2{}^+$, and the sum of total KER.

A.1.3 Sequential breakup and experimental data

Fig. A.6 shows the original version of Fig. 4.7(a) and (c), before background subtraction and without applying any selection conditions. The scaling ratios applied to the momen-

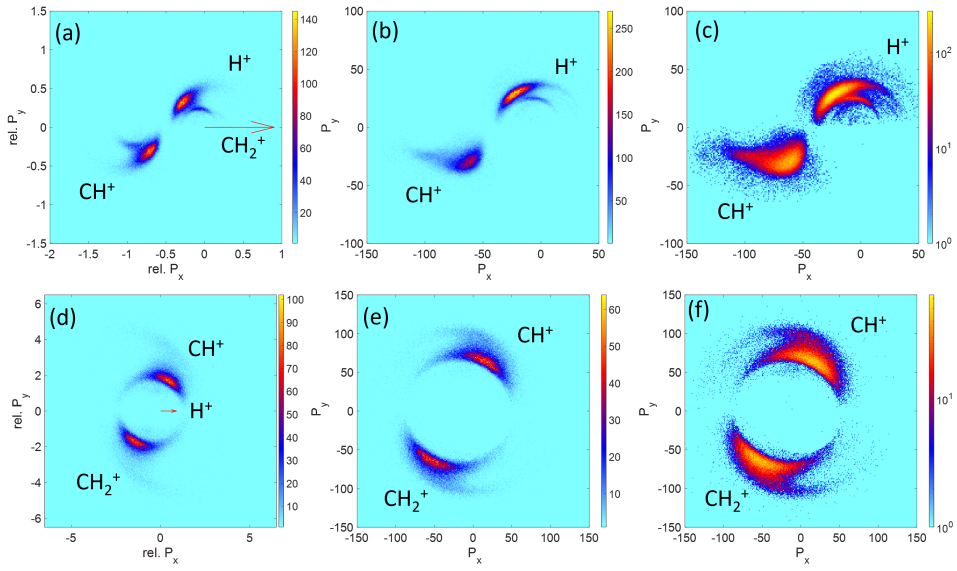

Figure A.3: *Newton diagrams for three-body concerted breakup of ethylene experimental data.*
(a) and (c) the relative normalized Newton diagrams measured in coincidence in linear scale color map. For (a), the momentum of $CH_2{}^+$ is normalized to 1, pointing to the P_x axis (orange arrow),and the relative momenta of H^+ and CH^+ fragment ions are plotted in the upper and lower half. For (d), the momentum of H^+ is normalized to 1, pointing to the P_x axis (orange arrow), and the relative momenta of CH^+ and $CH_2{}^+$ fragment ions are plotted in the upper and lower half. (b) and (e) the relative non-normalized Newton diagrams measured in coincidence in linear scale color map. (c) and (f) the relative non-normalized Newton diagrams measured in coincidence in log scale color map. For (b)and(c), the momentum of $CH_2{}^+$ is pointing to the P_x axis (orange arrow),and the relative momenta of H^+ and CH^+ fragment ions are plotted in the upper and lower half. For (e)and(f), the momentum of H^+ is pointing to the P_x axis (orange arrow), and the relative momenta of CH^+ and $CH_2{}^+$ fragment ions are plotted in the upper and lower half.

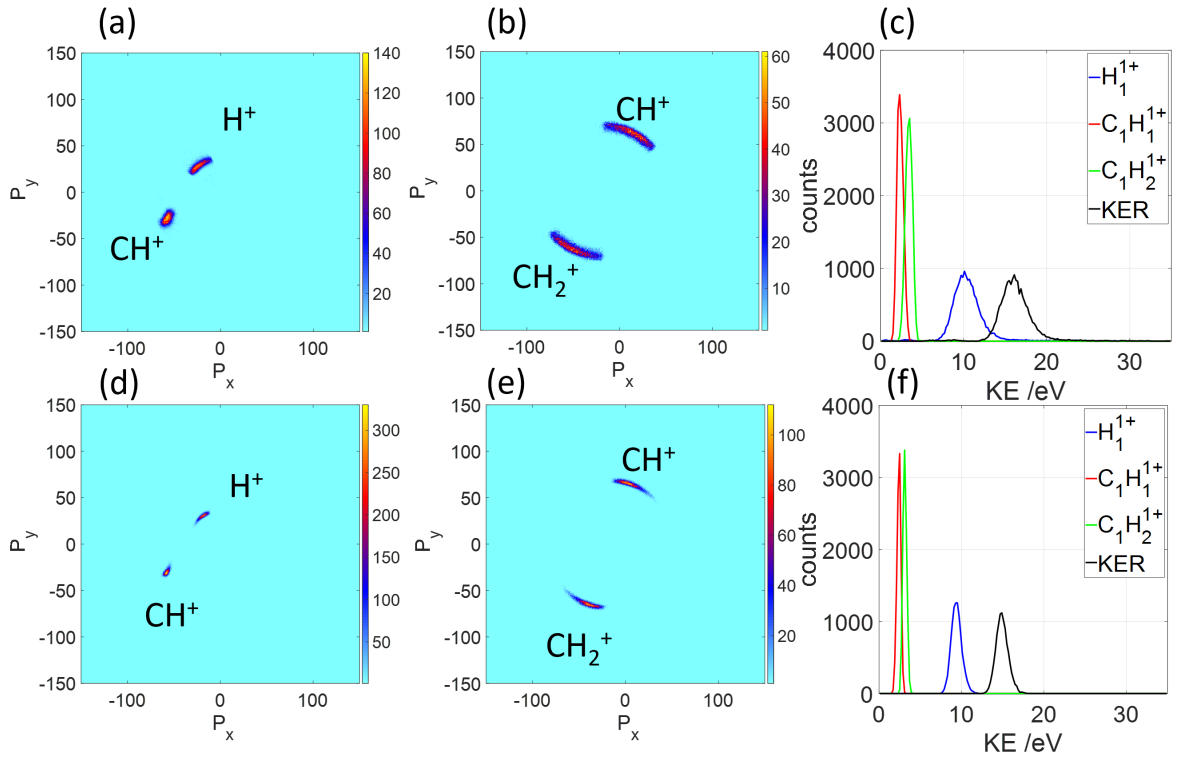

Figure A.4: *Separated three-body concerted breakup of ethylene experimental data and Coulomb explosion simulation comparison.*
(a)-(c) Separated concerted breakup events from experimental data. (d)-(f) Coulomb explosion Simulation of concerted breakup channel. (a)(b)(d)(e) are the relative non-normalized Newton diagrams and (c) is the kinetic energy release of experimental data, (e) KER from the Coulomb explosion simulation for concerted breakup using Wigner distribution at 60K of ground state ethylene optimized at the B3LYP/aug-cc-pVDZ level of theory with total KER ratioed to calculated Coulomb explosion KER of 16.5eV (to match the experiment KER)

tum distributions from the Coulomb explosion simulations were determined by matching the simulated kinetic energy releases (KERs) to the calculated energy differences of different potential surfaces (PESs). Specifically, each ratio was computed as the square root of the ratio between the simulated kinetic energy release (from two-body CES) and the corresponding calculated energy differences as shown in Table A.1:

Sequential breakup via $CH_2^+ + CH_2^+$

Fig. A.7 shows the non-normalized Newton diagrams version of Fig. 4.9.

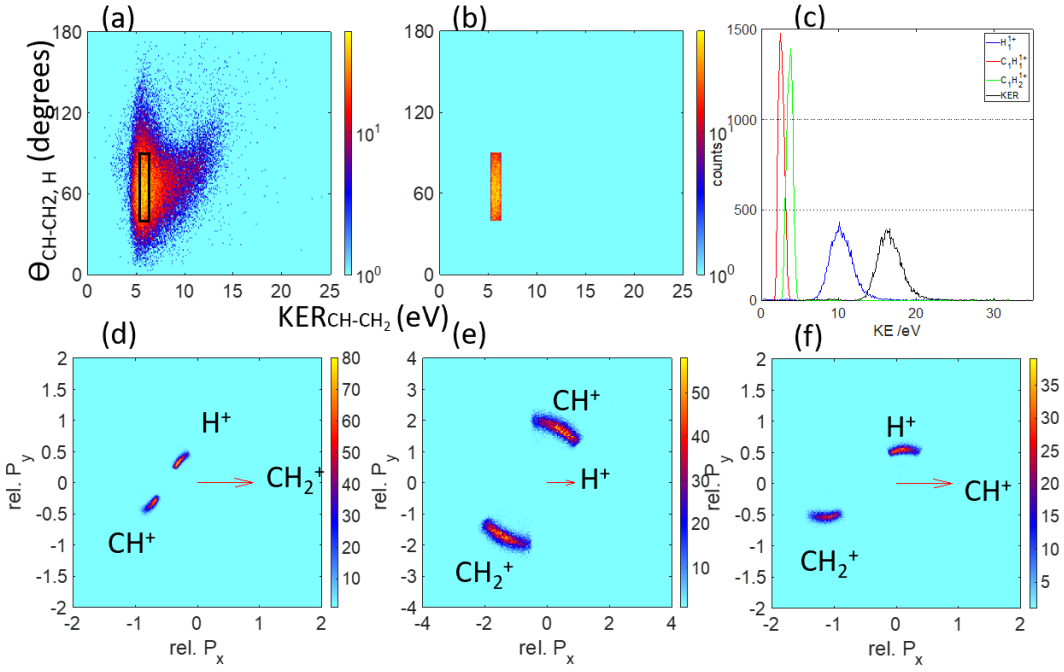

Figure A.5: *Three-body concerted breakup of ethylene experimental data separation. $N(KER_{CH-CH_2}, \Theta_{CH-CH_2,\,H})$distributions for three-body fragmentation channel for (a) all H^+ + CH^+ + $CH_2{}^+$ events, the black box are the selected region for gating out the concerted events , (b) the selected concerted events and (c) the KER for the complete H^+ + CH^+ + $CH_2{}^+$ fragmentation channel of the selected concerted events. (d)-(f) Relative Newton diagrams of the H^+ + CH^+ + $CH_2{}^+$ fragmentation channel of the selected concerted events.*

Breakup channels	1st step KER sim	1st step PES diff	1st step ratio	2nd step KER sim	2nd step PES diff	2nd step ratio
via $CH_2^+ + CH_2^+$	19.435 eV	11.679 eV	1.29	19.75 eV	4.751 eV	2.008
via $H^+ + C_2H_3^{2+}$	17.745 eV	11.941 eV	1.219	9.75 eV	2.527 eV	1.964

Table A.1: *Ratios used in different sequential breakup channels in two-step CES of ethylene.*

First, we investigated the two-body breakup channel $CH_2^+ + CH_2^+$ as a preliminary step in analyzing the sequential fragmentation pathway via $CH_2^{2+} + CH_2^+$. The experimentally obtained kinetic energy distribution for this two-body breakup shows a kinetic energy release (KER) of approximately 5.865 eV per fragment (both ions have the same KER due to equal mass), as shown in Fig. A.8, yielding a total KER of 11.73 eV. This value aligns well with our theoretical calculation, which predicts a total energy release of 11.678755 eV.

The theoretical energy corresponds to an energy release of 9.7175 eV (14.8247-5.10727)

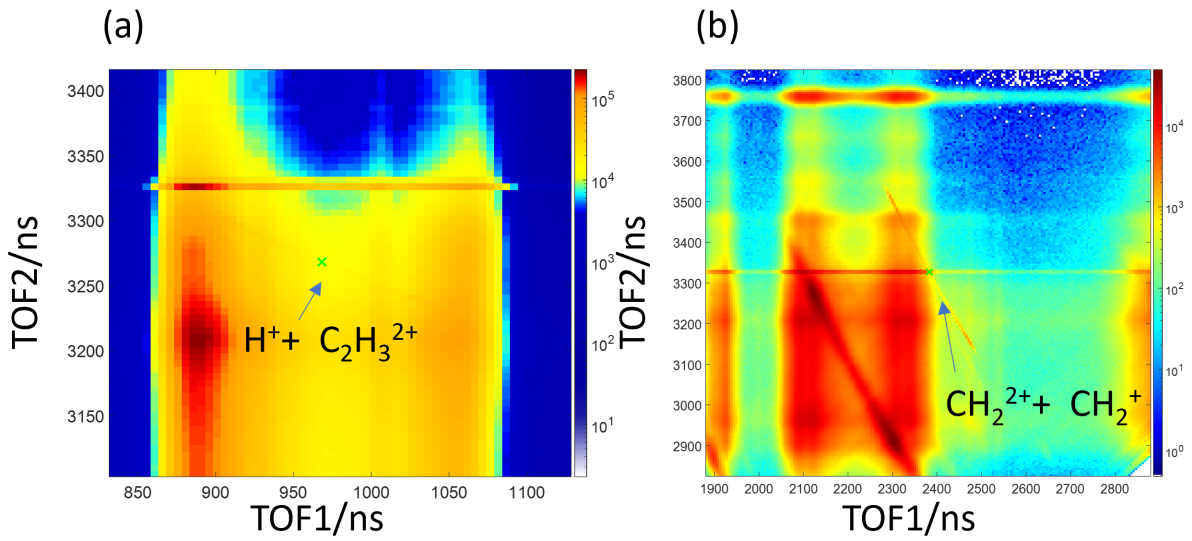

Figure A.6: *PIPICO maps of two-body fragmentation of ethylene used for analyzing the sequential breakup channels.*

The regions of the PIPICO map for (a) $H^+ + C_2H_3^{2+}$ *and (b)* $CH_2^+ + CH_2^{2+}$ *channels. Green crosses mark the centers of the time-of-flights (TOFs).*

from the C–C bond stretching, from the equilibrium bond length of 1.32 Å to 150.92 Å, with the C–H bond length fixed at 1.08 Å. A relaxation energy of 1.96125 eV, calculated by Dr. Paresh Modak (using r_{CH} = FC, with a C–C bond distance of 16.42 Å), is summed to obtain the final theoretical KER.

In the theoretical model, first step simulation corresponds to a near-asymptotic configuration where the C–H bond distance r_{CH} remains near its equilibrium value (i.e., the Franck–Condon point), while the C–C bond is significantly stretched, reaching r_{CC} = 150.92 Å releasing kinetic energy as shown in Fig. A.9. This configuration reflects the dissociative nature of this $CH_2^{2+} + CH_2^+$ sequential fragmentation pathway.

To model the sequential dissociation channel yielding CH_2^{2+} and CH_2^+, a two-body Coulomb explosion simulation is performed in the first step by assigning charges of +2 and +1 to the two CH_2 fragments, respectively. The resulting three-dimensional momentum vectors are scaled by applying the square root of the energy ratio, such that the kinetic

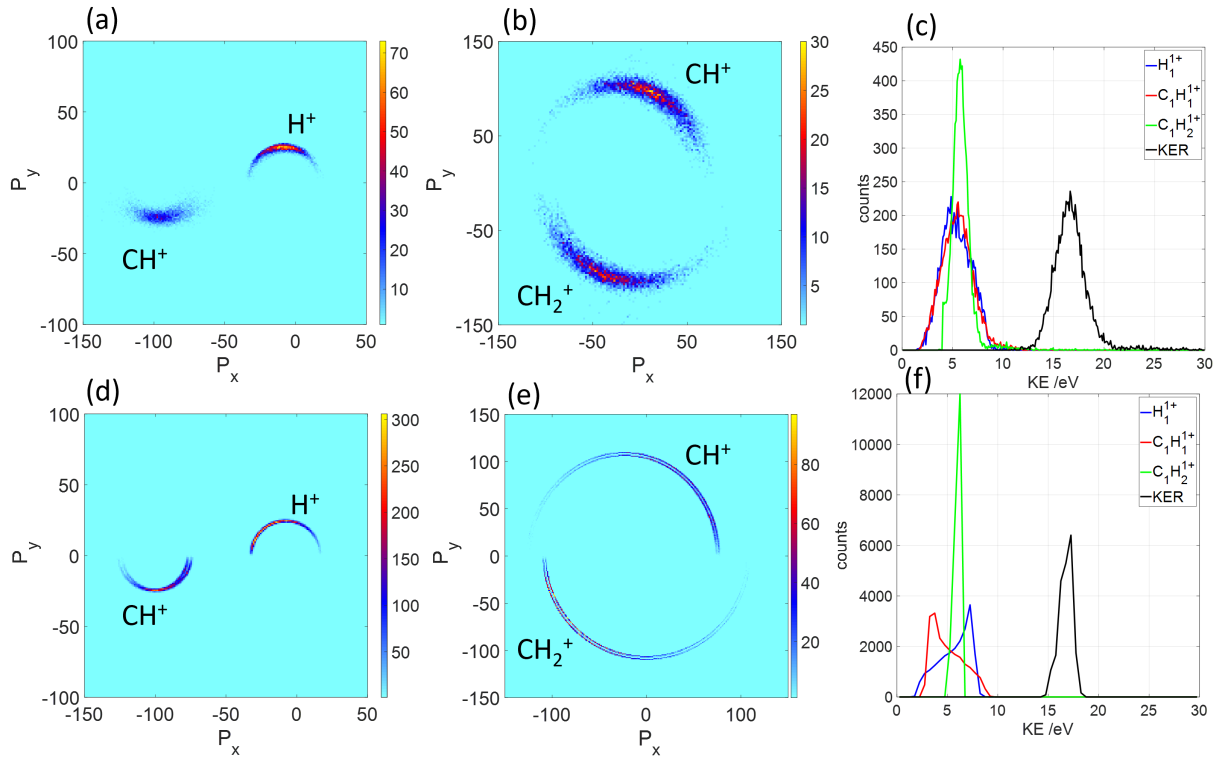

Figure A.7: *Three-body sequential fragmentation of ethylene via* $CH_2^+ + CH_2^{2+}$*: simulation and experimental data analysis.*

(a)-(c) Separated $CH_2{}^{2+}$ + $CH_2{}^{+}$ sequential breakup events from experimental data. (d)-(f) Coulomb explosion Simulation of sequential breakup channel via $CH_2{}^{2+}$ + $CH_2{}^{+}$. (a)(b) and (d)(e) are the relative non-normalized Newton diagrams. (c) and (f) are the kinetic energy distributions from experimental data and Coulomb explosion simulation respectively.

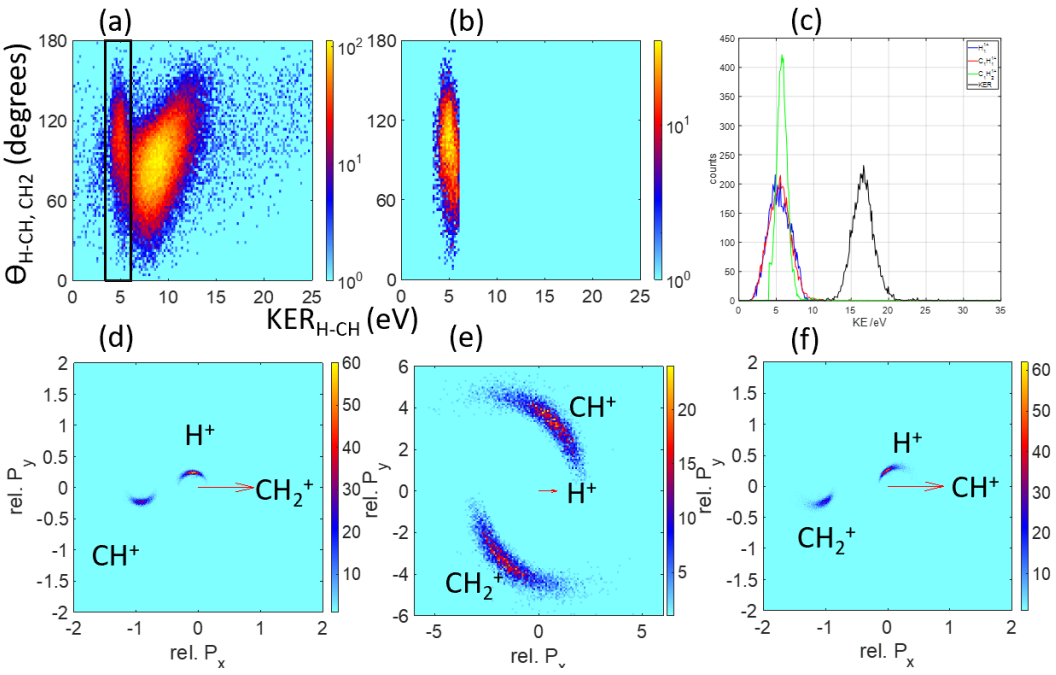

Figure A.8: *Separated three-body sequential fragmentation channel of ethylene experimental data via* $CH_2^+ + CH_2^{2+}$ *intermediate.*

$N(KER_{H-CH}, \Theta_{H-CH}, {}_{CH_2})$ distributions for three-body fragmentation channel for (a) all H^+ + CH^+ + $CH_2{}^+$ events, the black box are the selected region for gating out the sequential events, (b) the selected sequential events and (c) the KER for the complete H^+ + CH^+ + $CH_2{}^+$ fragmentation channel of the selected sequential events. (d)-(f) Relative Newton diagrams of the H^+ + CH^+ + $CH_2{}^+$ fragmentation channel of the selected sequential events.

energy release (KER) from the Coulomb repulsion between CH_2^{2+} and CH_2^+ after propagating for 50 ps matches the total energy release of 11.678755 eV, as predicted by quantum chemical calculations. The scaled momenta define the velocities of the fragments at a separation time of 50 ps. From this point onward, the CH_2^+ fragment is assumed to continue with constant velocity (i.e., without further interaction), while the CH_2^{2+} fragment undergoes random rotation and subsequent fragmentation in the second step.

In the second step, the CH_2^{2+} fragment is assumed to undergo random rotation about its center of mass before Coulomb exploding into H^+ and CH^+. We sampled 21 random rotation angles uniformly distributed in the interval $(0, 2\pi]$. At the instant of the second breakup, the +2 charge is redistributed to the centers of mass of the resulting fragments,

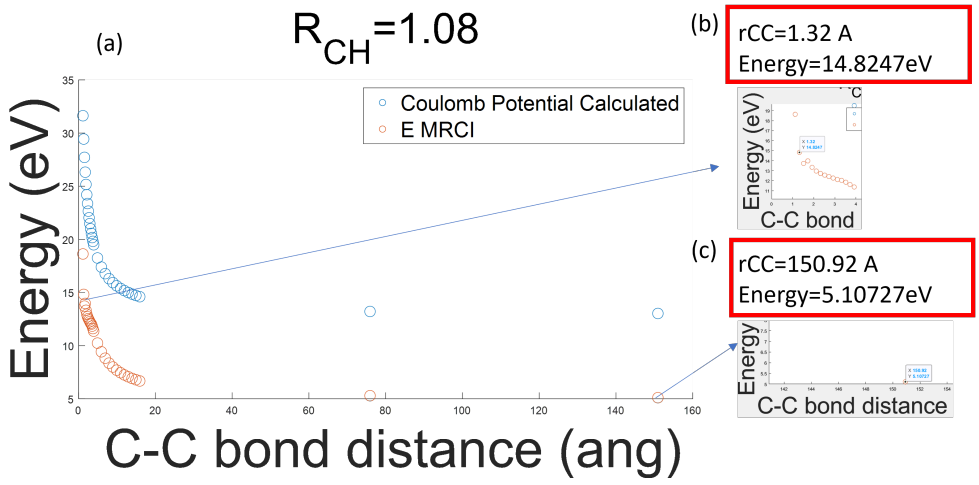

Figure A.9: *Energy difference from PES of triply-charged ethylene of C–C bond extension, C–H bond stays in Franck-Condon point. 1D projection of Fig. A.1.*

and a second Coulomb explosion simulation is performed. The momentum vectors of the second-step products are scaled to match a total KER of 4.75507 eV, as predicted by quantum chemical calculations. This energy release corresponds to the scenario of the energy difference calculated from the PES, where the C–H bond stretching with the C-C distance is fixed at 150.92 Å (in which C–C bonds are stretched in the first step).

This energy release 4.7507 eV (5.10727-0.3566) corresponds to the potential energy difference on the potential energy surface (PES), where the C–H bond is stretched (C–H bond stretch from the equilibrium bond length of 1.08 Å to 75.88 Å) while the C–C distance is fixed at 150.92 Å (the C–C bond was already stretched during the first step) as shown in Fig. A.10. In the second step, the CH_2^{2+} fragment is assumed to undergo random rotation (there are different types of rotations shown in Figs. A.12- and A.14. The discrete distribution from the Native frame plots in the simulations of CH_2^+ + CH_2^{2+} is due to only 21 angles chosen for sampling the simulation) about its center of mass before undergoing Coulomb explosion into H^+ and CH^+. We sampled 21 random rotation angles uniformly distributed over the interval $(0, 2\pi]$. At the moment of the second breakup, the +2 charge is redistributed to the centers of mass of the resulting fragments, and a second Coulomb ex-

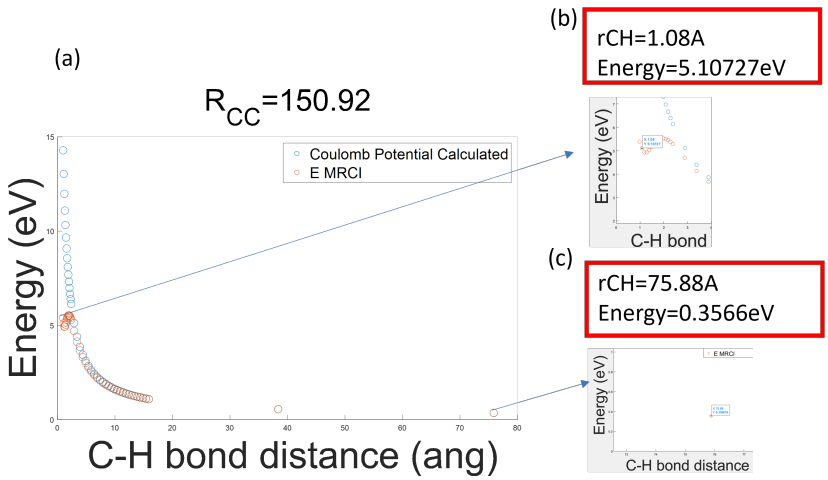

Figure A.10: *Energy difference from PES of triply-charged ethylene of C–H bond extension with C–C bond already extended to 150.92 Å. 1D projection of Fig. A.1.*

plosion propagating up to 1000 ps is performed. The momentum vectors of the second-step products are scaled to match a total kinetic energy release (KER) of 4.7507 eV.

The final momenta of CH^+ and H^+ are computed as the vector sum of the scaled momentum of the second-step fragments (from the Coulomb explosion of CH_2^{2+}) and the scaled momentum of the rotating CH_2^{2+} fragment from the first step. That is, both steps are individually scaled to match their respective energy releases before summation. The final momentum of the CH_2^+ fragment is taken directly as the scaled momentum from the first step, since it undergoes no further fragmentation.

In the second step from the Coulomb Explosion Simulation (CES), we tested several rotational scenarios (as shown in Fig. A.11, Fig. A.12, Fig. A.13, Fig A.14, and Fig. A.15) and found that the best agreement with experimental data is achieved when the intermediate fragment undergoes fully random rotation about a random axis passing through the center of mass of CH_2^{2+}.

The resulting Newton diagrams, shown in Fig. 4.9, successfully reproduce the experimental features. The black box in Fig. 4.4(a) corresponds to the same gating condition used to isolate the sequential breakup events via $CH_2^{2+} + CH_2^+$. The simulated Newton diagrams

exhibit good consistency with the experimental data, successfully reproducing the features of the random rotational dynamics of CH_2^{2+} following the initial two-body breakup.

For the three-body sequential fragmentation observed in the experimental data, a distinct feature can be extracted from the $N(\mathrm{KER}_{\mathrm{H-CH}},\ \Theta_{\mathrm{H-CH,\,CH_2}})$ distribution, where a characteristic band extends along the $\Theta_{\mathrm{H-CH,\,CH_2}}$ axis. By applying a gate to this region, we isolate events that exhibit clear signatures of sequential fragmentation, which become more evident under Newton diagram representations.

To distinguish this channel, we note that the rotation angle Θ between the $CH-CH_2$ fragment pair and the H^+ is not strongly correlated with the $\mathrm{KER}_{\mathrm{CH-CH_2}}$. The angular distribution of Θ spans nearly the entire range from 0° to 180°, indicative of random rotation of the intermediate species prior to breakup. Due to the finite detection efficiency of the microchannel plate (MCP) detector, event statistics are reduced near the angular edges.

By applying a gating condition along the sharp linear feature, as shown by the black box in Fig. 4.4(a)—where $\mathrm{KER}_{\mathrm{H-CH}}$ ranges from 3.4 to 6.1 eV and $\Theta_{\mathrm{H-CH,\,CH_2}}$ spans 0° to 180°—we successfully isolate the sequential fragmentation pathway via $CH_2^{2+} + CH_2^+$, as illustrated in Fig. 4.2.

Fig. A.15 shows the same simulation as Fig. A.13 but with 100 different angles sampledd with randomly chosen 1/10 of geometries of Fig. A.13 where it's sampledd with 21 different angles.

Sequential breakup via $H^+ + C_2H_3^{2+}$

The sequential fragmentation channel $H^+ + C_2H_3^{2+}$ is assumed to exhibit the same relative kinetic energy release (KER) to the hydrogen fragment as observed in the concerted breakup channel. In this mechanism, the H atom is first ejected from the molecule, and after a time delay, the remaining C_2H_3 fragment undergoes free rotation and spatial roaming before breaking apart. As a result, this sequential channel is modeled with increased angular freedom in the relative angle $\Theta_{\mathrm{CH-CH_2,\,H}}$.

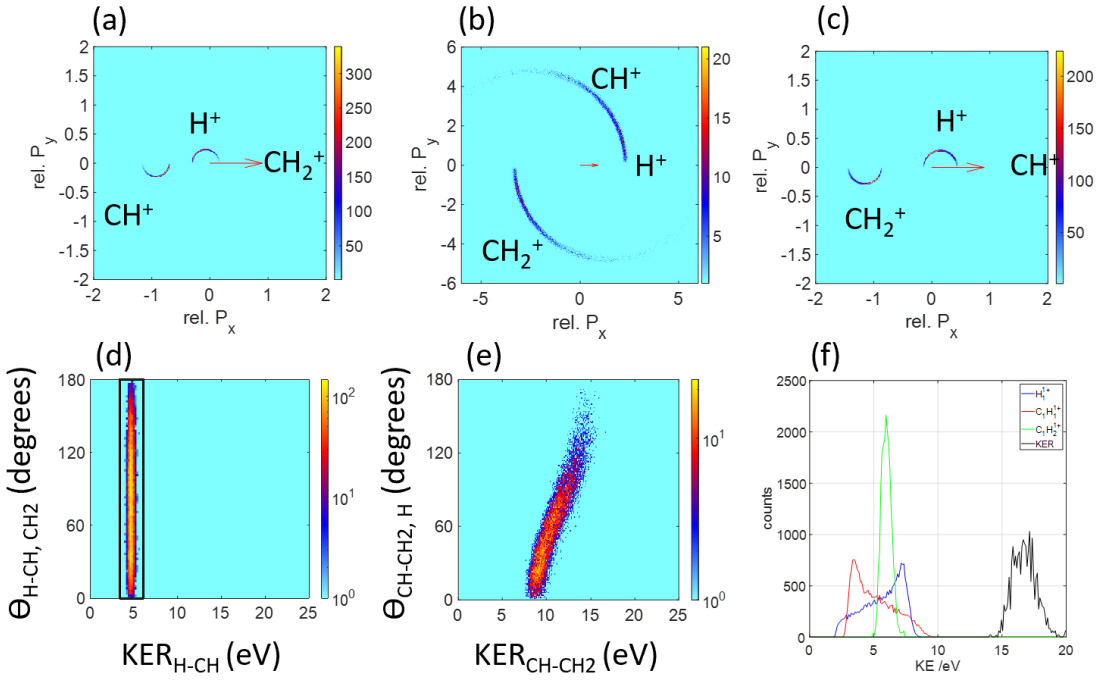

Figure A.11: *CES of three-body fragmentation of ethylene via CH_2^+ + CH_2^{2+} sequential breakup.*

(a)-(c)Relative Newton diagrams of the H^+ + CH^+ + $CH_2{}^+$ fragmentation channel from the Coulomb explosion simulation of CH_2^+ + CH_2^{2+} sequential breakup with a random rotation axis. (d) $N(KER_{H-CH}, \Theta_{H-CH}, {}_{CH_2})$ distributions for three-body fragmentation channel: H^+ + CH^+ + $CH_2{}^+$ from the Coulomb explosion simulation of CH_2^+ + CH_2^{2+} sequential breakup. (e) the $N(KER_{CH-CH_2}, \Theta_{CH-CH_2}, {}_{H})$ distributions for three-body fragmentation channel: H^+ + CH^+ + $CH_2{}^+$ from the Coulomb explosion simulation of CH_2^+ + CH_2^{2+} sequential breakup. (f) KER from the Coulomb explosion simulation of CH_2^+ + CH_2^{2+} sequential breakup.

To isolate this sequential breakup pathway, we applied a gating condition on the same KER window used for the concerted breakup—specifically, $\mathrm{KER}_{\mathrm{CH-CH_2}}$ ranging from 5.35 to 6.35 eV—and an angular range of $\Theta_{\mathrm{CH-CH_2,H}}$ spanning 0° to 180°. This gating, indicated by the black box in Fig. 4.4(b), allows us to distinguish the sequential breakup channel $\mathrm{H^+ + C_2H_3^{2+}}$, which reflects the broader angular distribution arising from the rotational motion of the intermediate fragment. For the dissociation channel yielding $\mathrm{H^+ + C_2H_3^{2+}}$, we also separate the simulation into two corresponding two-body breakup processes. The experimentally obtained kinetic energy distribution for this two-body breakup shows a kinetic energy release (KER) of approximately 11.37 eV, as shown in Fig. 4.7. This value is slightly

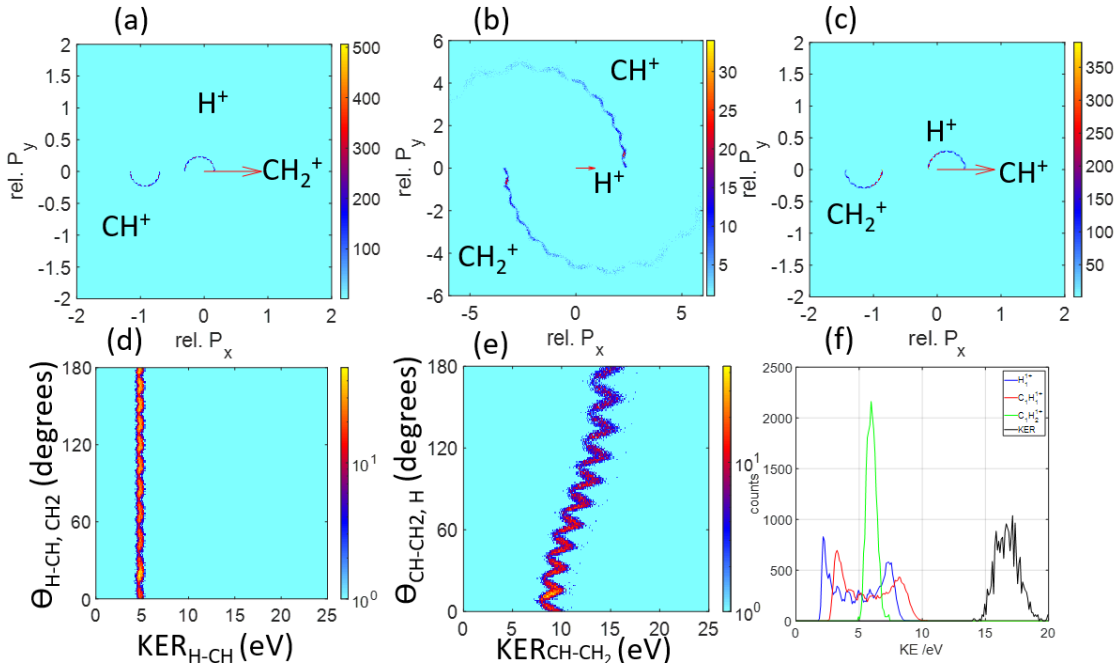

Figure A.12: *CES of three-body fragmentation of ethylene via CH_2^+ + CH_2^{2+} sequential breakup with different rotation in the second step v1.*

(a)-(c)Relative Newton diagrams of the H^+ + CH^+ + CH_2^+ fragmentation channel from the Coulomb explosion simulation of CH_2^+ + CH_2^{2+} sequential breakup with second step rotate according to an axis which is going through the COM of CH_2^{2+} and perpendicular to plane made up by the vectors pointing from the COM of CH_2^{2+} to the COM of CH and H fragments. (d) $N(KER_{H-CH}, \Theta_{H-CH}, {}_{CH_2})$ distributions for three-body fragmentation channel: H^+ + CH^+ + CH_2^+ from the Coulomb explosion simulation of CH_2^+ + CH_2^{2+} sequential breakup. (e) the $N(KER_{CH-CH_2}, \Theta_{CH-CH_2}, {}_{H})$ distributions for three-body fragmentation channel: H^+ + CH^+ + CH_2^+ from the Coulomb explosion simulation of CH_2^+ + CH_2^{2+} sequential breakup. (f) KER from the Coulomb explosion simulation of CH_2^+ + CH_2^{2+} sequential breakup.

lower than our theoretical prediction, which yields a total energy release of 11.9414 eV.

The theoretical energy of 11.9414 eV consists of a Coulomb energy release of 12.4197 eV (calculated as 14.8257 eV minus 2.4050 eV as shown in Fig. A.17) from C–H bond stretching, where the bond length increases from the equilibrium value of 1.08 Å to 75.88 Å, while the C–C bond length is fixed at its equilibrium value of 1.32 Å. A relaxation energy of 0.47829 eV, calculated by Dr. Paresh Modak (using r_{CC} = FC, with a C–C bond distance of 16.15 Å), is subtracted to obtain the final theoretical KER.

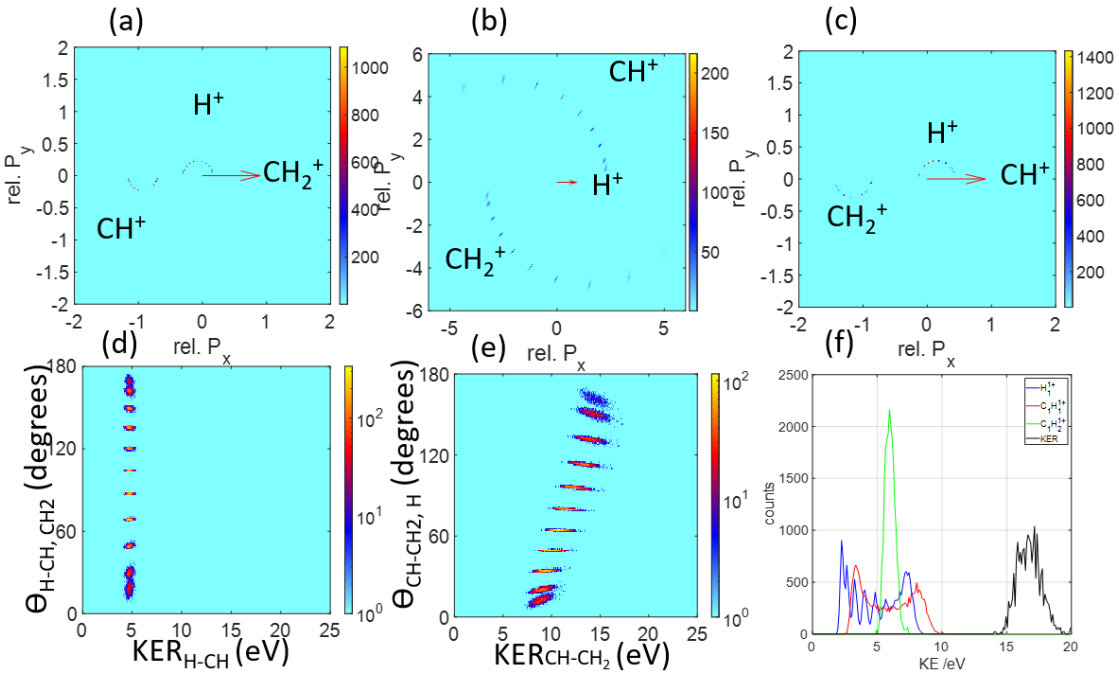

Figure A.13: *CES of three-body fragmentation of ethylene via CH_2^+ + CH_2^{2+} sequential breakup with different rotation in the second step v2.*

(a)-(c)Relative Newton diagrams of the H^+ + CH^+ + $CH_2{}^+$ fragmentation channel from the Coulomb explosion simulation of CH_2^+ + CH_2^{2+} sequential breakup with second step rotate according to an axis which is going through the COM of CH_2^{2+} and perpendicular to the C–C bond which is pointed from COM of CH_2^{2+} to COM of CH_2^+. (d) $N_{KER_{H-CH}}$, $\Theta_{H-CH,\ CH_2}$ distributions for three-body fragmentation channel: H^+ + CH^+ + $CH_2{}^+$ from the Coulomb explosion simulation of CH_2^+ + CH_2^{2+} sequential breakup. (e) the $N(KER_{CH-CH_2},\ \Theta_{CH-CH_2,\ H})$ distributions for three-body fragmentation channel: H^+ + CH^+ + $CH_2{}^+$ from the Coulomb explosion simulation of CH_2^+ + CH_2^{2+} sequential breakup. (f) KER from the Coulomb explosion simulation of CH_2^+ + CH_2^{2+} sequential breakup.

In the first-step simulation, we explored different lengths of propagation time for the two-body breakup channel $H^+ + C_2H_3^{2+}$.

In the theoretical model, first step simulation corresponds to a near-asymptotic configuration where the C–C bond distance r_{CC} remains near its equilibrium value (i.e., the Franck–Condon point), while the C–H bond is significantly stretched, reaching r_{CC} = 75.88 Å and releasing kinetic energy. This configuration reflects the dissociative nature of this $H^+ + C_2H_3^{2+}$ sequential fragmentation pathway.

To model the sequential dissociation channel yielding H^+ and $C_2H_3^{2+}$, a two-body Coulomb

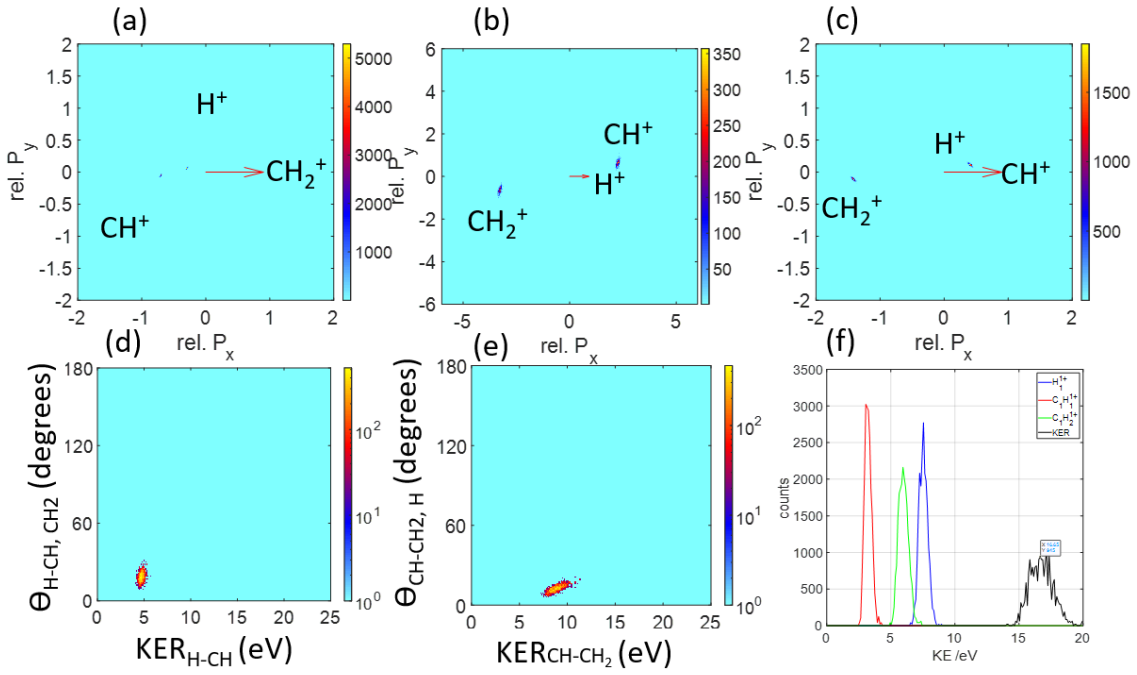

Figure A.14: *CES of three-body fragmentation of ethylene via CH_2^+ + CH_2^{2+} sequential breakup with different rotation in the second step v3.*

(a)-(c)Relative Newton diagrams of the H^+ + CH^+ + $CH_2{}^+$ fragmentation channel from the Coulomb explosion simulation of CH_2^+ + CH_2^{2+} sequential breakup with second step rotate according to an axis which is parallel to the C–C bond which is pointed from COM of CH_2^{2+} to COM of CH_2^+. (d) $N(KER_{H-CH}, \Theta_{H-CH,\ CH_2})$ distributions for three-body fragmentation channel: H^+ + CH^+ + $CH_2{}^+$ from the Coulomb explosion simulation of CH_2^+ + CH_2^{2+} sequential breakup. (e) the $N_{KER_{CH-CH_2}}$, $\Theta_{CH-CH_2,\ H}$ distributions for three-body fragmentation channel: H^+ + CH^+ + $CH_2{}^+$ from the Coulomb explosion simulation of CH_2^+ + CH_2^{2+} sequential breakup. (f) KER from the Coulomb explosion simulation of CH_2^+ + CH_2^{2+} sequential breakup.

explosion simulation is performed in the first step by assigning charges of +2 to the C_2H_3 and +1 to the H fragment. The resulting three-dimensional momentum vectors are scaled by applying the square root of the energy ratio such that the kinetic energy release (KER) from the Coulomb repulsion between H^{2+} and $C_2H_3^{2+}$ after propagating for 50 ps matches the total energy release of 11.5118 eV, as predicted by quantum chemical calculations. The scaled momenta define the velocities of the fragments at a separation time of 50 ps. From this point onward, the H^+ fragment is assumed to continue with constant velocity (i.e., without further interaction), while the $C_2H_3^{2+}$ fragment undergoes random rotation and subsequent

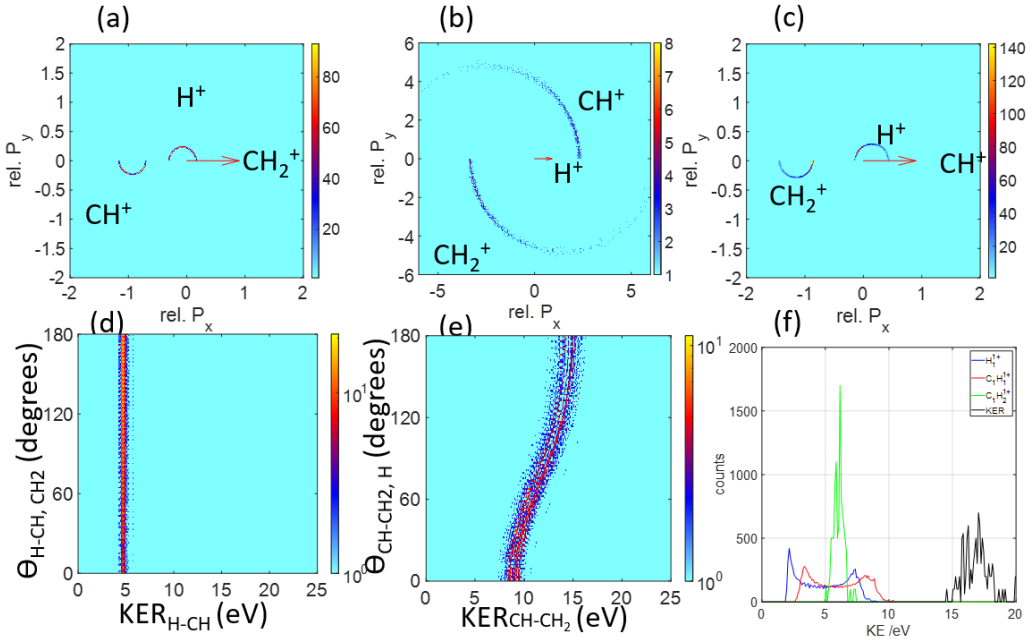

Figure A.15: *CES of three-body fragmentation of ethylene via CH_2^+ + CH_2^{2+} sequential breakup with different rotation in the second step v2 with more sampling angles.*

$N(KER_{H-CH}, \Theta_{H-CH, CH_2})$ distributions for three-body fragmentation channel for (a) all H^+ + CH^+ + $CH_2{}^+$ events, the black box is the selected region for gating out the sequential events , (b) the selected sequential events and (c) the KER for the complete H^+ + CH^+ + $CH_2{}^+$ fragmentation channel of the selected sequential events. (d)-(f) Relative Newton diagrams of the H^+ + CH^+ + $CH_2{}^+$ fragmentation channel of the selected sequential events.

fragmentation in the second step.

In the second step, the $C_2H_3^{2+}$ fragment is assumed to undergo random rotation about its center of mass before Coulomb exploding into CH^+ and CH_2^+. We sampledd 21 random rotation angles uniformly distributed over the interval $(0, 2\pi]$. At the instant of the second breakup, the +2 charge is redistributed to the centers of mass of the resulting fragments, and a second Coulomb explosion simulation is performed. The momentum vectors of the second-step products are scaled to match a total kinetic energy release (KER) of 2.5267 eV, as predicted by quantum chemical calculations.

This energy release corresponds to the potential energy difference calculated from the potential energy surface (PES), where the C–C bond is stretched while the C-H distance is

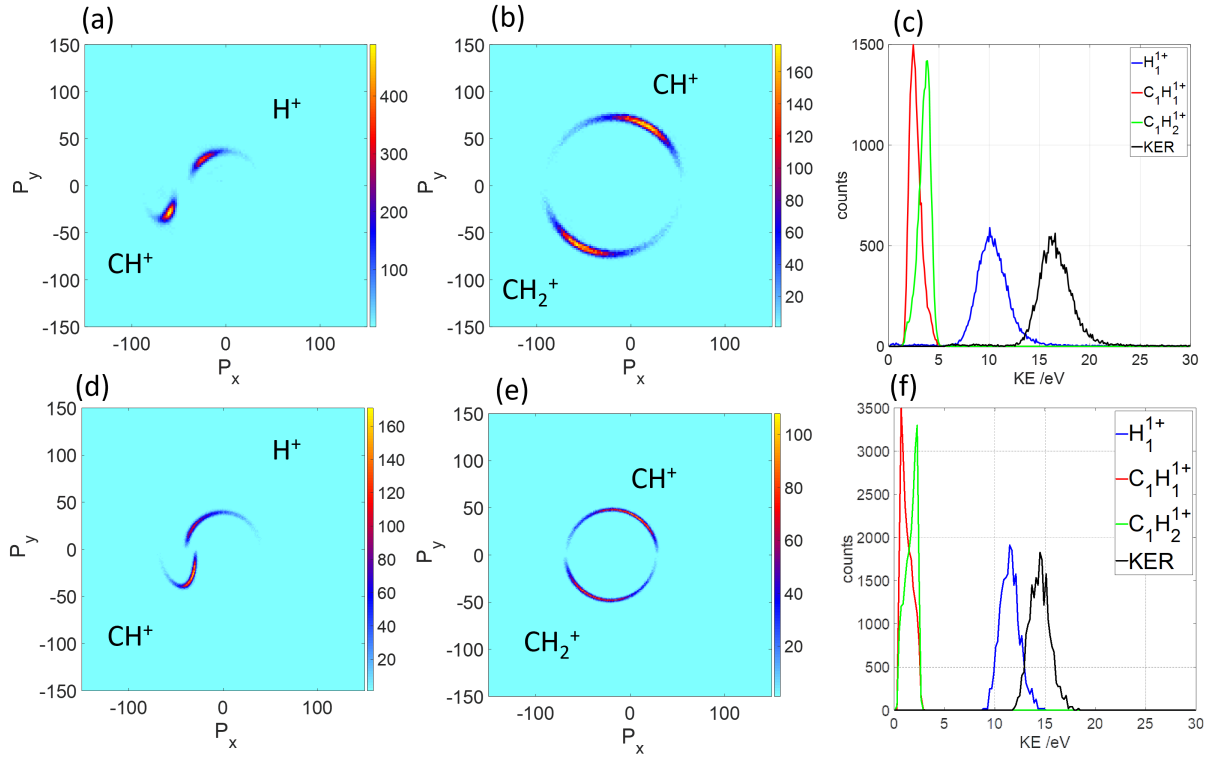

Figure A.16: *Three-body sequential fragmentation of ethylene via H^+ + $C_2H_3{}^{2+}$: simulation and experimental data comparison.*

(a)-(c) Separated H^+ + $C_2H_3{}^{2+}$ sequential breakup events from experimental data. (d)-(f) Coulomb explosion Simulation of sequential breakup channel via $CH_2{}^{2+}$ + $CH_2{}^+$. (a)(b) and (d)(e) are the relative non-normalized Newton diagrams. (c) and (f) are the kinetic energy distributions from experimental data and Coulomb explosion simulation respectively.

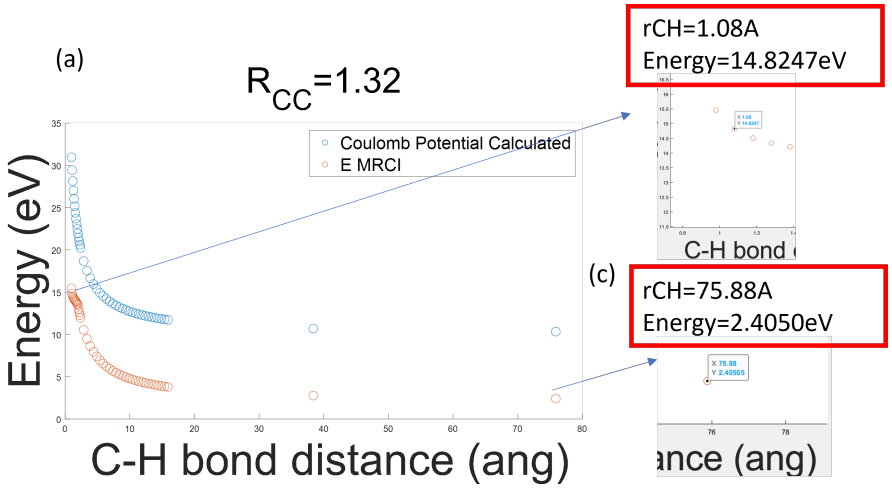

Figure A.17: *Energy difference from PES of triply-charged ethylene of C–H bond extension, C–C bond stays in Franck-Condon point. 1D projection of Fig. A.1.*

fixed at 75.88 Å (the C–H bond was already stretched in the first step).

The total calculated energy release of 2.5267 eV consists of a Coulomb energy release of 2.0484 eV (obtained from 2.4050 eV minus 0.3566 eV as shown in Fig. A.18), which corresponds to the potential energy difference when the C–H bond is stretched from its equilibrium length of 1.08 Å to 75.88 Å, while the C-C distance is held fixed at 150.92 Å (already stretched during the first step). An additional relaxation energy of 0.47829 eV, calculated by Dr. Paresh Modak (using r_{CC} = FC, with a C–C bond distance of 16.15 Å), is added to obtain the final theoretical KER.

In the second step, the $C_2H_3^{2+}$ fragment is assumed to undergo random rotation about its center of mass before undergoing Coulomb explosion into CH^+ and CH_2^+. We sampledd 21 random rotation angles uniformly distributed over the interval $(0, 2\pi]$. At the moment of the second breakup, the +2 charge is redistributed to the centers of mass of the resulting fragments, and a second Coulomb explosion propagating up to 1000 ps is performed. The momentum vectors of the second-step products are scaled to match a total kinetic energy release (KER) of 2.5267 eV.

The final momenta of CH^+ and CH_2^+ are computed as the vector sum of the scaled

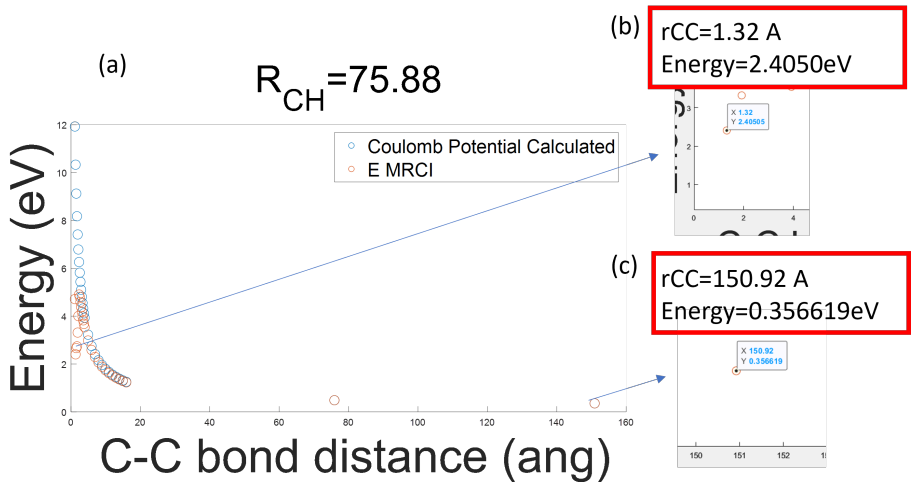

Figure A.18: *Energy difference from PES of triply-charged ethylene of C–C bond extension with C–H bond extended already to 75.88 Å. 1D projection of Fig. A.1.*

momentum of the second-step fragments (from the Coulomb explosion of $C_2H_3^{2+}$) and the scaled momentum of the rotating $C_2H_3^{2+}$ fragment from the first step. That is, both steps are individually scaled to match their respective energy releases before summation. The final momentum of the H^+ fragment is taken directly as the scaled momentum from the first step, since it undergoes no further fragmentation.

The resulting Newton diagrams, shown in Fig. 4.10. The gating condition used to isolate the sequential breakup pathway events via $H^+ + C_2H_3^{2+}$ is shown as the black box in Fig. 4.4(b).

The final simulation results for the sequential dissociation pathway via $H^+ + C_2H_3^{2+}$, as shown in Fig. 4.10, demonstrate good consistency with experimental observations of this isolated sequential fragmentation channel. However, the simulated kinetic energy (KE) distributions of CH^+ and CH_2^+ are lower than the experimental values. This discrepancy arises from the scaling factor used in the second step, where the predicted KER_{CH-CH_2} is 2.5267 eV, which is smaller than the experimentally observed value. Additionally, the simulated KE of H^+ is higher than that observed experimentally.

Nonetheless, the relative Newton diagram in Fig. 4.10 clearly exhibits features character-

istic of sequential fragmentation, including extended momentum tails that follow the initial two-body breakup of $H^+ + C_2H_3^{2+}$. These tails result from the spatial rotation of the $C_2H_3^{2+}$ fragment during the delay between fragmentation steps.

Fig. A.19, Fig. A.20, Fig. A.21, Fig. A.22, Fig. A.23, and Fig. A.24 are the different simulations for sequential breakup via different propagation time in the first step of $H^+ + C_2H_3^{2+}$ two-body Coulomb explosion simulation. These final simulation results of these different propagation times in the first step are not scaled.

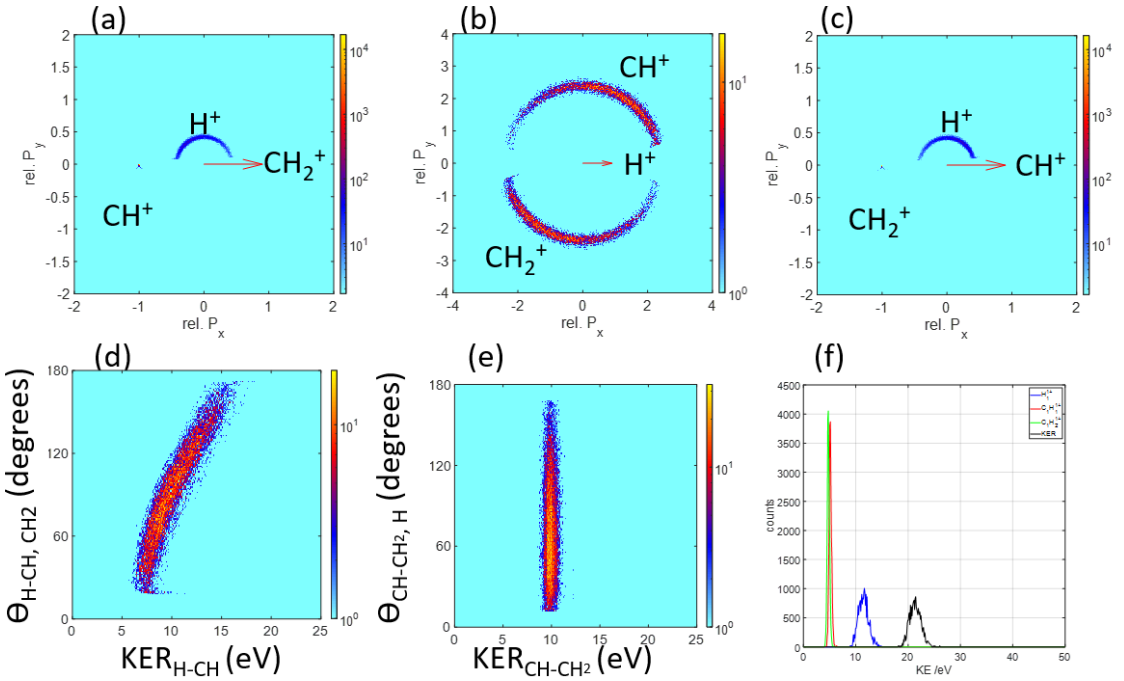

Figure A.19: *CES of three-body fragmentation of ethylene via $H^+ + C_2H_3^{2+}$ sequential breakup with initial propagation time at 1 ps.*

(a)-(c) Relative Newton diagrams of the $H^+ + CH^+ + CH_2^+$ fragmentation channel from the Coulomb explosion simulation of $H^+ + C_2H_3^{2+}$ sequential breakup of 1 ps propagation time after two-body Coulomb explosion. (d) $N(KER_{H-CH}, \Theta_{H-CH, CH_2})$ distributions for three-body fragmentation channel: $H^+ + CH^+ + CH_2^+$ from the Coulomb explosion simulation of $H^+ + C_2H_3^{2+}$ sequential breakup. (e) $N(KER_{CH-CH_2}, \Theta_{CH-CH_2, H})$ distributions for three-body fragmentation channel: $H^+ + CH^+ + CH_2^+$ from the Coulomb explosion simulation of $H^+ + C_2H_3^{2+}$ sequential breakup. (f) KER from the Coulomb explosion simulation of $H^+ + C_2H_3^{2+}$ sequential breakup.

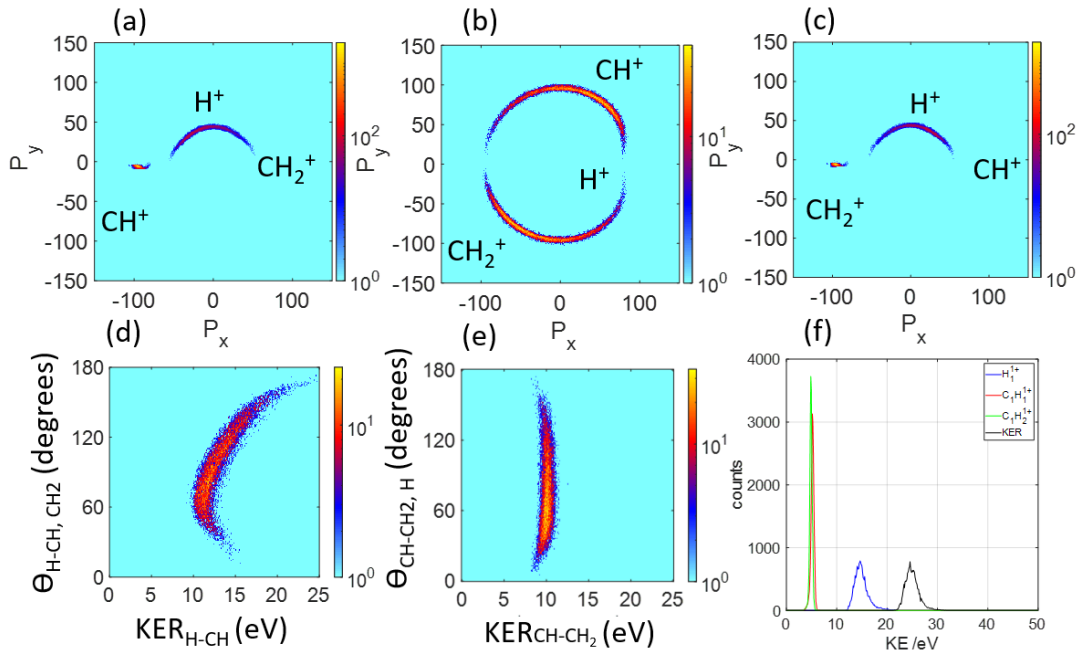

Figure A.20: *CES of three-body fragmentation of ethylene via H^+ + $C_2H_3^{2+}$ sequential breakup with initial propagation time at 100 fs.*

(a)-(c) Newton diagrams of the H^+ + CH^+ + $CH_2{}^+$ fragmentation channel from the Coulomb explosion simulation of H^+ + $C_2H_3^{2+}$ sequential breakup of 100 fs propagation time after two-body Coulomb explosion. (d) N (KER_{H-CH}, $\Theta_{H-CH,\ CH_2}$) distributions for three-body fragmentation channel: H^+ + CH^+ + $CH_2{}^+$ from the Coulomb explosion simulation of H^+ + $C_2H_3^{2+}$ sequential breakup. (e) the N(KER_{CH-CH_2}, $\Theta_{CH-CH_2,\ H}$) distributions for three-body fragmentation channel: H^+ + CH^+ + $CH_2{}^+$ from the Coulomb explosion simulation of H^+ + $C_2H_3^{2+}$ sequential breakup. (f) KER from the Coulomb explosion simulation of H^+ + $C_2H_3^{2+}$ sequential breakup.

A.2 Coulomb explosion imaging of four-body complete fragmentation of ethylene

A.2.1 Theoretical calculations provided

As shown in Fig. A.25, an energy difference of approximately 1 eV is observed between the cis- and trans-fragmentation pathways as shown in Fig. A.25, with the trans-fragmentation lying lower on the potential energy surface. This calculation is carried out by Dr. Paresh Modak (Kansas State University).

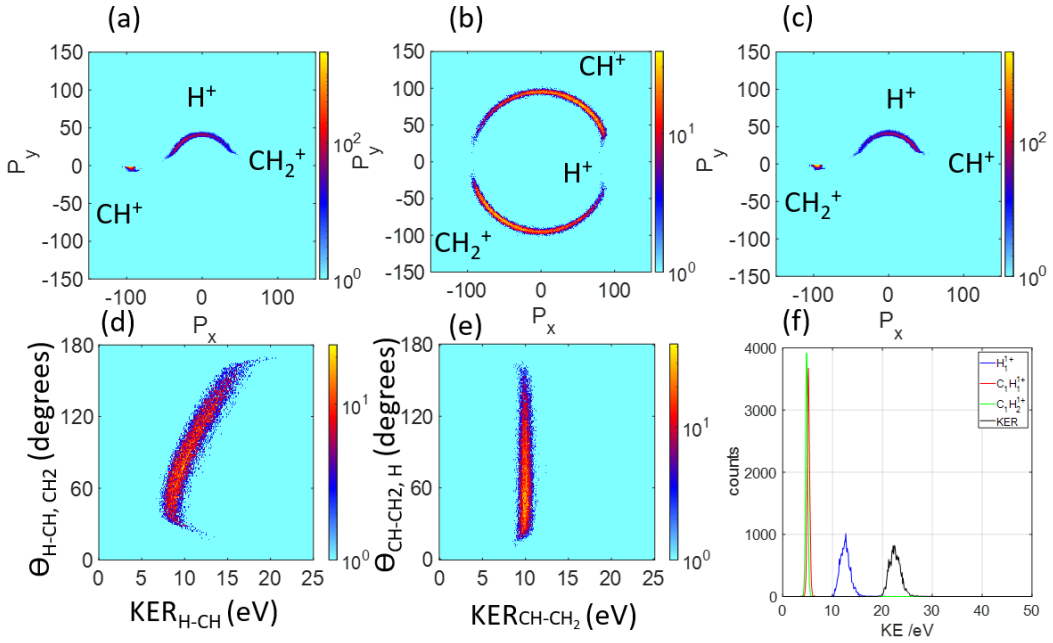

Figure A.21: *CES of three-body fragmentation of ethylene via H^+ + $C_2H_3^{2+}$ sequential breakup with initial propagation time at 300 fs.*

(a)-(c) Newton diagrams of the H^+ + CH^+ + $CH_2{}^+$ fragmentation channel from the Coulomb explosion simulation of H^+ + $C_2H_3^{2+}$ sequential breakup of 300 fs propagation time after two-body Coulomb explosion. (d) $N(KER_{H-CH}, \Theta_{H-CH,\ CH_2})$ distributions for three-body fragmentation channel: H^+ + CH^+ + $CH_2{}^+$ from the Coulomb explosion simulation of H^+ + $C_2H_3^{2+}$ sequential breakup. (e) the $N(KER_{CH-CH_2}, \Theta_{CH-CH_2,\ H})$ distributions for three-body fragmentation channel: H^+ + CH^+ + $CH_2{}^+$ from the Coulomb explosion simulation of H^+ + $C_2H_3^{2+}$ sequential breakup. (f) KER from the Coulomb explosion simulation of H^+ + $C_2H_3^{2+}$ sequential breakup.

A.2.2 Experimental data and simulation

Here we show the normalized and non-normalized Newton diagrams of four-body cis- (in Fig. A.28 and in Fig. A.27) and trans- (in Fig. A.28) fragmentation pathways. Fig. A.29 shows the four-body experimental data for 2000 V voltage difference along the spectrometer. Fig. A.30 shows the angular acceptance of 2000 V and 4000 V data sets. To analyze the angular acceptance distribution of each fragment ion, we plot the angular distribution of the detected ion fragments with respect to the laser polarization axis, alongside the corresponding kinetic energy distribution, using data from the four-body complete fragmentation

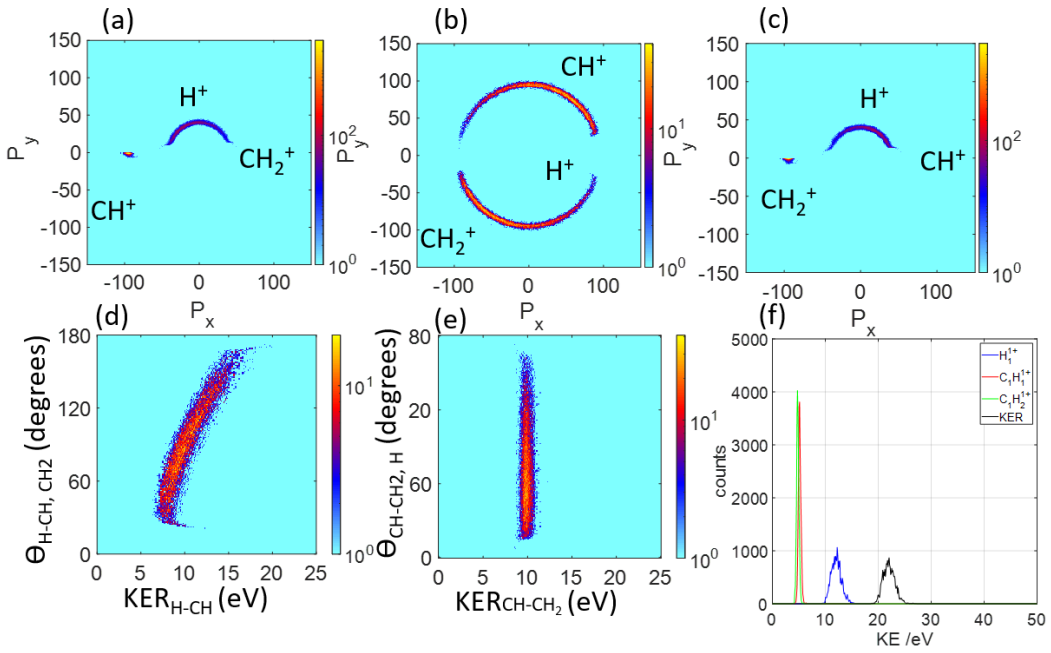

Figure A.22: *CES of three-body fragmentation of ethylene via* $H^+ + C_2H_3^{2+}$ *sequential breakup with initial propagation time at 500 fs.*

(a)-(c) Newton diagrams of the $H^+ + CH^+ + CH_2{}^+$ *fragmentation channel from the Coulomb explosion simulation of* $H^+ + C_2H_3^{2+}$ *sequential breakup of 500 fs propagation time after two-body Coulomb explosion. (d)* $N(KER_{H-CH}, \Theta_{H-CH,\ CH_2})$ *distributions for three-body fragmentation channel:* $H^+ + CH^+ + CH_2{}^+$ *from the Coulomb explosion simulation of* $H^+ + C_2H_3^{2+}$ *sequential breakup. (e) the* $N(KER_{CH-CH_2}, \Theta_{CH-CH_2,\ H})$ *distributions for three-body fragmentation channel:* $H^+ + CH^+ + CH_2{}^+$ *from the Coulomb explosion simulation of* $H^+ + C_2H_3^{2+}$ *sequential breakup. (f) KER from the Coulomb explosion simulation of* $H^+ + C_2H_3^{2+}$ *sequential breakup.*

channel of each data set.

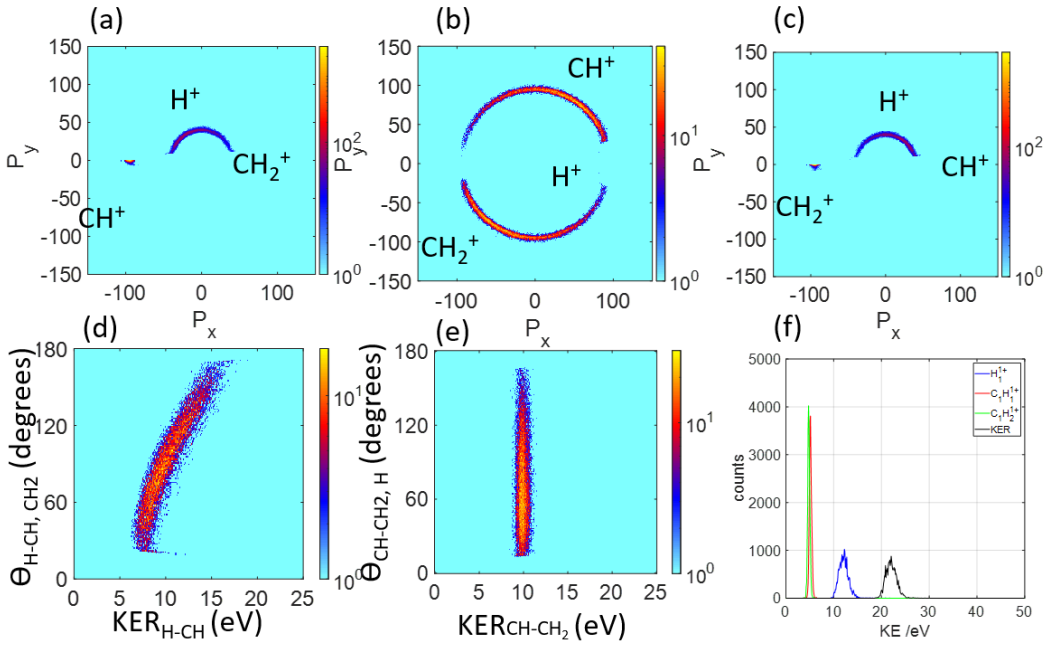

Figure A.23: *CES of three-body fragmentation of ethylene via H^+ + $C_2H_3^{2+}$ sequential breakup with initial propagation time at 700 fs.*

(a)-(c) Newton diagrams of the H^+ + CH^+ + $CH_2{}^+$ fragmentation channel from the Coulomb explosion simulation of H^+ + $C_2H_3^{2+}$ sequential breakup of 700 fs propagation time after two-body Coulomb explosion. (d) $N(KER_{H-CH}, \Theta_{H-CH,\ CH_2})$ distributions for three-body fragmentation channel: H^+ + CH^+ + $CH_2{}^+$ from the Coulomb explosion simulation of H^+ + $C_2H_3^{2+}$ sequential breakup. (e) the $N(KER_{CH-CH_2}, \Theta_{CH-CH_2,\ H})$ distributions for three-body fragmentation channel: H^+ + CH^+ + $CH_2{}^+$ from the Coulomb explosion simulation of H^+ + $C_2H_3^{2+}$ sequential breakup. (f) KER from the Coulomb explosion simulation of H^+ + $C_2H_3^{2+}$ sequential breakup.

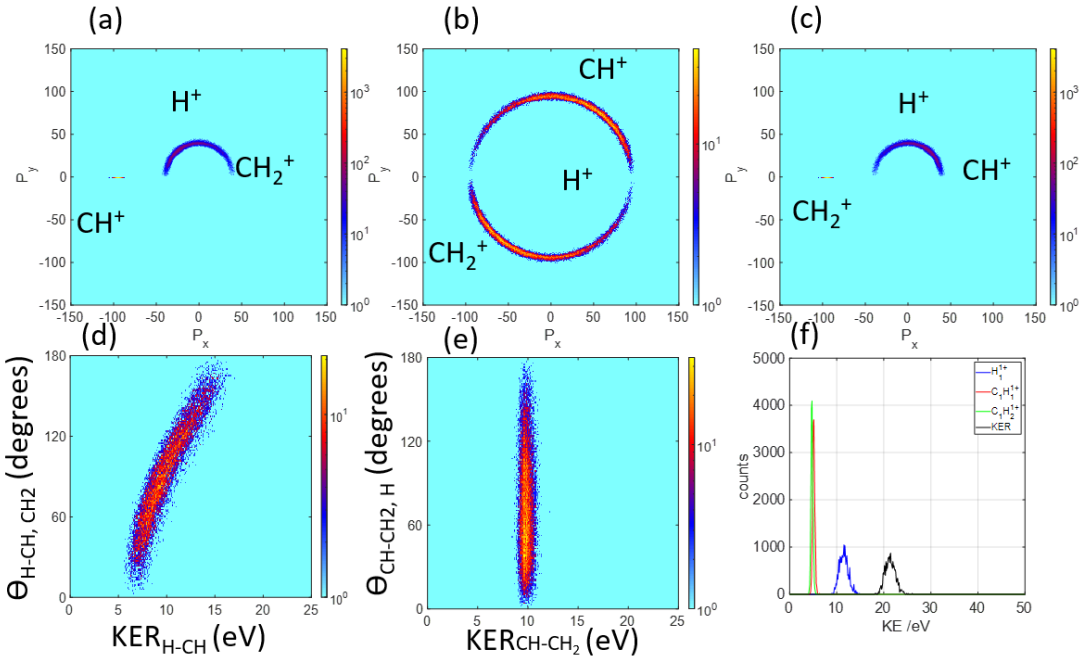

Figure A.24: *CES of three-body fragmentation of ethylene via H^+ + $C_2H_3^{2+}$ sequential breakup with initial propagation time at 50 ps.*

(a)-(c) Newton diagrams of the H^+ + CH^+ + $CH_2{}^+$ fragmentation channel from the Coulomb explosion simulation of H^+ + $C_2H_3^{2+}$ sequential breakup of 50 ps propagation time after two-body Coulomb explosion. (d) $N(KER_{H-CH}, \Theta_{H-CH, CH_2})$ distributions for three-body fragmentation channel: H^+ + CH^+ + $CH_2{}^+$ from the Coulomb explosion simulation of H^+ + $C_2H_3^{2+}$ sequential breakup. (e) the $N(KER_{CH-CH_2}, \Theta_{CH-CH_2, H})$ distributions for three-body fragmentation channel: H^+ + CH^+ + $CH_2{}^+$ from the Coulomb explosion simulation of H^+ + $C_2H_3^{2+}$ sequential breakup. (f) KER from the Coulomb explosion simulation of H^+ + $C_2H_3^{2+}$ sequential breakup.

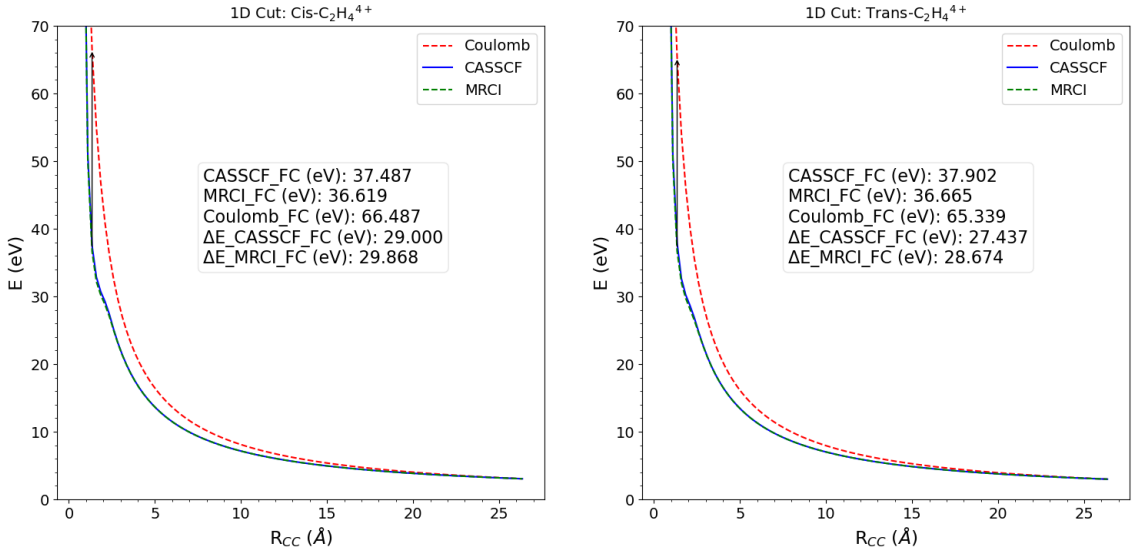

Figure A.25: *Theory calculation of quadruply-charged ethylene potential energy surface.*

1D cut of potential energy surfaces as a function of C–C bond distance calculated using different method combined with comparison. This calculation is carried by Dr. Paresh Modak (Kansas State University).

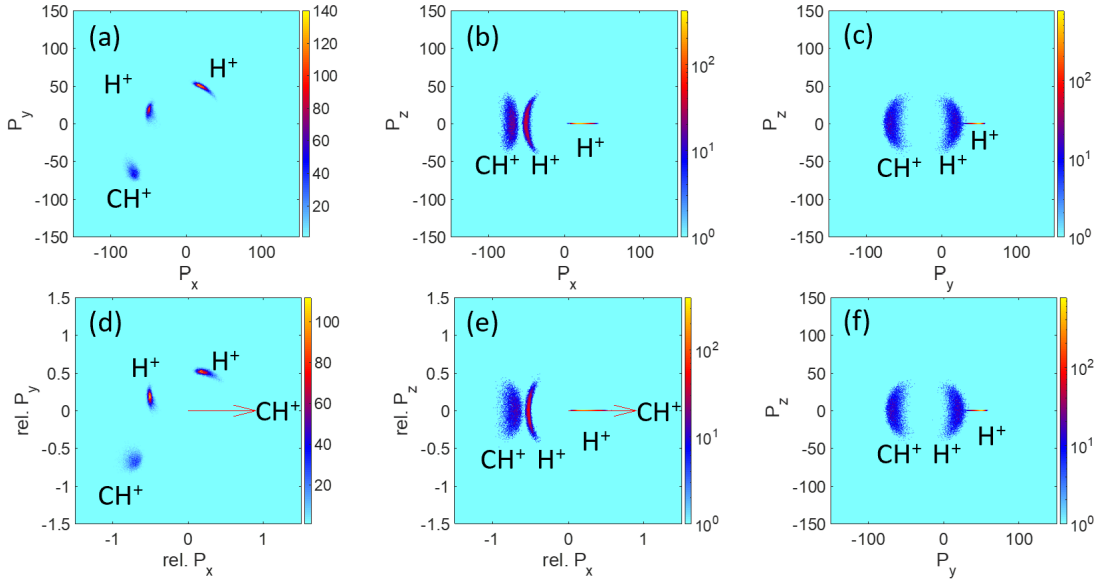

Figure A.26: *Newton diagrams of four-body cis-fragmentation of ethylene using CES. (a)-(c) are the non-relative Newton diagrams, the selected CH^+ ion fragment momentum used to define the P_x-axis is not plotted. (d)-(f) are the relative Newton diagrams, the selected CH^+ ion fragment momentum is plotted as a unit vector.*

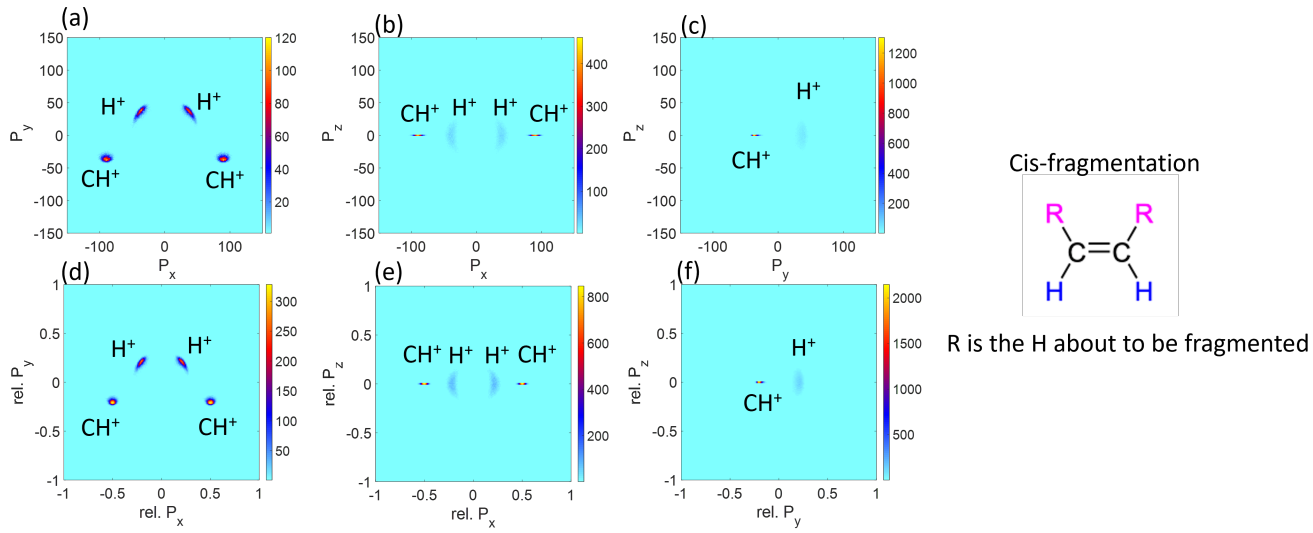

Figure A.27: *Modified Newton diagrams of four-body cis-fragmentation of ethylene from CES with different definitions of the momentum plane.*
(a)–(c) show the non-normalized Newton diagrams, while (d)–(f) show the corresponding normalized relative Newton diagrams. The momentum planes are shown as follows: (a) and (d) xy-plane, (b) and (e) xz-plane, and (c) and (f) yz-plane of the molecular frame.

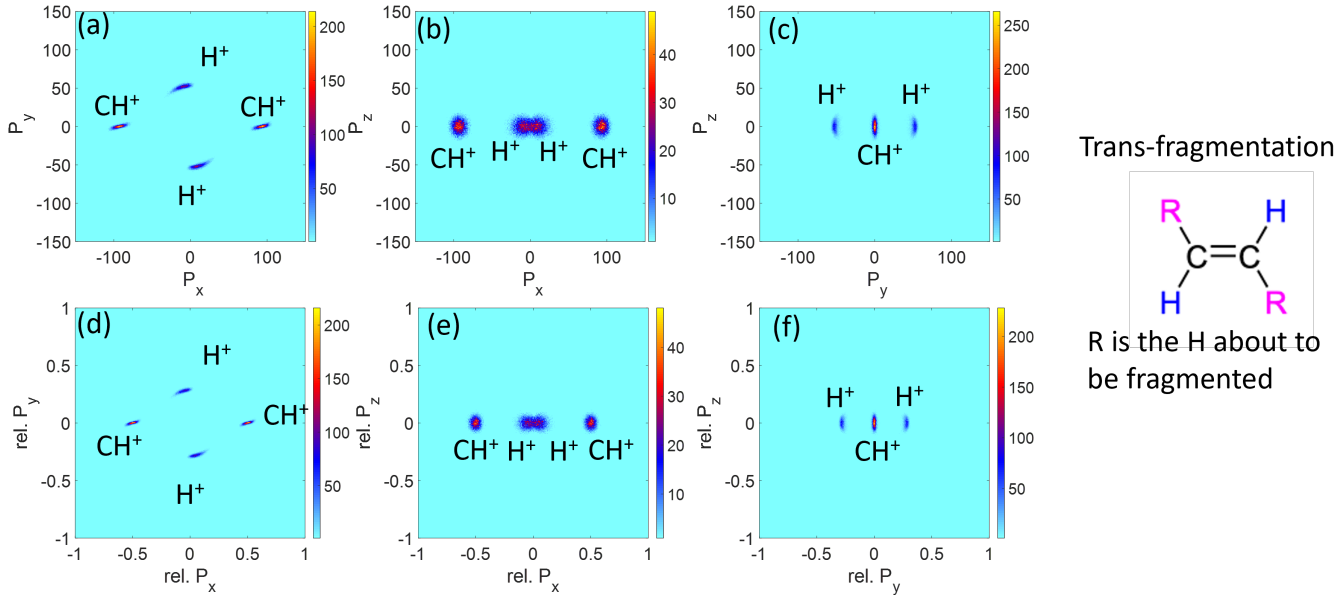

Figure A.28: *Modified Newton diagrams of four-body trans-fragmentation of ethylene from CES with different definitions of the molecular momentum plane.*
(a)–(c) show the non-normalized Newton diagrams, while (d)–(f) show the corresponding normalized relative Newton diagrams. The momentum planes are shown as follows: (a) and (d) xy-plane, (b) and (e) xz-plane, and (c) and (f) yz-plane of the molecular frame.

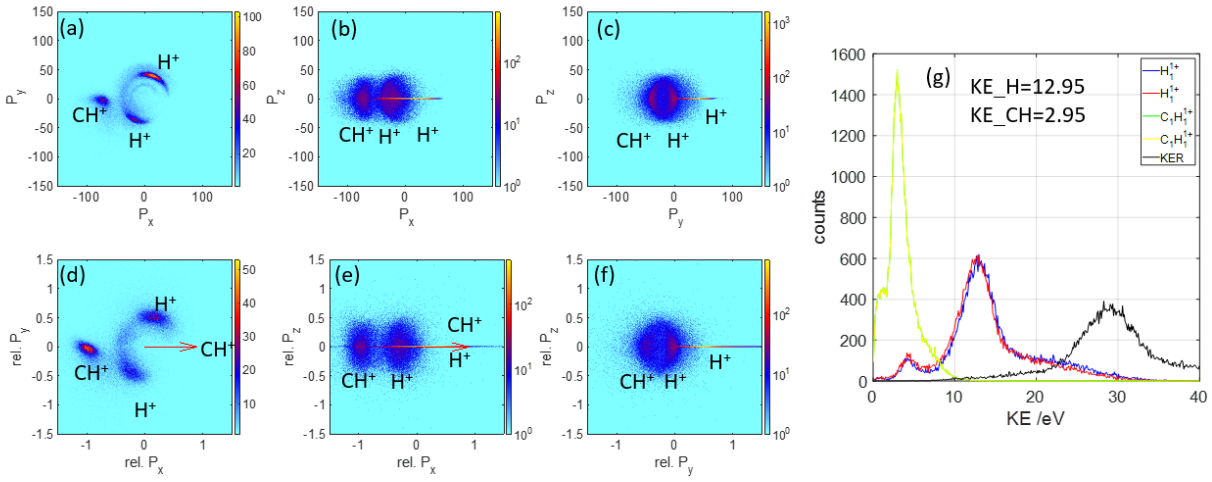

Figure A.29: *Newton diagrams of four-body complete fragmentation of ethylene (experimental data for 2000 V voltage difference along the spectrometer).*
(a)-(c) are the non-relative Newton diagrams, the selected CH^+ ion fragment momentum used to define the P_x axis is not plotted.(d)-(f) are the relative Newton diagrams, the selected CH^+ ion fragment momentum is plotted as a unit vector.(g) Kinetic Energy Release of the four-body complete fragmentation channel from the experiment.

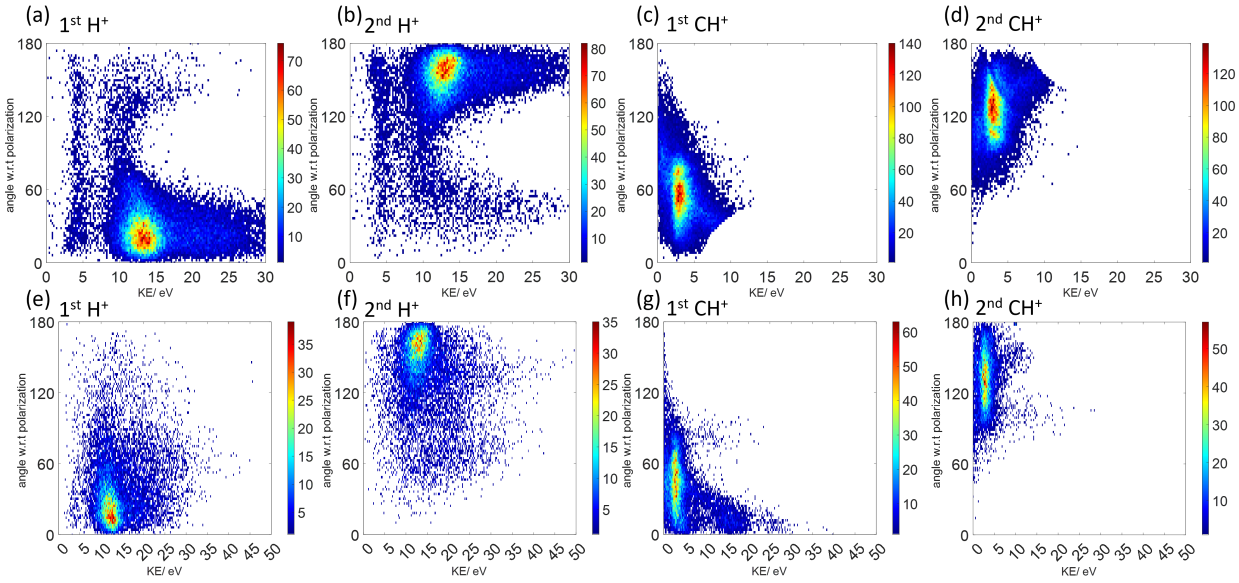

Figure A.30: *Detected ion fragments acceptance: angular distribution from four-body complete fragmentation of ethylene experimental data.*
(a)-(d) experimental data for 2000 V voltage difference along the spectrometer; (e)-(h) experimental data for 4000 V voltage difference along the spectrometer

Appendix B

Appendix B

This appendix includes content related to Chapters 3 and 5.

B.1 Appendix for Chapter 3

B.1.1 XFROG traces from third harmonic generation

The 400 nm cross-correlation signal from the XFROG trace from the experiment on thiophenone in Section 5.2, shown in Fig. B.1 in Appendix B.1, was used to characterize and optimize the prism-pair compressor in order to achieve the shortest possible third-harmonic pulse. The minimum calculated pulse duration for the 266 nm THG pulse was obtained when the prism position was near $X = -13$ (arb. units).

B.2 Appendix for Chapter 5

$H^+ + C^+ + O^+ + S^+$ **Coincidence fragmentation channel**

For further confirmation of pump–probe signal of thiophenone ring opening observed in Chapter 5, we also analyzed another four-body coincidence channel in addition to $C^+ +$

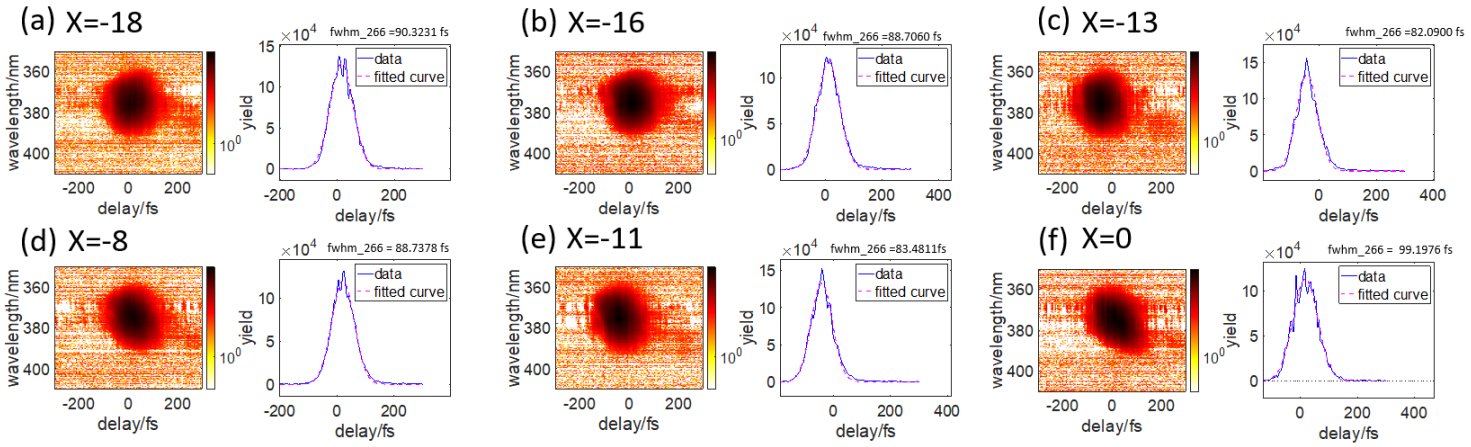

Figure B.1: *Prism compression of third harmonic generation*
Scanning the XFROG traces by varying the separation between the two prisms. The X value shown is in arbitrary units, representing the relative scanning distance.

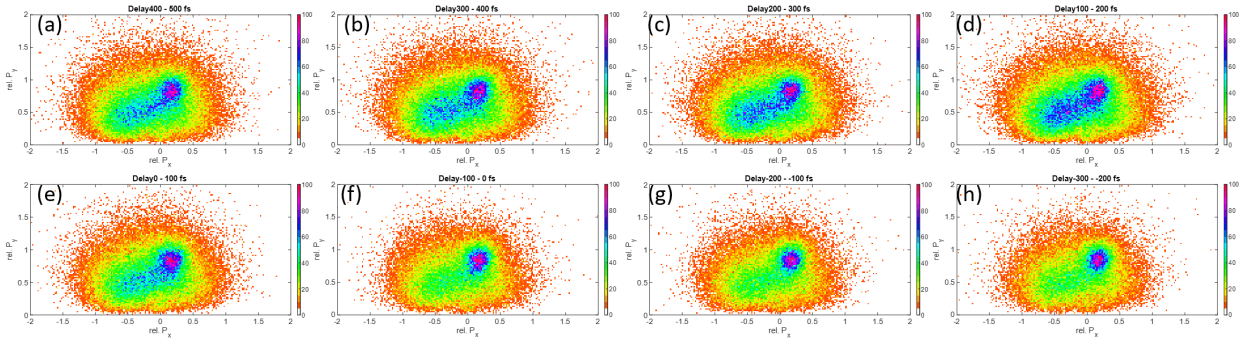

Figure B.2: *Newton diagrams of* O^+ *momentum distributions at different pump–probe delays from* $H^+ + C^+ + O^+ + S^+$ *coincidence channel of thiophenone experimental data.*

(a) UV–IR delay: 400–500 fs (UV early, IR late). (b) UV–IR delay: 300–400 fs (UV early, IR late). (c) UV–IR delay: 200–300 fs (UV early, IR late). (d) UV–IR delay: 100–200 fs (UV early, IR late). (e) UV–IR delay: 0–100 fs (UV early, IR late). (f) IR–UV delay: 0–100 fs (UV late, IR early). (g) IR–UV delay: 100–200 fs (UV late, IR early). (h) IR–UV delay: 200–300 fs (UV late, IR early).

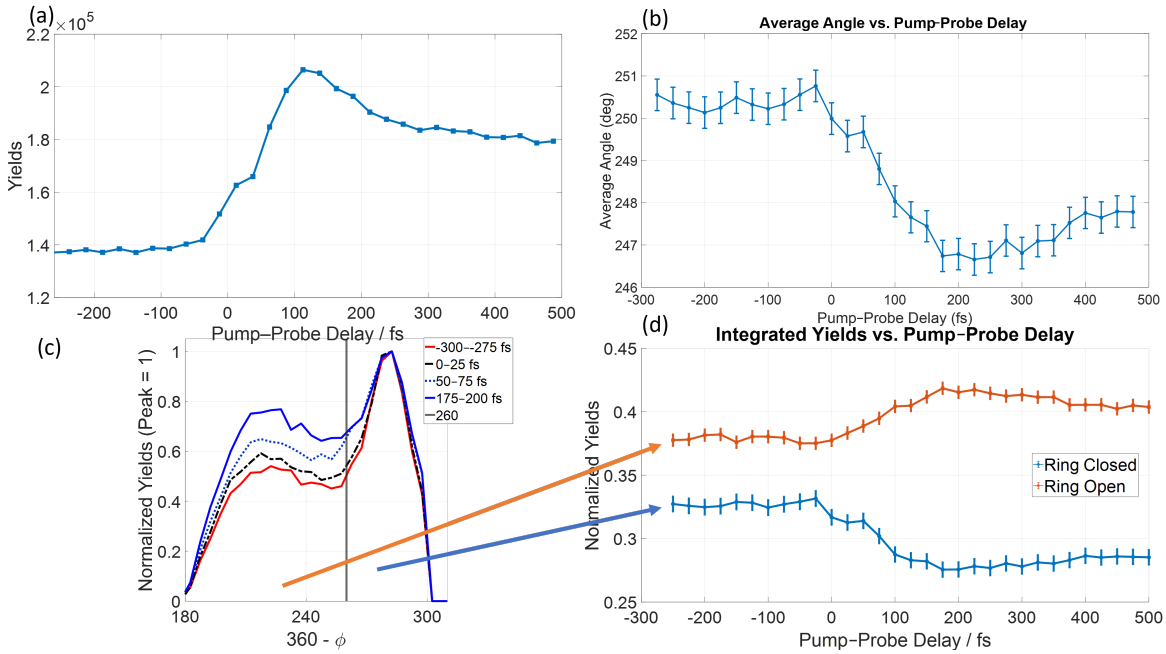

Figure B.3: *Quantified yield of* O^+ *momentum distribution projections from* $H^+ + C^+ + O^+ + S^+$ *coincidence channel of thiophenone experimental data.*

(a) Raw yield of the $C^+ + C^+ + O^+ + S^+$ *channel as a function of pump–probe delay, using a 25 fs time step. (b) Average relative angle of* (O^+, S^+) *at each pump–probe delay. (c) Normalized angular projections distribution relative angle of* (O^+, S^+) *from experimental data at pump–probe delay intervals of* -300 *to* -275 *fs, 0 to 25 fs, 50 to 75 fs, and 175 to 200 fs. The gray line is at* $\phi = 260°$*. (d) Integrated and normalized* O^+ *yield from (c) as a function of UV–IR pump–probe delay, grouped by angle: the orange curve corresponds to* $360° - \phi < 260°$ *(*$\phi > 100°$*), representing ring-open configurations; the blue curve corresponds to* $360° - \phi > 260°$ *(*$\phi < 100°$*), representing ring-closed configurations.*

$C^+ + O^+ + S^+$ channel discussed in Section 5.2.2, namely the $H^+ + C^+ + O^+ + S^+$ channel. Following the same analysis protocol described previously in Section 5.2.2, we examined the relative O^+ momentum angular distributions at various pump–probe delays. As shown in Fig. B.2, we observe a consistent trend: when the UV pulse arrives earlier, the O^+ momentum distribution becomes increasingly broad, indicating the onset of ring-opening dynamics. This broadening diminishes in the UV-late/IR-early regime, where the IR pulse precedes UV excitation and thus ionizes the molecule in its ground-state configuration before UV triggering conversion dynamics.

To quantify the pump–probe effect in this channel, we performed angular projections of the normalized relative O^+ momentum distributions, using the same definition of the azimuthal angle ϕ and the counterclockwise reference frame defined as $360° - \phi$, consistent with the analysis of the $C^+ + C^+ + O^+ + S^+$ channel, as shown in Fig. B.3(a). In this analysis, blue curves correspond to UV-early delays, while red curves represent IR-early delays. The normalized yields are presented in Fig. B.3(c), separated into two angular regions corresponding to ring-open configurations ($360° - \phi < 260°$) and ring-closed configurations ($360° - \phi > 260°$). The observed similar angular shift effect further supports our previous findings: when the UV pulse precedes the IR probe, the normalized yield of ring-opened structures increases, while the yield associated with ring-closed structures decreases.

The integrated yields are presented in Fig. B.3(b), and we observe the same trend as in the analysis of the previous coincidence channel. Specifically, the transition between ring-closed and ring-open configurations of thiophenone triggered by UV photons occurs predominantly within the first 200 fs when the UV pulse arrives early. This cross-channel consistency reinforces the robustness of our interpretation and further demonstrates the effectiveness of pump–probe Coulomb explosion imaging as a powerful technique for capturing ultrafast structural dynamics in photoexcited molecules.

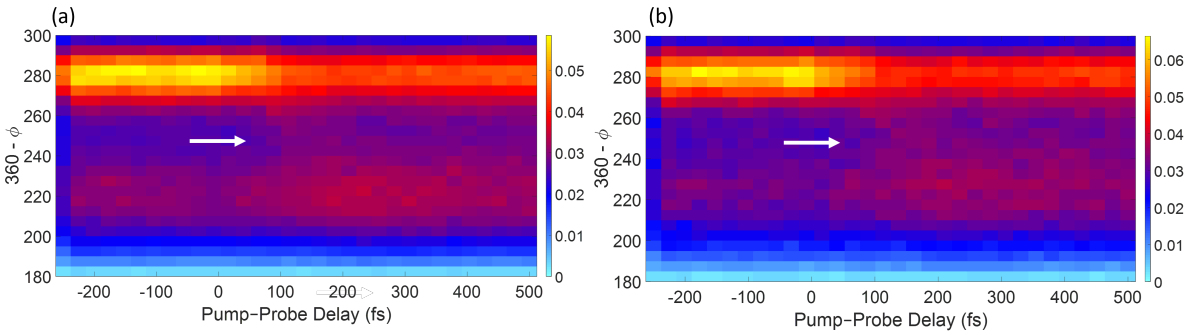

Figure B.4: *2D map of angular distribution of relative* O^+ *momentum yield of thiophenone experimental data.*

Linear scale of Fig. 5.14 (a) $H^+ + C^+ + O^+ + S^+$ *channel: 2D map of the angular distribution of relative* O^+ *momentum as a function of pump–probe delay. (b)* $C^+ + C^+ + O^+ + S^+$ *channel: 2D map of the angular distribution of relative* O^+ *momentum as a function of pump–probe delay. The white arrows indicate the ring-opening transition region.*

B.3 Acronyms

2,3-DHF	2,3-dihydrofuran
thiophenone	2(5H)-thiophenone
AIMS	Ab Initio Multiple Spawning
AIMD	Ab Initio Molecular Dynamics
CASSCF	Complete Active Space Self-Consistent Field
CE	Coulomb Explosion
CEI	Coulomb Explosion Imaging
CES	Coulomb Explosion Simulation
COLTRIMS	Cold Target Recoil Ion Momentum Spectroscopy
FEL	Free-Electron Laser
FC	Franck–Condon
fs, ps, ns	Femtosecond, picosecond, nanosecond
JRML	James R. Macdonald Laboratory
KE	Kinetic Energy
KED	Kinetic Energy Distribution
KER	Kinetic Energy Release
MRCI	Multi-Reference Configuration Interaction
PES	Potential Energy Surface
PIPICO	PhotoIon-PhotoIon Coincidence
THG	Third Harmonic Generation
TOF	Time-of-Flight
TRPES	Time-Resolved Photoelectron Spectroscopy
TSH	Trajectory Surface Hopping
UED	Ultrafast Electron Diffraction
XPS	X-ray Photoelectron Spectroscopy

B.4 List of Publications

1. Yanwei Xiong, Kurtis D. Borne, Andrés Moreno Carrascosa, Sajib Kumar Saha, Kyle J. Wilkin, Mengqi Yang, Surjendu Bhattacharyya, **Keyu Chen**, Wenpeng Du, Lingyu Ma, Nathan Marshall, João P. F. Nunes, Shashank Pathak, Zane Phelps, Xuan Xu, Haiwang Yong, Kenneth Lopata, Peter M. Weber, Artem Rudenko, Daniel Rolles, and Martin Centurion.
   Strong-field induced fragmentation and isomerization of toluene probed by ultrafast femtosecond electron diffraction and mass spectrometry.
   Faraday Discussions **228**, 39–59 (2021). doi:10.1039/D0FD00125B

2. Abdul R. Abid, Surjendu Bhattacharyya, Anbu S. Venkatachalam, Shashank Pathak, **Keyu Chen**, Huynh V. S. Lam, Kurtis D. Borne, Debadarshini Mishra, René C. Bilodeau, Ileana Dumitriu, Nora Berrah, Minna Patanen, and Daniel Rolles.
   Hydrogen migration in inner-shell ionized halogenated cyclic hydrocarbons.
   Scientific Reports **13**, 2107 (2023). doi:10.1038/s41598-023-28694-x

3. Huynh V. S. Lam, Anbu S. Venkatachalam, Surjendu Bhattacharyya, **Keyu Chen**, Kurtis D. Borne, Enliang Wang, Rebecca Boll, Till Jahnke, Vinod Kumarappan, Artem Rudenko, and Daniel Rolles.
   Differentiating three-dimensional molecular structures using laser-induced Coulomb explosion imaging.
   Physical Review Letters **132**, 123201 (2024). doi:10.1103/PhysRevLett.132.123201

4. Joseph C. Cooper, David M. P. Holland, Rebecca A. Ingle, Matteo Bonanomi, Davide Faccialà, Nelson de Oliveira, Abdul Rahman Abid, Julien Bachmann, Surjendu Bhattacharyya, Kurtis D. Borne, Michael Bosch, Martin Centurion, **Keyu Chen**, Ruaridh J. G. Forbes, Huynh V. S. Lam, Asami Odate, Artem Rudenko, Anbu Selvam Venkatachalam, Caterina Vozzi, Enliang Wang, Peter M. Weber, Michael N. R. Ashfold, Adam Kirrander, and Daniel Rolles.

Valence shell electronically excited states of norbornadiene and quadricyclane.
The Journal of Chemical Physics **160**, 064305 (2024). doi:10.1063/5.0187707

5. Surjendu Bhattacharyya, Enliang Wang, Kurtis D. Borne, **Keyu Chen**, Anbu S. Venkatachalam, Huynh V. S. Lam, Farzaneh Ziaee, Shashank Pathak, Anton Khmelnitskiy, Kevin D. Carnes, Charles W. Fehrenbach, Itzik Ben-Itzhak, Artem Rudenko, and Daniel Rolles.
Delayed dissociation and transient isomerization during the ultrafast photodissociation of the tribromomethane cation.
The Journal of Physical Chemistry Letters **15**(49), 12188–12196 (2024).
doi:10.1021/acs.jpclett.4c02838

6. Huynh V. S. Lam, Van-Hung Hoang, Anbu S. Venkatachalam, Surjendu Bhattacharyya, **Keyu Chen**, Sina M. Jacob, Sanduni Kudagama, Tu T. Nguyen, Daniel Rolles, Uwe Thumm, Artem Rudenko, and Vinod Kumarappan.
Simultaneous imaging of vibrational, rotational, and electronic wave-packet dynamics in a triatomic molecule.
Physical Review A **111**, L061101 (2025).

7. Till Jahnke, Sebastian Mai, Surjendu Bhattacharyya, **Keyu Chen**, Rebecca Boll, Maria Elena Castellani, Simon Dold, Ulrike Frühling, Alice E. Green, Markus Ilchen, Rebecca Ingle, Gregor Kastirke, Huynh V. S. Lam, Fabiano Lever, Dennis Mayer, Tommaso Mazza, Terence Mullins, Yevheniy Ovcharenko, Björn Senfftleben, Florian Trinter, Atia-Tul-Noor, Sergey Usenko, Anbu Selvam Venkatachalam, Artem Rudenko, Daniel Rolles, Michael Meyer, Heide Ibrahim, and Markus Gühr.
Direct observation of ultrafast symmetry reduction during internal conversion of 2-thiouracil using Coulomb explosion imaging.
Nature Communications **16**, 2074 (2025). doi:10.1038/s41467-025-57083-3

8. Alice E. Green, **Keyu Chen**, Surjendu Bhattacharyya, Felix Allum, Sergey Usenko,

Michael N. R. Ashfold, Thomas M. Baumann, Kurtis D. Borne, Mark Brouard, Michael Burt, Basile F. E. Curchod, Benjamin Erk, Ruaridh J. G. Forbes, Lea M. Ibele, Rebecca A. Ingle, Huynh V. S. Lam, Xiang Li, Kang Lin, Tommaso Mazza, Joseph W. McManus, Michael Meyer, Terrence Mullins, João P. F. Nunes, Daniel Rivas, Aljoscha Roerig, Arnaud Rouzée, Philipp Schmidt, John Searles, Björn Senfftleben, Henrik Stapelfeldt, Rico Mayro P. Tanyag, Florian Trinter, Anbu Selvam Venkatachalam, Enliang Wang, Emily M. Warne, Peter M. Weber, Thomas Wolf, Till Jahnke, Artem Rudenko, Rebecca Boll, and Daniel Rolles.

Visualizing the three-dimensional arrangement of hydrogen atoms in organic molecules by Coulomb explosion imaging.

Submitted (2025). Manuscript submitted for publication.

9. Enliang Wang, Surjendu Bhattacharyya, **Keyu Chen**, Kurtis D. Borne, Farzaneh Ziaee, Shashank Pathak, Huynh V. S. Lam, Anbu S. Venkatachalam, Xiangjun Chen, Rebecca Boll, Till Jahnke, Artem Rudenko, and Daniel Rolles.

   Time-Resolved Coulomb Explosion Imaging Unveils Ultrafast Ring Opening of Furan. *arXiv preprint* arXiv:2311.05099 (2023). Manuscript submitted for publication.